

Proceedings of **ISUD10**

The 10th International Symposium on Ultrasonic Doppler Methods
for Fluid Mechanics and Fluid Engineering

September 28-30, 2016
Tokyo, Japan



Edited by:
Hiroshige Kikura
Hideki Murakawa
Yuji Tasaka



Tokyo Tech



V.S.J.

Proceedings of the 10th International Symposium
on Ultrasonic Doppler Methods
for Fluid Mechanics and Fluid Engineering

28-30 September 2016, Tokyo, Japan

Editors:

- Hiroshige Kikura, Tokyo Institute of Technology
- Hideki Murakawa, Kobe University
- Yuji Tasaka, Hokkaido University

Organizing Committee:

- Hiroshige Kikura, Chair, Tokyo Institute of Technology
- Hideki Murakawa, Kobe University
- Sanehiro Wada, National Institute of Advanced Industrial Science and Technology
- Yuji Tasaka, Hokkaido University
- Masaaki Motozawa, Shizuoka University
- Nobuyoshi Tsuzuki, The Institute of Applied Energy
- Daisuke Ito, Kyoto University
- Tomonori Ihara, Tokyo University of Marine Science and Technology

Scientific Committee:

- V. Bareš, Czech Technical University in Prague, Czech Republic
- B. Birkhofer, Sika Services AG, Switzerland
- G. De Cesare, Ecole Polytechnique Fédérale de Lausanne (EPFL), Switzerland
- S. Eckert, Helmholtz-Zentrum Dresden-Rossendorf, Germany
- S. Fischer, UBERTONE, France
- D. Hurther, Université Grenoble Alpes, Laboratoire des Ecoulements Géophysiques et Industriels
- H. Kikura, Tokyo Institute of Technology, Japan
- R. Kotzé, Cape Peninsula University of Technology, South Africa
- M. Mori, Hokkaido University, Japan
- C. Rennie, University of Ottawa, Canada
- Y. Tasaka, Hokkaido University, Japan
- J. Wiklund, SP-Technical Research Institute of Sweden, Sweden
- J. Windhab, Chair, Swiss Federal Institute of Technology Zürich (ETH), Switzerland

Copyright © 2016 by Tokyo Institute of Technology

Published and distributed by:

Laboratory for Advanced Nuclear Energy
Institute of Innovative Research
Tokyo Institute of Technology
2-12-1 Ookayama, Meguro-ku, Tokyo, 152-8550 JAPAN

Table of Contents

Keynote Lecture 1

Non-destructive inspection & sub-wavelength characterization Robert MALKIN	1
--	---

Applied flows (1)

Quantitative evaluation of rheological properties for complex fluids using ultrasonic spinning rheometry Taiki YOSHIDA, Yuji TASAKA, Yuichi MURAI	5
Ultrasound measurements in a physical model of Czochralski crystal growth in a horizontal magnetic field Josef PAL, Ilmars GRANTS, Sven ECKERT, Gunter GERBETH	9
Influence of surface roughness on the flow behavior in TVF and WVF Lea POKORNY, Nayan J. SAIKIA, Yasushi TAKEDA, Erich J. WINDHAB.....	13
Ultrasonic flow measurement in liquid metal models of continuous steel casting Klaus TIMMEL, Thomas WONDRAK, Sven FRANKE, Sven ECKERT	17
Ultrasonic velocity profiling as a wall shear stress sensor for turbulent boundary layers Yuichi MURAI, Yuji TASAKA, Hyun Jin PARK.....	21

Next generation UVP session

A Miniature UVP hardware dedicated to process and environmental monitoring Marie BURCKBUCHLER, Stéphane FISCHER	25
Flow-Viz pulsed ultrasonic Doppler system with auto tuning of analog-, digital gain and threshold Johan WIKLUND, Stefano RICCI, Valentino MEACCI, Reinhardt KOTZÉ, Beat BIRKHOFFER	29
Development of a budget multiwave UVP system for two-phase flow measurement and some applications Tat Thang NGUYEN, Hideki MURAKAWA, Ngoc Hai DUONG, Hiroshige KIKURA.....	33
Influence of velocity distribution on accuracy of transit-time ultrasonic flow meter Ei MURAMATSU, Hideki MURAKAWA, Daiki HASHIGUCHI, Hitoshi ASANO, Saneshiro WADA, Noriyuki FURUICHI.....	37

Signal processing and methodology (1)

Evaluation of measurement accuracy of a dealiasing method for use with ultrasonic pulsed Doppler Daiki HASHIGUCHI, Hideki MURAKAWA, Ei MURAMATSU, Katsumi SUGIMOTO, Nobuyuki TAKENAKA, Noriyuki FURUICHI.....	41
--	----

Implementation of a staggered trigger algorithm by velocity difference dealising rules Fábio Rizental COUTINHO.....	45
Measuring error estimation of the ultrasound array flow mapping system by means of numerical simulations Sven FRANKE, Sven ECKERT.....	49
The signal processing of ultrasonic reflector recognition and tracking technique Antonin POVOLNY, Tomonori IHARA, Hiroshige KIKURA	53
Application of Partial Inversion Pulse on velocity profile and flowrate measurement using Ultrasonic Time-Domain Correlation method Sanehiro WADA, Takashi SHIMADA	57
Acoustic characterization of pulsed ultrasound sensors for improved non-invasive Pulsed Ultrasound Velocimetry through high-grade stainless steel pipes Tafadzwa J. SHAMU, Reinhardt KOTZÉ, Johan WIKLUND	61
 Keynote Lecture 2	
Positioning and navigation for free-fall type underwater observation system Yoshikazu KOIKE, Hiroaki MORINO, Etsuro SHIMIZU	65
 Signal processing and methodology (2)	
3D interpolation in a velocity field in sewers Sebastian CEDILLO, Mathieu LEPOT, Stéphane FISCHER, François H.L.R. CLEMENS.....	69
Development of focused air-coupled ultrasound velocity profiler for steam jet flow velocity measurement Keisuke TSUKADA, Hiroshige KIKURA.....	73
Simulation of ultrasound signals for the study of velocity estimation technique Fabio Rizental COUTINHO, Cesar Yutaka OFUCHI, Lucia V. R. de ARRUDA, Flavio NEVES Jr, Rigoberto E. M. MORALES	77
 Flow metering and flow mapping	
Non-intrusive flow velocity measurements in pressurized pipe with orifice Nicolas J. ADAM, Giovanni DE CESARE, Anton J. SCHLEISS	81
Flow rate measurement after 90 degrees bended pipe using multi-path ultrasound shift method Kei KURAMOTO, Tatsuya KAWAGUCHI, Isao SATOH, Takushi SAITO	85
Low velocity measurement on the Joule-heating flow by ultrasound velocity profiler method Jiaju ZHOU, Tomonori IHARA, Hiroshige KIKURA	89
Development of two-dimensional vector UVP with phased array technique Hiroshige KIKURA, Ari HAMDANI, Tomonori IHARA	93

Fundamental flows

- Ultrasonic characterization of 3-D thermal turbulence confined by moderate aspect ratio box**
Megumi AKASHI, Yuji TASAKA, Yuichi MURAI, Takatoshi YANAGISAWA97
- Appearance of 3D structures on quasi-2D convection rolls in a Rayleigh-Bénard convection imposed by horizontal magnetic field**
Wataru ISHIMI, Tobias VOGT, Yuji TASAKA, Takatoshi YANAGISAWA, Ataru SAKURABA,
Yuichi MURAI, Sven ECKERT101
- Ultrasonic Doppler velocimetry experiment of lead-lithium flow**
Yoshitaka UEKI, Yuya NOGUCHI, Juro YAGI, Teruya TANAKA, Takehiko YOKOMINE,
Masaru HIRABAYASHI, Kuniaki ARA, Tomoaki KUNUGI, Akio SAGARA105
- Transition of patterns in liquid metal convection under a horizontal magnetic field**
Takatoshi YANAGISAWA, Yuji TASAKA, Ataru SAKURABA, Takehiro MIYAGOSHI,
Yozo HAMANO109
- Measurements of a three-dimensional flow in a cube by means of an ultrasound array Doppler velocimeter (UADV)**
Vladimir GALINDO, Richard NAUBER, Sven FRANKE, Dirk RÄBIGER, Lars BÜTTNER,
Norman THIEME, Hannes BEYER, Jürgen CZARSKE, Sven ECKERT113
- On some influences of the geometry of a simplified flip-flop jet nozzle**
Hiroyuki OTA, Kazuki UMEMURA, Tatsuya INOUE, Hirochika TANIGAWA, Katsuya HIRATA117

Applied flow (2)

- A novel design of ultrasonic spinning rheometry**
Yuji TASAKA, Taiki YOSHIDA, Yuichi MURAI121
- Determining the thermal flow structure inside fermenters with different shapes using Ultrasonic Doppler Velocimetry**
Heiko MEIRONKE, David KASCH, Richard SIEG125
- Bubbly flow measurement in high temperature molten salt**
Tomonori IHARA, Keisuke TSUKADA, Hiroshige KIKURA, Horst-Michael PRASSER129
- Study of the rheological properties of the retropulsive jet build by the antral contraction wave in a simplified artificial stomach**
Damien DUFOUR, Franz X. TANNER, Kathleen FEIGL, Yasushi TAKEDA, Stéphane FISCHER,
Erich J. WINDHAB133

Environmental flows

- Velocity profile measurements in bore waves**
Davide WÜTHRICH, Michael PFISTER, Giovanni DE CESARE, Anton J. SCHLEISS137

Velocity profiles of turbidity currents flowing over a flat bed	
Sabine CHAMOUN, Giovanni DE CESARE, Anton J. SCHLEISS	141
Suspended sediment characterization by multifrequency acoustics	
Philippe SCHMITT, Anne PALLARÈS, Stéphane FISCHER, Marcus Vinicius DE ASSIS	145
Local velocity measurements in gravity-driven flows with intense bedload of coarse particles	
Vojtěch BAREŠ, Štěpán ZROSTLÍK, Tomáš PICEK, Jan KRUPIČKA, Václav MATOUŠEK	149
Instantaneous ultrasonic velocity profiling using in-situ sensor in real sewer flow	
Martin JAEGER, Frank BLUMENSAAT, Vojtěch BAREŠ, Stéphane FISCHER	153
Special Lecture	
Access technology using robots for decommissioning tasks	
Gen ENDO	157

Author Index

Adam, N.J.	81	Miyagoshi, T.	109
Akashi, M.	97	Morales, R.E.M.	77
Ara, K.	105	Morino, H.	65
Asano, H.	37	Murai, Y.	5, 21, 97, 101, 121
Bareš, V.	149, 153	Murakawa, H.	33, 37, 41
Beyer, H.	113	Muramatsu, E.	37, 41
Birkhofer, B.	29	Nauber, R.	113
Blumensaat, F.	153	Neves Jr, F.	77
Burckbuchler, M.	25	Nguyen, T.T.	33
Büttner, L.	113	Noguchi, Y.	105
Cedillo, S.	69	Ofuchi, C.Y.	77
Chamoun, S.	141	Ota, H.	117
Clemens, F.H.L.R.	69	Pal, J.	9
Coutinho, F.R.	45, 77	Pallarès, A.	145
Czarske, J.	113	Park, H.J.	21
De Arruda, L.V.R.	77	Pfister, M.	137
De Assis, M.V.	145	Picek, T.	149
De Cesare, G.	81, 137, 141	Pokorny, L.	13
Dufour, D.	133	Povolny, A.	53
Duong, N.H.	33	Prasser, H.-M.	129
Eckert, S.	9, 17, 49, 101, 113	Räbiger, D.	113
Endo, G.	157	Ricci, S.	29
Feigl, K.	133	Sagara, A.	105
Fischer, S.	25, 69, 133, 145, 153	Saikia, N.J.	13
Franke, S.	17, 49, 113	Saito, T.	85
Furuichi, N.	37, 41	Sakuraba, A.	101, 109
Galindo, V.	113	Satoh, I.	85
Gerbeth, G.	9	Schleiss, A.J.	81, 137, 141
Grants, I.	9	Schmitt, P.	145
Hamano, Y.	109	Shamu, T.J.	61
Hamdani, A.	93	Shimada, T.	57
Hashiguchi, D.	37, 41	Shimizu, E.	65
Hirabayashi, M.	105	Sieg, R.	125
Hirata, K.	117	Sugimoto, K.	41
Ihara, T.	53, 89, 93, 129	Takeda, Y.	13, 133
Inoue, T.	117	Takenaka, N.	41
Ishimi, W.	101	Tanaka, T.	105
Jaeger, M.	153	Tanigawa, H.	117
Kasch, D.	125	Tanner, F.X.	133
Kawaguchi, T.	85	Tasaka, Y.	5, 21, 97, 101, 109, 121
Kikura, H.	33, 53, 73, 89, 93, 129	Thieme, N.	113
Koike, Y.	65	Timmel, K.	17
Kotzé, R.	29, 61	Tsukada, K.	73, 129
Krupička, J.	149	Ueki, Y.	105
Kunugi, T.	105	Umemura, K.	117
Kuramoto, K.	85	Vogt, T.	101
Lepot M.	69	Wiklund, J.	29, 61
Malkin, R.	1	Wada, S.	37, 57
Matoušek, V.	149	Windhab, E.J.	13, 133
Meacci, V.	29	Wondrak, T.	17
Meironke, H.	125	Wüthrich, D.	137

Yagi, J.	105	Yoshida, T.	5, 121
Yanagisawa, T.	97, 101, 109	Zhou, J.	89
Yokomine, T.	105	Zrostlík, Š.	149

Non-destructive inspection & sub-wavelength characterization

Robert Malkin¹

¹Ultrasonics and Non Destructive Testing, Mechanical Engineering, Queens School of Engineering, University of Bristol, Bristol, United Kingdom

Phased array transducers have in recent years allowed for ever increasing imaging capabilities in the field of non-destructive inspection. By capturing the maximum possible amount of acoustic information we are able to utilize imaging algorithms which bring unparalleled resolution and flexibility to industrial inspections. This talk will cover the background of acoustic array imaging and detail current trends and ongoing challenges being addressed at the University of Bristol.

Keywords: total focusing method, phased array transducer, ultrasonic, sub-wavelength imaging, defect characterization,

1. Introduction

Collectively the terms non-destructive inspection (NDI), non-destructive testing (NDT) and non-destructive evaluation (NDE) cover a range of analysis techniques to assess the properties of a material/structure without causing damage. They play a central role in inspections of safety critical structures in areas such as aerospace, nuclear engineering and the oil & gas industries. Common methods include; visual inspections (economical, safe and rapid but limited to surfaces only), dye penetrant (economical and minimally invasive but limited to surface breaking defects), x-ray (inspects whole structure at high resolution but dangerous, slow and size limited), eddy current (high resolution but offers relatively shallow surface penetration) and ultrasonic testing (safe, deep sample penetration but can be limited by acoustic scattering and physical access).

Ultrasonic testing was first utilized in 1931 to locate flaws in solid metal sheets. Since then it has become an advanced inspection technique amenable to a range of materials, including numerous applications in medicine. Here we present an overview of the acoustic NDT imaging research conducted at the University of Bristol.

2. Array imaging

The current ‘gold standard’ array imaging technique, developed at Bristol, is the total focusing method (TFM). It allows for unprecedented imaging resolution and flexibility. TFM relies on acquiring the maximum amount of acoustic information possible and then applying post-capture processing for imaging. It is best described in two stages, the data acquisition and the TFM algorithm.

2.1 Phased array transducer

In recent years phased array transducers have become more sophisticated and affordable. Traditionally they come in linear, annular or 2D array types with element numbers from 16 to 256. The most common inspection materials in engineering are metallic and given their finite grain sizes (which result in scattering and signal degradation) the acoustic frequencies used are usually between 2-20MHz. For flat surfaces, arrays can be used

in direct contact (with coupling gel applied at the interface) or for complex geometries they may be used in immersion where water couples the acoustic wave from the array to the material/structure under inspection.

2.2 Full matrix capture

TFM relies on acquiring all the possible acoustic information for a phased array [1]. This is done by transmitting an acoustic pulse on a single element and receiving the time-domain data on all others. This is done sequentially for all elements in the array (this places some limits on using TFM for non-stationary objects). For an array with n elements this results in n^2 measurements. The transmitting, receiving and digitizing of the acquired data is usually performed with an array controller, see Figure 1.



Figure 1: A commercial phased array controller, phased array, metal sample and imaging software. (Image courtesy of MicroPulse USA.)

2.3 Total focusing method

In TFM we first define an imaging area of interest within close proximity to the array, shown in Figure 2. Within this region we generate a grid of imaging pixels.

The intensity of the image at each point is given by $I(x,z)$ as shown in Eq 1.

$$I(x, z) = \left| \sum h_{t_x, r_x} \left(\frac{\sqrt{(x_{t_x} - x_{ref})^2 + z_{ref}^2} + \sqrt{(x_{r_x} - x_{ref})^2 + z_{ref}^2}}{c} \right) \right| \quad (1)$$

Where h is Hilbert transform of the time domain signal and c the wave speed.

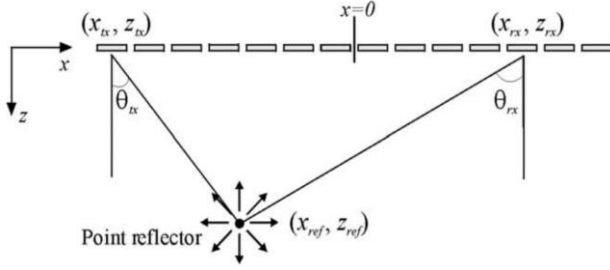


Figure 2: Imaging area of interest below a transducer. Here we show 14 elements (where subscript t_x and r_x are transmit and receive elements respectively) of a transducer and a single point in the TFM image (at x_{ref}, z_{ref}).

An example TFM image is shown in Figure 3.

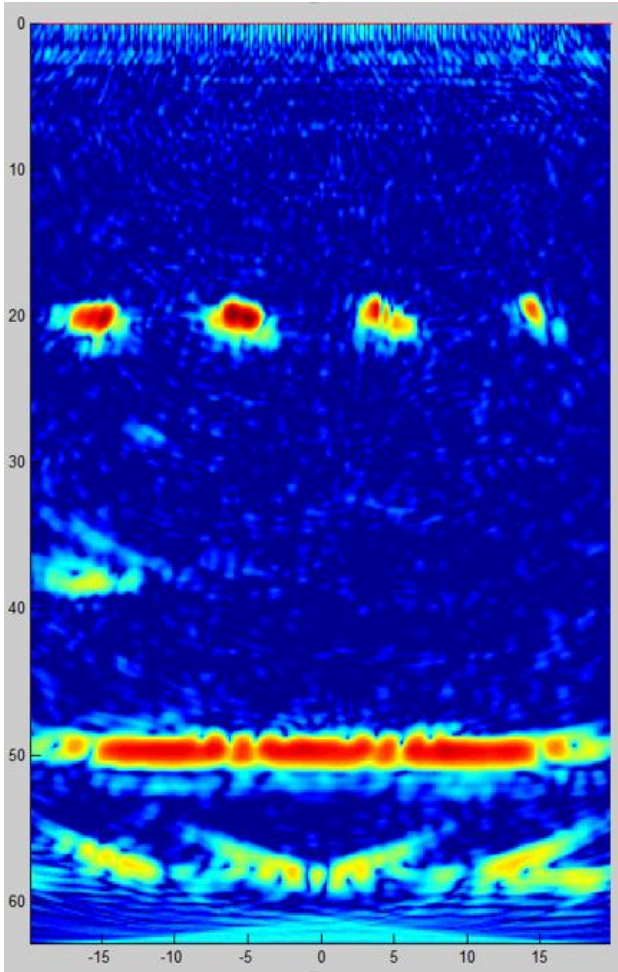


Figure 3: TFM image of stainless steel test specimen. Image shows 4 defects at 20mm depth and the back face of the specimen at 50mm.

2.4 Complex geometries

For inspections where the surfaces of the material/structure are not suitable for direct contact with the probe, immersion imaging is undertaken. To compensate for the combination of water between the array elements and surface, and a non-flat surface, the TFM imaging algorithm is modified using delay laws and ray tracing. This added complexity increases the computational resources needed for imaging (although this is becoming

less of an issue).

3D volumetric imaging using TFM is also possible using a 2D array type transducer. Computational resources for 3D imaging are however significantly higher given the additional dimension for a 3D image.

3. Sub-wavelength characterization

For safety critical systems where a defect is identified there is a worst-case scenario approach to assessing the severity of the defect. This will often result in structures with benign defects being taken out of service needlessly. This has been a key driver in our work to accurately characterize a defect.

The image shown in Figure 3 shows 4 approximately circular defects. In reality these defects are 4 flat slots 1mm in length at 4 different rotations (i.e. $- / / \backslash$). At 5MHz in stainless steel the wavelength is ≈ 1.2 mm (while higher frequencies would theoretically yield increased resolution they also result in greater scattering which limits imaging resolution). Using TFM our resolution is approximately equal to that of 1-2 wavelengths.

Characterizing a defect smaller than a wavelength can be performed by examining the scattering matrix of a defect.

3.1 S-matrix

The scattering matrix, or S-matrix, describes the amplitude and phase of the scattered field of a defect in the far field, and has been shown to encode the far-field information arising from all wave-scatterer interactions [2]. Let \mathbf{r} be the position vector of a point in the x - z plane which in polar coordinates is given by, $\mathbf{r} = (r, \theta)$; here $r = |\mathbf{r}|$ and θ is measured from the positive z -axis. For 2-D problems, the far-field scattering amplitude is defined by Eq 2, [3].

$$u^{SC}(\mathbf{r}) = \sqrt{\frac{2}{\pi}} e^{-\frac{i\pi}{4}} \frac{e^{ikr}}{\sqrt{kr}} S(\theta) \quad (2)$$

Where $i^2 = -1$, $k = \omega/c_L$ and c_L is the longitudinal wave velocity. For a given angular frequency, ω , $S(\theta, \omega)$ gives the field scattered in the direction θ [4]. An example S matrix is shown in Figure 4.

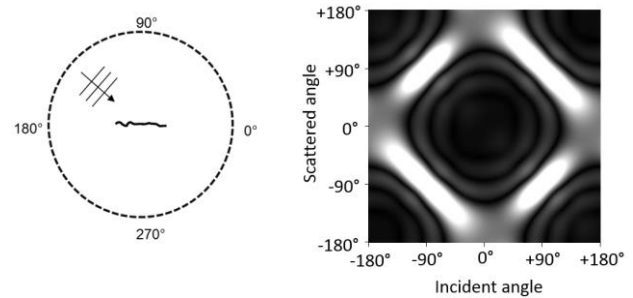


Figure 4: S-Matrix. Left: The S-matrix is defined as the far-field amplitude of a scattered plane wave (shown with an incidence angle of $\approx 135^\circ$) for all incidence angles. Right: Normalized scattering matrix of a defect (amplitude shown from 0-1). The S-matrix for a 2mm flat crack at 5MHz. Each S-matrix is singular and unique for a given defect.

3.2 Defect database

Given that each S-matrix maps uniquely to a single defect

geometry if we compare an experimentally acquired S-matrix, S_{EXP} , to a database of pre-calculated S-matrices, S_{CALC} , we should be able to characterize the defect (for a flat crack this would be its length and rotation). This relies on S_{EXP} being contained within our S_{CALC} database. To demonstrate this we compute a large number of S-matrices covering a limited type of defect: flat cracks from 0.2-2.0mm in length, at all rotations, at frequencies between 2-20MHz. Per frequency this gave us 5400 S_{CALC} entries in our database. S_{CALC} were computed using a highly efficient finite element approach [5].

3.3 Comparison of S-matrices

An important aspect of searching our database for a match between S_{CALC} and S_{EXP} is the comparison metric. We have used the structural similarity metric (SSIM) which gives a correlation (0 to 1) of the similarity between two datasets. The SSIM has been shown to be well suited to such an application [6].

When comparing the 4 S_{EXP} from Figure 3 to our database the SSIM correlation values were >0.97 . Low SSIM values would indicate that the real defect is not contained within our database.

3.4 Measurement certainty

The usual outcome of a database search will be a number of SSIM scores (the number being equal to the number of database entries). While choosing the maximum SSIM score tells us which pair of S_{EXP} & S_{CALC} are most similar it does not give us any information on the possible error tolerance of our comparison result. By exploring the information contained within an S-matrix and incorporating measurement noise we have proposed a method of measuring the error of our characterization, e.g. crack length 1.2 ± 0.2 mm, rotation $74 \pm 6^\circ$ (detailed in [4]).

3.5 General classification

In order to expand the classification capability of our database based approach we can ‘simplify’ the geometry of a defect using principle component analysis (PCA) and dynamic classifiers [7]. This approach allows us to classify the general nature of a defect with estimates of its shape/orientation without having to use an impractically large database, the approach also benefits from being inherently insensitive to noise as may be contained within an S_{EXP} . Recent results, shown in Figure 5, demonstrate that we can accurately estimate the shape of a defect. More accurate geometry estimates may be theoretically possible, but may not yield real world benefits.

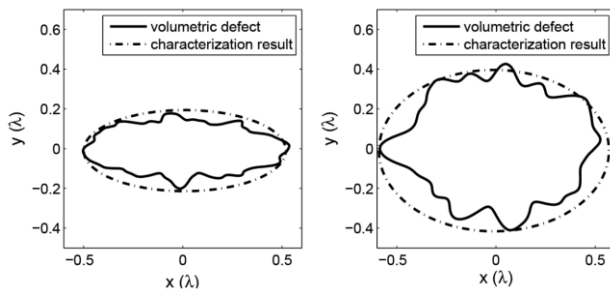


Figure 5: Accurate characterization of volumetric defects using a dynamic classifier approach.

4. Future work

With increasing computing power, phased array acoustic imaging systems are likely to become a ubiquitous part of inspection regimes. Phased array transducers are now offered in a range of types across a wide range of frequencies. The work of the Ultrasonics and Non Destructive Testing group at the University of Bristol will continue to develop imaging algorithms and characterization approaches to increase the capabilities of phased array transducers. Explorations into non-linear acoustic imaging are currently underway with promising initial results.

5. Summary

Non destructive inspections of materials/structures is a growing field of academic study and industrial utilisation. Advancements in computational techniques have allowed for the imaging of internal structures with unprecedented detail. Along with large defect databases and efficient searching algorithms we are able to locate a defect and classify its shape, which is vital for assessing its severity.

References

- [1] Holmes C, *et al.*: Post-processing of the full matrix of ultrasonic transmit–receive array data for non-destructive evaluation, *NDT&E*. 38 (2005), 701-711.
- [2] Achenbach JD: Quantitative nondestructive evaluation, *Int J Solids Struct*. 37 (2000), 13-27.
- [3] Martin PA: Multiple Scattering - interaction of time-harmonic waves with N obstacles. Cambridge University Press, Cambridge (2006).
- [4] Malkin R, *et al.*: A numerical database for ultrasonic defect characterisation using array data: Robustness and accuracy, *NDT&E*. 83 (2016), 94-103.
- [5] Velichko A, *et al.*: A generalized approach for efficient finite element modeling of elastodynamic scattering in two and three dimensions. *J Acoust Soc Am*. 128 (2010) 1004-14.
- [6] Bai L, *et al.*: Ultrasonic characterization of crack-like defects using scattering matrix similarity metrics. *IEEE Trans Ultrason Ferroelectr Freq Control* 62 (2015) 545–59.
- [7] Bai L, *et al.*: Characterization of Defects Using Ultrasonic Arrays: A Dynamic Classifier Approach. *IEEE Trans Ultrason Ferroelectr Freq Control* 62 (2015) 2146–60.

Quantitative evaluation of rheological properties for complex fluids using ultrasonic spinning rheometry

Taiki Yoshida, Yuji Tasaka, and Yuichi Murai

Graduate School of Engineering, Hokkaido University, N13W8, Kita-ku, Sapporo, 060-8628, Japan

We have proposed a novel methodology using ultrasonic velocity profiling for quantitative evaluations of complex fluids in a cylindrical vessel with unsteady rotations. The methodology is expected to acquire various rheological properties in a single run. In this study, enhancement of applicable targets in “ultrasonic spinning rheometry” for measuring various rheological properties was achieved. For the quantitative evaluation, we focus on momentum propagation by unsteady shear flows in an oscillating cylindrical container. The momentum propagation is represented as radial profiles of phase lag of velocity fluctuations in the shear flow. Obtaining the phase lag information using discrete Fourier transform (DFT) on spatio-temporal velocity distributions, it was found that the phase lag changes substantially as rheological properties change in the test fluids. For example, it is possible to evaluate viscosity change and physical property of the test fluid by analyzing the phase lag. In addition, for thixotropic fluids, assuming that a viscosity in pure viscous regime is comparable to Newtonian viscosity, shear stress distributions were calculated using Newton’s law of viscosity for the velocity distribution. Since it is possible to distinguish physical properties such as yielded and un-yielded region, we estimated a yield stress by evaluating shear stress distributions.

Keywords: ultrasound, rheometry, viscosity, thixotropy, shear flow

1. Introduction

Rheology dealing with deformational properties of materials has been discussed in the field of chemical engineering, biology, food processing, and dispersion system and so on. In the management of homogeneity and safety of various fluid products, such as highly polymerized compound and plastic processing, it is important to quantitatively evaluate their rheological properties. Most are non-Newtonian fluids, which have various complex behaviors, such as shear-rate-dependent viscosity, shear banding [1], velocity slip on the wall [2] and so on. Therefore, interests in the rheology have been stimulated, in part, by the necessity of measurements in the industry. Conventional rheometers investigating torque response against steady or oscillatory simple Couette-type shear, however, can only evaluate comprehensive physical properties such as apparent viscosity and properties in linear viscoelastic regime. In addition, it is inadequate for multi-phase fluids which have interfaces in physical property distributions. The limitations of rheometry assuming constant shear rate is overcome by solving a problem called “Couette inverse problem” [3]. To solve these problems, another approach of rheometry with considering velocity profiles in test fluids has been proposed as velocity profiling rheometry. Ultrasonic velocity profiling (UVP) [4] is the suitable velocimetry to realize the rheometry because of applicability for opaque fluids such as concentrated suspensions, and this method has been developed [3,5-6]. Shiratori T, *et al.* reported about applicability as a practical method of ultrasonic spinning rheometry by measuring a torque value combined with a widened circular Couette flow. However, there are very little studies of quantitative evaluations of rheological properties for general complex fluids using UVP.

We have proposed a novel methodology using UVP to quantitatively evaluate viscosity of complex fluids in a cylindrical vessel with unsteady rotations. This methodology has been termed “ultrasonic spinning rheometry” and has major advantages, such as being able to evaluate various rheological properties from single set of velocity distributions measured in test fluids. Hitherto, various approaches have been endeavored for the development of this methodology. Tasaka *et al.* reported that the phase lag of velocity fluctuations from the cylinder wall with a sinusoidal oscillation reflects the changes of the effective viscosity [6]. Shiratori *et al.* proposed ‘model-free ultrasonic rheometry’, which provides quantitative evaluation of shear-rate-dependent viscosity without using rheology models that are constitutive equations describing relation between stress, strain and strain rate of materials [5]. In these studies, however, there has been little effort to evaluate the properties for complex fluids with yield stress or highly concentrated dispersions.

The purpose of this study is to expand the applicable regime with newly developed methodology for general complex fluids. To obtain rheological properties in these fluids, such as thixotropic fluids and multi-phase fluids, we focused on momentum propagations by unsteady shear flows in an oscillating cylindrical container. The propagations appear with a phase lag of the velocity fluctuation from the wall of the container. This paper attempts to quantitatively evaluate rheological properties by the analysis of obtained velocity distribution of complex fluids.

2. Experiments

2.1 Experimental apparatus

The experimental apparatus is shown in Fig. 1. The

experiments were conducted in a rotating cylinder whose inner diameter is 145 mm ($= 2R$), height is 65 mm and thickness of the lateral wall is 2.0 mm. The cylinder is made of acrylic resin and is filled with test fluids. The cylinder has no lid and thus the top surface of fluid layer is stress free. The cylinder was mounted at the center of a water chamber to keep uniform temperature and to allow transmission of ultrasonic wave from the outside of the cylinder. The oscillation of cylinder is controlled by a stepping motor, where its oscillation angle and oscillating frequency are defined as $\theta = 90$ degree and $f = 1.0$ Hz, respectively.

During the cylinder oscillation, velocity distributions of the fluid are measured by UVP. The obtained ultrasonic echo signals were processed by UVP monitor model Duo (Met-Flow S.A.) into spatio-temporal velocity distribution. An ultrasonic transducer with 4 MHz resonance frequency was fixed in the chamber with a horizontal displacement Δy from the center line of the cylinder to obtain the azimuthal velocity component. Velocity fluctuations are measured on the UVP measurement line ξ at each measurement point and the velocity component u_ξ is parallel to the measurement line ξ . Assuming that the axisymmetric flow field and the velocity component in the radial direction are negligibly small compared to the azimuthal velocity component, the component u_θ is obtained as

$$u_\theta = \frac{u_\xi r}{\Delta y} \quad (1)$$

at a radial position r .

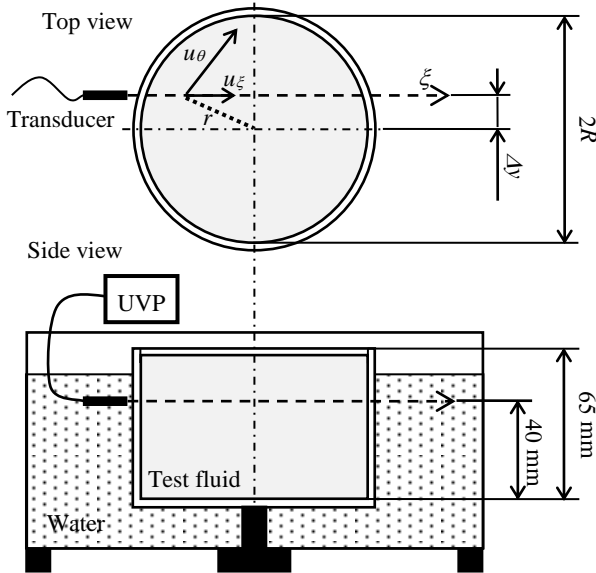


Figure 1: Schematic diagram of experimental setup and arrangement of the measurement line.

Empirically, $\Delta y = 15$ mm was selected based on the results of previous studies [5-6] with consideration of incidence of ultrasonic wave against curved cylinder wall and suitable velocity range of projection component of the velocity. The transducer was set 40 mm from the bottom of the cylinder to avoid effects of shear stress due

to oscillation at the cylinder bottom plate. Table 1 summarizes the setting parameters of UVP measurement in this study.

Table 1 Setting parameters of UVP

Parameter	Value	Unit
Base frequency	4.0	MHz
Temporal resolution	25	ms
Spatial resolution	0.74	mm
Velocity resolution	1.304	mm/s
Number of cycles	4	-
Number of repetitions	32	-

2.2 Test fluid

In this study, a montmorillonite suspension was examined to demonstrate the applicability of the present rheometry. Montmorillonite is a kind of clay mineral having a deviation of electric charges between an edge and face in the particle. In the left illustration of Fig 2, we show the schema of stable structure dispersed montmorillonite particles in the solvent. The structure is termed “Card house structure”, and is kept stable by interaction between particles such as Coulomb force. The interaction forms clusters of the particles with leaving the suspensions at rest.

In the schematic illustration shown by the others illustrations in Fig. 2, these clusters become smaller influenced by disturbances such as shear stress. Decrease of the cluster size accompanies decrease of a viscosity in the suspension. As the results the suspension has complex behaviors like time-dependent gelling behavior and high shear thinning flow behavior. In case the card house structure of the suspension keeps stable the structure, the suspension has viscoelastic behaviors against a disturbance such as shear stress. These behaviors are termed thixotropy. To attain details for thixotropy refer to past studies [7]. As yet, nothing is established to evaluate these behaviors quantitatively in a single run. However, the behaviors of suspensions have been estimated by results attained from various investigations in the past. So, we demonstrate the applicable methodology using this suspension.

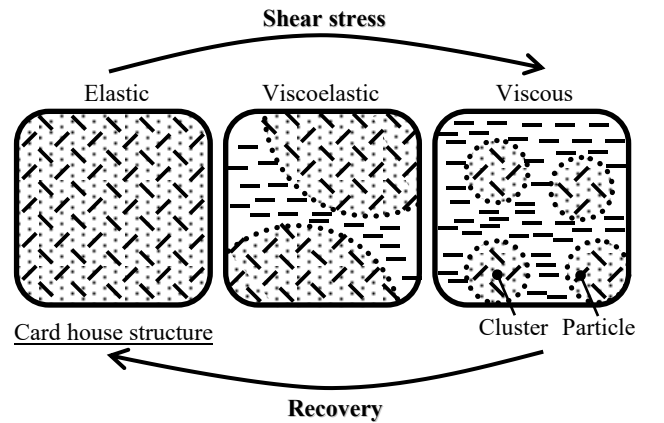


Figure 2: Schema of breakdown in the card house structure

Montmorillonite suspensions were prepared by adding the 4.0 wt. % powder to 0.01 mol/L NaCl aqueous solutions: rheological properties relating card house structure strongly depends on concentration of NaCl. Abend and Lagaly have studied the dependence of viscosity changing in salt concentration of montmorillonite suspensions [8]. In order to fully swell the suspension, it was left for over a day before measuring began. After filling the cylinder with the suspension, the suspension was stirred vigorously to abolish shear stress history. The structural recovery time of the suspension was defined as $T = 100$ min.

3. Results and discussions

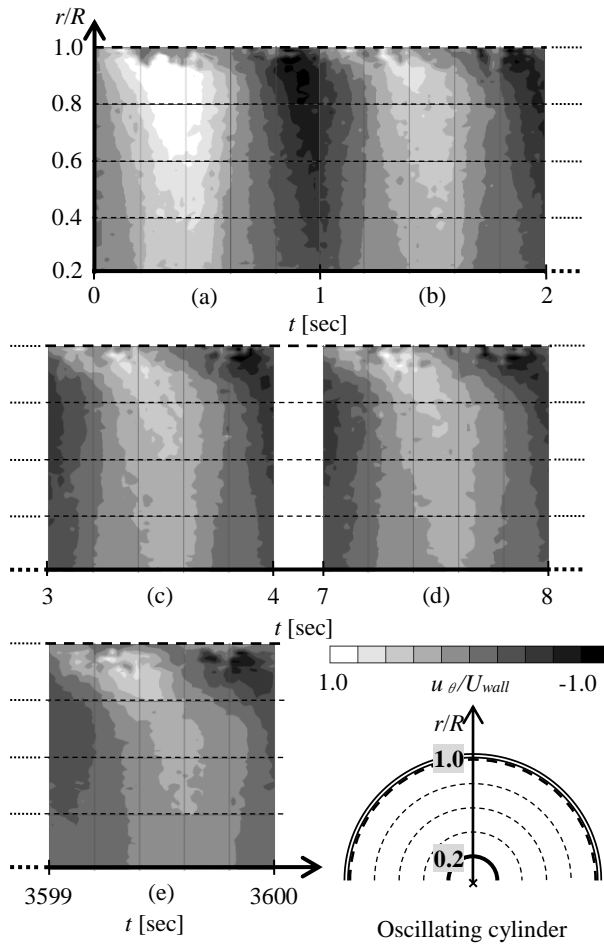


Figure 3: Spatio-temporal velocity distributions changing with spin-cycle time and schematic illustration of the cylindrical configuration

With the assumption of axisymmetric, one-directional flow in the azimuthal direction, the spatio-temporal velocity map obtained by UVP can be converted into radial-temporal distribution of the azimuthal velocity component. In Fig. 3, the vertical axis indicates the radial positions normalized by radius of the cylindrical container ($= R$) and the horizontal axis indicates the spin-cycle time. The shades of black-and-white represent the spatio-temporal distribution of the azimuthal velocity normalized by maximum azimuthal velocity at the cylinder wall, U_{wall} ($= 2\pi fR$). Oscillation of the azimuthal

velocity propagates from the wall to center of the cylinder as a damping wave.

As shown in Fig. 3, phase lag from the cylinder wall to inner suspensions occurs on the velocity distribution. Since the suspensions have thixotropic behaviors such as decreases of viscosity by shear stress, the phase lag appears as the time-dependent viscosity decrease in the suspensions by shear stress oscillating the cylinder wall. To quantify and clarify the phase lag, the velocity distributions were analyzed by time-directional discrete Fourier transform (DFT) for 1 s measurement. The analysis results are shown in Fig. 4. The axes represent the radial positions normalized by R and the phase lag of the local velocity fluctuations from a cylinder wall. Different symbols labelled (a) to (e) represent time steps corresponding to spatio-temporal velocity map in Fig. 3.

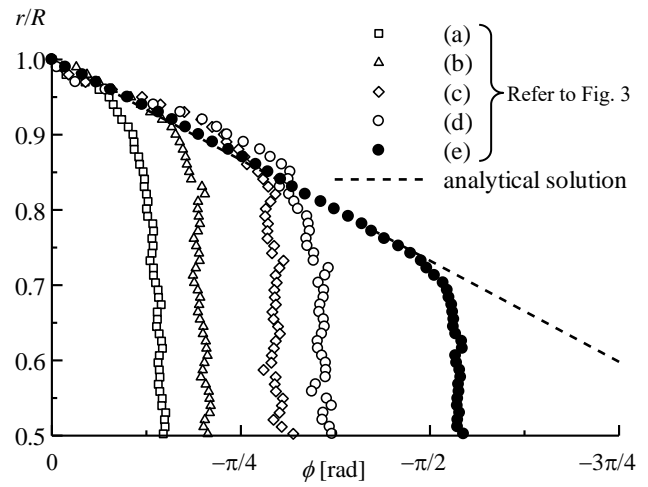


Figure 4: Phase lag of the local velocity fluctuations from a cylinder wall for different waited cycles

In the result of (a) in Fig. 4, the phase lag has almost constant value except near the wall, $r/R = 1.0$. With increasing oscillation time, however, the curve of the phase lag from the cylinder wall changes progressively. This is because the viscosity of suspensions in the cylinder was decreased by shear stress acting on the fluid from the oscillating cylinder. Eventually, the curve of the phase lag converges at time step (e). Also information included in Fig. 4 is the dependence of viscosity on a gradient phase lag from the cylinder wall. This result is shown in short dash line of Fig. 4. The line was provided by comparing analytical solution in Newtonian fluids [6] and the best given gradient of phase lag at $0.8 < r/R < 1.0$ by least squares method. By this methodology, we obtained the viscosity, $\mu = 0.489$ Pa·s. This methodology is based on the assumption that behavior of test fluids is nearly that of Newtonian fluids. In addition, these results can be used to distinguish physical properties such as yielded and un-yielded region. A knee in the curve as shown in each plots of Fig. 4 has been suggested to indicate a boundary between yielded and un-yielded region.

In a past study [9], the value was estimated as 0.528 Pa·s using a conventional rheometer. One of the uncertainties of this measurement is estimated as 20 % measurement error, and it is thought to be due to the influences by shear banding, slip on the wall, and so on [10]. Since the viscosity value obtained by our rheometry is observed by velocity distributions of experimental results, this value is superior to the viscosity value from results obtained by the conventional rheometer.

Furthermore, to discuss deeply, we focus here on only the analysis result of Fig. 4 (e). In the Fig.4, the phase lag of the experimental and analytical results coincides with the curve approximately above $0.7 < r/R$. Therefore, it is reasonable to assume that the viscosity of test fluids behaved like Newtonian viscosity in the region, which is defined as the pure viscous region. Here it is possible to use Newton's law of viscosity for this region. The law is given by

$$\tau(r,t) = \mu \left(\frac{\partial u_\theta(r,t)}{\partial r} - \frac{u_\theta(r,t)}{r} \right). \quad (2)$$

By using the law for measurement results of the velocity distribution, it is possible to measure shear stress distribution only in the range of this region. In Fig. 5, the vertical axis indicates the radial position normalized by radius of cylindrical container ($= R$) and the horizontal axis indicates shear stress τ . Here plots of maximum shear stress value at each radial point in the time series are shown in Fig. 5. We compare the experimental results to the result obtained by analytical solution applying estimated viscosity. Near the cylinder wall, they do not agree with the curve and plots because of high velocity fluctuations. In contrast, near the cylinder center, they mostly coincide with the curve and plots.

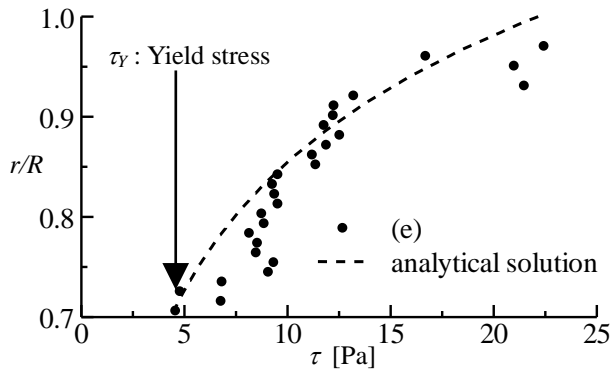


Figure 5: Radial profile of maximum shear stress detected

As written above, these results can be used to distinguish physical properties such as yielded and un-yielded region. Therefore, there are boundary regions between yielded and un-yielded region and for this experimental condition, the boundary region is present in the vicinity of $r/R = 0.7$. From Fig. 5, the shear stress value at $r/R = 0.7$ may suggest the yield stress value of the suspension, $\tau_Y = 4.57$ Pa. This is indicated by the arrows in Fig. 5. Thus, even though it is difficult to evaluate the yield stress value for conventional rheometer, our rheometry has the ability to measure this value.

4. Conclusions

We proposed a novel methodology using UVP to quantitatively evaluate various rheological properties of complex fluids in a cylindrical vessel with unsteady rotations. Oscillation of the azimuthal velocity propagates from the wall to center of the cylinder as a damping wave. In this study, a montmorillonite suspension which has various complex behaviors was used to demonstrate as test fluids. Since the suspensions have thixotropic behaviors such as decrease of viscosity by shear stress, the phase lag appears as the time-dependent viscosity decrease in the suspensions affected by shear stress due to oscillating the cylinder wall. In this experimental result, viscosity was estimated as $\mu = 0.489$ Pa·s. This value may be more reliable than that determined by a conventional rheometry because of inverse problem algorithm such as measuring from velocity fluctuations. Since the phase lag of the experimental results agrees well with analytical solutions assuming ideal Newtonian viscosity in a range of $0.7 < r/R$, it is reasonable to assume that the viscosity of test fluids behave like Newtonian viscosity in the region, which is defined as the pure viscous region. Thus shear stress distributions were measured using Newton's law of viscosity for this region. In addition, since there are boundary regions ($r/R = 0.7$) between yielded and un-yielded region and for this experimental condition, the shear stress value τ at $r/R = 0.7$ may suggest the yield stress value τ_Y of the suspension. In this experimental result, the yield stress value τ_Y obtained are as follows: $\tau_Y = 4.57$ Pa.

References

- [1] Divoux T, *et al.*: Shear banding of complex fluids, *Annu. Rev. Fluid Mech.*, 48:81-103 (2016).
- [2] Rodrigez-Gonzalez F, *et al.*: Rheo-PIV analysis of the slip flow of a metallocene linear low density polyethylene melt, *Rheol. Acta.*, 49:145-154 (2010).
- [3] Shiratori T, *et al.*: Ultrasonic velocity profiling rheometry based on a widened circular Couette flow, *Meas. Sci. Technol.*, 26:085302 (2015).
- [4] Takeda Y: Ultrasonic Doppler velocity profiler for fluid flow, Springer, (2012).
- [5] Shiratori T, *et al.*: Development of ultrasonic visualizer for capturing the characteristics of viscoelastic fluids, *J. Visualization*, 16.4:275-286 (2013).
- [6] Tasaka Y, *et al.*: Estimating the effective viscosity of bubble suspensions in oscillatory shear flows by means of ultrasonic spinning rheometry, *Exp. Fluids*, 56:1867 (2015).
- [7] Haward A B: Thixotropy – a review, *J. Non-Newtonian Fluid Mech.* 70.1:1-33 (1997).
- [8] Abend S & G Lagaly: Sol-gel transitions of sodium montmorillonite dispersions, *Applied Clay Sci.* 16.3:201-227 (2000).
- [9] Suzuki K, *et al.*: Factors affecting to the viscosity of montmorillonite/water suspension: 2. Relationship between aspect ratio of montmorillonite particles and viscosity of aqueous suspensions, 50.3:162-174 (2012).
- [10] Shimizu M & Sato F: Repeatability and reproducibility on measuring of viscosity (Properties of instruments), Miyazaki prefecture foods development center study report, 54:9-14 (2009).

Ultrasound measurements in a physical model of Czochralski crystal growth in a horizontal magnetic field

Josef Pal¹, Ilmars Grants^{1,2}, Sven Eckert¹, and Gunter Gerbeth¹

¹ Helmholtz-Zentrum Dresden-Rossendorf, Bautzner Landstr. 400, 01328 Dresden, Germany

² Institute of Physics, University of Latvia, Salaspils, Latvia

A horizontal magnetic field (HMF) may improve conditions in the melt during large silicon single crystal growth by the Czochralski technique. This observation is counter-intuitive as the HMF evidently breaks the rotational symmetry. A previous study has shown that the HMF is not able to significantly delay the Rayleigh-Bénard instability in a rotating cylinder. It has been observed that an oscillating flow sets in soon after the linear onset. Can we expect a stabilizing effect of the HMF in the Czochralski growth? Why the symmetry breaking by the HMF is eventually not so relevant? These are two central questions for our primarily experimental study. Besides, it is also meant as a benchmark for comparison with the numerical codes. To serve the latter purpose the boundary conditions should be preferably well defined. Having this in mind the temperature boundary conditions are defined as follows. An isothermal heating is applied at the bottom of a cylindrical cell filled with GaInSn alloy. The side wall is thermally insulated. An optionally rotating isothermal cooler models the growing crystal. A water-cooled layer of an alkaline solution keeps the rest of the metal surface free from oxides and models the radiation heat loss. The maximum HMF strength is 0.3 T that corresponds to a Hartmann number of about 1200. Velocity profiles are measured by ultrasound Doppler velocimetry.

Keywords: Czochralski crystal growth, Horizontal magnetic field, Ultrasound Doppler velocimetry

1. Introduction

HMF has emerged as one of the most promising magnetic field configurations in the single crystal silicon growth by the Czochralski (CZ) technique. Various numerical simulations of the process [1, 2] have shown that HMF strongly stabilizes the melt under characteristic growth conditions. This observation contrasts with the linear instability results [3] in a cylindrical Rayleigh-Bénard (RB) cell predicting onset far below the typical CZ conditions. The linear instability is monotonic that means another steady solution sets in. Such instability by itself is practically harmless in the sense that it brings no instationarity. However, it is known from experiments in a rectangular RB cell [4] that the first linear onset is soon followed by secondary instability which leads to oscillating flow. One of the main tasks of our study is to address this apparent contradiction in a physical model of the CZ process with HMF.

The RB cell is a rough model of CZ focused on the basic instability driving mechanism by unstable stratification of the melt. One of the key differences between RB and CZ configurations is the intrinsic radial temperature gradient in the latter. This gradient drives a flow in the CZ melt for an arbitrary small temperature gradient. This flow should be proportional to the driving buoyancy force (temperature gradient) when it is small enough. In the RB, in turn, the flow is zero unless the linear instability creates it at a sufficiently high temperature gradient. One may expect that instead of instability the CZ melt will develop a flow regime with a faster-than-linear dependency of velocity vs the temperature gradient. This “ghost” of the linear instability is another target of our study.

Instationarity may be produced in the CZ process also by a completely stable three-dimensional flow. A stationary

but non-uniform azimuthal distribution of velocity and temperature in the melt produces oscillating conditions on the surface of a rotating crystal. The HMF evidently breaks the rotational symmetry. It is, therefore, puzzling how it may produce satisfactory growth conditions. In the current study we consider only a stationary crystal that can hardly solve this puzzle. The measurements are more intended to quantify the maximum initial degree of the azimuthal non-uniformity of the flow in the bulk of melt. These results should serve as an input for the design of further model experiments with HMF and the crystal rotation.

2. Basic principles in modelling the Czochralski technique

The simplest model of the CZ facility might be a RB configuration, in particular a cylindrical cell heated from below and cooled at the top which is characterized by a height H and diameter $2R$ and adiabatic insulated side walls. Applying a temperature gradient $\Delta T = T_b - T_t$ between the bottom and top sides, buoyant convection occurs when ΔT exceeds some critical value.

The dynamics of the mere thermally induced convection may be described by three control parameters. First of all the dimensionless Rayleigh number Ra is the crucial parameter in modelling buoyancy and describes its strength: $Ra = \beta g \Delta T H^3 / \nu \chi$, where β is the thermal expansion coefficient, ν the kinematic viscosity, χ the thermal diffusivity of the fluid, and g the gravitational acceleration. The second control parameter, the Prandtl number Pr , takes into account the heat transport within the fluid and is given by the ratio of the thickness of viscous and thermal boundary layers: $Pr = \nu / \chi$. In general, molten metals and semiconductor melts are low Prandtl number fluids with Pr in the order of 10^{-2} , which

means that the heat diffuses quickly in comparison with the convective transport.

The third control parameter, the aspect ratio $a = H/(2R)$ concerns the geometry of the setup and affects crucially the developed convective pattern inside the melt. More details, in particular about varying aspect ratios, can be found in [5, 6] and references therein. The initial filling level in a real industrial CZ facility does not reach $a = 1$, it is even lower than $a = 0.5$ and decreases continuously during the process.

The Hartmann number $Ha = BL(\sigma/\rho\nu)^{1/2}$ occurs as another control parameter if external magnetic fields are exposed to the system. Thereby B is the magnetic induction, L a typical length scale in the system, and σ the electrical conductivity of the melt. The Hartmann number represents a measure for the ratio between the electromagnetic body force and the viscous force.

3. Description of the model

The object of the investigation is a modified Rayleigh-Bénard (RB) configuration, a cylindrical melt column of variable aspect ratio homogeneously heated from below. The photo in Fig. 1 illustrates the experimental setup mounted between the HMF producing coils. As working fluid the ternary alloy GaInSn [7] was used because it remains liquid at room temperature and as distinguished from mercury it is non-poisonous. Moreover, its low Prandtl number is similar to that of molten silicon.

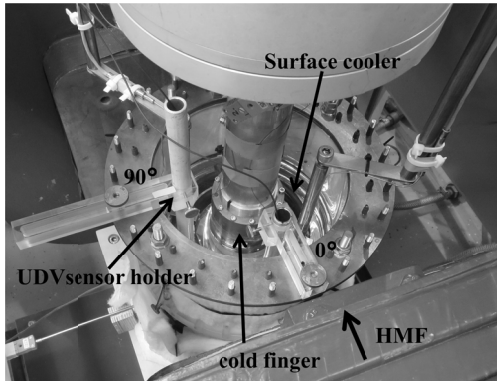


Figure 1: Oblique view to the experimental setup mounted inside the HMF coil system. The inner diameter of the cylindrical melt volume is 178 mm whereas that of the cold finger is 70 mm.

The heating was realized by an electrical heating plate embedded in a massive copper disc to achieve isothermal boundary condition. Several thermocouples were installed inside the copper disc to monitor its temperature. The upper thermal boundary condition in a CZ system is accounted for by a partially cooled surface. The partial cooling in our experiment covers approximately the same fraction area as the crystal does in an industrial facility. It is realized with a circular heat exchanger (cold finger) mounted concentrically at the top of the experimental cell. The cold finger is optionally rotatable, a precise control of the temperature is realized by supplying it with coolant fluid at high flow rate from a thermostat having a large reservoir. The latter is regulated

by a PID circuit. The temperature of the cold finger is also monitored at various positions. For the purpose to achieve adiabatic boundary conditions at the side walls a borosilicate glass pipe was chosen as experimental cell owing to its poor heat conductivity. During the measurements, the apparatus was embedded in mineral wool to minimize the lateral heat loss.

In the industrial Czochralski facility thermal radiation from the hot silicon melt surface to the ambience is a considerable heat sink. A distinctive feature of the present setup is the possibility to model the heat loss from the melt surface. The surface is therefore covered by an electrolyte layer which is cooled by a copper spiral completely immersed into this layer (cf. Fig. 1). Such a system can be described by the dimensionless Biot number Bi . For a detailed meaning of this dimensionless heat transfer coefficient [8] is referred to.

Flow velocities were measured by the UDV technique, the principle of operation is described in the pioneering work of [9]. Mainly two features render UDV predestinated for the present work. Firstly, it works for opaque media including liquid metals. Secondly, it allows the quasi-simultaneous measurement of an entire profile of the local velocity component in direction of the sound propagation along the ultrasonic beam. The readings of the ultrasound transducers were taken by a DOP2000 velocimeter (Signal-Processing, Lausanne, Switzerland).

A simplified numerical model has been used for comparison purposes. It is implemented as the spectral three-dimensional time-dependent direct numerical solution developed for the linear instability analysis in the RB cell [3]. The flexibility of this model is restricted by boundary conditions that must be of a fixed type on each of the principal surfaces (bottom, side, top). This introduces a difficulty to model the top surface consisting of two distinct regions. The central part below the cold finger has no-slip conditions for the velocity field and, effectively, a constant temperature. The outer part, in turn, has stress-free conditions for the velocity and boundary conditions of the third kind for the temperature. Since the area of the cold finger is much smaller than the area of the free surface the latter conditions are applied for the entire top surface:

$$\left(\frac{\partial v_r}{\partial z}\right)_{z=1} = 0 \quad \text{and} \quad \left(T + Bi^{-1} \frac{\partial T}{\partial z}\right)_{z=1} = T_e(r).$$

The ambient temperature profile is set to $T_e(r) = -1/8 + 3/2 T_2(r) - 3/8 T_4(r)$, where $T_i(r)$ are the Chebyshev polynomials used to express the numerical solution [3]. The value of Biot number is set to $Bi=2$. The above boundary conditions constitute the basic deviation from the physical model.

4. Results

For the present investigation mainly flow velocity measurements were performed in the range $Ra = [10^4 : 10^7]$ and different magnetic fields $B = [86, 160, 326]$ mT which correspond to the Hartmann numbers $Ha = [300, 600, 1200]$. The cell filling height was kept constant at $H = 89$ mm and results in an aspect ratio of $a = 0.5$. To measure

the vertical velocity component two UDV sensors were positioned 25 mm away from the rim of the cylinder. Since the HMF breaks the rotational symmetry, one of the sensors was in the plane parallel ($\varphi=0^\circ$) to the HMF direction, the second one in the plane perpendicular ($\varphi=90^\circ$) to the HMF (see Fig. 1).

Fig. 2 shows exemplarily a selection of the experimentally and numerically determined mean velocity profiles at both distinguished positions for $Ha=300$. Why the numerical data do not reproduce quantitatively very well the experimental ones might have several reasons, such as the modeling of the thermal boundary condition by the Bi number. This is still under development. On the other side, see Fig. 2b, for the higher Ra the curvature of the velocity profile is quite good reproduced with both local maxima.

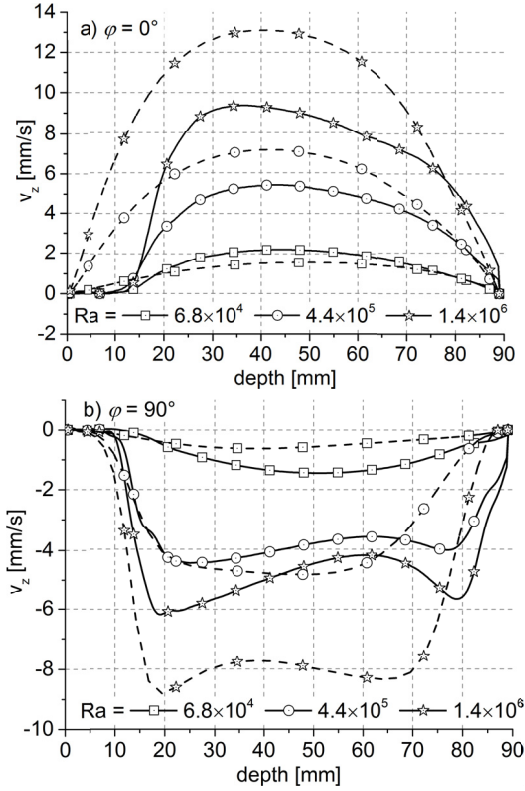


Figure 2: Experimental (solid lines) and numerical (dashed) vertical velocity profiles for $Ha=300$ for selected Ra . Profiles with positive sign (a), indicate a downward oriented flow and the negative sign in (b) stands for upward flow direction.

For further comparison purposes the dimensionless velocity expressed by the Reynolds number Re is useful which gives the ratio of the inertial to the viscous forces. Here Re is calculated from the maximum v_z value of the velocity profile by $Re=v_{z,max} R/\nu$. Fig. 3 summarizes Re as function of Ra and of Ha , and shows, additionally, a comparison with first numerical results. For $Ha=300$ the experimental results are interesting because the average velocity decreases as the heating power increases for $Ra>4.8\times 10^6$ ($\varphi=90^\circ$) and $Ra>5.5\times 10^6$ ($\varphi=0^\circ$), respectively. This is probably because of roll movement and requires more attention in subsequent investigations.

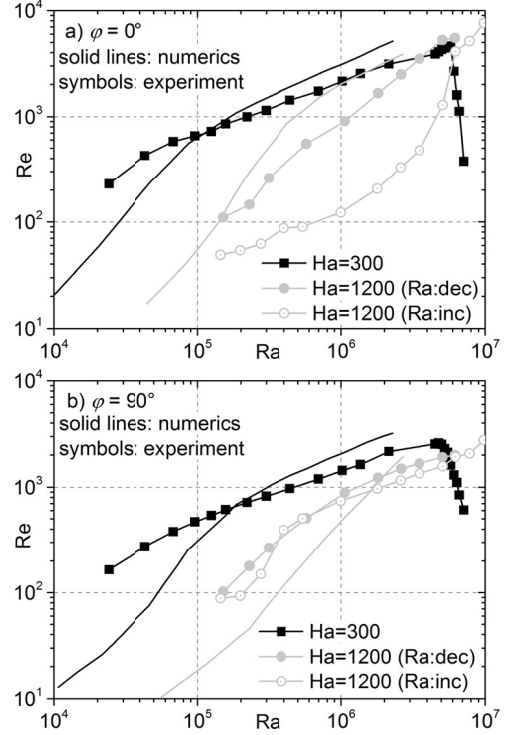


Figure 3: Comparison between the experimental and numerical Re as function of Ra for two different Ha numbers.

A kind of velocity “boost” is observed in the numerical results shown in Fig. 3. This cannot be validated by the experiment because of the limited resolution of the UDV technique. Velocities lower than approximately 1 mm/s (which correspond in the present setup to $Re \leq 260$) are hardly measurable and depend extremely from the UDV signal quality. For $\varphi=0^\circ$ a distinct hysteresis behavior is observed for $Ha=1200$ depending from the ramp direction by varying the Ra number. The symbols with open circles indicate the case when Ra was increased, the filled ones are for decreasing Ra . The difference is small for the lower Ra range, but a difference of almost one order of magnitude occurs for around $Ra=10^6$.

Concerning the spatio-temporal behavior of the flow for $Ha=300$, the measurements show signs of different oscillation mode competitions. First of all Fig. 4 shows the cases before instabilities develop. First instability comes with an oscillation frequency of $f=0.123$ Hz at $Ra=2.1\times 10^6$, disappears and a low frequency oscillation with $f=0.071$ Hz occurs at $Ra=2.6\times 10^6$. Increasing further the Ra number this oscillation mode stops too and a high frequency mode starts from $Ra=3.1\times 10^6$ up to $Ra=5.1\times 10^6$ with slightly increasing frequency between $f=0.221$ Hz and $f=0.281$ Hz, respectively. In the latter range, interestingly, the oscillations are only present for $\varphi=90^\circ$. For Ra between $[5.3\times 10^6 \dots 5.8\times 10^6]$ the oscillations disappear again but restart with a very low frequency and large amplitude at $Ra=6.1\times 10^6$ for up to $Ra=6.7\times 10^6$. The spatio-temporal process in Fig. 5 illustrates this behavior, whereas Fig. 6 shows the time variation of the vertical velocity at some selected deeps of the melt column. It can be seen that higher amplitude oscillations occur for $\varphi=0^\circ$ than for $\varphi=90^\circ$. For the

highest measured $Ra=7.1\times 10^6$ the oscillations broke down and an irregular flow structure was observed.

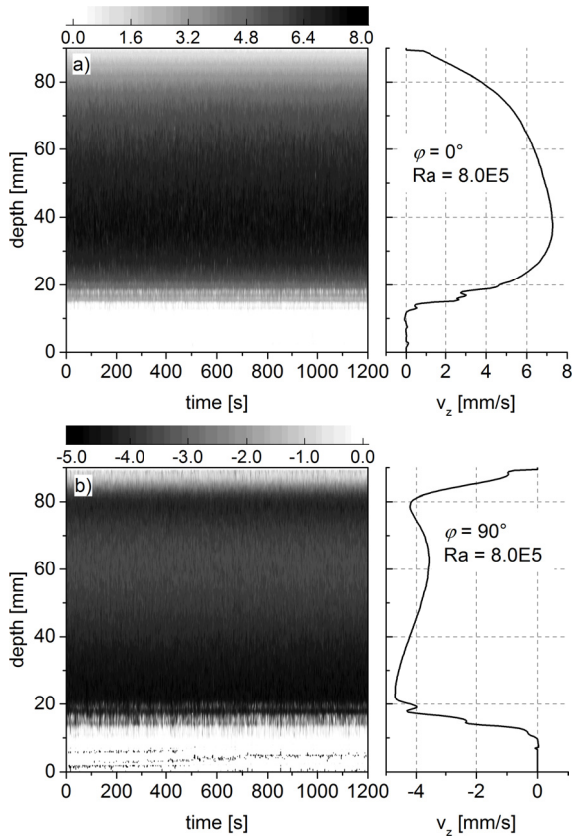


Figure 4: Time series and the mean profile of the vertical velocity measured at the $\varphi=0^\circ$ (a) and $\varphi=90^\circ$ (b) positions. Yet, no oscillations are observed for $Ra=8\times 10^5$.

5. Summary

A CZ-like crystal growth model exposed to a HMF was the object of the present investigation. Ultrasound measurements of the vertical component of the fluid flow were performed by varying the strength of the magnetic field (Ha) and that of the buoyancy (Ra). Because the HMF breaks the rotational symmetry the velocities were recorded at two distinct azimuthal positions. The experimental data serve as a benchmark object for numerical codes which are still under development.

6. Acknowledgements

Financial support by the German Helmholtz Association in the framework of the Helmholtz-Alliance LIMTECH is gratefully acknowledged.

References

- [1] V. V. Kalaev, J. Cryst. Growth 303 (2007), 203–210.
- [2] X. Chen, J. Zhan, Y.-S. Li, X. Cen, J. Cryst. Growth 389 (2014), 60–67.
- [3] I. Grants, G. Gerbeth, J. Cryst. Growth 358 (2012), 43–50.
- [4] U. Burr, U. Müller, J. Fluid Mech. 453 (2002), 345–369.
- [5] F. Hébert, R. Hufschmid, J. Scheel, G. Ahlers, Phys. Rev. E 81 (2001), 046318.
- [6] J. Niemela, L. Skrbek, K. Sreenivasan, R. Donnelly, J. Fluid Mech. 449 (2001), 169–178.
- [7] Y. Plevachuk, V. Sklyarchuk, S. Eckert, G. Gerbeth, R.

Novakovic, J. Chem. Eng. Data 59(3) (2014), 757–763.

[8] J. Pal, A. Cramer, I. Grants, S. Eckert, G. Gerbeth, J. Cryst. Growth 432 (2015), 69–77.

[9] Y. Takeda, Nucl. Eng. Des. 126 (1991), 277–284.

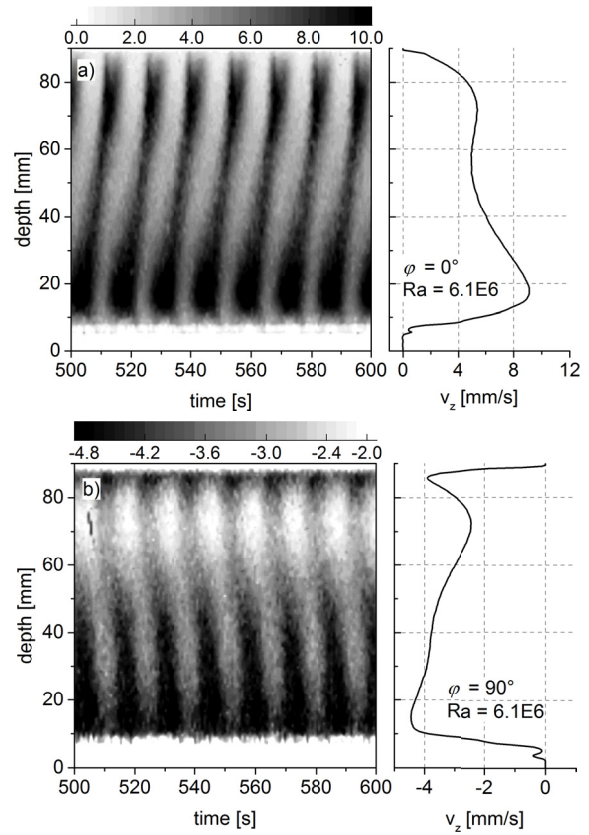


Figure 5: Low frequency and large amplitude oscillations ($f=0.073$ Hz) for $Ra=6.1\times 10^6$.

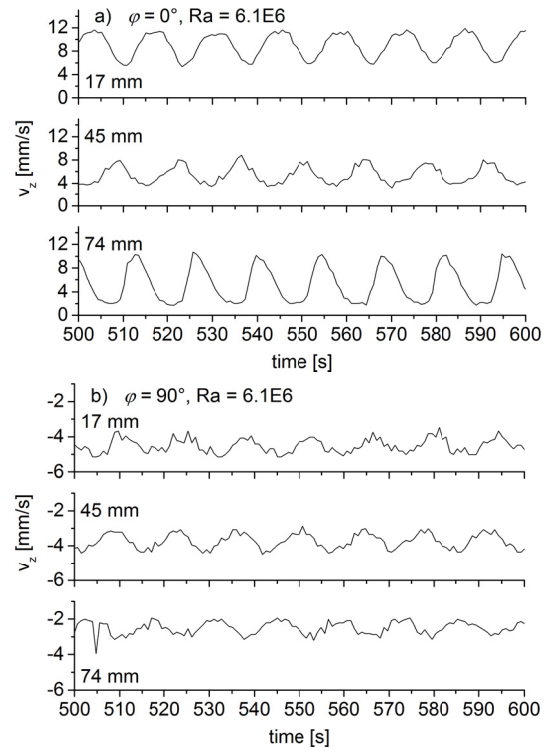


Figure 6: Time variation of the vertical velocity as shown in Fig. 5 at selected deeps of the melt, (a) $\varphi=0^\circ$ and (b) $\varphi=90^\circ$.

Influence of surface roughness on the flow behavior in TVF and WVF

L. Pokorny¹, N.J. Saikia¹, Y. Takeda¹ and E.J. Windhab¹

¹Laboratory of Food Process Engineering, Institute of Food, Nutrition and Health
ETH Zurich, Schmelzbergstrasse 9, 8092 Zurich, Switzerland

Taylor Couette flow starts with a laminar azimuthal state, over going into an intermediate state with Taylor vortices by increasing rotational speed. These vortices are characterized by their axisymmetric toroidal shape. When exceeding a critical rotational speed, various wavy modes set in first, then leading to turbulent Taylor Vortex Flow. The onset of TVF, and the transition to WVF strongly depends on the geometry of the system in use. In this study, an important additional factor, namely the surface roughness was investigated using UVP and visual analysis. Radial and axial velocity components were profiled to get information on the vortex shape. Additionally, the onset of TVF and WVF and the frequency of the wavy structure were obtained measuring the radial velocity profile, verifying the visual analysis using Kalliroscope reflective particles. Three different surfaces on the inner rotating cylinder were analyzed for the TVF and WVF regimes. Observing and characterizing the shape of Taylor vortices, a transition point to TVF and WVF was found to be influenced by surface roughness. Namely, the rougher the surface is, the earlier the onset, whereas the onset of WVF is more affected by the geometrical parameter such as the gap size. In addition it can be shown that the surface does not influence the oscillation frequency in the wavy regime but more the gap size. Regarding the shape of vortices, it can be stated out that the ratio between the axial positive velocity ($+V_{z,max}$, upward) and the axial negative velocity ($-V_{z,max}$, downward) is unequal to 1 at the rough wall. In contrast, the ratio at the smooth outer wall is equal to 1 for the whole flow states.

Keywords: Surface Roughness, Taylor-Couette flow, Wavy Vortex flow, Couette cell

1. Introduction

The flow behavior in a rotating coaxial cylinder shows a high periodicity in space and time, and is a well-known platform where flow instability or flow transition to turbulence is investigated. To evaluate the flow state, the Reynolds number or Taylor number is taken into account. Increasing these numbers, shows a sequential transition from Couette flow (CF) to Taylor Vortex Flow (TVF) and Wavy Vortex Flow (WVF) [1]. During such a transition sequence, the flow structure keeps a considerably clear spatial and temporal periodicity. Namely, a roll structure of TVF persists all through and remains even in the highly turbulent regime. WVF shows a clear temporal periodicity arising from an azimuthally wavy structure traveling around the axis. These flow structures were studied since almost 100 years, first by Taylor (1923) [2].

These flow structures offers an efficient continuous cleaning procedure in dynamic membrane filtration. Dispersed particles accumulate on the filter pores and reduce the flux quanti- and qualitatively. The essence of this dynamic filters is a membrane with a rough surface. The influence of the rough surface on the flow structure is rarely analyzed for Taylor Couette cells, more for pipe flow [3-6]. In addition to the roughness of the membrane itself, particles can increase the rough structure when accumulating on the membrane. The formation of TVF in such membrane devices is crucial. It helps to increase the shear on the surface, forcing accumulated particles back into the massflow again.

The aim of this work is to study the influence of the rough surface on the onset and toroid shape of TVF and

WVF. In addition, the oscillation frequency in WVF was analyzed for different rough surfaces in a concentric cylinder device.

2. Experimental

2.1 Fluid system for flow analysis

Glycerol solution (83 wt.%, Thommen-Furler AG) was used to investigate the flow pattern of Newtonian fluids in the flow cell. It has a density of 1,217 g/cm³, with a dynamic viscosity of 65 mPas. Polyamid tracer particles with an averaged size of 90 μ m and a density of 1,07 g/cm³ (PSP, Met-Flow) were added to the Glycerol solution with a fraction of 1wt.% for UVP measurements and 2wt.%. Kalliroscope particles (Kalliroscope Corporation) were mixed in for visualization of the flow structure.

2.2 Taylor Couette Cell and Surface Roughness measurement

The Couette cell used for the experiments consists of a non-transparent inner PVC cylinder with a radius of $R_I = 59$ mm and a transparent outer Plexiglas cylinder with a radius of $R_O = 70$ mm. Thus, the gap width is $d = 11$ mm and the radius ratio $\eta = R_I/R_O$ is 0,843. The height of the inner cylinder is $L = 250$ mm resulting in an aspect ratio of $\Gamma = d/L = 22,72$. Both ends of the present configuration are attached to the stationary outer cylinder. The inner cylinder was coupled to a motor, which was controlled by a speed inverter (IKA, Staufen, Germany). The gap space between inner and outer cylinder was filled with the fluid system to be measured. The theoretic critical rotational Reynolds number for the onset of TVF is calculated to be

Recrit = 104 [7].

For the simulation of a rough surface, two different sandpapers P80 and P40 (Brütsch & Rüeegg Werkzeuge AG, Switzerland) were used. Therefore, they were glued on the smooth surface cylinder, which increased the inner radius, followed by a reduced gap size. It affects the radius ratio and the critical Reynolds number. The detailed values are summarized up in Table 1.

The difference between smooth and smooth L is the gap width, where the gap of smooth L is adapted to the gap width of P80 and P40. The roughness of P80 corresponds to the roughness of a conventional metal meshed membrane, whereas P40 simulates the membrane with accumulated particles with a size of around 80 μ m.

Table 1: Dimensions of Taylor Couette cell with and without rough surface

	Smooth	Smooth L	P80	P40
Roughness R_a (μ m)	2.1	2.1	45	118
Gap width (mm)	11,0	9,0	9,3	9,0
Radius Ratio (-)	0.84	0.87	0.87	0.87
Critical Reynolds (-)	104	117	116	117

2.3 Instrumentation - UVP

An UVP-Duo instrument (Met-Flow SA, Lausanne, Switzerland) was used to measure the velocity profiles in the flow cell. An ultrasound transducer with 4 MHz basic frequency and 5 mm active and 8 mm housing diameter (Imasonic) was used for axial flow measurements. Profiling of the radial velocity was performed with an 8 MHz transducer with an active diameter of 2.5 mm (8 mm housing). The velocity of sound in the glycerol was measured to be 1794 m/s at 25°C. Further settings are described in Table 2.

Table 2: Setting for the UVP measurements

<i>Axial Velocity Profiling (4MHz)</i>	
PRF	3.56 kHz
Distance between channels	1.12 mm
Cycles per pulse	4
Position of 1. channel	3.14 mm
Amplification (gain)	6-9
<i>Radial Velocity Profiling (8MHz)</i>	
PRF	5.31 kHz
Distance between channels	0.67 mm
Cycles per pulse	4
Position of 1. channel	0.67 mm
Amplification (gain)	6-9

2.4 Procedure

Onset of TVF and WVF and oscillation frequency of WVF – A radial velocity profiling

For onset measurements, the transducer was placed horizontally pointing in the radial direction towards the gap at approximately half of the cylinder height. The frequency of oscillation and radial velocity of the flow in the gap was measured at this position using the UVP with the corresponding setting presented in Table 2. The oscillation frequency could be analyzed with the

corresponding power spectrum. The flow state where a clear peak could be observed was set to be the onset of wavy vortex flow. Similarly, the transition from Taylor flow to azimuthal Couette flow corresponds to the rotational speed of the inner cylinder where Taylor vortices disappear and thus the measured radial velocity component of the flow becomes zero. The UVP data was verified using a visualization technique with Kalliroscope.

Shape of vortices - An axial velocity profiling

The axial velocity profiles in the flow cell were measured with UVP using a 4 MHz - transducer. The transducer was placed in axial position on the bottom close to the inner cylinder and close to the outer cylinder to be able to analyze the whole vortex shape in vertical direction. Therefore, the axial velocity profile could be measured along the inner gap. The resulting output describes the downward (towards the transducer) and upward (away from the transducer) flow. The maximal values of downward and upward flow could be fitted and analyzed.

3. Results and Discussion

3.1 Variation of onset of TVF and WVF

The variation of onset Reynolds number of TVF and WVF is illustrated in Figure 1. The x-axis represents the gap of the concentric cylinder device, where the y-axis shows the onset of TVF (Figure 1a) and WVF (Figure 1b).

Regarding the onset of TVF, it can be stated that it strongly depends on the surface roughness. Both smooth surfaces have an onset of around $Re/Re_{crit} = 0.97$, whereas with increasing roughness the onset is earlier. For P80 it already starts to form vortices at $Re/Re_{crit} =$

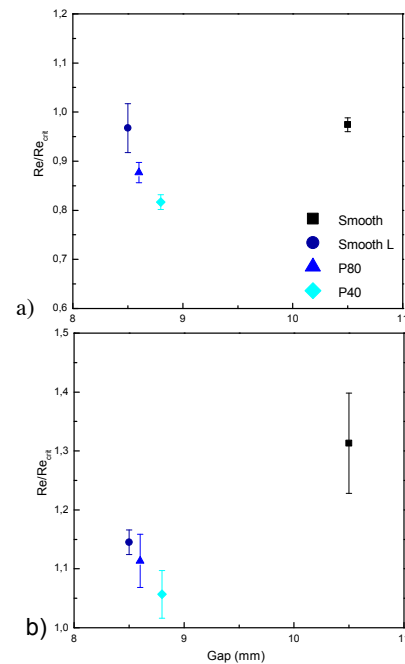


Figure 1: Onset of instabilities with different surface roughness and gap size (a) Onset of TVF is influenced by the surface roughness, whereas, (b) onset of WVF is influenced by the gap size.

0.87 (10% lower) and with P40 it is even more pronounced with an earlier onset of 17% ($Re/Re_{crit} = 0.81$).

In contrast, the onset of WVF is less influenced by the surface roughness, but more on the gap size. Here, smooth L, P80 and P40 have similar gap sizes and onsets of $Re/Re_{crit} = 1.14 / 1.11 / 1.05$. The onset for the smooth surface with a larger gap size is increased to $Re/Re_{crit} = 1.31$.

From these results it can be concluded that the onset of TVF is influenced by a small noise on the surface. The rough surface triggers the flow instabilities and can lead to an overall drag increase [8]. On the other hand, the second instability, WVF, is affected by the spatial characteristics, resulting in a faster onset with increasing gap width.

Another observation is the similar decrease of the onset values for TVF and WVF. The ratio between WVF/TVF-onset is for all cases around 1.3. The energy cascade might explain this phenomenon in flow instability. The increase in Reynolds number means the increase of the energy supply, which is structured in cascade.

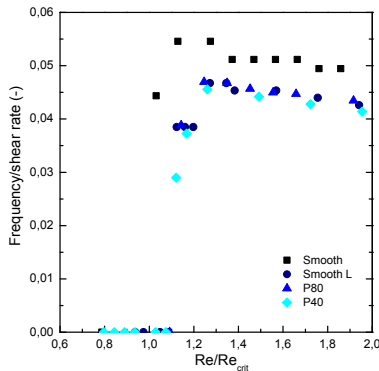


Figure 2: Normalized oscillation frequency of WVF over a range of Re/Re_{crit} for smooth, smooth L, P80 and P40.

3.2 Oscillation frequency of WVF

A detailed observation of the oscillation frequency of wavy flow superimposing the TVF is presented in Figure 2. The azimuthal wavenumber is assumed to be constant for all measurement. The frequency is plotted over the entire range of Re/Re_{crit} and normalized by the shear rate. It gives information on the influence of the rough surface independent on the increase of rotational speed. It can be observed that there is no change in oscillation frequency depending on roughness. It supports the results with the onset of WVF that the gap width more affects the wavy state. The small inner, smooth cylinder has a slightly increased normalized frequency. This leads to an increased travelling speed of the wavy flow, which can be again explained by the spatial characteristics of the wider gap or the change in number of modes.

The decreasing slope could be explained by the non-linear increase of supplied energy to reach a next

energetic mode (modulated wavy). Here a second wave flow is superimposed, which needs energy to be constructed taking it from the wavy state.

3.3 Shape of vortices

In case of smooth cylinder surface, the Taylor vortices adapt the size of the gap and where the ratio of axial upward ($+V_{z,max}$) and axial downward ($-V_{z,max}$) velocity is equal to 1. This is demonstrated in Figure 3, where the round dots represent the smooth cylinder surface. The ratio is the same for the inner and the outer wall of the gap.

Regarding the cylinders with the rough surface, the ratio

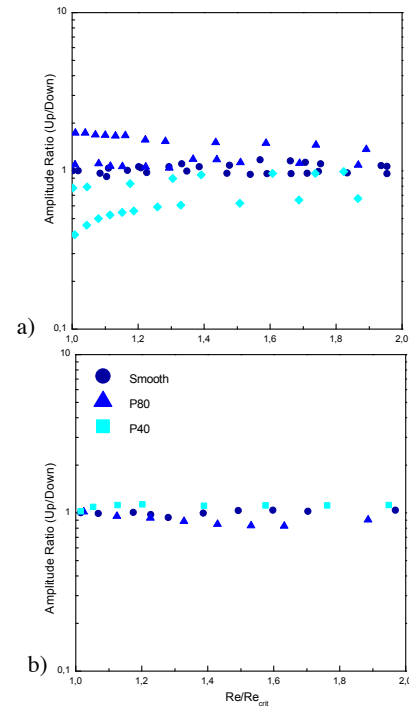


Figure 3: Ratio of $+V_{z,max}$ and $-V_{z,max}$ for different critical Reynolds numbers Re/Re_{crit} for a) inner surface, b) outer surface.

is not equal to 1 for the flow at the inner wall. In case of P80 the upward ($+V_{z,max}$) flow is slightly increased compared to the downward flow at the inner wall. Whereas in case of the rough surface P40 the downward flow is increased at the inner wall, leading to a ratio lower than 1.

A possible explanation is the presence of micro-vortices in the depths of the rough structure. The rotational direction of the inner cylinder forces these vortices into the same direction, which is in this case the downward ($-V_{z,max}$) direction.

4. Conclusion

In this study, the influence of rough surface on flow structure in Taylor Couette cell was analyzed.

It can be concluded that the onset of TVF is strongly influenced by the rough surface. It supports the onset

taking place at lower Reynolds numbers, whereas the onset of WVF is more influenced by the gap width of the system. In addition, it can be stated that the oscillation frequency in WVF regime is not influenced by the roughness but more by the gap width.

Axial velocity measurement showed that the shape of the vortices, namely, the ratio between upward flow and the downward flow is influenced by the rough surface.

These findings have a huge impact on the application fields where dynamic membrane technologies are used and in general, where a rough surface is present in flow. For the calculation of the Reynolds number, the roughness factor has to be considered.

5. Acknowledgements

D. Dufour for introduction into UVP measuring principles; D. Kiechl and B. Pfister for construction of the experimental setup and B. Koller for giving a helpful IT-support.

References

[1] Andereck, C. D., Liu, S. S., Swinney, H. L.: Flow regimes in a circular Couette system with independently rotating cylinders.

Journal of Fluid Mechanics 164 (1986), 155–183.

[2] Taylor, G. I.: Stability of a viscous liquid contained between two rotating cylinders. *Philosophical Transactions of the Royal Society of London A: Mathematical, Physical and Engineering Sciences* 223 (1923), 289–343.

[3] Vijiapurapu, S., Cui, J.: Performance of turbulence models for flows through rough pipes. *Applied Mathematical Modelling* 34 (6) (2010), 1458–1466.

[4] Shockling, M. A., Allen, J. J., Smits, A. J.: Roughness effects in turbulent pipe flow. *Journal of Fluid Mechanics* 564 (2006), 267–285.

[5] Jimnez, J.: Turbulent flows over rough walls. *Annual Review of Fluid Mechanics* 36 (1) (2004), 173–196.

[6] Robertson, J. M., Martin, J. D., Burkhart, T. H.: Turbulent flow in rough pipes. *Industrial & Engineering Chemistry Fundamentals* 7 (2) (1968), 253–265.

[7] Di Prima, R., Swinney, H. L.: Instabilities and transition in flow between concentric rotating cylinders. In: Swinney, H. L., Gollub, J. P. (Eds.), *Hydrodynamic Instabilities and the Transition to Turbulence*. Vol. 45 of *Topics in Applied Physics*. Springer Berlin Heidelberg (1985), 139–180.

[8] van Gils, D. P. M.: Highly turbulent Taylor-Couette flow. Ph.D. thesis, Enschede, 2011.

Ultrasonic flow measurement in liquid metal models of continuous steel casting

Klaus TIMMEL, Thomas WONDRAK, Sven FRANKE, Sven ECKERT

Helmholtz-Zentrum Dresden-Rossendorf (HZDR), P.O. Box 510119, 01314 Dresden, GERMANY

Model experiments with low melting point liquid metals are an important tool to investigate the flow structure and related transport processes in melt flows relevant for metallurgical applications. One very important industrial process is the continuous casting of steel. But there exist almost no measurement data of the inner mold flow from real casting plants and there are no satisfying measurement techniques available for those harsh conditions. By this, e.g. a detailed understanding of the action of electromagnetic brakes on the complex flow is missing. Therefore we built model experiments for the continuous casting process of steel by using low melting liquid metals and investigated the mold flow under different conditions. The main value of cold metal laboratory experiments consists in the capabilities to obtain quantitative flow measurements by ultrasonic flow measurements with a reasonable spatial and temporal resolution. Standard transducers were used at the model operating at room temperature with the eutectic alloy of GaInSn. Ultrasonic transducers for high temperatures and ultrasonic waveguide sensors were used at the big model, which uses the alloy Sn60Bi40 as model liquid and is operated at temperatures of 200-350 °C. Results from the mold flow measurement will be presented, showing the effect of a static magnetic field on the flow structure. It turned out, that the magnetic field can locally accelerate the flow, contrary to the expected action as a brake. The ultrasonic velocity measurement data were further used for validation and for comparison with other measurement techniques at the model experiment.

Keywords: Continuous casting of steel, electro-magnetic flow control, liquid metal models, applied Ultrasonic Doppler Velocimetry, ultrasonic wave-guides, high temperature transducers

1. Introduction

The persistent effort to achieve a better product quality and higher productivity of the continuous casting of steel implies the high importance of powerful capabilities to control the flow in tundish and mold, and the initial solidification in the mold. Numerous sophisticated numerical simulations concerned with the metal flow during the casting process need a fundamental experimental validation. The use of water models has the advantage to save expenses and to be able to apply a number of well-proved measuring methods. However, a generalization of these results to liquid metal flows has to be considered as questionable because the realistic values of flow parameters (Re, Pr, Gr, Ha, etc.) are difficult to meet. In many cases, for instance liquid metal flows with strong temperature gradients, with an additional gaseous phase or under the influence of electromagnetic fields, the flow phenomena cannot reasonably be modelled by means of water experiments.

The application of electromagnetic fields provides a considerable potential to control the fluid flow in the mold and to influence the solidification in the strand. First strategies for EM applications in steel casting were mainly guided by simplified pictures of the magnetic field impact on the global flow field. Many numerical investigations have been reported until now to improve the understanding of the magnetic field influence on the mold flow (see for instance [2-5]). However, the problem has to be considered as challenging because of the complex geometry, the highly turbulent flow, and specific peculiarities occurring in case of MHD turbulence. Obviously, a validation of the numerical predictions by liquid metal experiments is indispensable.

However, related experimental studies are rather scarce until now. Several plant trials were carried out [6, 7] to test the efficiencies of electromagnetic brakes in the real casting process. Because of the lack of suitable measuring techniques for liquid steel at 1500 °C such trials cannot provide any reliable knowledge about the magnetic field effect on the flow in the mold. First model experiments employing simplified mercury models have been reported by Japanese [8, 9] and French [10] groups. With our work we want to continue the strategy of cold metal models. The main value of such cold metal laboratory experiments consists in the capabilities to obtain quantitative flow measurements with a reasonable spatial and temporal resolution. The key measurement technique for flow characterization in our experiments is the Ultrasonic Doppler Velocimetry. It reveals the mold flow structure under different casting conditions and allows a validation of new liquid measurement techniques, like the Contactless Inductive Flow Tomography [11,12].

2. Experimental facilities

The experimental program of the LIMMCAST facilities at HZDR aims to model the essential features of the flow field in the continuous casting of steel. Basically, these are the flow fields in the tundish, in the submerged entry nozzle (SEN) and in the mold cavity, the complex two-phase flow in SEN and mold due to argon injection as well as the effect of electromagnetic actuators at the mold. For this purpose, there have been build three experimental facilities dealing with the modelling of the continuous casting process.

A photograph showing an overall view of the

LIMMCAST facility is displayed in Fig. 1. All components are made of stainless steel, including the tundish, the SEN and the mold. The low melting point alloy Sn60Bi40 is used as model liquid. The liquidus temperature of 170°C allows for an operation of the facility in a temperature range between 200 and 350°C. The schematic sketch in Fig. 1 illustrates the setup comprising two test sections. A simple pipe test section is used for general testing of measurement techniques for hot liquid metals. The continuous casting strand contains the models of a tundish, a SEN and a mold. The test sections are filled with liquid metal from the storage tank by pressurized Argon. An unused test section can be sealed by valves (not displayed in the sketch). When the loop is filled, the melt is driven by an induction pump through the corresponding test section.

The investigations on continuous casting will be explicitly focused on the behavior of the isothermal melt flow. Argon gas bubbles can be injected with tunable flow rates through the stopper rod into the SEN resulting in a two-phase flow inside the nozzle and the mold. Pipe connections with flanges are realized at various locations within the loop allowing in principal a replacement of the particular components, which gives us a flexibility to modify the flow geometries for miscellaneous requirements.

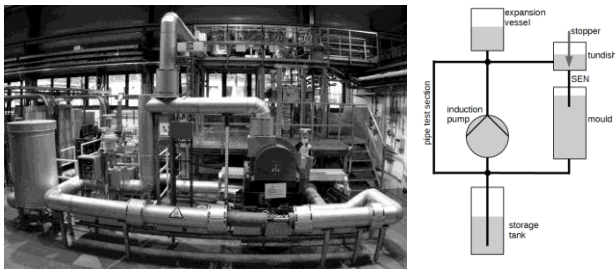


Fig. 1: LIMMCAST – large scale (250 °C) liquid metal experiment for continuous flow measurement in tundish, SEN and mold (left) and a schematic setup (right).

Fig. 2 shows the small-scale setup Mini-LIMMCAST, which is operated with the eutectic alloy GaInSn as model fluid. The experiments at this setup allow for flow measurements at room temperature (Liquidus temperature of the alloy is 10°C) and gained in valuable experiences for the detailed design of the larger LIMMCAST facility during its build-up.

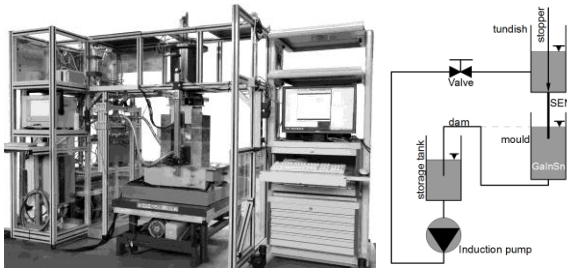


Fig. 2: Mini-LIMMCAST – small scale acrylic glass model for experimental flow investigations at room temperature using GaInSn (left) and a sketch of the operation principle (right).

The results of this setup were gained at a discontinuous

operation. The melt was conveyed from the storage tank into the tundish by an induction pump. When the tundish was filled, the stopper rod was pulled and the melt was flowing through the SEN into the mold. From the mold the melt is flowing over a dam back into the storage tank. Meanwhile, a continuous operation of this setup is also possible, but the quality of ultrasonic signal for velocity measurements is degrading in this operation mode due to increased damping of the ultrasonic signal.

The third setup, the X-LIMMCAST, is specialized in visualization of liquid metal – Argon two-phase flows by X-ray imaging. It will be therefore not considered in this paper.

Velocity measurements by the Ultrasound Doppler Velocimetry were done at LIMMCAST and Mini-LIMMCAST by using the devices DOP2000 or DOP3010 from Signal Processing. Different kinds of transducers were applied, like standard ones, high temperature transducers and transducers equipped with a wave-guide. The quantity of operated transducers in multiplexer mode ranged from two to the maximum possible of ten. The next section will give an overview on the measurement conditions and present some measurement results.

3. Experimental results

3.1 Mini-LIMMCAST – room temperature

Previous experiments showed a dramatic influence of a static magnetic field on the liquid metal flow in the mold [13]. Low frequency oscillations of the horizontal jet flow were detected as well as a local acceleration of the flow. The jet is deflected upwards by the static magnetic field resulting in a strong upwards flow near the narrow wall. This strong upward flow was measured now in the vertical velocities with the Ultrasonic-Doppler-Velocimetry (UDV) [14]. Two standard transducers with an acoustic diameter of 5 mm and an ultrasonic frequency of 4 MHz were used (TR0405LS).

During the measurement, the two transducers were in direct contact with the liquid metal. They dipped from top through the free surface into the melt. The challenge was the lift of the free surface of several centimeters between the rest and the running condition. The transducers were floating above the free surface at the start of the experiment, where the melt is at a rest. When the experiment and melt flow starts, the liquid metal level in the mold rises due to the hydrodynamic resistance in the whole outflow pipe as the outflow is driven only by gravity. Oxides at the free surface laid themselves on the transducers face and blocked the acoustic coupling into the liquid metal. A gadget with a covering plate had to protect the transducers faces and had to be pivoted away once the liquid metal level rose above the transducers contact face. With this gadget it was than possible to measure the vertical flow in the mold from the top. A measurement in vertical direction from the bottom through the bottom wall was not possible because of the high thickness of the bottom wall, the great measurement distance from the bottom towards the jet flow and the

settling of particles / impurities at the bottom which block the ultrasonic coupling into the melt.

The two ultrasonic transducers (labeled with “US” in Fig. 3) were mounted one in each mold half symmetrically with respect to the mid-plane or the SEN, respectively. The mean vertical velocity profile along the narrow mold wall recorded with this configuration is shown in Fig. 3.

The liquid metal jet emerging from the SEN is impinging at the narrow wall and splitting in a strong downward stream and a weaker upward stream under the reference condition without magnetic field. The splitting can be well detected in the measurement of vertical velocity next to the narrow wall in Fig. 3 by a change in flow direction. The static magnetic field is causing a local increase in the upward velocity which is very obvious in Fig. 3. The feature of increased upward flow was found in numerical simulations of the mold flow, too [15]. The standard configuration at Mini-LIMMCAST represents electrically isolating boundary conditions as the mold is made of acrylic glass. The rigid and conducting shell of already solidified steel at the mold wall has been modelled with thin brass plates. This brass plates had a strong influence on the temporal behavior of the jet flow (see [13]), but the strong upward flow along the narrow mold is still present (Fig. 3).

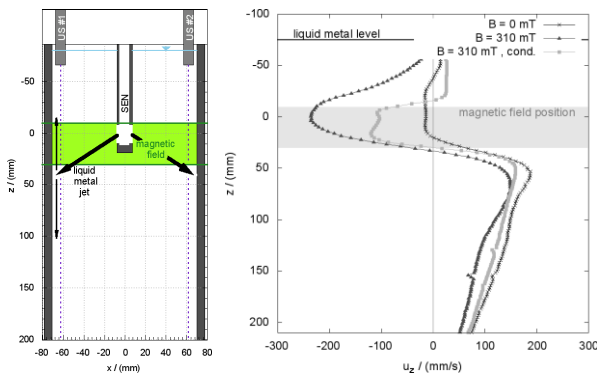


Fig. 3: Measurement configuration for mean vertical velocity along the narrow mold wall at the Mini-LIMMCAST setup (left) and corresponding results of one sensor for different experimental conditions (right).

Experiments at Mini-LIMMCAST for a closer look on the connection between jet flow and free surface shape are ongoing at the moment.

3.2 LIMMCAST – high temperature experiments

The LIMMCAST facility operates at temperatures of 200 to 350 °C. The facility comprises two test sections. The horizontal section is a closed pipe loop and serves as test section of liquid metal measurement techniques for velocity or flow rate, for instance. The UDV-method with high temperature transducers (TR0405LTH) has been tested at this section for the operation with the tin-bismuth alloy at about 200 °C.

The ultrasonic transducers were mounted with special adapters and holders with a Doppler-angle of 45° to the stainless steel pipe with an inner diameter of 54.5 mm. The measurement was performed through the stainless steel wall of the measurement adapter.

The velocity profile in the pipe flow is shown in Fig. 4. The velocity profiles had to be corrected at both ends. At the beginning, the ultrasonic echo from the melt is superimposed by the much stronger signal of multiple echoes inside the wall. The velocities at the first 5 mm are therefore much too low. At the other end, the velocity remains too high and did not converge to a wall velocity of almost zero. This is related to the existence of multiple echo paths from the scattering particles to the ultrasonic transducer with different time of flights or different apparent positions. Additionally, the measurement volume is relatively large compared to the thickness of the boundary layer. By this and because of the inclined ultrasonic path of 45°, the measurement in the region of strong velocity gradients within the measurement volume can become complicated. Therefore, the measured profile did not necessarily converge with the perfect theoretical velocity profile of a pipe flow. The measured profiles were corrected at the first and the last 5 mm by setting the velocity directly at the wall to zero and by an interpolation to the next measured velocities at a greater distance than 5 mm to the wall. The resulting velocity profiles in the pipe are shown in Fig. 4.

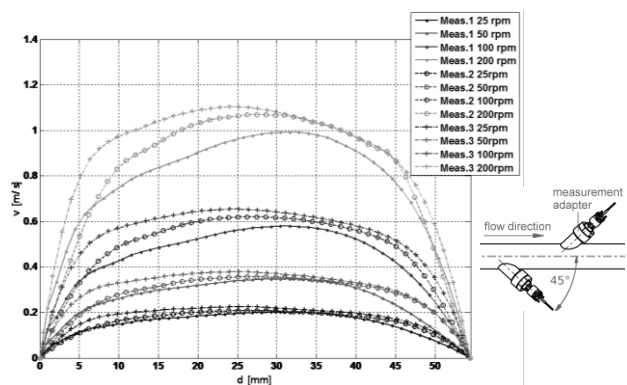


Fig. 4: Velocity profiles of the pipe flow at the horizontal test section of the LIMMCAST facility for different pump speeds.

The second test section comprises the continuous casting modelling. It is again a liquid metal loop containing the main parts of a continuous casting machine, which are the tundish, the SEN and the mold. There are free melt surfaces in the tundish and the mold, just like in the real casting process. The effect of a static magnetic field was investigated at the big LIMMCAST facility too. The mold is made of stainless steel and represents electrically conducting boundary conditions therefore. The vertical velocity was measured again with the UDV-method. This time transducers with wave-guides (TR0408W30) had to be used due to the higher temperature of the melt in the LIMMCAST facility.

Before putting the transducers with wave guides into operation, the contact face of the wave guide has to be prepared. Just like in soldering, impurities and oxides have to be removed from the surface (mostly done by an acid). Afterwards a thin initial layer of the operating metal was deposited on the cleaned facing by dipping the sensor in a liquid melt pool with clean free melt surface. The LIMMCAST facility is operating with an alloy of

tin-bismuth, so the same alloy was used to produce the initial wetting of the wave guide. The ultrasonic wave guides were than mounted at the top lid of the model mold with a special compression type fitting. The melt is rising in the mold from the bottom to the top just like at Mini-LIMMCAST although it has other reasons at LIMMCAST. This time, no special gadget was used to protect the wave guide face from impurities on the free surface. Potential impurities have to be flushed away from the sensors facing by the liquid metal flow itself.

Fig. 5 shows the result of the velocity measurements with the mean vertical velocity for different strengths of the magnetic field and the reference case without field. The effect of increased local vertical velocity due to the static magnetic field could be observed at the big LIMMCAST just like at Mini-LIMMCAST.

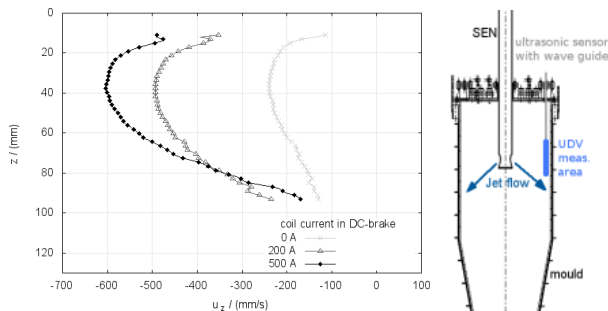


Fig. 5: Vertical velocity along the narrow mold wall (left) and sketch of measurement configuration (right).

The use of wave guides is a useful extension of the Ultrasonic Doppler Velocimetry to higher temperatures. However, it needs a careful preparation of the wave guides contact face for a good wetting to the liquid and a good acoustic coupling into it. Further, experimental conditions can have an influence on the wetting behavior even during an experimental run and therefore on the quality of the velocity measurement. So, the application of ultrasonic sensors with wave guides can be still a challenging task.

Conclusions

For physical modelling of the continuous casting process, it is essential to use liquid metals for conducting the experiments when regarding special effects, e.g. in case of two-phase flows or magnetic fields. To provide an experimental tool for these cases, the three experimental facilities LIMMCAST, Mini-LIMMCAST and X-LIMMCAST were built up at HZDR with slightly different scopes. This paper shortly presented two of them.

Measurement results of the liquid metal velocity by the Ultrasonic Doppler Velocimetry (UDV) were presented. The results were gained at different measurement configurations for different measurement conditions. Standard transducers were operated at the cold experimental setup, meanwhile high temperature sensors were used at the hotter LIMMCAST. The measurement was done either with a direct contact of the transducer to the liquid metal, or by pulsing through a wall, or by

directing the ultrasound in an ultrasonic wave guide to the liquid metal.

The selected results from velocity measurements showed a strong influence of the static magnetic field on the vertical velocity near the face of the narrow mold. The flow intensity was locally increased, which is in contradiction to the supposed action of a static magnetic field as contactless and overall brake. The increase in flow intensity can lead to an unstable, fluctuating surface profile. The presented results were achieved from two different facilities with different length scales, but similar scales in dimensionless numbers. The basic information agrees therefore very well.

The measurement results of the liquid metal experiments represent a valuable data base for the validation of numerical models, e.g. [15-18].

Acknowledgment

The authors acknowledge the financial support from the German Helmholtz Association in the framework of the Helmholtz Alliance LIMTECH.

References

- [1] K. Timmel, S. Eckert, G. Gerbeth (2011), *Metall. Mater. Trans. B* 42, 68-80.
- [2] B.G. Thomas, L. Zhang, (2001), *ISIJ Int.* 41, 1181-1193.
- [3] K. Takatani, K. Nakai, T. Watanabe, H. Nakajima (1989), *ISIJ Int.* 29, 1063-1068.
- [4] B. Li, F. Tsukahashi (2006), *ISIJ Int.* 45, 1833-1838.
- [5] K. Cukierski, B.G. Thomas (2008), *Metall. Mater. Trans. B* 39, 94-107.
- [6] P. Gardin, J.-M. Galpin, M.-C. Regnier, J.-P. Radot (1996), *Magnetohydrodynamics* 32, 189-195.
- [7] K.H. Moon, H.K. Shin, B.J. Kim, J.Y. Chung, Y.S. Hwang, J.K. Yoon (1996), *ISIJ Int.* 36, S201-203.
- [8] K. Okazawa, T. Toh, J. Fukuda, T. Kawase, M. Toki (2001), *ISIJ Int.* 41, 851-858.
- [9] H. Harada, T. Toh, T. Ishii, K. Kaneko, E. Takeuchi (2001), *ISIJ Int.* 41, 1236-1244.
- [10] J. Etay, Y. Delannoy (2002), *PAMIR conference, Proc. Vol. 2*, 277-284.
- [11] Wondrak, T.; Galindo V. and Gerbeth, G.; Gundrum, T.; Stefani, F. & Timmel, K.: *Measurement Science and Technology* 21 (2010), 045402
- [12] Wondrak, T.; Eckert, S.; Gerbeth, G.; Klotsche, K.; Stefani, F.; Timmel, K.; Peyton, A. J.; Terzija, N.; Yin, W.: *Metallurgical and Materials Transactions B* 42 (2011), P. 1201-1210
- [13] Timmel, K.; Eckert, S.; Gerbeth, G: *Metallurgical and Materials Transactions B* 42 (2011), P. 68-80
- [14] Gerbeth, G.; Eckert, S.; Timmel, K.; Wondrak, T.: *Journal for Manufacturing Science and Production* 15 (2015), P. 131-139.
- [15] Miao, X.; Timmel, K.; Lucas, D.; Ren, Z.; Eckert, S.; Gerbeth, G.: *Metall. Mater. Trans. B* 43 (2012), P. 954-972.
- [16] Chaudhary, R.; Ji, C.; Thomas, B.G.; Vanka, S.P.: *Metall. Mater. Trans. B* 42 (2011), P. 987-1007.
- [17] Singh, R.; Thomas, B.G.; Vanka, S.P.: *Metall. Mater. Trans. B* 45 (2014), P. 1098-1115.
- [18] Kratzsch, C.; Timmel, K.; Eckert, S.; Schwarze, R.: *steel research int.* 86 (2015), P. 400-410.

Ultrasonic velocity profiling as a wall shear stress sensor for turbulent boundary layers

Yuichi Murai, Yuji Tasaka, and Hyun Jin Park

Faculty of Engineering, Hokkaido University, N13W8, Kita-ku, Sapporo, 060-8628, Japan

There are a number of technical problems pointed out in wall shear stress measurement as it is directly sensed with a shear transducer. This is because most of the sensors adapt mechanical displacement principle intrusively to boundary layer before converted to electric signals. Here we propose an alternative method that excludes mechanical parts, based on ultrasound velocity profiling (UVP) technique. By introducing universal turbulent log-law theory to UVP data, accurate wall shear stress measurement has been realized, which was successfully demonstrated by application to turbulent channel flows at $10^4 < Re < 10^5$ in this report. Our demonstrative experiments have confirmed that there is bias error less than 1 % in the wall shear stress while random error takes within 3 % as compared with Blasius' formula. In addition, we present its extended application to bubbly turbulent channel flows in which bubbles reduced wall shear stress, i.e., drag reduction, via modification of the turbulent velocity profiles in the log-law regions.

Keywords: Wall shear stress, turbulent flow, boundary layer, ultrasound velocity profiling, drag reduction

1. Introduction

Drag reduction is a major issue in fluid engineering, that contributes to energy saving. In turbulent boundary layers along a wall, frictional drag is originated by active fluid mixing in the buffer layer that lies between viscous sublayer and outer flow regions. For single-phase turbulent flows, plenty number of studies have been reported historically to elucidate the inner layer structure of wall turbulence and its correlation to wall shear stress. As its scientific understanding progresses, there comes up demands to measure the local wall shear stress accurately. For example, drag reduction by injection of additives such as polymer and bubbles induces significant fluctuation of wall shear stress both in time and space [1-3]. Artificial modification of wall surface such as by riblet and wettability also requires assessment with resolving their space-time effects.

There are some commercially available produces for local wall shear stress measurement, e.g. shear transducer so-called. Most cases are fluid-contact types which require a small tolerance allowing shear-sensing displacement as flash-mounted on the target wall [4]. If the sensing area is reduced to improve the spatial resolution, the contact problem leads to more serious error especially for high Re -number flows. This does because the tolerance alters original boundary layer structures as it faces with viscous sublayer on the order of a few micrometer. The authors have such rich experiences how natural contamination and artificial mixing of dilute particles/microbubbles lose the accuracy of shear transducers.

To exclude such a contact issue, we have here developed a new method of local wall shear stress measurement. It is based fully on ultrasound velocity profiling (UVP), and therefore the measurement procedure and the applicable targets are the same as UVP.

2. Measurement Principle

2.1 Log-law theory of turbulent boundary layer

In turbulent boundary layer, non-dimensionalized fluid velocity u^+ has the following profile within the logarithmic layer,

$$u^+ = \frac{1}{\kappa} \log y^+ + B, \quad (1)$$

where

$$u^+ = \frac{u(y)}{u_f}, \quad y^+ = \frac{y}{l_f}, \quad \text{and} \quad l_f = \frac{\nu}{u_f}. \quad (2)$$

Here y is the spatial coordinate from the wall surface. u_f and ν are friction velocity and kinematic viscosity, respectively. The length scale l_f is called wall unit. Substituting all the definitions in Eq. (2) into Eq. (1) gives

$$\frac{u(y)}{u_f} = \frac{1}{\kappa} \log \left(\frac{u_f y}{\nu} \right) + B. \quad (3)$$

Two parameters, κ and B , are known to be constants since the equation stands universally, and these are approximately given by $\kappa = 0.4$ (called von Kármán's universal constant), and $B = 0.41$. Nishioka [5] suggested the best accurate values on these parameters to be $\kappa = 0.379$, and $B = 0.406$, which the present authors employ in this study.

Friction velocity u_f is defined by the wall shear stress τ_w and fluid density ρ as

$$u_f = \sqrt{\tau_w / \rho}. \quad (3)$$

Here the wall shear stress is generally described by

$$\tau_w = C_f \frac{1}{2} \rho U^2, \quad (4)$$

where C_f and U are friction coefficient and outer flow

velocity, respectively. Substituting Eq. (4) into Eq. (3) gives the following relationship;

$$u_f = \sqrt{\frac{C_f}{2}} U. \quad (5)$$

Further substituting Eq. (5) to Eq. (3) obtains

$$\frac{u(y)}{U} \sqrt{\frac{2}{C_f}} = \frac{1}{\kappa} \log \left(\frac{Uy}{\nu} \sqrt{\frac{C_f}{2}} \right) + B. \quad (6)$$

2.2 Estimation of friction coefficient

As velocity profile $u(y)$ is measured, all the values in Eq. (6) is fully given except the friction coefficient C_f . Therefore, C_f can be determined and Eq. (6) is satisfied. Unfortunately Eq. (6) cannot be converted to explicit equation regarding C_f , it needs graphical work or numerical approach to solve. Clauser [6] proposed graphical way, which is today known as Clauser's method. In principle, a single velocity data u at an arbitrary position of y within the logarithmic layer is enough for Eq. (6) to estimate C_f value. However, before knowing the velocity profile, y -coordinate range of the buffer layer is not judged as in practical applications. Thus, advantage of UVP takes place here. UVP obtains velocity profile $u(y)$ that constitutes the left-hand side of Eq. (6), and the logarithmic range can be identified.

Not only for the profile judgment, but also for accurate estimation of C_f , UVP has another advantage. That is, many equations can stand for Eq. (6) onto all the points of the measurable coordinate y . Hence, least square approach is introducible. We define local residual of Eq. (6) as two functions of C_f and y as

$$g(C_f, y) = \frac{u(y)}{U} \sqrt{\frac{2}{C_f}} - \frac{1}{\kappa} \log \left(\frac{Uy}{\nu} \sqrt{\frac{C_f}{2}} \right) + B. \quad (7)$$

To have the minimum residual along all the range of logarithmic layer, we further define a squared cumulative function to best estimate C_f value as

$$G(C_f) = \int_{y_1}^{y_2} g(C_f, y)^2 dy \rightarrow \min., \quad (8)$$

where y_1 and y_2 are the lower and the upper borders of the logarithmic layer. Consequently, the friction coefficient C_f is determined to minimize the cumulative residual. Partial derivative of Eq. (8) respect to C_f only produces an implicit equation which needs numerical search to find the best estimate of C_f . After the search, the wall shear stress is immediately obtained by Eq. (4). Some other approaches are examined using DNS database [7], but which assumes zero-noise in measurement, being inapplicable to experimental measurement.

3. Channel Flow Measurement

The proposed method has been validated by application to a water channel flow measurement at turbulent flow states. In this section, applications to single-phase and bubbly two-phase turbulent flows are presented.



Fig. 1 Overview of horizontal channel flow facility

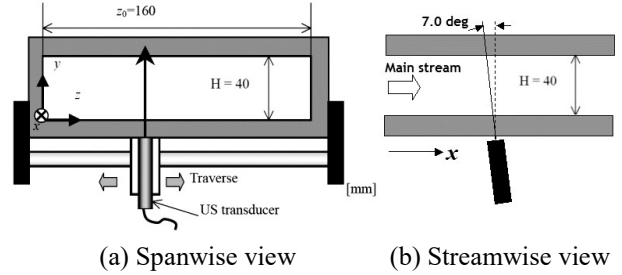


Fig. 2 Measurement line of UVP

Fig. 1 shows overview of the experimental facility. The main channel flow section is $L = 6$ m in total length, $H = 40$ mm in height, and $W = 160$ mm in span width. Water flow rate is varied with a pump at less than $Q = 0.01$ m³/s (600 l/min.). In case of bubbly flow experiments, air bubbles are injected from a hole-arranged plate mounted on the top wall of the channel.

Fig. 2 shows how the UVP measurement line was set at the rectangular channel section. The head of the transducer is submerged in a small water jacket to allow sufficient quality of ultrasound pulse. Setting parameters of UVP operation are summarized in Table 1. The beam angle uncertainty is estimated around 0.5 degree, but which does not affect the wall shear stress estimation significantly because of logarithmic impact as afore mentioned. We employ 4 MHz in basic frequency so that UVP covers all log-law region considering future application to ship boundary layers.

Table 1 Setting parameters of UVP

Parameter	Value	Unit
Base frequency	4.0	MHz
Temporal resolution	17	ms
Spatial resolution	0.78	mm
Beam angle	7	degree
Number of cycles	4	-
Number of repetitions	32	-

3.1 Single-Phase Flow Conditions

For a single-phase flow, channel flow structures keep dynamic similarity characterized by Reynolds number. We here define it using the channel central fluid velocity U and the channel half height $H/2$ as

$$Re = \frac{UH/2}{\nu} \quad (9)$$

Fig. 3 depicts water velocity distribution measured by UVP, which is expanded in space–time domain. At $Re = 28000$, we can confirm significant velocity fluctuation activated by wall turbulence in the channel flow. Fig. 4 represents time-averaged velocity profiles as water flow rate Q increases, i.e., Re number increases. The data points at $y/H < 0.25$ include structured noises due to near-field beam characteristics of the ultrasound transducer which is set outside the channel wall with 10 mm in thickness. To the contrary, the data at $y/H > 0.25$ is obtained without noise, and we target this zone for the wall shear stress analysis.

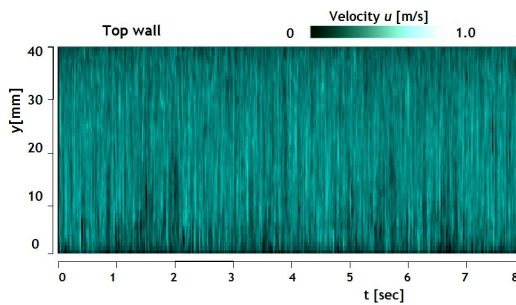


Fig. 3 Velocity distribution at $Re=28000$.

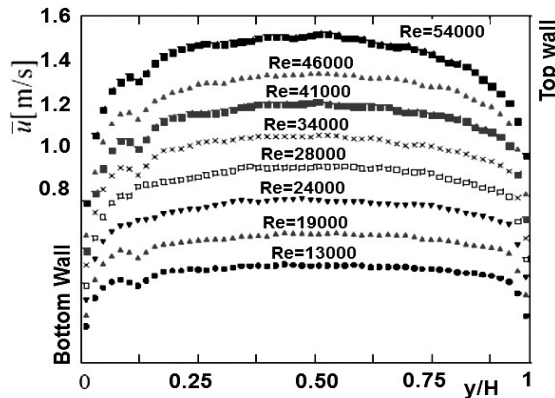


Fig. 4 Mean velocity profiles as water volume flow rate changes. Ultrasound transducer is outside the left edge of the graph. The wall surface coordinate was judged by an echo profile.

Fig. 5 shows a velocity profile obtained by UVP at $Re = 54000$, represented in semi-log graph. Many inclined lines are theoretical velocity profiles of Eq. (6) as various C_f -values are assumed. We made a numerical software which automatically finds the best C_f value. The matching accuracy has five significant numbers in digits.

Fig. 6 shows the friction coefficients C_f measured by the present method at eight different Re numbers. A curve in the graph is Blasius formula of the friction coefficient for a turbulent pipe flow in the same range of pipe-equivalent Re number. It is confirmed that the present method and Blasius theory agree to each other very well. There is no significant bias error while a small random error less than 3% comes up but which seems to be negligible in the authors' point of view as compared with

unstable performance of existing shear transducers. Fig. 7 shows the wall shear stress, which is our final goal of the measurement. On the graph, error bars mean $\pm 5\%$ in relative error.

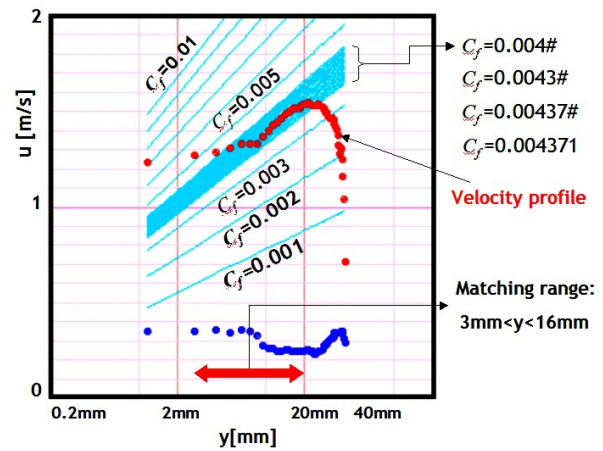


Fig. 5 Semi-log representation of measured velocity profile at $Re = 54000$ compared with theoretical log-law profiles with different friction coefficient C_f assumed in the process of numerical search for Eq. (8).

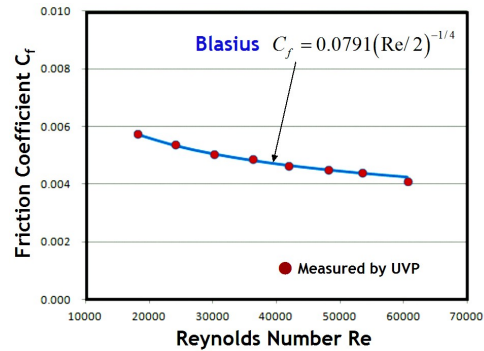


Fig. 6 Friction coefficients measured from UVP

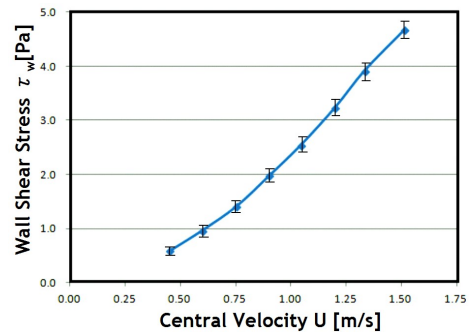


Fig. 7 Friction coefficients measured from UVP

3.2 Bubbly Two-Phase Flow Conditions

We have applied the present method to bubbly two-phase flow using the same channel flow facility. Bubble size ranges from 1 mm to 20 mm, subject to a broad deviation. We understand that Clauser's method is valid only for single-phase flow, but here we discuss its extensibility to

multiphase flows as engineering purpose, expecting practical applications.

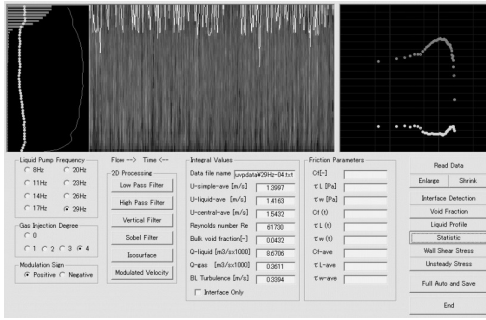


Fig. 8 UVP data analyzer for multiphase flow

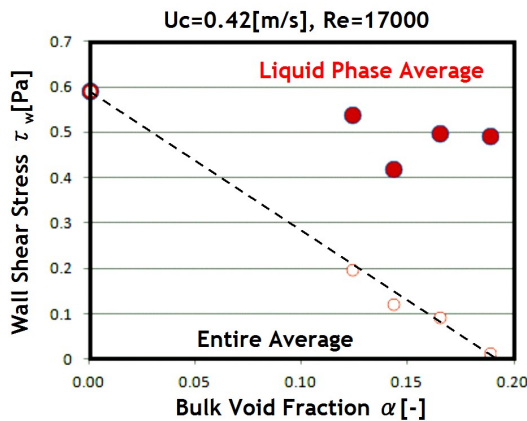


Fig. 9 Drag reduction performance at low speed flow

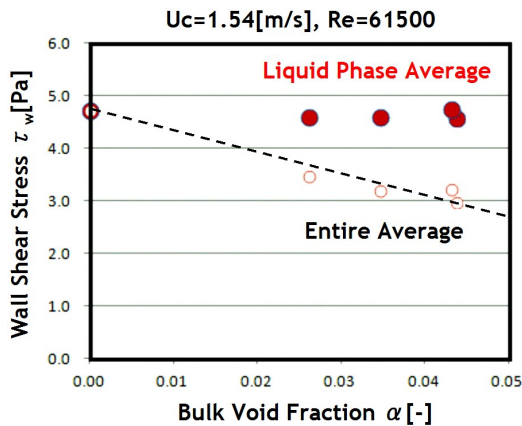


Fig. 10 Drag reduction performance at high speed flow

Fig. 8 shows a program window to process UVP data obtained for bubbly two-phase turbulent flow conditions. The process starts with interface detection based on Sobel filtering [8], and ends with wall shear stress estimation via log-law fitting. Details are explained in the presentation in ISUD.

Fig. 9 shows measured wall shear stresses as bulk void fraction of the channel increases. U_c is time-average flow speed of liquid phase at the center of the channel. Solid circles indicate the data of liquid in-phase value,

and open circles are entire averages of the wall shear stress where the local wall shear stress is assumed to be approximately zero inside bubble passing periods (i.e. free-slip wall, evidenced by Murai et al [4]). The dotted line in the graph means linear fitting of the drag reduction, which has 5.2 factor to bulk void fraction. As entire drag is reduced, we can see that the liquid in-phase drag also decreases at around 10–30 %. To the contrary, a high-speed flow condition (see Fig. 10) has smaller impact to the in-phase wall shear stress but higher factor to bulk void fraction at around 8.2. These results infer that bubbles in high-speed flow, i.e. high Weber number bubbles ($We > 200$), can reduce entire drag effectively.

4. Conclusions

We proposed in this paper a method of wall shear stress measurement from UVP data as applied for velocity profiling of turbulent boundary layers. The measurement principle of Clauser's graphical approach has been converted to data processing software which numerically finds log-law region automatically and extracts corresponding friction coefficient. The method is applicable to any liquid which UVP can measure. By application to turbulent water channel flows, the present measurement principle has been validated successfully. The method was extendedly applied to bubbly two-phase channel flow, and drag reduction performance due to injection of bubbles has been obtained only by UVP information.

Acknowledgment

The present study is supported by Japan Soc. Promotion of Science: JSPS-KAKENHI (Grant No. 24246033). The authors also thank to Mr. J. Nagao for his supporting work for UVP measurement of two-phase channel flows.

References

- [1] Murai Y: Frictional drag reduction by bubble injection (review), *Exp. Fluids*, 55: 1773 (2014)
- [2] Park HJ, Tasaka Y, Oishi Y, Murai Y: Drag reduction promoted by repetitive bubble injection in turbulent channel flows, *Int. J. Multiphase Flow*, 75: 12–25 (2015)
- [3] Park HJ, Tasaka Y, Murai Y: Ultrasonic pulse echography for bubbles traveling in the proximity of a wall, *Measurement Science and Technology*, 26: 085302 (2015)
- [4] Murai Y, Fukuda H, Oishi Y, Kodama Y, Yamamoto F: Skin friction reduction by large air bubbles in a horizontal channel flow, *Int. J. Multiphase Flow*, 33: 147–163 (2007)
- [5] Nishioka M: A new method for estimating friction velocity in turbulent boundary layers, *Nagare* (Bulletin of Japan Soc. Fluid Mechanics), 397–402 (2015)
- [6] Clauser FH: The turbulent boundary layer, *Adv. in Applied Mech.*, 4: 1–51 (1956)
- [7] Rodriguez-Lopez E, Bruce PJK, and Buxton ORH: A robust post-processing method to determine skin friction in turbulent boundary layers from the velocity profile, *Exp. Fluids*, 56: 56–68 (2015)
- [8] Murai Y, Tasaka Y, Nambu Y, Takeda Y, Gonzalez SR: Ultrasonic detection of moving interfaces in gas-liquid two-phase flow, *Flow Meas. Instr.*, 21: 356–366 (2010)

A Miniature UVP Hardware Dedicated to Process and Environmental Monitoring

Marie Burckbuchler¹, Stéphane Fischer¹

¹ Ubertone, 11 rue de l'Académie, 67000 Strasbourg, France

Ubertone has developed a new hardware for industrial and low power applications. This new development pushes further the technological limits of UVP to reach a lighter and smaller board. The electronics consumes less and powers up very quickly. The device communicates through the Modbus protocol over RS485. The comparison with a reference UVP proved that the velocity measurement reached same accuracy and comparable noise level. The first measurements on river are promising for environmental applications. The device provided a velocity profile over 1,50m deep section and the bottom tracking showed good results. The range-velocity ambiguity was optimized by shifting the minimum velocity. The ghost echoes could be filtered thanks to the phase coding method.

Keywords: Hardware, Environmental flows, Flow metering and flow mapping, Flow field monitoring.

1. Introduction

The UVP technology has been introduced to Fluid Mechanics in 1985 by Prof. Takeda [1]. Since then, many researchers have shown promising applications, especially in flow metering, rheometry and flow mapping. Nevertheless, robustness and power consumption are two major obstacles for environmental and industrial application of UVP (or UDV).

Ubertone has shown the possibility to embed a complete UVP in a single probe, the UB-Flow, allowing the measurements of high resolution velocity profiles in open channels and harsh environments. This hardware was presented six years ago at the 8th ISUD [2] and the 6th ISCE [3]. In these papers, the characteristics of the UB-Flow device, the measurement principle and first results were described. The new device presented in this paper is based on the same measurement principle. However, the size, the weight and the power consumption were reduced. In this paper, the characteristics of the new device, as well as the first results on two flumes and an urban river are presented.

2. Materials, experiments and methods

2.1 Mini UVP Hardware

The Mini UVP Hardware (see Fig. 1) is based on a completely new design, including innovation in the emitting circuit and the demodulation process. The signal processing was optimized for this new architecture and includes coherent Doppler estimation, automatic gain control, static echo filter, phase coding and blind zone compensation.



Figure 1: The new Mini UVP Hardware

This results in a much lighter, smaller and low power circuit that can drive two transducers, opening several application perspectives. Communication goes through Modbus protocol via RS485, which can be wired through USB directly on the computer. The user can access to many information as the velocity profile, SNR (signal-to-noise ratio) profile, echo profile, temperature, pitch and roll. Its main characteristics are given in Table 1.

Table 1: Main characteristics of the Mini UVP Hardware

POWER	
Input	5V DC
Consumption	0,5 to 1W
Power up	0.6s
PHYSICAL	
Size	21 x 85mm
Weight	14g
ACOUSTICS	
Number of transducers	2
Emitting frequency	400kHz to 3,6MHz
PROFILING PERFORMANCES	
Spatial resolution	1 to 2mm (frequency dependent)
Number of cells	100
EMBEDDED SENSORS	
Temperature	± 0.5°C
Pitch + Roll	± 0.5°

2.2 Experiments

This article presents three sets of experiments. The first one was done at Ubertone's office. The performances of the new device were compared to a reference UVP: the UB-Lab profiler [4]. The measurements were made in a small flume (8 x 30 x 200cm) and the same transducer of 3MHz was used for both devices. It was placed horizontally outside the flume, on the wall, with a Doppler angle β of 70° between the transducer axis and the flow axis (see Fig. 2 - a). Ultrasonic transmission gel

was put between the transducer and the wall.

For the second and the third experiment, two 1 MHz transducers were fixed on a floating board with a Doppler angle β of respectively 65° and 97° . The transducers were connected to the Mini UVP Hardware, which was plugged on a Raspberry Pi board. A computer could communicate with it through Wi-Fi.

The second experiment was done on the flume (0.6 x 15m) of ICube (Strasbourg, France). The floating board was maintained at a position with a rope (see Fig. 2 - b). Measurements have been done for two flow rates: about $266\text{m}^3/\text{h}$ and about $436\text{m}^3/\text{h}$, with water levels of resp. 43 and 50cm.

The third experiment was done on the Aar, a branch of the river Ill (Alsace, France). The board was moved on the water surface along the transect with a rope (see Fig. 2 - c). As a consequence, the board was never completely immobile, the trajectory was not exactly straight-lined and the translation speed was approximated.



Figure 2: Measurement on Ubertone's flume (a), on ICube's flume (b) and on river Aar (c)

2.3 Method

As it is not common to use the UVP technology in rivers, the setup of the device is a critical point in this environment. The configuration is mainly constrained by the velocity range. Indeed, the velocity range along the flow direction R_v is given by the pulse repetition frequency PRF and the emitting frequency f_0 :

$$2.f_0.R_v.\cos(\beta) = c.PRF \quad (1)$$

c is the sound speed in the water. If the scatterer velocity exceeds R_v , a Nyquist jump occurs.

The fact is that the velocity range is a limiting factor of the exploration depth H_v [5]:

$$H_v.R_v = c^2.\tan(\beta)/(4.f_0) \quad (2)$$

In the small flume used for the comparison between Mini UVP Hardware and UB-Lab, the speed is quite slow, 10 to 20cm/s. In this case, it is easy to measure through the full flume width (8cm) or the water depth (<30cm). However, the velocities in rivers can be much faster. For example the Aar reaches 50 to 100cm/s where the measurements were done. Thus, the explorable depth for the velocity profile is limited in comparison to the river

depth (~2m).

One more limitation of the UVP technology is the bias induced by "ghost echoes", i.e. echoes from a previous pulse. For all the results presented in this study, the phase coding method was used to differentiate echoes from the current pulse and echoes from previous ones. The ghost echoes are turned into white noise and can thus easily be identified in the SNR. This filtering method is part of a unique technological system devised by Ubertone.

3. New UVP Hardware vs. UB-Lab

3.1 Noise

The measurement of the RMS value of the noise is done by setting the cell thickness to 0 (no emission pulse) and the gain to the maximum. The results show that both devices have almost the same noise level, i.e. $2,5 \mu\text{V}$.

3.2 The velocity

Table 2: setup used for velocity measurement in the flume

	UB-Lab	Mini UVP HW
f_0 [MHz]	2,88	3,0
PRF [Hz]	799	800
Number of cells	30	30
Position of 1 st cell [mm]	9,08	8,76
Cell thickness [mm]	3,30	3,21
Inter-cell distance [mm]	3,49	3,45
Number of samples	128	128
Gain	Auto	Auto

Fig. 3 shows the velocity profile in the flume for both hardwares. The depth is given along the horizontal axis, perpendicular to the flow direction. These measurements have been made with the setup given in Table 2.

Discussion: The profiles of both devices are almost perfectly superimposed and give similar values of SNR. The profile is typical of a turbulent flow between smooth walls.

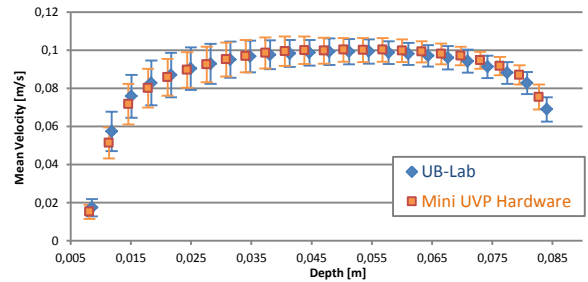


Figure 3: Horizontal velocity profiles in a rectangular flume. Average and standard deviation over 240 instantaneous profiles.

4. Measures on flume with Mini UVP HW

In Fig. 4, the average of 50 velocity profiles for two flow rates: about $266\text{m}^3/\text{h}$ and about $436\text{m}^3/\text{h}$, are given. The measures have been done with the same configuration in both cases (see Table 3).

Discussion: On Fig. 4, the bottom of the flume could not be reached with the velocity profile because of the bottom blind zone due to the side lobes of the acoustic beam.

Table 3: ICube flume velocity measurement configuration

f_0 [MHz]	1
PRF [Hz]	600
Min measurable velocity [m/s]	-0.03
Nyquist Range [m/s]	1.05
Number of cells	100
Position of 1 st cell [mm]	9.64
Cell thickness [mm]	5.93
Inter-cell distance [mm]	5.93
Number of samples	128
Number of profiles	10
Gain	auto

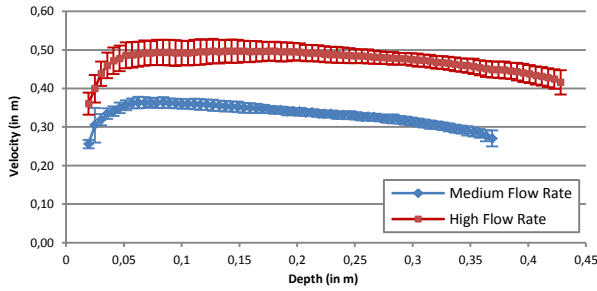


Figure 4: Average velocity profiles and standard deviation for two flow rates in the flume of the ICube Laboratory

5. Measurements on river with Mini UVP HW

For the river measurements, three sets of configuration (see Table 4) have been used: one for the bottom tracking through the transect, another for the velocity profile on a fixed position and a last one for the velocity profile through the transect.

Table 4: Measurement settings for river measurements

	Bottom Tracking	Velocity Profile	Transect Velocity
Doppler angle [°]	97	65	65
f_0 [MHz]	1	1	1
PRF [Hz]	300	420	420
Min velocity [m/s]		-0.10	-0.03
Nyquist Range [m/s]		0.74	0.74
Number of cells	82	85	85
Position of 1 st cell [mm]	19,6	96.74	96.74
Cell thickness [mm]	20,0	20.02	20.02
Inter-cell distance [mm]	29,7	18.53	18.53
Nb of samples	50	128	128
Nb of profiles	10	10	10
Gain	20 dB	auto	auto

5.1 Bottom tracking

An estimation of the river bed (see Fig. 6) was obtained pulling the board manually across the river and using the

settings given in Table 4. The bottom of the river is located by a peak in the backscattered echo profile.

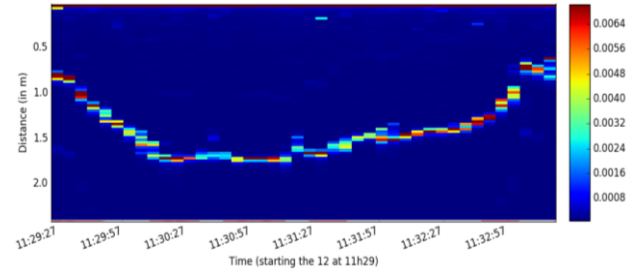


Figure 5: Amplitude profiles over the river (V)

The Fig. 5 represents the echo amplitude of the transducer ($\beta=97^\circ$) and shows the evolution of the depth. Each vertical is an amplitude profile. An algorithm of level detection is able to give automatically the position of the river bottom, as shown on Fig. 6.

The bottom tracking (Fig. 5 and 6) and the velocity measurement (Fig 8) were made simultaneously: the board was moved along the transect in 4 minutes. In Fig. 6 and 8, the position on the transect is given as abscissa. The 0 and 10m positions are related to the first and last measurements that were made. Both are located at about 1.5m from the shore.

Discussion: On Fig. 6, when the algorithm does not find the bottom peak, the point is missing on the curve. Irregularities are due to the manually transect crossing. The position on the transect is given approximatively. A precise bathymetry could be obtained by recording precisely the position of the board (with an external positioning system) and by taking into account the pitch and roll angles (given by the Mini UVP Hardware).

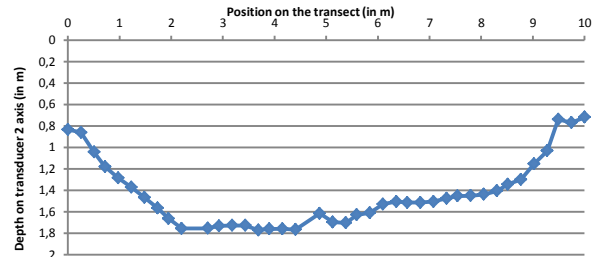


Figure 6: Bottom tracking with the Mini UVP Hardware

5.2 Velocity profile in the river

The following measurement (Fig. 7) was done at a fixed position using the settings given in Table 4, in the middle of the river, with a depth of 1.80m.

The first 20cm of the measured profile have been rejected because of ghost echoes. From there, the velocity decreases starting at a velocity of about 31cm/s in flow axis.

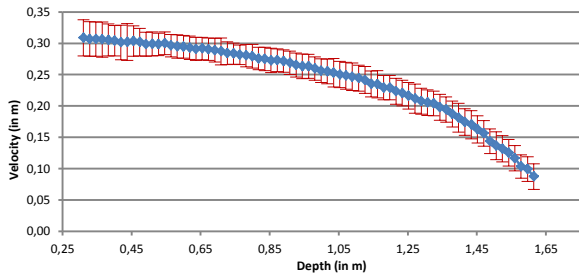


Figure 7: River velocity profile with the Mini UVP Hardware

Discussion: Fig. 7 shows a velocity profile for which the standard deviation is quite constant along the whole measured depth. The velocity profile is obtained almost until the river bottom, but not in the first 30cm. In the rejected 20cm, the velocity could be obtained by changing the PRF, which shifts the ghost echoes [5].

As for the configuration, it is important to pay attention to the Nyquist range, which is given by the PRF, and to the minimal measurable velocity to set. Here, the PRF of 420Hz gives a range of 74cm/s. Setting the minimal velocity to -10cm/s in case of turbulences leads to a maximal measurable average velocity of 64cm/s. Knowing that the maximal velocity is around 31cm/s we can say that this configuration leaves margin for turbulences and is therefore well suited.

5.3 Mean velocity through the transect

When measuring the velocity by coherent Doppler method, the visibility may be limited by the presence of ghost echoes. In this case, it is possible to use phase coding and to apply a SNR filter to improve the velocity profile.

This filter was applied on the velocity data of the first transducer ($\beta=65^\circ$) during the crossing of the transect (see Fig. 8 – a) and we obtained the evolution of the mean velocity when moving away from the shore (see Fig. 8 - c). Moreover, the values beneath the bottom given by the water level algorithm were suppressed. And as in paragraph 4, there may be a blind zone at the bottom, so the values in this area have also been removed.

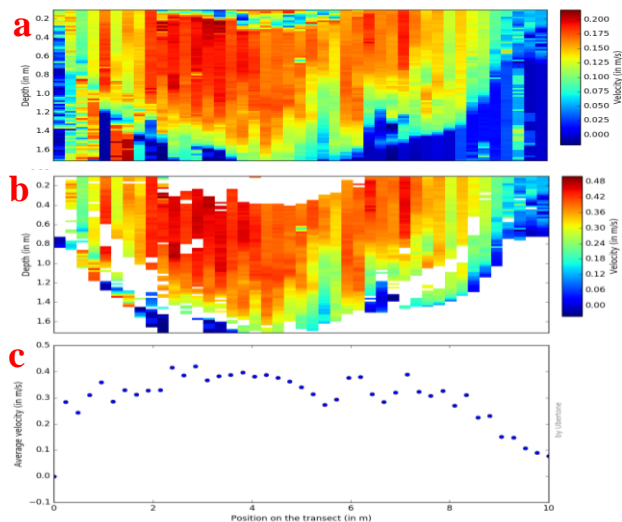


Figure 8: River raw (a), filtered (b) and mean filtered (c) velocity on flow axis, along the transect

Discussion: The filter is determined on the mean SNR profile of each mean velocity profile (one column on the color plots). Each profile is actually an average of 10 profiles. Thus, there are still some values that are not properly filtered as shown on the color plot in Fig. 8. Filtering individually each of the 10 profiles with its corresponding SNR profile before averaging would enhance the result.

Moreover, the board was moving with the waves and the pitch and roll angles have not been taken into account, nor for the bottom tracking in part 5.1, neither for the velocity profiles here.

6. Summary and outlooks

With this new hardware development, we pushed further the technological limits of UVP to reach a lighter and smaller board. The electronics consumes less and powers up very quickly. It is equipped with two transmit/receive channels allowing to measure up to 100 cells in a profile. The communication protocol allows easy usage of the device. The main features remain: automatic gain control, static echo filter, phase coding, blind zone compensation, signal-to-noise ratio estimation.

The Miniature UVP Hardware shows results close to the devices already commercialized by Ubertone. These first measurements are promising for application in small rivers and open channels. The main limitation for this application is the range-velocity ambiguity which is inherent to the coherent Doppler method. To be able to see deeper in the river even with high velocities, other methods [6] have to be explored.

The missing values due to ghost echoes could be measured by changing the PRF, which shifts the ghost echoes.

The specifications of this new UVP Hardware devised by Ubertone break new ground for a wide range of applications. Indeed, this 14g board will be embedded on a flying drone for flow measurement on rivers. This project is in partnership with LORIA, Pedon Environnement and Alerion and is co-funded by the European Union as part of the operational program “Feder-FSE Lorraine et massif des Vosges 2014-2020”.

References

- [1] Takeda Y: Velocity profile measurement by ultrasound Doppler shift method. In: Harada M, Pergamon (eds) Fluid control and measurement, FLUCOME TOKYO '85, Tokyo, 1985, p 851.
- [2] Fischer S: A new high resolution velocity and acoustic turbidity and acoustic turbidity profiler for open-channels, ISUD, 2010.
- [3] Fischer S: Evaluation of a High Resolution Acoustic Profiler for Hydraulic Erosion Studies, ICSE, 2012.
- [4] Ubertone: UB-Lab User Manual, Rev140906, www.ubertone.com.
- [5] Kenichi T., Michitsugu M., Takeshi S., Toshomasa K.: Ultrasonic pulse-Doppler flow meter application for hydraulic power plants, Flow measurement and Instrumentation 19, 2008.
- [6] Franca M J and Lemmin U: Eliminating velocity aliasing in acoustic Doppler velocity profiler data, LHE, Ecole Polytechnique de Lausanne, Switzerland, 2006.

Flow-Viz Pulsed Ultrasonic Doppler System with Auto Tuning of Analog-, Digital Gain and Threshold

Johan Wiklund¹, Stefano Ricci², Valentino Meacci², Reinhardt Kotzé³ and Beat Birkhofer⁴

¹ SP-Technical Research Institute of Sweden, Gothenburg, Sweden, johan.wiklund@sp.se

² Information Engineering Dept., University of Florence, Florence, Italy

³ FPRC, Cape Peninsula University of Technology, Cape Town, South Africa

⁴ Sika Services AG, Zürich, Switzerland

In all industrial applications and installations, it is important to have a robust system that is capable of performing accurate velocity profile measurements with minimum operator influence. Some critical measurement parameters need to be set and optimized prior to the measurement for the particular configuration. For example; acquisition depth, number of acquired samples, decimation, PRF, gain and velocity estimation parameters etc. The measurement accuracy will depend on how well the critical parameters are set. In this work, we present the latest revision of the developed Flow-Viz rheometric system that is equipped with a new firmware that allows the automatic tuning of some of the critical control parameters, and which is now optimized for real-time on-board data processing and onboard profile estimation. It is demonstrated that the auto tuning capabilities of the Flow-Viz system leads to improved measurement accuracy compared to the conventional instruments with manual, operator dependent setting of the critical measurement parameters.

Keywords: Ultrasound, Doppler, Pulsed Ultrasound Velocimetry (PUV), rheometry, industrial process monitoring

1. Introduction

Flow properties such as the shear rate dependent viscosity, are directly linked to product quality and therefore represent important control parameters. The continuous monitoring of these parameters of industrial fluids during production is of paramount importance for process and quality control. Typical industrial fluids are multiphase systems that are transported via pipes between process steps within a plant. For industries, understanding the fluid behavior and flow dynamics is also fundamental in optimizing such processes [1]. Until Flow-Viz was introduced, only time discrete laboratory measurements on fluids specimens were possible and no other practical in-line solution exists for non-Newtonian and opaque industrial fluid [1]. It has previously been demonstrated in the literature that measurement of the velocity profile of the flow moving in the pipe when combined with pressure measurements, allows an accurate rheological characterization according to the PUV+PD method [2-5]. The Flow-Viz, which is the only commercially available fully integrated ultrasound system for in-line fluid characterization, and its development has been presented in the literature, see e.g. [2-5]. In this work, the second generation of the Flow-Viz rheometric system is presented, which is now equipped with a new firmware that allows the automatic tuning of some of the critical control parameters and which is now also optimized for real-time on-board data processing and onboard profile estimation.

2. The Flow-Viz in-line rheometer system

The Flow-Viz system is based on the enhanced tube viscometry concept combining Pulsed Ultrasound

Velocimetry + Pressure Difference (PUV+PD). The methodology has been described in numerous publications and will not be described here, see e.g. [3-7].

2.1 The operator's panel housing all electronics

The Flow-Viz system consists of an operator's panel and a remote sensor unit. The panel, shown in Figure 1, houses the proprietary electronics (see next section) and an industrial PC (Beckhoff Automation, Germany) that displays the user interface. In particular, the system embeds all of the electronics required for the conditioning, acquisition and processing of the ultrasonic and pressure signals. The Flow-Viz was presented in detail in [6].

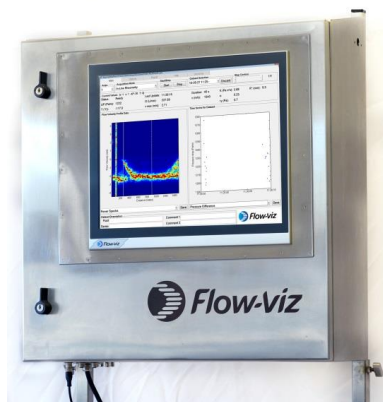


Figure 1: The Flow-Viz operator's panel.

2.2 Non-invasive sensor technology

The sensor unit holds all of the sensors and is installed in the process network and makes up the measuring section. Industrial applications require complete non-invasive ultrasound sensors due to high temperatures, pressures and possible abrasive fluids. Flow-Viz therefore developed a wide range of industrial sensors that consists

of several components such as a high power ultrasound transducer, wedge, attenuator as well as different mounting designs for easy installation on pipes [6]. The complete sensor unit setup enables non-invasive Doppler measurements through high grade stainless steel and can be installed on pipes with diameters from 0.5 up to 6 inch with different pipe wall thickness (Flow-Viz, Sweden), see Figure 2.

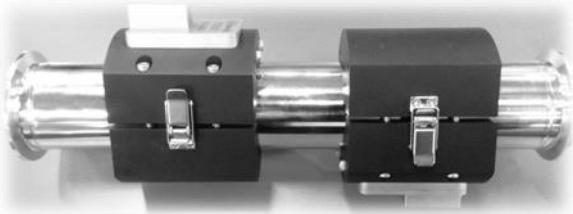


Figure 2: The Flow-Viz non-invasive sensors

The sensor unit typically comprises also a differential pressure sensor with remote seals (ABB Automation Technology Products AB, Sollentuna, Sweden) and a non-invasive PT-100 sensor (Pentronic, Gunnebo, Sweden).

2.3 Overview of the Flow-Viz electronics

The Flow-Viz system includes all the electronics necessary for processing and conditioning the ultrasound signal. The system measures the velocity profile of the fluid moving in a pipe through pulsed Doppler ultrasound, and combines it with the pressure drop. The electronics, featuring two ultrasound transmission/reception channels used alone or in pitch-catch configuration, includes powerful digital processing capabilities for real-time velocity profile calculation, and is fully programmable. It is very compact (10 × 12 cm total dimension), low power (5 W max.) and made up of two boards: The Analog Front-End and the Digital Board. The system is connected to a board of the sbRIO family (National Instruments, Austin, TX), which includes an Ethernet network connection. The details of the system are also presented elsewhere, for example in [7].

2.4 The analog front-end

The analog front-end is subdivided in two equivalent channels, shown in Figure 3. The transmission section (Tx) of each channel amplifies the transmission burst by a current feedback linear amplifier, which can reach 40 V_{pp}, and a transformer, that raises the signal up to 80 V_{pp}, and adapt the amplifier output to transducers impedance. The Tx devices are turned on only during the transmission to minimize the noise and optimize the power consumption. The receiving section (Rx) amplifies the backscattered echoes and consists of an impedance matching transformer and a single chip, which integrates a Low Noise Amplifier (LNA) and the Programmable Gain Amplifier (PGA), which, together, produce a gain from 7 to 55 dB with bandwidth between 0.8 and 7 MHz. The selection of the Rx and Tx channels is managed by suitable switches, controlled by the Field Programmable Gate Array (FPGA), located on the Digital board.

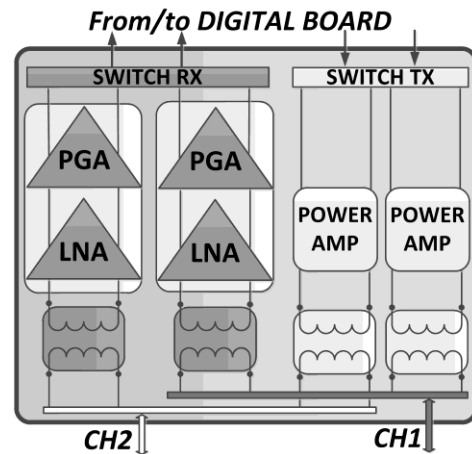


Figure 3: Analog Board with ultrasound front-end. Switches are used in TX/RX to manage 2 different transducers.

The Digital Board, shown in Figure 4, is based on the EP3C25F256 FPGA from the Cyclone family of Altera (San Jose, CA), which manages all of the digital devices present on the board. During the transmission, the burst is generated with programmable amplitude, frequency, number of cycles and tapering, by a Digital Direct Synthesizer (DDS) implemented on the FPGA. Transmission of coded excitations is possible as well. The burst is then converted by a 14-bit resolution, 100 MSPS Digital to Analog Converter (DAC) and sent to the analog front end. During the reception phase, the conditioned echoes are digital converted by an AD9265 (Analog Devices, Norwood, MA) at 100 MSPS with 16-bit resolution.

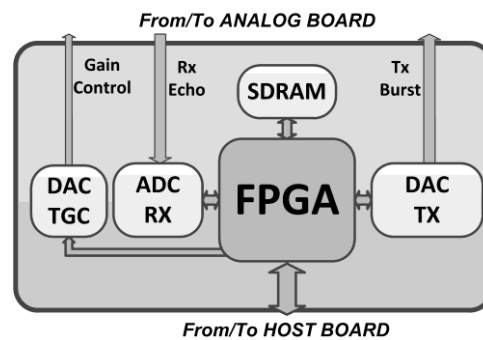


Figure 4: Digital Board. A FPGA manages all of the devices

The acquired data is then processed in the FPGA according to the flowchart presented in Figure 5. Samples are coherently demodulated by a multiplication to two, 16-bit resolution, quadrature-phase sinusoidal signals, which have the same frequency as the transmission burst. The resulting 32-bit, in-phase (I) and quadrature (Q) components are filtered by a Cascaded Integrator Comb (CIC) filter with a programmable cut off frequency and down-sampling factor. Each chain has 4 stages with input/output at 32 bit. The filtered samples are stored in the 64 MB SDRAM buffer at 32+32 bit per complex sample.

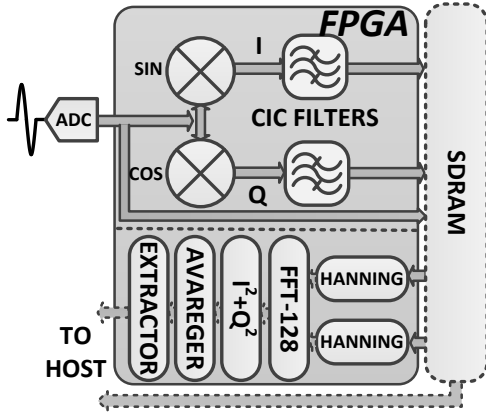


Figure 5: Signal processing chain for real-time profile calculation implemented in the FPGA.

3. Onboard data processing procedure

3.1 Velocity estimation methodology

In Pulsed Ultrasound Velocimetry (PUV) a burst is transmitted every Pulse Repetition Interval (PRI) into the medium. When moving particles are encountered, the burst produces an echo affected by a frequency shift that correlates to the particle axial velocity component, according to the Doppler effect. When a sufficient number of PRIs are stored, the velocity can be determined using methods described e.g. in [6].

3.2 Onboard data processing procedure

The latest revision is the first pulsed ultrasound system capable of automatically tuning the Analog and Digital gain parameters as well as the threshold applied to the FFT used for onboard profile estimation. When enough data has been stored in the SDRAM, the multi-gate spectral analysis starts, reading from the SDRAM to the FPGA blocks of 128 complex samples acquired from the same depth. The Hanning window is applied to each block and a block-floating point complex FFT processes the results. The sum of the square of the FFT output, converted to 32-bit floating-point format is used to determine the power spectrum. All the available depths are processed and the results are stored in the rows of a Doppler spectral matrix. A programmable number of matrices are averaged for improving the signal to noise ratio before the frequency profile is extracted. From each row of the denoised spectral matrix, the normalized frequency profile n_d is calculated with a discrete version of (5):

$$n_d = \frac{1}{N} \sum_{i=0}^{N-1} i \cdot |C_{d,i}|^2 / \sum_{i=0}^{N-1} |C_{d,i}|^2 \quad (1)$$

Where $C_{d,i}$ is the matrix element corresponding to depth d and FFT bin i , and N is the FFT size. The frequency profile is obtained by dividing n_d to T_{PRI} , i.e. the temporal length of the PRI. The frequency profile is moved to the PC where the velocity profile is finally calculated by applying (1) and the rheological parameters are extracted and shown in real-time results. The Flow-Viz system offers the possibility to use both FFT and time domain

(cross-correlation and auto-correlation) methods for velocity estimation. The autocorrelation method is robust and requires smaller footprint for its implementation but if the waveform is not perfectly repetitive due to noisy velocity signal, the autocorrelation peak will be shifted and inaccurate. Having access to the FFT power spectra provides “all” the velocity peaks, meaning that the correct velocity can be determined even from a noisy signal. With good data processing it is thus possible to obtain more accurate results but the estimation process is then slower.

3.3 Dynamic checks and auto-tuning capabilities

The tuning of the Analog and Digital gain parameters operation is based on a few RF acquisitions and the auto-tuning procedure is using an acquisition window corresponding to the internal diameter of the pipe. The automatic threshold tuning system evaluates all of the FFT lines that are calculated based on the current parameter settings and automatically adjusts the threshold value. If one or more parameters change, the tuning procedure is repeated to ensure optimal measurement accuracy. The system can check the dynamics used by the internal mathematics during the last acquisition. In particular this feature is useful to check if some saturation occurred and/or the signal was too weak in some point of the calculation chain. In case the risk of saturation is high, the number of bits used for velocity estimation is reduced. In this case, one or several bits are still available to accommodate larger signals. The automatic analog gain then tunes the gain to achieve so that the register value for the ADC range is set so that an optimal margin is left. If the signal is saturated in one of the stages of the CIC filter, resetting the dynamics of the filter to its default value is made since no digital saturation can occur (but the signal can be low and not optimized). The automatic tuning process is then repeated. The operation lasts, at maximum, 64 PRIs, which is fast enough to be used in a “real-time” application. The automatic tuning of the threshold that is applied to FFT for profile calculation is automatically estimated by the system by evaluating a sort of simplified average on all of the FFT lines that are calculated based on the current parameter setting. The threshold is set equal to the noise floor level and then corrected by a correction factor, calculated by the system or set by the operator. The threshold is tuned by over the depth range restricted by the dimensions of the pipe so that only data originating from within the fluid is used for the automatic tuning. The procedure takes longer time than the automatic tuning of the gain and is therefore made between actual measurements. The maximum time required, using 128 FFT_lines is:

$$\text{Time} = 38\mu\text{s} * \text{FFT_lines} \quad (2)$$

The auto-tuning procedure works on the configuration set by the user and if the parameter changes, the tuning procedure should be run again. The tuning procedure is based on the data acquired during the few PRIs. If something “strange” happens during such a period (e.g. a big air bubble) it is feasible that the found parameters are

not optimal so one may have to repeat the procedure several times before the optimal threshold is found.

4. Results

The successful implementation of the velocity estimation on the FPGA of the processing chain is demonstrated in Figures 6 and 7. An application is presented where the system, coupled to a non-invasive ultrasound sensor unit, performs in-line velocity profile measurements through the wall of a high-grade stainless steel pipe. The presented velocity profiles were measured in a 1Pa.s industrial liquid containing tubular micelles. The inner pipe diameter was 22.6 mm, at a volumetric flow rate of 14-15 L/min. Figure 6 shows a comparison between a velocity profile calculated in the FPGA onboard with parameter auto tune switched on and the corresponding profiles calculated in Matlab® (The MathWorks Inc., Natick, MA) using demodulated I/Q and onboard spectra data downloaded from the SDRAM. If the threshold is set manually (and incorrectly) by the operator (IQ and onboard spectra case) it may lead to inaccurate velocities to be determined, especially if the data is noisy with several peaks in the spectra. The automatic optimization of the threshold and subsequent processing however allows the selection of the correct velocity peak. This is shown in Figure 6 where a difference in measured velocities is obtained, especially in the center of the pipe where the noise was the highest.

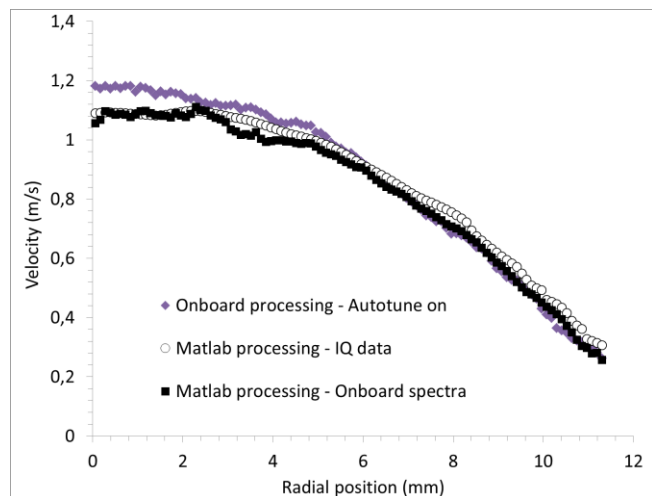


Figure 6: Velocity profiles calculated in the FPGA (diamonds) and in Matlab® using I/Q data (circles) and from onboard spectra data (squares).

The effect of the automatic tuning of the analog and digital gain in an attenuating industrial fluid is demonstrated in Figure 7. When the gain was set manually and too low by the user it is clear that the obtained velocity profile do not correspond with the expected theoretical profile. However, when the gain was automatically tuned to the optimal settings a realistic profile was obtained. It should however be noted that the same results are obtained if the parameters are set manually to the equivalent settings by the operator but this is often difficult to do, especially without a priori knowledge about the fluid and its properties. It should further be noted that if flow velocity changes so that aliasing occurs then the PRI must also be changed to a

new value. The PRI parameter is however very difficult to tune automatically but does not influence the automatic gain or threshold settings.

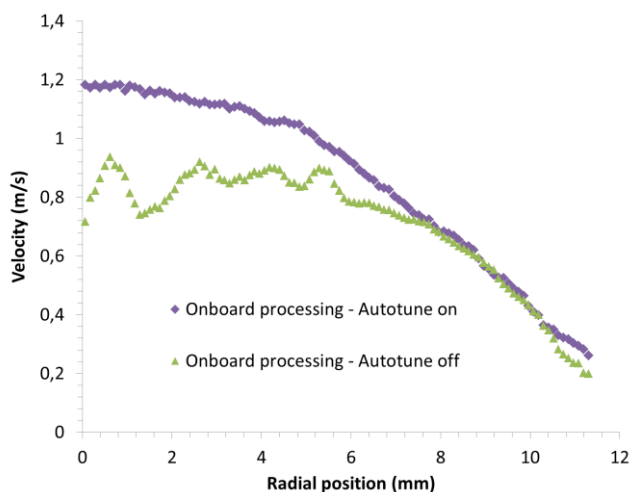


Figure 7: Velocity profile calculated in the FPGA (diamonds) with auto tune switched on and off (triangles).

5. Summary

This work presents the latest commercially available version of the Flow-Viz system featuring upgraded electronics and firmware features an Analog Front-End and a Digital Board that offers on-board processing and velocity estimation capabilities. It was demonstrated that the data processing can be performed directly in the FPGA and that automatic tuning of the analog-, digital gain and threshold results in more accurate velocity profiles in comparison with the traditional method where these parameters are set by the operator. Next step is the automatic tuning of the PRI acquisition parameter.

References

- [1] I. Roberts, "In-line and online rheology measurement", Kress-Rogers & Brimelow (eds), Instrumentation and sensors for the food industry. 2^o ed. Woodhead Publishing Limited, Abington Hall, Cambridge (2001), page 403-419, ISBN: 978-1855735606
- [2] B. Birkhofer, A. Debacker, S. Russo, S. Ricci, D. Lootens, "In-line rheometry based on ultrasonic velocity profiles: comparison of data processing methods", *Appl. Rheol.*, Vol. 22, no. 4, 44701, 2012, <http://dx.doi.org/10.3933/ApplRheol-22-44701>
- [3] S. Ricci, M. Liard, B. Birkhofer, D. Lootens, A. Brühwiler, and P. Tortoli. "Embedded Doppler system for industrial in-line rheometry". *IEEE Trans. Ultrason. Ferroelectr. Freq. Control*, Vol. 59, no. 7, pp. 1395-1401, 2012, <http://dx.doi.org/10.1109/TUFFC.2012.2340>
- [4] J. Wiklund, R. Kotzé, B. Birkhofer, S. Ricci, V. Meacci, R. Haldenwang and M. Stading. "Flow-Viz™ – A fully integrated and commercial in-line fluid characterization system for industrial applications". Proc. of 9th Ultrasonic Doppler Methods for Fluid Mechanics and Fluid Engineering (ISUD9), pp. 165-168, 2014, Strasbourg, http://www.isud-conference.org/proc/split/ISUD-09/Wiklund_ISUD-2014.pdf
- [5] R. Kotzé, S. Ricci, B. Birkhofer, J. Wiklund, "Performance tests of a new non-invasive sensor unit and ultrasound electronics", *Flow Meas. Instrum.*, vol. 46, 2015, in press, <http://dx.doi.org/10.1016/j.flowmeasinst.2015.08.013>
- [6] Y. Takeda, H. Murakawa, M. Mori (editors) "Ultrasonic Doppler Velocity Profiler for Fluid Flow", Springer Japan, (2012), page 43-69 ISBN 9784431540267 • 9784431540250, DOI10.1007/978-4-431-54026-7.

Development of a Budget Multiwave UVP System for Two-phase Flow Measurement and Some Applications

Tat Thang Nguyen¹, Hideki Murakawa², Ngoc Hai Duong³ and Hiroshige Kikura⁴

¹ Department for Industrial and Environmental Fluid Dynamics, Institute of Mechanics - IMECH, Vietnam Academy of Science and Technology - VAST, 264 - Doi Can, Ba Dinh, Hanoi, Vietnam

² Department of Mechanical Engineering, Graduate School of Engineering, Kobe University, 1-1 Rokkodai, Nada-ku, Kobe 657-8501, Japan

³ Graduate University of Science and Technology, VAST, 18 - Hoang Quoc Viet, Cau Giay, Hanoi, Vietnam

⁴ Institute of Innovative Research, Tokyo Institute of Technology, 2-12-1 Ookayama, Tokyo 152-8550, Japan

The ultrasonic velocity profile (UVP) method is a powerful tool for the measurement of spatio-temporal velocity distribution of fluid flows. The multiwave UVP method is capable of measuring simultaneously and separately instantaneous velocity profiles of the liquid- and bubble-phase in bubbly flow. Reducing the cost of the UVP systems is always of significance and interest, especially for developing countries. This paper presents the development of a budget multiwave UVP method. Instead of using costly tone-burst pulser/receivers (P/Rs), inexpensive spike P/Rs are exploited. The P/Rs generate spike signal to excite ultrasonic sensors. The auto-correlation pulsed Doppler signal processing is used. The spike-excitation multiwave UVP method is first validated by the measurement of single-phase pipe flow. For two-phase flow, the method is validated by the measurement of air-water counter-current bubbly flow in a vertical pipe. The system is used in a new method to measure the bubble condensation rate in subcooled boiling. Measurements of other two-phase flow configurations with heat/mass transfer are undergoing. The cost of a custom-built spike-excitation multiwave UVP system is approximately about less than one third of that of a commercial UVP system. Consequently, the application of the UVP method can be more expanded.

Keywords: UVP, Two-phase flow, Spike excitation, Damping effect, Boiling two-phase flow

1. Introduction

In the study of fluid thermodynamics, the spatial-temporal velocity distribution of fluid flows is of great importance. For single-phase flow, instantaneous velocity profile is required to analyze the flow characteristics in, for example, turbulent flow, etc. In such cases, there is no analytical description of the flow parameters. For two-phase bubbly flow, the problem is more complicated since instantaneous velocity profiles of both phases are required. Therefore, the development of the methods to measure instantaneous velocity profiles of fluid flows without/with heat mass transfer is crucially important.

There are very few methods for the measurement of the velocity distribution of fluid flows. These methods include the PIV (Particle Image Velocimetry), PTV (Particle Tracking Velocimetry) and UVP methods. The PIV and PTV methods require optical access into the flow field. Moreover, PIV/PTV measurement of two-phase flow is highly complicated. On the other hand, the ultrasound techniques, for example, the UVP and multiwave UVP methods for single- and two-phase flow measurements, respectively, can also measure instantaneous velocity distributions along the sound path. Measurements do not require optical access into the flow field. Moreover, non-intrusive, non-contact measurement of existing flows can be possible. These characteristics make the methods powerful for the study of fluid dynamics. However, the commercial ultrasonic systems are high cost. As a result, the development of budget

systems is of considerable interest.

In the UVP method, the active element of the ultrasonic sensor emits ultrasound when it is stimulated by an electrical excitation signal. Commercial systems typically use constant amplitude tone-burst (or sinusoidal) excitation signal. The hardware is therefore high cost. In contrast, spike signal is most widely used in the nondestructive testing (NDT) industry. The signal generated from spike pulsers has a wideband frequency spectrum. Previously, it was not used with the Doppler method. The spike length is usually shorter than that of the tone-burst. Hence, the spike signal enables high spatial-resolution measurements. In addition, the spike-pulsar circuit has simple design and is less expensive. Hence, the application of the spike excitation to the Doppler UVP measurement can significantly reduce the hardware cost. Besides, it can exploit the advantages of the Doppler signal processing.

This paper presents the use of the spike excitation with the Doppler signal processing for UVP measurement. The damping of the spike excitation has been found to be the key. Slowly damped spike excitation can enable velocity measurement by using the Doppler signal processing and the UVP sensor of the Doppler method. A multiwave UVP system has been developed. A satisfactory accuracy of the measured data of single- and two-phase flows has been confirmed. Some measurement applications carried out in the Laboratory for Industrial and Environmental Fluid Dynamics, IMECH, VAST are presented.

2. Development of the spike-excitation multiwave UVP system

2.1 Spike-excitation for the UVP method (single-phase flow measurement)

In conventional UVP systems, tone-burst signal of constant amplitude, specific number of wave cycles, and center frequency f_0 (Fig.1(a)) is used. f_0 is set the same as the sensor resonant frequency. Under such excitation, the emitted ultrasound typically has the shape shown in Fig.1(b). The number of wave cycles is an adjustable parameter, in advanced UVP systems. The design and implementation of such P/R hardware is complicated and expensive.

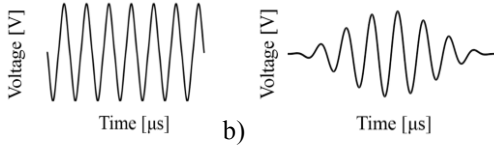


Figure 1: (a) Sinusoidal excitation signal, (b) emitted pulse.

Spike excitation is widely used in the ultrasonic testing and imaging. Under spike excitation, the sensor emits short pulses that help to improve the spatial resolution. Excitation spike (Fig.2) is characterized by a short length and a wide frequency band. A spike can be defined by a time varying voltage $V_i(t)$ as shown in Eq.1.

$$V_i(t) = \begin{cases} 0 & t \leq 0 \\ -V_\infty [1 - \exp(-\alpha_1 t)] & 0 \leq t \leq t_0 \\ -V_0 \exp[-\alpha_2 (t - t_0)] & t \geq t_0 \end{cases} \quad (1)$$

where $V_\infty = V_0 / (1 - e^{-\alpha_1 t_0})$. The parameters t_0 , α_1 , α_2 and V_0 specify the spike amplitude, rise and fall characteristics. Intuitively, the signal's fall characteristic which is determined by the signal damping has decisive effect on its power spectrum. Slowly damped signal lasts longer than highly damped one.

The excitation method affects the number of wave cycles N and the center frequency f_0 of the emitted pulse. In the Doppler method, N and f_0 are required to calculate the spatial uncertainty and the flow velocity, respectively. When the tone-burst is used, the length and frequency of the emitted ultrasonic pulses depend on the excitation signal characteristics, the sensor damping, etc. The emitted-pulse's length can be controlled by using the excitation-signal's length N . The tone-burst excitation optimizes the generation of high signal to noise ratio (SNR) ultrasound. When the spike excitation is used, the frequency of the emitted pulses is primarily decided by: (a) the forced oscillations imposed by the spike, (b) the ringing of the sensor's active element (i.e. the resonant frequency f_0). The emitted ultrasound has a wide bandwidth, low SNR.

Experimental investigations have been carried out and the following conclusions have been obtained. When the excitation spike is highly damped (i.e. at minimum damping parameter R_d or Min R_d shown in Fig.3), the emitted ultrasound has poor SNR and cannot be used

with the Doppler signal processing. When it is slowly damped (i.e. at maximum R_d or Max R_d in Fig.3), the emitted pulse is well defined and has good SNR. It can be used with the Doppler signal processing. Experimental measurements have confirmed the high accuracy of the measured velocity profiles [1]

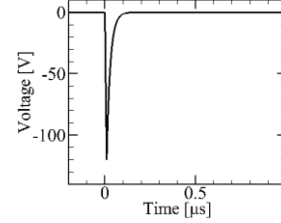


Figure 2: Theoretical spike with $t_0 = 0.01 \mu s$, $\alpha_1 = 0.2$, $\alpha_2 = 50$, $V_0 = 120 V$.

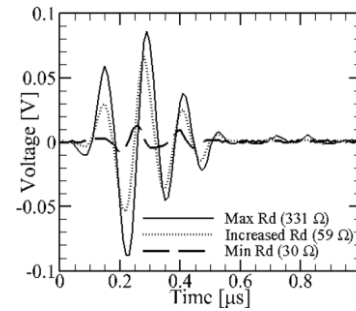


Figure 3: Emitted ultrasonic pulses corresponding to varied damping parameter R_d of the spike P/R.

2.2 Spike-excitation multiwave UVP method

The spike excitation and the Doppler signal processing are then applied to the multiwave UVP method. The program flowchart is shown in Fig.4.

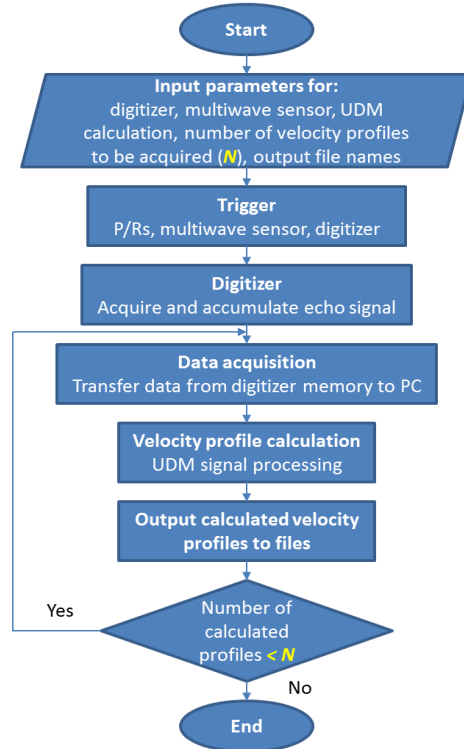


Figure 4: The flowchart of the multiwave UVP method.

2.3 Auto-correlation Doppler signal processing

The received echo signal is digitized by using a high-speed digitizer. The digitized signal is demodulated into in-phase and quadrature-phase components. The auto-correlation signal processing which is based on the Wiener-Khinchine theorem is exploited for the detection of the Doppler shift frequency. This technique might be most suitable for the processing of wide bandwidth signal. Our pilot investigations showed that high-accuracy velocity measurement by using spike excitation is enabled by the combination of spike signal and the auto-correlation signal processing.

2.4 Spike-excitation multiwave UVP system

The system is shown in Fig.5 [2]. It consists of:



Figure 5: The multiwave UVP system in IMECH, VAST.

- Multiwave sensor (Japan Probe Co. Ltd.): 2 and 8 MHz frequencies;
- Two spike P/Rs (JSR DPR300 and JSR DPR35+, JSR Ultrasonics Co., Ltd.);
- Two-channel digitizer (NI PCI-5112, National Instrument Co. Ltd.): resolution: 8 bits; max. sampling rate: 100 MHz; 16 MB memory;
- PC for data acquisition and signal processing.

The software has been developed by using LabView (for signal acquisition), C++ (for Doppler signal processing).

3. Comparison with commercial UVP

As mentioned previously, the most important aspect of the custom developed system is the lower cost. In addition, one more advantage of the system is the ability to classify exactly between zero velocity (no fluid flow) and the no velocity value (failure calculation of velocity) at a point along a measured profile. In a commercial UVP, usually, no velocity value is assigned to be zero.

4. Applications

4.1 Measurement of single-phase flow

A schematic drawing of the apparatus is shown in Fig.6. The 8 MHz element of the multiwave sensor is used. The sensor is fixed at $64D$ from the pipe inlet, $14D$ from the pipe end (D : pipe inner diameter). Nylon powder is used as the seeding particles. Reynolds number (Re) is 5500. A water box is used to couple the sensor to the test pipe.

The Doppler angle is 45° . Figure 7 shows the mean velocity profile u^+ in the wall unit y^+ . Good agreement between the measured profile and the logarithmic law has been obtained. The error bars show the standard deviation from the mean value. By using the measured velocity

profile, a comparison with the flowmeter data showed a small error which is less than 1%.

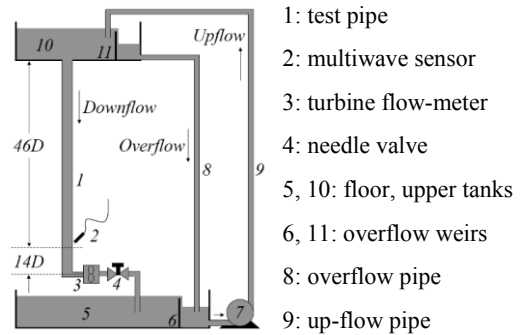


Figure 6: Experimental apparatus for the measurement of single-phase flow.

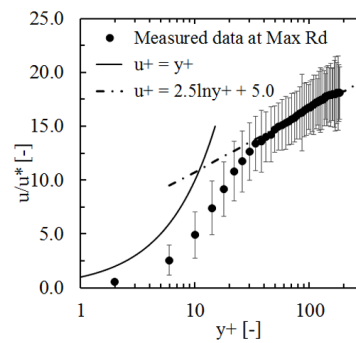


Figure 7: Comparison with the logarithmic law.

4.2 Measurement of air-water bubbly flow

Counter-current bubbly flow is generated in the test pipe ($D = 50$ mm) made of transparent acrylic (Fig.8). Water flows down; air bubbles rise upwards.

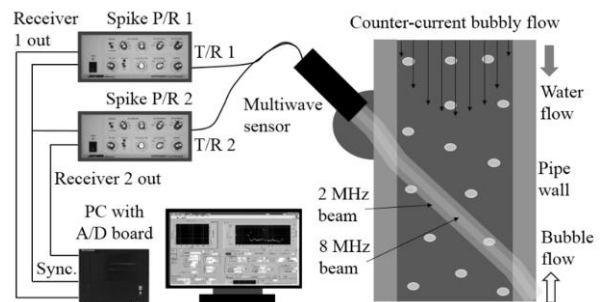


Figure 8: Spike excitation multiwave UVP system and the test section of the flow.

Liquid velocity profile is measured by the 8 MHz frequency. Bubble velocity profile is measured by the 2 MHz frequency. The velocity probability density functions (PDFs) at the pipe center are shown in Fig.9. The PDF of the 2 MHz data shows only one peak that occurs at the dominant bubble velocity. The 8 MHz data mainly contains liquid velocity but includes some bubble data. The PDF of the 8 MHz data has two peaks corresponding to the liquid and bubble velocities.

It would be worth mentioning that, with our custom-developed multiwave UVP system, the same pulse repetition frequency (PRF) is used for both frequencies.

Hence measurement of phase velocity profiles at the same time is secured by using the same number of pulse repetitions for velocity calculation. The same spatial resolution is absolutely assured by choosing the same number of digitized data points in the spatial domain for each measurement volume of both frequencies.

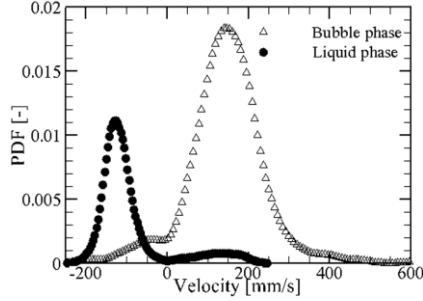


Figure 9: Velocity PDFs calculated from the measured data of the 2 MHz and 8 MHz frequencies at pipe center.

4.3 Measurement of subcooled boiling

The condensation rate of vapor bubbles (defined by $v_c = -dR/dt$ where R is the spherical-equivalent bubble radius) can be calculated by using the measured data of two simultaneous UVP measurements. The two sensors TDX1 and TDX2 are arranged as shown in Fig.10. The top- and bottom-surface velocities of vapor bubbles are measured by TDX1 and TDX2, and denoted by V_{TDX1} and V_{TDX2} , respectively. The bubble condensation decreases the velocity of the top interface. Hence, the measured data by TDX1 can be expressed as:

$$V_{TDX1} = V_b \cos\theta - v_c \quad (2)$$

where V_b is the bubble rising velocity. On the other hand, the condensation increases the velocity of the bottom

interface of the bubble. Hence, the measured data by TDX2 can be written as:

$$V_{TDX2} = -(V_b \cos\theta + v_c) \quad (3)$$

where the minus sign implies that the bubble movement in the sound path of the TDX2 is away from the sensor surface. From Eq.2 and 3, the condensation rate v_c can be calculated by eliminating the bubble velocity V_b [3]:

$$v_c = -(V_{TDX1} + V_{TDX2})/2. \quad (4)$$

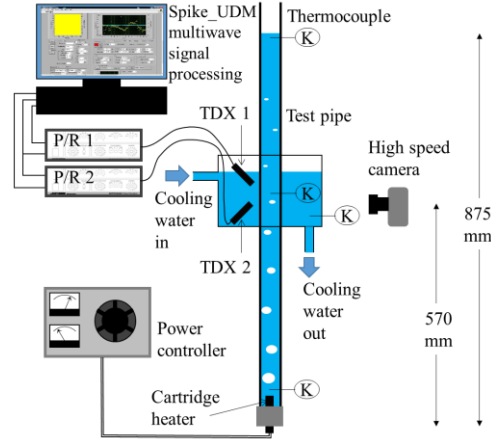


Figure 10: Experimental apparatus of subcooled boiling.

Based on the principle of condensation-rate measurement, experiments have been carried out for varied liquid subcooling temperature. In addition, flow visualization has also been carried out. The measured data are shown in Table 1. By using the measured v_c , the interfacial condensation Nusselt number Nu_c is calculated and compared with the published correlations. Fairly good agreement has been obtained as shown in Fig.11.

Table 1: Average condensation rate, bubble rising velocity and bubble diameter for varied degrees of liquid subcooling.

Liquid subcooling degree (°K)	4.6	4.4	4
Condensation rate v_c measured by using spike-excitation UVP (mm/s)	21.1	12.9	5.4
Bubble rising velocity measured by using spike-excitation UVP (mm/s)	303	246	179
Average spherical-equivalent bubble diameter measured by optical visualization (mm)	13	9.4	4.5

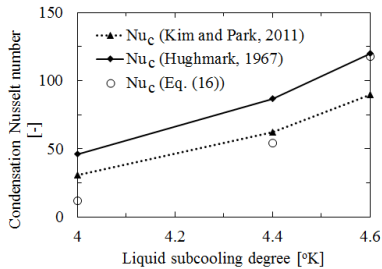


Figure 11: Comparison between the measured Nu_c with the results of other correlations.

5. Concluding remarks

Spike excitation and the pulsed Doppler signal processing have been successfully applied to the UVP method.

Based on the spike excitation technique, a multiwave UVP system for two-phase flow study has been

developed. The cost of the system can be reduced significantly as compared with the commercial UVP.

Applications of the custom developed system to fluid dynamic research at the IMECH, VAST have been successfully carried out.

References

- [1] Nguyen TT, *et al.*: Ultrasonic Doppler velocity profile measurement of single- and two-phase flows using spike excitation, *Exp. Techniques* (2016), 1-14.
- [2] Nguyen TT, *et al.*: Development of multiwave method using ultrasonic pulse Doppler method for measuring two-phase flow, *J. Japan Soc. Exp. Mech.* 13 (2013), 277-284.
- [3] Nguyen TT, *et al.*: Measurement of the condensation rate of vapor bubbles rising upward in subcooled water by using two ultrasonic frequencies, *Int. J. Heat Mass Transfer* 99 (2016), 159-169.

Influence of velocity distribution on accuracy of transit-time ultrasonic flow meter

Ei Muramatsu¹, Hideki Murakawa¹, Daiki Hashiguchi¹, Hitoshi Asano¹,
Sanehiro Wada², Noriyuki Furuichi²

¹ Department of mechanical engineering, Kobe University, 1-1 Rokkodai, Nada, Kobe, 657-8501, Japan

² National Institute of Advanced Industrial Science and Technology, Tsukuba Central 3, 1-1-1 Umezono, Tsukuba, 305-8563 Japan

The transit-time ultrasonic flow meter (TOF) derives flow rate from line-average velocity based on transit time of ultrasonic pulse on the ultrasonic path. Hence, accuracy of the TOF is strongly influenced by the velocity profile in a pipe. Velocity profile depends on not only Reynolds number but also the upstream condition and sensor pocket on the pipe wall. Therefore, on-site calibration is desirable by measuring velocity profile. In this study, a measuring system which can measure velocity profile using ultrasonic pulsed Doppler method and the transit time simultaneously was developed, and the simultaneous measurements were carried out. In the experiments, velocity profiles were distorted by installing an obstacle plate upstream of the test section and influence of the velocity profiles on accuracy of the TOF are discussed. As a result, error of the TOF is found to be 1% for axisymmetric flow and 4% for asymmetrical flow without calibration. However, if the TOF is calibrated by the velocity profiles obtained using the pulsed Doppler method, the error can be reduced to approximately 1%. Furthermore, fluctuations of the transit time are in good agreement with that of velocity profiles.

Keywords: Transit-time ultrasonic flow meter, Flow rate, Velocity profile, Ultrasonic pulsed Doppler method

1. Introduction

Transit-time ultrasonic flow meter (TOF) has been widely applied in industrial field due to its advantages, such as small pressure loss, applicability to opaque fluid and large diameter pipe. The TOF derives flow rate from the difference of the transit time of ultrasonic pulse which is related with the line-average velocity on ultrasonic path. Hence, velocity profiles are assumed and the profile factors which converts the transit time to the flow rate are calibrated under the ideal flow conditions. However, it is well known that the velocity profile changes by the upstream pipe layout, the Reynolds number and the inner pipe surface roughness, and so on. Furthermore, Cordova et al. [1] pointed out that sensor pockets on the pipe wall is considered to distort the velocity profile and degrade accuracy of the TOF. Since it is impossible to take into account all these influences for the profile factor, the calibration test in the actual field, called on-site calibration, is desired to be carried out by measuring the velocity profile in the pipe.

The ultrasonic pulsed Doppler method (UDM) derives velocity profile on the ultrasonic path from reflected signals on ultrasonic reflectors in the flow. Integrating the obtained velocity profile over the pipe, flow rate can be calculated. Therefore, even if velocity profile in the pipe is distorted, flow rate can be obtained accurately using multiple measuring lines [2]. Hence, a hybrid ultrasonic flow meter which calibrates TOF by using UDM has been proposed [3]. However, because maximum detectable velocity of the UDM was limited by the Nyquist sampling theorem, the hybrid ultrasonic flow meter could be applied only for low flow-rate conditions. Authors developed a dealiasing method, namely, the feedback method for measuring higher flow rate and six

times higher flow rate could be measured [4,5].

In this study, a measurement system which can perform simultaneous measurement of velocity profile using the UDM and the transit time of ultrasonic pulse was developed, and influence of the velocity profile on accuracy of the TOF was investigated.

2. Measurement principles

2.1 Transit-time measurement

Measurement principle of the TOF is depicted in Figure 1. The t means transit time of ultrasound between sensors in stagnant flow. If ultrasonic pulse is emitted from the upstream transducer, transit time is shortened to $t - \Delta t$ by the flow velocity. On the other hand, transit time from the downstream transducer is delayed to $t + \Delta t$. Relationship between the Δt and the line-average velocity between sensors, V_L , is expressed as

$$V_L = \frac{c^2}{D \tan \theta} \Delta t. \quad (1)$$

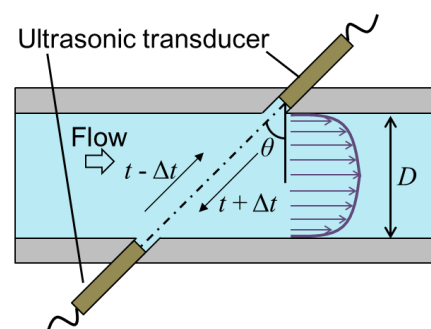


Figure 1: Measurement principle of the TOF

Where c , D , θ are the sound speed, the inner diameter of pipe and the contact angle of transducer, respectively.

Power-law velocity [6] is known as a velocity profile in fully-developed turbulent pipe flow and expressed as

$$U(y) = \frac{(n+1)(2n+1)}{2n^2} \frac{4Q}{\pi D^2} \left(\frac{2y}{D}\right)^{1/n}. \quad (2)$$

Where U , y , Q denote the axial velocity component, the distance from the pipe wall and the flow rate, respectively. n is a parameter that depends on the Reynolds number. Using Eq. (2), V_L in the power-law velocity can be calculated as

$$V_L = \frac{4n+2}{n} \frac{Q}{\pi D^2}. \quad (3)$$

Since change of n with Re is small, it can be said that V_L is almost proportional to Q if velocity profile is assumed to be power-law.

2.2 Ultrasonic pulsed Doppler method

In this study, velocity profile in a pipe is obtained by using the UDM. In the conventional UDM, maximum detectable velocity to flow direction, U_{\max} , and the maximum measurable range from the sensor, L_{\max} , are determined by the pulse emission interval, T , and expressed as

$$U_{\max} = \frac{c}{4f_0 T \sin \theta}, \quad (4)$$

$$L_{\max} = \frac{cT}{2} \cos \theta. \quad (5)$$

Where f_0 is the basic frequency of the ultrasound. In order to obtain velocity profile over the pipe, L_{\max} should be larger than D . Hence, velocity profile cannot be measured under high flow-rate condition with the conventional method which employs single pulse emission interval.

In order to overcome this limitation, the authors developed a dealiasing method referred to as feedback method [4,5]. In the method, two pulse emission intervals, T and $T + T_s$ are employed and the U_{\max} is expressed as

$$U_{\max} = \frac{c}{4f_0 T_s \sin \theta}. \quad (6)$$

Comparing Eqs. (4) and (6), the U_{\max} becomes T/T_s times higher. Since the L_{\max} in the feedback method is the same with Eq. (5), higher velocity can be measured decreasing T_s . Using the feedback method, velocity profile under high flow-rate condition is obtained, and V_L can be obtained from the velocity profile.

3. Measurement system and experimental facility

Developed measuring system consists of an ultrasonic pulser/receiver (JPR-2CH-KB, Japan Probe, Co., Ltd.), a high-speed digitizer (PXI-5114, National Instruments Corp.), a programmable function generator (AFG-2005, Good Will Instrument Co., Ltd.) and a personal computer.

The measurement software is laboratory-made and developed using C++ and LabView (National Instruments Corp.). The function generator controls the pulse emission interval in the pulser/receiver. A couple of ultrasonic transducers are connected to the pulser/receiver. One transducer emits ultrasonic pulse and receives echo signals, and the other transducer receives transmitted ultrasonic pulse. Thus, both of echo and transmitted signals can be simultaneously recorded.

Experiments were conducted at a flow rate calibration facility of National Metrology Institute of Japan (NMIJ) of Advanced Industrial Science and Technology (AIST). In this facility, flow rate is measured by using the weighing tank and its relative expanded uncertainty is 0.027%. Further details of the facility is described in [7]. Working fluid was water. Figure 2 shows the test section. Test section was horizontal pipe and its inner diameter, D , was 200 mm. A couple of transducers were set at $\theta = 45^\circ$ and submerged into the water. f_0 of the transducers was 1 MHz and its effective diameter was 12 mm. Small air bubbles were injected into the flow as ultrasonic reflector, and a rectifier was installed at upstream of the test section. The distance from the rectifier and the test section was $55D$. Installing the obstacle plate at $8D$ upstream from the test section, flow can become asymmetric. The obstacle plate has a semicircle-shaped aperture and its aperture ratio is 0.66. The flow rate ranged from 80 to 500 m³/h. Water temperature was at 20°C and $c = 1480$ m/s. The measurement parameters of tabulated in Tables 1 and 2. For all conditions, T was set at 0.5 ms. The spatial resolution along the measuring line, ΔL , can be controlled by changing the number of cycles in an ultrasonic pulse. The ΔL was varied depending on the Q because larger ΔL is required for measuring the higher velocity [4].

Table 1: Measurement parameters for symmetrical flow

Q	81.7 m ³ /h	162.0 m ³ /h	321.1 m ³ /h	500.6 m ³ /h
ΔL	1.48 mm	1.48 mm	2.22 mm	2.96 mm
T_s	-	0.167 ms	0.083 ms	0.071

Table 2: Measurement parameters for asymmetrical flow

Q	81.7 m ³ /h	162.0 m ³ /h	321.1 m ³ /h
ΔL	1.48 mm	1.48 mm	2.96 mm
T_s	0.25 ms	0.167 ms	0.071 ms

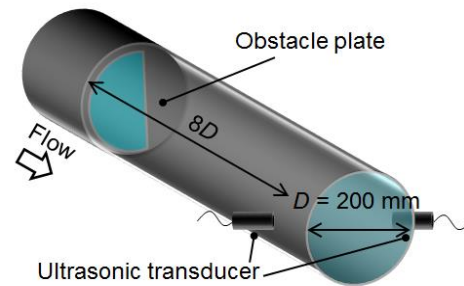


Figure 2: Layout of the test section

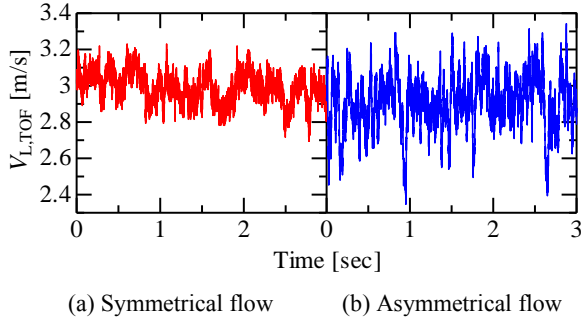


Figure 3: Time-series of $V_{L,TOF}$ at $Q = 321.1 \text{ m}^3/\text{h}$

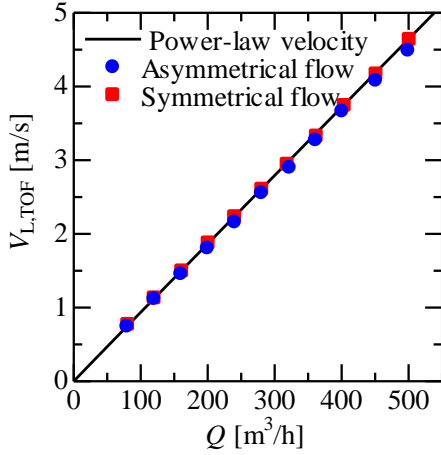


Figure 4: Comparisons between power-law and $V_{L,TOF}$

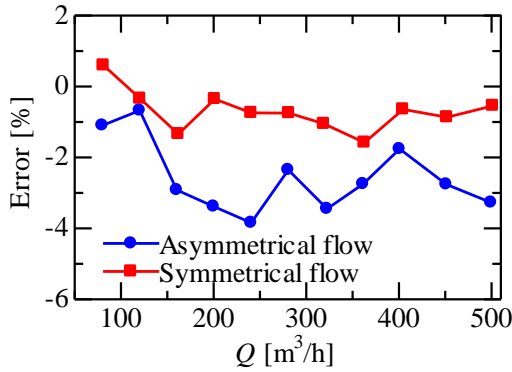


Figure 5: Error of $V_{L,TOF}$ for power-law velocity

Table 3: Standard deviations of $V_{L,TOF}$

Q	Symmetrical flow	Asymmetrical flow
81.7 m^3/h	0.038 m/s	0.095 m/s
162.0 m^3/h	0.058 m/s	0.154 m/s
321.1 m^3/h	0.120 m/s	0.211 m/s

4. Results and discussions

4.1 Measurement results of TOF

Δt was measured 1000 times, and line-average velocity, $V_{L,TOF}$, was calculated using Eq. (1) in each condition. Figure 3 shows time-series of $V_{L,TOF}$ in symmetrical and asymmetrical flow at $Q = 321.1 \text{ m}^3/\text{h}$. Although the flow

rate was quite stable in this facility, $V_{L,TOF}$ fluctuated due to the turbulence in the flow. Standard deviations of $V_{L,TOF}$ were tabulated in Table 1. It can be said that if the velocity profile is distorted and/or flow rate is higher, the fluctuation become larger and the more number of Δt should be measured for accurate measurement. Averaging 1000 $V_{L,TOF}$, time-average $V_{L,TOF}$ was calculated as shown in Figure 4. The solid line indicates Eq. (3). Although the $V_{L,TOF}$ was almost the proportional to Q , the errors between Eq. (3) and $V_{L,TOF}$ were several percent as shown in Figure 5. The errors for asymmetrical flow were larger than that for symmetrical flow, and its maximum value was 3.8%. It is because velocity profile in asymmetrical flow was distorted. In addition, maximum error was 1.6% for symmetrical flow. These errors were considered to be influence of the transducer pockets. Hence, even if the velocity profile in a pipe is considered to be fully-developed, the TOF may cause error up to 2%.

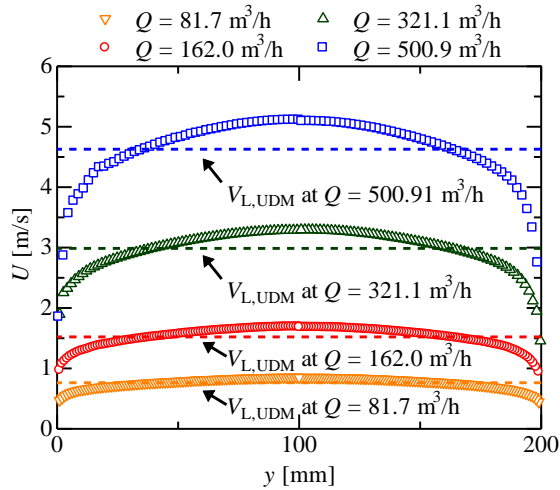
4.2 Velocity profile measurement

Time-average velocity profiles were calculated by averaging 1,000 velocity profiles measured by using the UDM. Measurement parameters are tabulated in Tables 2 and 3. Spatial resolution along the measuring line, ΔL , was changed depending on the flow rate condition because larger ΔL is required for measuring the higher velocity [4]. T_s was changed considering the flow velocity and Eq. (6). Although U_{max} was 1.05 m/s in the conventional UDM, higher U_{max} could be set using the feedback method. The results are shown in Figure 6. The line-average velocities calculated from the obtained velocity profiles, $V_{L,UDM}$, are also shown. It can be confirmed that velocity profiles were distorted by installing the obstacle plate. Velocity profile at $Q = 500.6 \text{ m}^3/\text{h}$ for asymmetrical flow could not be measured due to its high turbulence. However, velocity profiles could be accurately measured in the other flow conditions using the feedback method.

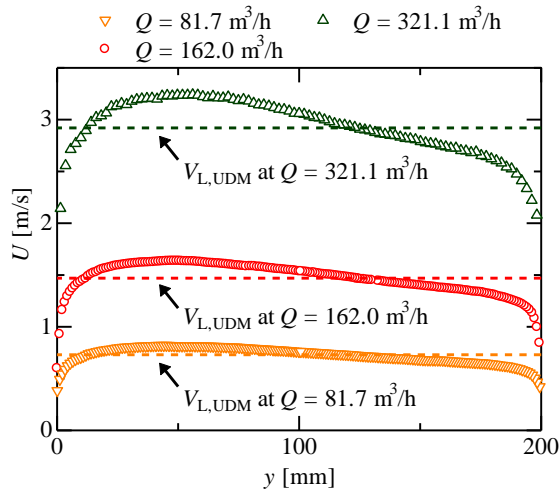
4.3 Comparisons of line-average velocities

The $V_{L,TOF}$ and $V_{L,UDM}$ were tabulated in Tables 4 and 5. Error between $V_{L,TOF}$ and $V_{L,UDM}$ were below 1% for symmetrical flow and below 2% for asymmetrical flow. Because Eq. (1) is well-established principle, these errors are considered to be caused by error in measured velocity profile by using UDM. However, calibrating the TOF by obtained velocity profile, error of the TOF can be improved particularly in distorted flow.

In order to evaluate relationship between the fluctuations of velocity profile and the transit time, time-series $V_{L,TOF}$ and $V_{L,UDM}$ were calculated at $Q = 321.1 \text{ m}^3/\text{h}$ and shown in Figure 7. Temporal resolution of the UDM was 69 ms. For direct comparisons, moving average was applied for $V_{L,TOF}$. Tendencies of $V_{L,UDM}$ were in good agreement with that of $V_{L,TOF}$. Thus, Eq. (1) can be applied for such short time scale and simultaneous measurement of velocity profile and transit time is effective for evaluating the influence of transducer pocket.



(a) Symmetrical flow



(b) Asymmetrical flow

Figure 6: Time-average velocity profiles and $V_{L,UDM}$

Table 4: Comparisons V_L for symmetrical flow

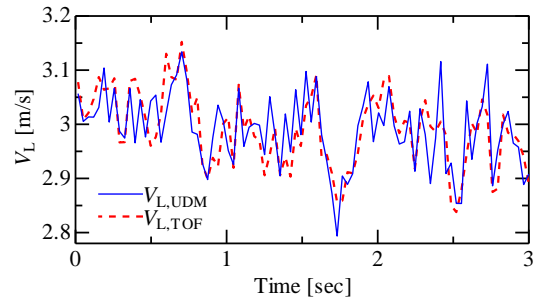
Q	80.8 m ³ /h	162.0 m ³ /h	321.1 m ³ /h	500.6 m ³ /h
$V_{L,UDM}$	0.75 m/s	1.51 m/s	2.98 m/s	4.63 m/s
$V_{L,TOF}$	0.76 m/s	1.50 m/s	2.96 m/s	4.64 m/s
Error	-0.87 %	0.99 %	0.63 %	-0.25 %

Table 5: Comparisons V_L for asymmetrical flow

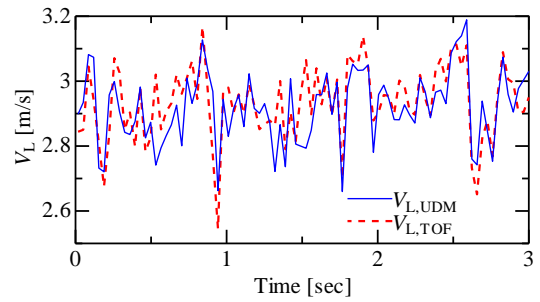
Q	80.8 m ³ /h	162.0 m ³ /h	321.1 m ³ /h	500.6 m ³ /h
$V_{L,UDM}$	0.74 m/s	1.46 m/s	2.92 m/s	-
$V_{L,TOF}$	0.75 m/s	1.47 m/s	2.88 m/s	4.50 m/s
Error	-1.85 %	-0.34 %	1.18 %	-

4. Summary

In order to evaluate influence of velocity profile on accuracy of the TOF, a measuring system which can measure the velocity profile and the transit time of ultrasonic pulse simultaneously was developed. The



(a) Symmetrical flow



(b) Asymmetrical flow

Figure 7: Results of simultaneous measurement of V_L by using UDM and TOF for $Q = 321.1 \text{ m}^3/\text{h}$

simultaneous measurements were carried out for symmetrical and asymmetrical flows. Velocity profile was measured using the UDM. It was confirmed that without calibration, the TOF may cause the error of 1% even if pipe length at the upstream is sufficient. Furthermore, if the TOF is installed for distorted flow condition, the error may dramatically increase. However, it was shown that the TOF error can be reduced by on-site calibration using the UDM. In addition, line-average velocities obtained by using the TOF and the UDM in short time scale were also in good agreement.

References

- [1] Cordova L, *et al.*: Qualification of an ultrasonic flow meter as a transfer standard for measurements at Reynolds numbers up to 4×10^6 between NMIJ and PTB, *Flow Meas. Inst.*, 45 (2015), 28-42.
- [2] Wada S *et al.*: Development of pulse ultrasonic Doppler method for flow rate measurement in power plant: multilines flow rate measurement on metal pipe, *J. Nucl. Sci. Technol.*, 41 (2004), 339-346.
- [3] Tezuka K *et al.*: Ultrasonic pulse-Doppler flow meter application for hydraulic power plants, *Flow Meas. Inst.*, 19 (2008), 155-162.
- [4] Murakawa H *et al.*: A dealiasing method for use with ultrasonic pulsed Doppler in measuring velocity profiles and flow rates in pipes, *Meas. Sci. Tech.*, 26 (2015), 085301, 11pp.
- [5] Muramatsu E *et al.*: Multi-wave ultrasonic Doppler method for measuring high flow-rates using staggered pulse intervals, *Meas. Sci. Tech.*, 27 (2016), 025303, 11pp.
- [6] Davies, J.T., *Turbulence phenomena*, Academic Press, New York, 1972
- [7] Furuichi N *et al.*: Calibration facilities for water flowrate in NMIJ, *Proc of 7th ISFFM* (2009), 7pp.

Evaluation of measurement accuracy of a dealiasing method for use with ultrasonic pulsed Doppler

Daiki Hashiguchi¹, Hideki Murakawa¹, Ei Muramatsu¹, Katsumi Sugimoto¹,
Nobuyuki Takenaka¹ and Noriyuki Furuichi²

¹ Dept. Mechanical Engineering, Kobe Univ., 1-1 Rokkodai, Nada, Kobe, 657-8501 Japan

² National Institute of Advanced Industrial Science and Technology, Tsukuba Central 3, 1-1-1 Umezono, Tsukuba, 305-8563 Japan

Ultrasonic pulsed Doppler method has a limitation that both the maximum measurable velocity and the length cannot be increased at the same time. In order to overcome this limitation, the dual PRF (pulse repetition frequency) method and the feedback method have been proposed for measuring flow rate in a pipe. In this study, a rotating cylinder device was employed for evaluating accuracy of the velocities obtained by means of the dealiasing methods. Effects of the velocity extension number, the measurement volume and the number of pulse repetition for obtaining an instantaneous velocity profile on the uncertainties of the velocities are evaluated by comparing standard deviations of the velocities. It is shown that the extension number has an optimum value in each condition, and it should be set as small as possible to avoid the velocity aliasing. Furthermore, increasing size of the measurement volume is more effective for improving the measurement uncertainty in comparison to increasing the number of pulse repetition.

Keywords: Dealiasing, staggered trigger, dual PRF method, feedback method

1. Introduction

The ultrasonic pulsed Doppler method (UDM) is a useful technique for measuring one-dimensional velocity profile along the ultrasonic beam line. Thus, it has been utilized for measuring flow rate for integrating the velocity profiles over the pipe [1]. However, it is well known that the maximum measurable velocity and the length are limited by the Nyquist sampling theorem, and both them cannot be increased at the same time. Therefore, the greater the velocity in a large-diameter pipe is (*i.e.* the higher flow rate), the more difficult it is to measure the velocity using the conventional pulsed Doppler method. In order to overcome this limitation, several dealiasing methods have been developed [2,3].

The authors employed dealiasing methods, *i.e.* the dual PRF method and the feedback method, to measure velocities in a pipe. It was shown that the method made it possible to accurately determine flow rates six times greater than those that can be determined using the conventional UDM in a pipe [4,5]. However, size of the measurement volume was shown to be an important parameter in measuring velocities. With increases of the velocity, size of the measurement volume should be increased. However, the effects of the measurement parameters such as the measurement volume, range of the maximum measurable velocity on the measurement uncertainty has not been completely understood.

In this study, the target velocity and the measurement length are more than 3 m/s and 200 mm. Velocity measurements were carried out using a rotating cylinder device which covers the requested specification. The uncertainty of the velocity with the dealiasing method was investigated.

2. Dealiasing method

In the conventional UDM, multiple pulses are used to estimate the velocity of moving target [4]. Hence, it is well known that the maximum detectable velocity, $v_{\max, \text{conv.}}$, and the maximum measurable length, L_{\max} are expressed as;

$$v_{\max, \text{conv.}} = \frac{c}{4f_0T}, \quad (1)$$

$$L_{\max} = \frac{cT}{2} \quad (2)$$

,where c is sound speed in the medium, f_0 is the basic frequency of the ultrasonic pulses and $T = 1/f_{\text{prf}}$ is the pulse repetition interval. Hence, it is impossible to increase the both $v_{\max, \text{conv.}}$ and L_{\max} at the same time.

A staggered trigger method is one of the dealiasing method. With this method, some pulse emission intervals are employed and velocities are calculated based on the phase shifts between the pulses. In this study, two pulse repetition intervals known as the dual PRF method was employed. Pulses are emitted at the intervals of T and $T+T_s$, the maximum detectable velocity, $v_{\max, \text{dual}}$, is expressed as [4];

$$v_{\max, \text{dual}} = \frac{c}{4f_0T_s} \quad (3)$$

Comparing the Eq.(3) with Eq.(1), it is known that the maximum detectable velocity can be increased with T/T_s times. It has been confirmed that the dual PRF method has large uncertainty in comparison to the conventional pulsed Doppler method by experiment. In order to improve the accuracy of the velocity estimation with the dual PRF method, the feedback method was proposed [4,5]. With the conventional method, if the velocity exceed $v_{\max, \text{conv.}}$ several times and the Nyquist folding

number, m , is unknown, the true velocity cannot be determined. On the other hand, with the feedback method, the m is corrected by the velocity which obtained using the dual PRF method. Velocity obtained by using the dual PRF method is used as a velocity index to determine the Nyquist folding number. Consequently, the velocity with the feedback method, v_f , is obtained as

$$v_f = v_{\text{conv}} + 2mv_{\text{max, conv}}, \quad (4)$$

where v_{conv} is the velocity obtained using the conventional method. The m is estimated to satisfy following requirement:

$$v_{\text{dual}} - v_{\text{max}} < v_f \leq v_{\text{dual}} + v_{\text{max}}, \quad (5)$$

where v_{dual} is the velocity obtained using the dual PRF method and v_{max} is the maximum velocity based on the pulse interval. In the measurements, the same echo signals are used for the calculations in the conventional and dual PRF methods.

3. Experimental facilities

To evaluate the uncertainty of the velocity estimation, experiments were carried using a rotating cylinder. Schematic of the facility is shown in Figure 1. O is the center of rotation, d [m] is the distance between O and the measurement line, ω [rad/s] is angular velocity. If the rotating speed is X [rpm], ω is expressed as $\omega = 2\pi X / 60$. y is the distance from the inner wall surface along the measurement line, and Y is the half of length of measurement line in the cylinder. The inner diameter of the cylinder is 412 mm, and the cylinder height is 150 mm. d was set at 148 mm. Since the UDM obtains velocity components along the measurement line, if the rotated fluid and reflector can be considered as a rigid body rotation, the measured velocities along the measurement line are constant at $d\omega$ ($= v_{\text{theory}}$). The system can avoid any turbulence in the flow, and it allow to focus on the performance of the signal processing in

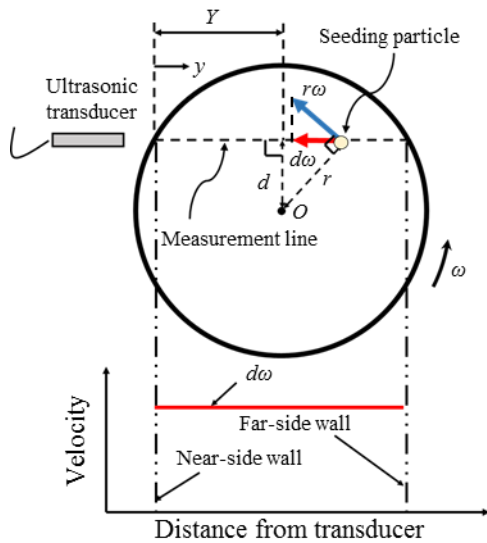


Figure 1: Experimental apparatus.

this ideal flow conditions. Sucrose aqueous solution with concentration of 4.7 wt.% was used as the working fluid to adjust the density with Nylon tracer particles (1.02 g/cc, 100 μm) to avoid precipitation. The sound speed, c , is 1.52×10^3 m/s.

The experimental conditions were $v_{\text{theory}} = 1.550 \sim 3.100$ m/s which correspond to $X = 100 \sim 200$ rpm. T was constant at 5.56 ms, and the expansion number, P ($= T/T_s$), was ranged between 9 and 40. Diameter of the ultrasonic beam was 10 mm with $f_0 = 2$ MHz. The number of pulse repetition for obtaining an instantaneous velocity profile, N_{pulse} , was 512 or 1024. Spatial resolution along the ultrasonic beam direction, ΔL , was 1.48, 2.22, 3.70 mm.

A laboratory-made measurement system [4,5] was used for the measurements. Reflected echo signals were recorded in a PC, and velocities were calculated after the measurements. 500 instantaneous velocities were used for calculating the time-average velocity profile.

4. Results and discussions

4.1 Time-average velocity profile

A time-average velocity profile obtained with the dual PRF method is shown in Figure 2. The rotating speed was 100 rpm and $v_{\text{theory}} = 1.550$ m/s. After 5 min from the start-up of the rotating cylinder, the measurement was conducted. It took approximately 20 min for measuring 500 profiles. The dashed line in the figure indicates $v_{\text{max, conv}}$. The velocity profile takes almost constant value in each measurement position except the near-side wall region. Thus, much higher velocity than $v_{\text{max, conv}}$ was accurately obtained with the dual PRF method. Furthermore, the velocity distributions can be considered to be rigid body rotation during the measurement.

Ultrasonic reflection on the wall surface of the rotating cylinder degraded accuracy of the velocity error in the near-wall region. Therefore, velocity data at the center, $y/Y = 1$, is used for the velocity evaluation.

4.2 Time-series Velocities

Time-series velocities with the dual PRF method and the feedback method at $y/Y = 1$ are shown in Figure 3. The rotating speeds are 100 and 150 rpm which correspond to $v_{\text{theory}} = 1.550$ and 2.325 m/s, respectively. The horizontal axis expresses the profile number. The other conditions

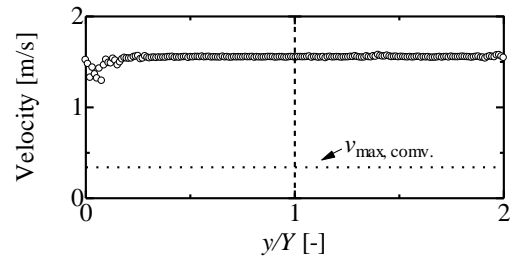


Figure 2: Time-average velocity distribution ($v_{\text{theory}} = 1.550$ m/s, 100 rpm)

are $\Delta L = 1.48$ mm, $P = 9$ and $N_{\text{pulse}} = 512$. Dashed lines indicate $v_{\text{theory}} \pm v_{\text{max}}$. Here, v_{max} is defined as;

$$v_{\text{max}} = (v_{\text{max1}} + v_{\text{max2}})/2 \quad (6)$$

,where v_{max1} and v_{max2} are expressed as;

$$v_{\text{max1}} = \frac{c}{4f_0T}, \quad (7)$$

$$v_{\text{max2}} = \frac{c}{4f_0(T+T_s)}. \quad (8)$$

As mentioned in the chapter 2, the feedback method employs the velocity with the dual PRF method, v_{dual} , to determine the Nyquist holding number. If difference between v_{dual} and v_{theory} is more than $\pm v_{\text{max}}$, misdetection of the Nyquist holding number may occur. Hence, the values of $v_{\text{theory}} \pm v_{\text{max}}$ can be considered to determine whether the misdetection of the Nyquist holding number may occur with the feedback method.

Time-average velocities with the dual PRF and the feedback methods are tabulated in Table 1. It can be confirmed that the time-average velocities with the both methods are in good agreement with v_{theory} in each velocity. Thus, it is found that the velocity error randomly occurs, and the averaging the instantaneous velocities converges to the v_{theory} .

Table 1: Time-average velocity with the dual PRF and the feedback methods

v_{theory}	v_{dual}	v_{f}
1.550 m/s (100 rpm)	1.548 m/s	1.557 m/s
2.325 m/s (150 rpm)	2.327 m/s	2.324 m/s

However, variability of the velocity with the dual PRF method is strongly influenced by the measuring velocities. At $v_{\text{theory}} = 1.550$ m/s, the time-series velocities range within $v_{\text{theory}} \pm v_{\text{max}}$. On the other hand, velocities with the feedback method takes almost constant value at v_{theory} . It can be confirmed that the feedback method has lower uncertainty for the velocity estimation in comparison to the dual PRF method, and the feedback method could accurately estimate the velocities under such condition.

At $v_{\text{theory}} = 3.100$ m/s, the velocities with the dual PRF method include much error in comparison to those at $v_{\text{theory}} = 1.550$ m/s. Furthermore, time-series velocities with the feedback method take almost constant values at v_{theory} except at some profile number. If velocities with the dual PRF method are beyond $\pm v_{\text{max}}$ from the v_{theory} , the velocities with the feedback are misdected.

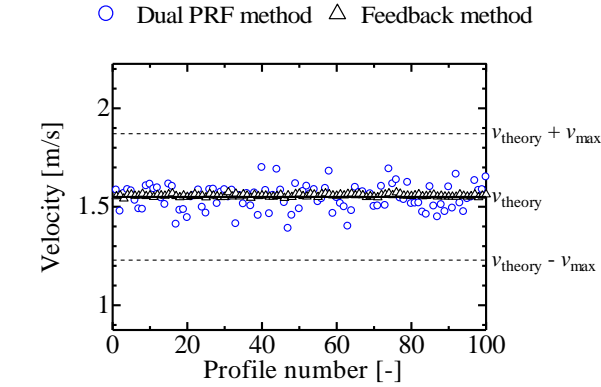
4.3 Velocity Standard Deviation

The velocity standard deviations, σ , were calculated from the instantaneous velocities. The σ is theoretically zero if the measurement and experimental errors do not occur. Figure 4 represents the relation between v_{theory} and 2σ with different ΔL . P was set constant at 9 and the v_{max} was 0.321 m/s. Assuming that the velocity error is followed by the normal distribution, 95% of instantaneous velocities are ranging within $v_{\text{theory}} \pm 2\sigma$. Thus, if 2σ is smaller than v_{max} , the velocity has more than 95 % accuracy

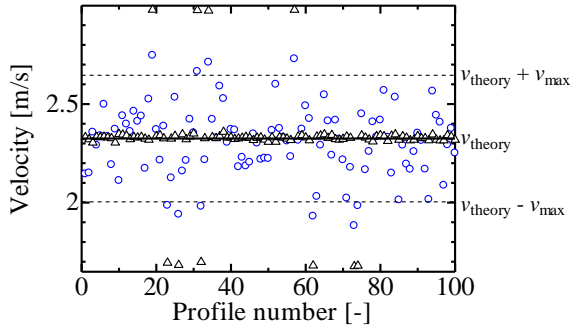
2σ with the dual PRF method, $2\sigma_{\text{dual}}$, takes around 0.14 m/s at 1.550 m/s. Therefore, the v_{dual} includes much error even though the measurement velocity is not so high. With increases of the measurement velocity, $2\sigma_{\text{dual}}$ gradually increases and it reaches v_{max} around $v_{\text{theory}} = 2.325 \sim 2.480$ m/s.

On the other hand, 2σ with the feedback method, $2\sigma_{\text{f}}$, takes almost zero at $v_{\text{theory}} = 1.550 \sim 1.860$ m/s for $\Delta L = 1.48$ mm, and the value rapidly increases at $v_{\text{theory}} = 2.015$ m/s. When v_{theory} is less than 2.015 m/s, error of v_{dual} was not significant, and misdetection of the Nyquist holding number hardly occurs. It can be said that the velocity estimations can be accurately conducted under such conditions. If the Nyquist holding number differs by ± 1 , v_{f} varies $v_{\text{theory}} \pm 2v_{\text{max}}$ as shown in Figure 3(b). Thus, $2\sigma_{\text{f}}$ rapidly increases although the $2\sigma_{\text{dual}}$ gradually increases with v_{theory} . Since $2\sigma_{\text{dual}}$ for $\Delta L = 1.48$ mm is just beyond v_{max} at $v_{\text{theory}} = 2.325$ m/s, it can be seen that 95% of v_{f} was accurately obtained under the condition.

$2\sigma_{\text{dual}}$ for $\Delta L = 2.22$ mm is slightly lower than that for $\Delta L = 1.48$ mm. Thus, v_{f} could be obtained with 95% accuracy at $v_{\text{theory}} = 2.480$ m/s for increasing ΔL to



(a) $v_{\text{theory}} = 1.550$ m/s ($X = 100$ rpm)



(b) $v_{\text{theory}} = 2.325$ m/s ($X = 150$ rpm)

Figure 3: Time-series velocities with the dual PRF method and the feedback method ($\Delta L = 1.48$ mm, $N_{\text{pulse}} = 512$)

100 120 140 160 180 200
X [rpm]

Dual PRF method: ○ $\Delta L = 1.48$ mm △ $\Delta L = 2.22$ mm
Feedback method: ● $\Delta L = 1.48$ mm ▲ $\Delta L = 2.22$ mm

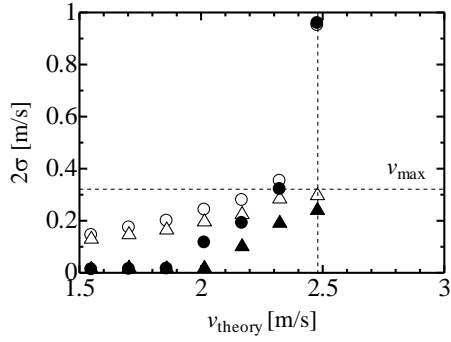


Figure 4: Relation between the standard deviation and the rotating speed.

2.22 mm. This result indicates that large measurement volume is appropriate for measuring higher velocity.

Relation between $2\sigma_{\text{dual}}$ and P at $v_{\text{theory}} = 3.100$ m/s ($X=200$ rpm) is shown in Figure 5. ΔL was set at 1.48, 2.22, 3.70 mm, and 512 or 1024 pulses were used for a velocity estimation. v_{max} depends on P which is related to T_s . Therefore, the relation between v_{max} and P can be obtained from Eqs. (6)–(8), and it is expressed as;

$$v_{\text{max}} = \frac{c(2P+1)}{8f_0T(P+1)} \quad (P > 1) \quad (9)$$

Eq. (9) is indicated as a dashed line in the figure.

For $\Delta L = 1.48$ mm with $N_{\text{pulse}} = 512$, $2\sigma_{\text{dual}}$ takes minimum value at $P = 18$. Please note that the $2\sigma_{\text{dual}}$ at $P = 30$ and 40 were much large and these were over ranged in the vertical axis. If the P is smaller than 18, the velocity aliasing was caused in the velocities with the dual PRF method because of low accuracy of the velocity estimation. On the other hand, effects of the uncertainty of the measurement system such as T , T_s and noise effects become significant with increasing P . The appropriate P were 13 for $\Delta L = 2.22$ mm and 12 for $\Delta L = 3.7$ mm. It can be said that the appropriate P exists in each condition and it should be determined as low as possible not to occur the velocity aliasing. The $2\sigma_{\text{dual}}$ at appropriate P decreases with increasing of ΔL . Difference of $2\sigma_{\text{dual}}$ between at $\Delta L = 1.48$ mm and 2.22 mm is significant. In addition to ΔL , N_{pulse} is an important parameter for the velocity estimation. $2\sigma_{\text{dual}}$ decreases with increases the N_{pulse} although the velocity time-resolution becomes worse. $2\sigma_{\text{dual}}$ with the same ΔL and P is roughly proportional to $1/\sqrt{N_{\text{pulse}}}$, and the difference of $2\sigma_{\text{dual}}$ for $N_{\text{pulse}} = 512$ and 1024 is not significant. Hence, increasing ΔL is effective to reduce the velocity uncertainty in comparison to increasing N_{pulse} . However, $\Delta L = 3.7$ mm with $N_{\text{pulse}} = 1024$ was required for measuring velocities with 95% accuracy at $v_{\text{theory}} = 3.100$ m/s ($X = 200$ rpm).

v_{max}
0 10 20 30 40 50
 P [-]
 $N_{\text{cycle}} = 512$: $\Delta L =$ ○ 1.48 mm △ 2.22 mm □ 3.7 mm
 $N_{\text{cycle}} = 1024$: $\Delta L =$ ● 1.48 mm ▲ 2.22 mm ■ 3.7 mm

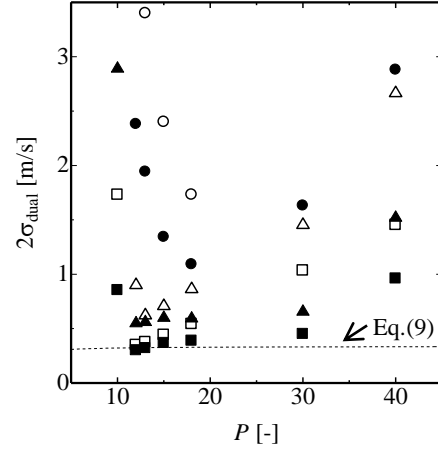


Figure 5: Effects of P , N_{pulse} and ΔL on the velocity estimation. ($v_{\text{theory}} = 3.100$ m/s)

5. Summary

In order to evaluate the uncertainty of velocity estimations with the dual PRF and the feedback methods, basic experiments using a rotating cylinder device were carried out. The velocity estimation with the dual PRF method includes larger uncertainty in comparison to that with the conventional pulsed Doppler method, *i.e.* single PRF method. Thus, the feedback method is appropriate for the dealiasing. Accuracy of the feedback method could be evaluated with the standard deviation of velocity with the dual PRF method. If $2\sigma_{\text{dual}}$ is lower than v_{max} , the velocities have more than 95% accuracy. P has appropriate value in each condition. In order to increase the accuracy of the velocity estimation, increasing the ΔL is more effective than increasing the N_{pulse} .

References

- [1] Wada S, et al.: Development of pulse ultrasonic Doppler method for flow rate measurement in power plant: multilines flow rate measurement on metal pipe, J. Nuclear Science and Technology 41 (2004), 339-346.
- [2] Joe P & May PT: Analysis correction of dual PRF velocity errors for operational Doppler weather radars, J. Atmos. Oceanic Technol. 20 (2003), 429-442.
- [3] Nishiyama H & Katakura K: Non-equally spaced pulse transmission for non-aliasing ultrasonic pulsed Doppler measurement Journal of the Acoustical Society of Japan 13 (1992), 215-222.
- [4] Murakawa H, et al.: A dealiasing method for use with ultrasonic pulsed Doppler in measuring velocity profiles and flow rates in pipes, Measurement Science and Technology 26 (2015), 085301 (11pp).
- [5] Muramatsu E, et al.: Multi-wave ultrasonic Doppler method for measuring high flow-rates using staggered pulse intervals, Measurement Science and Technology 27 (2016), 025303 (11pp).

Implementation of a staggered trigger algorithm by velocity difference dealiasing rules

Fábio Rizental Coutinho¹

¹ Department of Electronic Engineering, Federal University of Technology-Paraná (UTFPR) Campus Toledo-PR 85902-490 Brazil

The staggered trigger technique consists of alternating between a long and a short Pulse Repetition Time (PRT) to mitigate the range-velocity ambiguity. Due to the two PRT, two different velocities can be estimated. The difference of these two velocities can be used to determine in which Nyquist interval is the real flow velocity. This method was originally proposed for Doppler weather radar where velocity folding factors are restricted to 2 times the conventional maximum velocity of the short PRT. In this work the staggered trigger method using the velocity difference for dealiasing purpose is further extended to a higher velocity folding factor. We show that emitting a 4-cycle ultrasound pulse this method can reach up to 5 times the conventional maximum velocity of the long PRT. The algorithm was tested using ultrasound simulation software - Field II. The simulation consisted of a piston transducer emitting in a flow with a uniform velocity profile. The performance of the technique was also evaluated on several low SNR conditions.

Keywords: staggered trigger, dealiasing, velocity aliasing, ultrasound velocity profiling.

1. Introduction

Ultrasonic Doppler velocity profiler (UVP) is a fundamental technique for research in fluid engineering filed [1]. The method estimates the velocity along the measurement line by using periodic short bursts of ultrasound. However this pulsed strategy limits the maximum range that can be measured. Increasing the time period between bursts can extend the measurement range but comes with a proportional reduction in the maximum velocity that can be measured. If the real velocity is higher than the maximum velocity allowed then velocity aliasing will occur [2]. The velocity aliasing problem can be overcome by dealiasing techniques. Insonating the flow using two transducers with different frequencies is a method that can resolve velocity aliasing problem. This method, also called multi-frequency has been proposed by [3-5]. In this technique the information of the velocity from each transducer are combined in such a way that the whole system can be viewed as one, whose frequency is the difference between the two transducers frequencies. Another technique to avoid alias is the velocity-matched spectrum analysis [6]. In this approach the data from each pulse emission are arranged in a two dimensional matrix. A velocity spectrum is obtained by analyzing the shift in each pulse emission through iso-velocity lines [6]. Since the method results in a spectrum of velocities, this technique is computational intensive. Wide band or time-shift estimation techniques such as cross-correlation [7] do not suffer from aliasing under a high SNR condition. However cross-correlation algorithms usually are more time consuming than the conventional autocorrelation algorithm. Extend autocorrelation technique [8] combines phase-shift estimation with cross-correlation. The combination can reduce significantly the amount of computation. However, the processing time of this approach is still very high (approximately 55 times slower) than the autocorrelation algorithm [9]. Staggered trigger or

staggered PRT (Pulse Repetition Time) is characterized by using a non-uniform pulse repetition time. Staggered trigger alternate the pulse emission with a long and a short PRT. Contrasting to multi-frequency, staggered PRT only needs one transducer. And the processing time is comparable with the autocorrelation. This technique was first introduced for blood flow measurement [10]. Later, it was also further extended for weather radar field [11-12]. Recently, Murakawa et al [13] adapted it to fluid engineering, implementing a higher flowrate measurement system. They reported that the velocity error of the practical system was too high to measure velocity directly. Thus they used the staggered PRT velocity only to discover the number of aliasing or aliasing factor. However, this strategy still was not enough to deliver an accurate velocity profile. Therefore, they have used a moving average filter and relaxed the velocity time resolution. The measurement configuration used a high number of pulse ($N_{\text{pulse}}=512$) for every velocity estimate, and velocity profile was obtained through averaging 1,000 instantaneous velocity profiles. They reported an error of -0.8% and maximum measured velocity of 6 times larger than the conventional UVP method [13]. Torres and Dubel [14] proposed a new algorithm for staggered trigger that uses the velocity difference from the velocities estimated by the long and short PRT to decide the velocity dealiasing factor. Their work was focused in weather radar and they showed that their method could measure velocity up to 3 times greater than the maximum conventional velocity regarding the long PRT. In this work we adapted the methodology of [14] for fluid engineering. It is also showed that the method proposed can reach even higher velocities than described in [14]. The algorithm was implemented and tested using an ultrasound simulator. The result shows that it is possible to measure velocity up to 5 times higher than the conventional velocity regarding the long PRT. Also this technique does not need intensive averaging or high N_{pulse} . The results are also tested under low SNR

simulated condition.

2. Staggered trigger by velocity difference method

2.1 Foundation of staggered trigger method

In staggered trigger, an ultrasonic pulsed wave is emitted in alternating time intervals, T_1 and T_2 , with $T_2 > T_1$. Velocity estimation is evaluated by the lag one autocorrelation algorithm [7] using only adjacent pulses whose time interval is equal. So the velocity relative to T_1 , v_1 , and the velocity relative to T_2 , v_2 , can be estimated using the following relations

$$v_1 = \frac{c}{4\pi f T_1} \arg(R(T_1)), \quad (1)$$

$$v_2 = \frac{c}{4\pi f T_2} \arg(R(T_2)), \quad (2)$$

respectively, where c denotes the sound velocity in the considered medium, f represents the transducer central frequency, \arg is the principal argument restricted to the range $(-\pi, \pi]$ and $R(\cdot)$ is the autocorrelation function. The maximum measured velocity is determined by the range of the principal argument as

$$v_{a1} = \frac{c}{4fT_1}, \quad (3)$$

$$v_{a2} = \frac{c}{4fT_2}. \quad (4)$$

Staggered trigger method combines each lag one autocorrelation to result in a dealiased velocity estimated by

$$v_{st} = \frac{c}{4\pi f(T_2 - T_1)} (\arg(R(T_1)) - \arg(R(T_2))). \quad (5)$$

And the staggered trigger maximum velocity will be

$$v_{max,st} = \frac{c}{4f(T_2 - T_1)}, \quad (6)$$

which will be higher than Eqs. (3) and (4) if $T_2 - T_1$ were small relatively to T_1 or T_2 . However, velocity estimated using Eq. (5) will have a high uncertainty for some velocity intervals. Because of this Eq. (5) is not used in practical implementation. Therefore, to measure velocity above Nyquist limit, Eqs. (1) and (2) are combined with some rule to discover the velocity aliasing factor.

2.2 Velocity difference dealiasing rules

The $v_1 - v_2$ velocity difference can be used to determine the aliasing factor of v_1 or v_2 if the ratio $T_1/T_2 = m/n$, follow the condition that m and n should be relatively prime integers [14]. Applying this ratio, the maximum unambiguous velocity that can be measure are $v_{ua1} = mv_{a1}$ and $v_{ua2} = nv_{a2}$, for v_1 and v_2 , respectively. The velocity difference rule can be demonstrated graphically. The velocity aliasing incurs that v_1 or v_2 cannot be higher than $\pm v_{a1}$ or $\pm v_{a2}$, respectively. By plotting the real velocity versus $v_1 - v_2$ the graph of Fig. 1 is obtained, for $m/n = 3/4$. Note in Fig.1, that, when v_1 is aliased, or $v_{a1} < v_1 < 3v_{a1}$, the velocity difference assumes two unique constant values ($-0.5v_{a1}$ and $+v_{a1}$).

A similar behavior happens to negative aliasing in v_1 , or the condition that $-3v_{a1} < v_1 < -v_{a1}$, in this case $v_1 - v_2$ assumes $+0.5v_{a1}$ and $-v_{a1}$. In the case of aliasing in v_2 , one can notice (Fig.1) that for the first aliasing, i.e. when $v_{a2} < v_2 < 3v_{a2}$ (or $-3v_{a2} < v_2 < -v_{a2}$ for negative aliasing) the velocity difference assumes $2v_{a2}$ and $-0.5v_{a1}$ (or $-2v_{a2}$ and $+0.5v_{a1}$ for negative aliasing). When v_2 aliases for the second time, i.e. when $v_2 > 3v_{a2}$ (or $v_2 < -3v_{a2}$ for negative aliasing) then $v_1 - v_2$ equals to v_{a1} (or $-v_{a1}$ for negative aliasing). Therefore, $v_1 - v_2$ maps the aliasing factor in v_1 or v_2 . In [14] it is show that this function bijection occurs for any m/n , if m and n are relatively prime integers. However, they mention that in practical implementation only $m/n = 2/3$ showed good results.

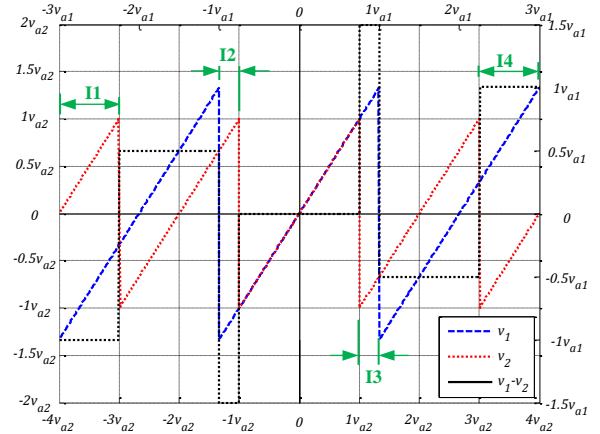


Figure 1: Velocity difference ($v_1 - v_2$) and aliased velocities v_1 and v_2 as a function of the real Doppler velocity. Time interval ratio used was $T_1/T_2 = m/n = 3/4$.

3. Simulation procedure

The algorithm was tested using Field II (release 3.24) simulation software running under Matlab R2013a environment. Field II uses linear system theory to evaluate the pulsed ultrasound field as a function of time at a specific point in space [15-16]. Simulations were carried at a 100 MHz sampling frequency. The transducer simulated was a piston shaped transducer with 10 mm diameter. Transducer geometry was divided into 1.2 mm x 1.2 mm square mathematical elements (Fig. 2). Since the real transducer edges might vibrate less than the center, apodization coefficients were defined based in a 2D hanning mask (Fig. 2). Ultrasound central frequency was 4 MHz and transducer excitation was performed by a 4-cycle sinusoidal burst. The flow was simulated in a section of 30 mm ID pipe (Fig. 3). Transducer was positioned 25 mm from pipe and at an angle of 45 degrees with respect to the z axis (Fig. 3). The number of reflectors was set-up to 10 scatterers per measurement volume. Pipe wall thickness was defined as 2 mm. The amplitude from moving reflectors was configured to be 100 times greater than the amplitude of echoes from pipe wall. This configuration was used to avoid using clutter filters that could introduce bias in the results. Sound velocity in the flow was set-up to 1480 m/s. A flow with uniform velocity profile was simulated. Five

combinations of PRTs were tested. Short PRT was fixed in $T_1 = 0.5$ ms and a set of long PRT were tested: $T_2 = \{0.667, 0.571, 0.625, 0.6, 0.583, 0.571\}$ ms which gives the following PRT ratios $T_1/T_2 = m/n = \{3/4, 4/5, 5/6, 6/7, 7/8\}$, respectively. Flow velocities simulated were based in multiples of the maximum conventional velocity of the short PRT, v_{a1} . The maximum dealiased velocities that can be measured by the proposed algorithm are $3v_{a1}, 4v_{a1}, 5v_{a1}, 6v_{a1}$ and $7v_{a1}$, for $m/n = 3/4, 4/5, 5/6, 6/7$ and $7/8$, respectively.

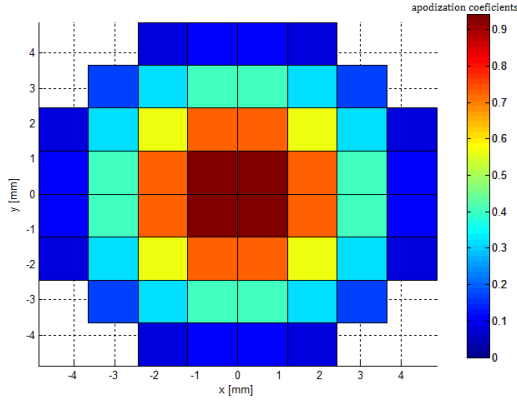


Figure 2: Display of the geometry and apodization of the piston shaped transducer simulated.

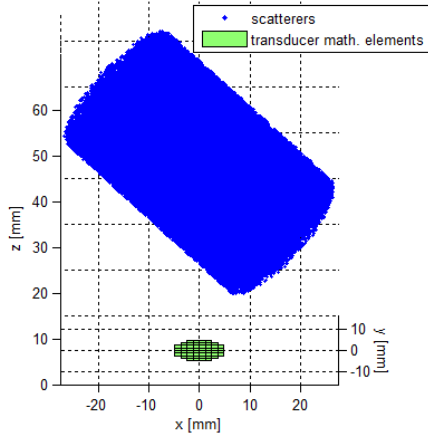


Figure 3: 3D graph of scatterers distribution with respect to the ultrasound transducer (x-y plane). Pipe walls were suppressed.

Therefore velocities from $0.5v_{a1}$ up to maximum dealiased were tested for each case. For each flow, a total of 2000 ultrasound emissions were simulated which give roughly 1 second of acquired data. To evaluate the performance of the algorithm under real conditions, signal-to-noise ratio from 50 dB to 0 dB were performed. Velocity estimation was carried by an autocorrelation algorithm followed by applying the velocity difference dealiasing rules algorithm. The number of pulses used to estimate the velocity was $N_{\text{pulse}}=50$. To calculate the velocity profile, 40 instantaneous profiles were averaged for $N_{\text{pulse}}=50$. Velocity profiles were obtained using raw estimated velocities, i.e., without any kind of velocity post-processing techniques.

4. Results

Mean spatial velocity profile estimation was evaluated

using Eq. 5 for each PRT ratio. The error became very high at the vicinities of $1v_{a1}, 3v_{a1}, 5v_{a1}$ regarding the PRT ratio (Fig. 4). This problem occurs whenever v_2 is aliased but v_1 is still non aliased (Fig. 1 intervals: I1, I2, I3 and I4). In this condition $\arg(R(T_2))$ of Eq. 5 is negative while $\arg(R(T_1))$ is positive which will result in an erroneous velocity estimate using Eq. 5. Because of this large error, Eq. 5 is usually not used.

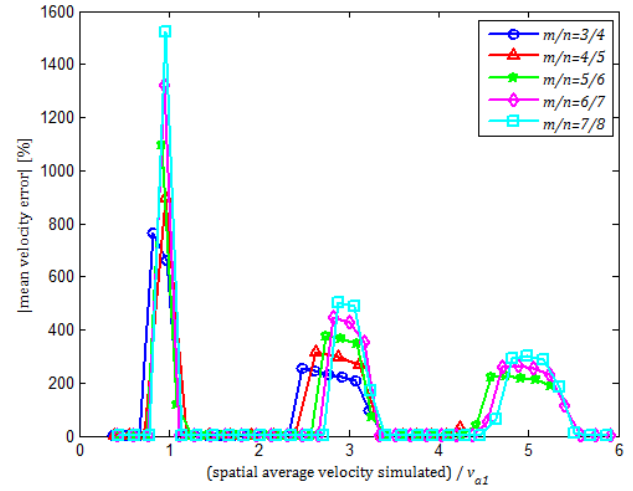


Figure 4: Mean spatial velocity profile relative error evaluated using Eq. 5.

To verify the maximum PRT ratio that can be used in the aforementioned simulated conditions, the mean spatial velocity simulated versus the mean spatial velocity measured plot were evaluated for each PRT ratio (Fig. 5).

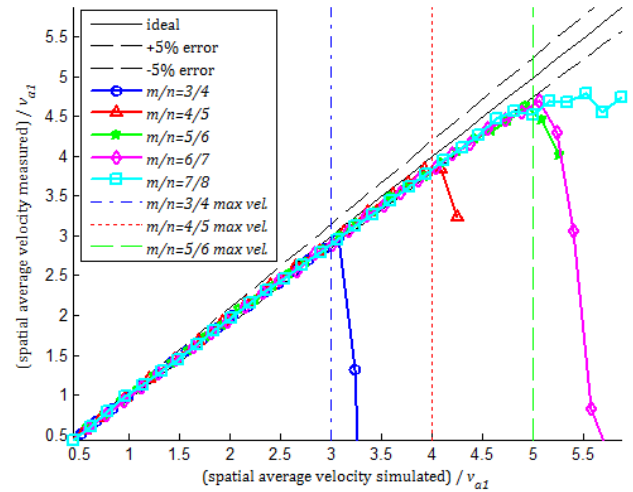


Figure 5: Spatial averaged velocity simulated versus spatial average velocity measured (normalized by conventional maximum velocity relatively to T_1) for $\text{SNR}=30$ dB, $N_{\text{pulse}}=50$.

Velocity was estimated under a $\text{SNR}=30$ dB. Velocities were normalized by the maximum conventional velocity regarding T_1 , v_{a1} . Note that for PRT ratios: $3/4, 4/5$ and $5/6$ the mean velocity measured deviates abruptly from the 5% error line after surpassing the maximum dealiased velocity regarding each ratio (Fig. 5). However, PRT ratios $6/7$ and $7/8$ deviate earlier than expected (theoretically maximum dealiased velocity should be

$6v_{a1}$ and $7v_{a1}$, respectively) at $5v_{a1}$. It should be noted that as the mean simulated velocity increases (for values under the maximum dealiased velocity) the mean spatial velocity begins to be underestimated. Such behavior may be improved by the use of post-processing techniques or increasing the N_{pulse} .

Velocity profile reproducibility was assessed using the mean squared error, MSE, of the velocity profile for PRT ratios from 3/4, 4/5 to 5/6 (Fig. 6). Performances under different SNR conditions, from 20 dB to 0 dB were evaluated. Spatial velocity profile estimation becomes worse for velocities above Nyquist limit (when (spatial average velocity simulated)/ $v_{a1} \geq 1$). This behavior occurs mainly under low SNR conditions. It is expected that the error increases with velocity because the variance of the velocity estimate increases due to intrinsic spectral broadening. The MSE climbs up for flow velocities higher than $3v_{a1}$, $4v_{a1}$ and $5v_{a1}$ in Fig. 6, respectively, regarding the SNR condition. This result agrees with the maximum dealiased velocity that can be measured in each case. Profile reproducibility also becomes worse when having simultaneously low SNR condition (10-0 dB) and low PRT ratio (Fig. 6c). Depending on the accuracy needed, this condition can limit the maximum dealiased velocity to a lower value.

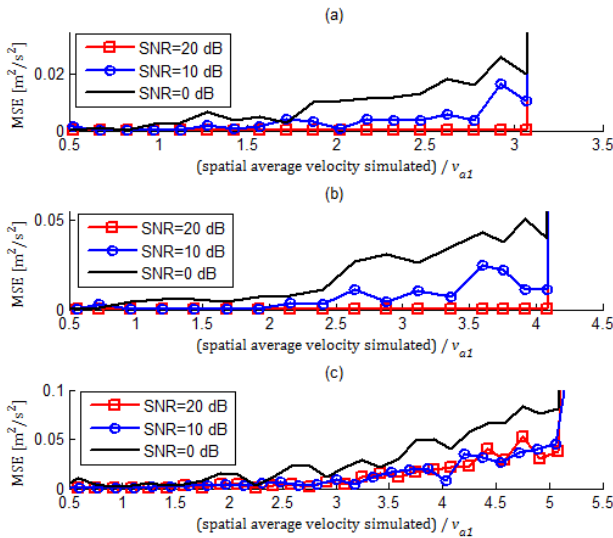


Figure 6: Velocity profile mean squared error for ($N_{\text{pulse}}=50$): (a) $m/n = 3/4$, (b) $m/n = 4/5$, and (c) $m/n = 5/6$.

5. Conclusions

The algorithm for staggered trigger by using velocity difference dealiasing rules originally proposed by [14] was adapted to fluid engineering application. It was showed that the implementation of [14] can be further extended to PRT ratios lower than $m/n = 2/3$ thus allowing measurement of higher velocities than the conventional. Simulation results shown that using a 4 Mhz transducer with 4-cycle sinusoidal burst excitation and a low PRT of 0.5 ms the maximum practical PRT ratio is $m/n = 5/6$. In this condition it is possible to measure velocities up to 5 times the Nyquist limit. However, using a lowest possible PRT ($m/n = 5/6$) is only feasible at relatively high SNR conditions. Under low SNR, PRT

ratios of 4/5 and 3/4 should perform better regarding the reproducibility of the velocity profile. We believe that the reason for the proposed implementation to reach lower PRT ratio than the one described in [14] is because of the 4-cycle excitation versus the 1-cycle excitation used in WSR-88D weather radars. Experimental tests should be conducted to confirm the simulated results in a future work. Also, relationship between transducer frequency, excitation, etc with maximum dealiased velocity that can be measured should be investigated.

6. Acknowledgments

This work was carried out with the support of Fundação Araucária (grant 06A/2014) and Secretaria de Estado da Ciência, Tecnologia e Ensino Superior do Paraná (SETI).

References

- [1] Takeda Y: Velocity profile measurement by ultrasonic Doppler method, *Exp. Fluids*, 10 (1995), 444-453.
- [2] Takeda Y: *Ultrasonic Doppler fluid flow*, Springer, Japan (2012).
- [3] Fer R, *et al.*: New Advances in colour flow mapping: quantitative velocity measurement beyond Nyquist limit. *Br J Radio* 64 (1991), 651.
- [4] Nitzpon HJ, *et al.*: A new pulsed wave Doppler ultrasound system to measure blod velocities beyond Niquist limit. *IEEE Trans Ultrason. Ferroelec. Freq. Contr.* 42 (1995), 265-279.
- [5] Zedel L & Hay AE: Design and performance of a new Multi-frequency coherent Doppler profiler. 33rd IAHR Congress, 2009.
- [6] Torp H & Kristoffersen K: Velocity matched spectrum analysis: a new method for suppressing velocity ambiguity in pulsed-wave Doppler. *Ultrasound Med. Biol.* 21(1995), 937-944.
- [7] Jensen, JA: *Estimation of blood velocities using ultrasound: A signal processing approach*. Cambridge. University Press, New York, (2006).
- [8] Lai X & Torp H: An Extended Autocorrelation Method for Estimation of Blood Velocity, *IEEE Trans. Ultrason., Ferroelec., Freq. Contr.* 44 (2007), 1332-1342.
- [9] Ofuchi, CY, *et al.*: Extended autocorrelation velocity estimator applied to fluid engineering, *Proc. of the 9th ISUD, Strasbourg* (2014), 109-112.
- [10] Nishiyama H & Katakura K. Non-equally-spaced pulse transmission for non-aliasing ultrasonic pulsed Doppler measurement, *J. Acoust. Soc. Jpn.* 13, 4 (1992), 215-222.
- [11] Franca MJ & Lemmin U: Eliminating velocity aliasing in acoustic Doppler velocity profiler data, *Meas. Sci. Tech.* 17 (2006), 313-322.
- [12] Holleman I & Beekhuis H: Analysis and Correction of Dual PRF Velocity Data, *J. Atmos. Ocean. Technol.* 20 (2003), 443-453.
- [13] Murakawa H, *et al.*: Higher flowrate measurement using ultrasonic pulsed Doppler method with staggered trigger. *Proc. of the 9th ISUD, Strasbourg* (2014), 117-120.
- [14] Torres SM & Dubel Y: Design, implementation, and demonstration of a staggered PRT algorithm for the WSR-88D. *J. Atmos. Oceanic Tech.* 21 (2004), 1389-1399.
- [15] Jensen JA & Svendsen NB: Calculation of pressure fields from arbitrarily shaped, apodized, and excited ultrasound transducers. *IEEE Trans. Ultrason., Ferroelec., Freq. Contr.* 39(1992), 262-267.
- [16] Jensen JA: A program for simulating ultrasound systems. *Med. Biol. Eng. Comp.*, 10th Nordic-Baltic Conf. on Biom. Imag., Vol.4, Supplement 1, Part1 (1996b), 351-353.

Measuring error estimation of the ultrasound array flow mapping system by means of numerical simulations

Sven Franke¹ and Sven Eckert¹

¹Helmholtz-Zentrum Dresden-Rossendorf, Institute of Fluid Dynamics, Department Magnetohydrodynamics, P.O. Box 510119, 01314 Dresden, Germany

A new two-dimensional ultrasound Doppler flow mapping system based on the application of linear arrays has been developed recently. A main feature involves a multi-beam operation facilitating a high frame rate. Previously, the effect of crosstalk between the beams was investigated in a rotational flow by comparing the results of multi- and single-beam operation with each other. However, due to slight variations in the flow conditions and the scattering particle distribution the determined systematic error of measurement was not very reliable. Likewise, flow phantoms suffer from a number of shortcomings as fluctuations of rotational speed of the phantom drive or inadequate parameters of scattering particles. For this reason, we developed a numerical model of our flow mapping system providing the echo signals of the particle motion in a model flow being similar to our typical small scale experiments. For each particle the scattering signal is calculated by solving the Rayleigh integral by means of systems theory and summed to the total echo signal. This task was performed by the *FieldII* toolbox for *MATLAB*. In our paper we will present a detailed analysis of the systematic error depending on the flow structure. The error of the multi-beam mode in comparison to the single beam operation will be estimated.

Keywords: Ultrasound array, flow mapping, numerical simulation of ultrasound systems, FIELD II

1. Introduction

The pulsed ultrasound Doppler method has proved as a reliable and attractive flow measuring technique for non-transparent fluids including liquid metals [1]. A detailed study of unsteady multi-dimensional flow structures often requires the measurement of instantaneous flow velocity fields instead of merely velocity profiles. However, previous approaches of flow field measurements with the ultrasound Doppler method suffer from a lack of sufficient spatial and temporal resolution for such studies [2]. Recently, an enhanced measurement method for a multidimensional transient flow mapping based on the application of linear ultrasonic transducer arrays was developed [3] to overcome these drawbacks by implementing specific array driving techniques.

A main feature providing the high mapping rates deploys simultaneous measuring ultrasonic beams. However, this multi-beam operation induces a bias in the measured velocity of the flow map by acoustic crosstalk between the ultrasound fields. An experimental study revealed a sufficient small systematic error [4] of the multi-beam measurement compared to a velocity profile measured only with a single beam. However, this approach suffers from different issues: the reference flow (in a liquid metal driven by a rotating magnetic field) was not strictly steady-state and the velocity bias depends on the flow structure. Other flow phantoms as a rotating cylinder (filled with a particle-water mixture [1]) corresponding to a rigid-body motion also lacks in precision as a result of variations in mechanical and electrical components of the flow model setup. Furthermore random errors caused by the statistical distribution of the scattering particles as well as electrical noise could not be replicated for other conditions in a parametric study.

For these reasons a numerical approach based on linear

acoustics for the investigation of velocity deviations and bias of the flow mapping system was chosen. After providing a brief outline of the system's principles the numerical method as well as the simulation model including the signal processing will be explained. Finally, some of the simulation results will be presented.

2. Ultrasound flow mapping system

The flow mapping method is based on the application of linear ultrasonic transducer arrays. The current technical implementation applies linear arrays composed of 25 plane transducer elements (transmission frequency 8 MHz) of $2.3 \times 5 \text{ mm}^2$ with an element pitch of 2.7 mm (Fig. 1) which spans a measuring field length of 67 mm. A single array facilitates the measurement of the flow velocity component perpendicular to the transducer surface. Multiple array arrangements facilitate e.g. the measurement of both in-plane velocity components in a field or the measurement of several planes side by side.

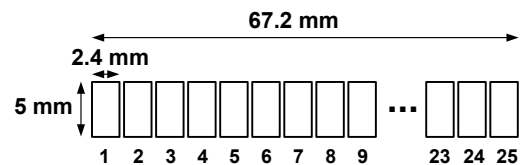


Figure 1: Configuration of linear transducer array

A specific electronic traversing scheme and pulsing strategy promote enhanced spatial and temporal resolution capabilities. An improvement of the spatial resolution is achieved by the application of the segmental array principle: During operation two adjacent transducer elements are interconnected to operate as one aperture of approx. $5 \times 5 \text{ mm}^2$ reducing the beam divergence over the fixed measuring depth. The active transducer aperture can be traversed by one pitch length. This additionally

facilitates the measurement of intermediate velocity lines thereby taking account of the self-focusing effect of plane apertures which makes the ultrasonic beam width closer than the aperture size over a specific depth.

Two enhanced approaches are applied to extend the temporal resolution: The first method implements a multi-beam operation which targets to scan as many profiles measuring lines (respectively transducer pairs) simultaneously as possible, thereby taking into account a sufficient small acoustic crosstalk. The second method is related to the pulsing strategy: As generally known the pulse repetition frequency of the ultrasound Doppler method is selected according to the velocity measuring range as well as the measuring depth. For small scale experiments with moderate flow velocities the time required for recording one echo signal (according to the measuring depth) is much lower than the pulse repetition time inducing an idle time between end of one echo acquisition and the begin of the following one. Contrary to previous multiline systems our approach applies this idle time for the echo acquisition of further measuring lines according to the multiplex pattern in Fig. 2 (in combination with the multi-beam and segmentation operation). Prerequisite is a fast changeover between the transducer channels by means of fast electronic switches.

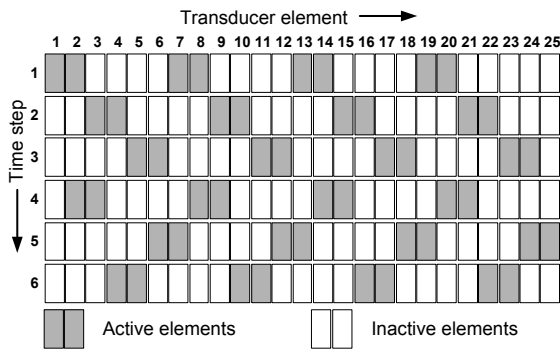


Figure 2: Pulsing scheme of a single array

3. Simulation of the ultrasound system

3.1 Numerical methods

The Rayleigh integral as a surface integral of an acoustic aperture allows the calculation of the acoustic pressure field at arbitrary points in space. This integral can be expressed in terms of linear system theory where every field point is described by an individual spatial impulse response for arbitrary aperture geometries. One method for calculating spatial impulse response is to integrate over the bounding lines of the aperture which will be applied in this paper due to its high accuracy. Another algorithm divides the aperture into small rectangle sub-apertures and summing up the far field approximations of all sub-apertures.

The interchangeability of acoustic source and receiver also permits the calculation of the pulse-echo field. The convolution of transmit and receive spatial impulse response (which may be assumed to be the same if the transmitting aperture is also the receiving aperture),

electromechanical impulse response of the transducer and voltage excitation signal results in the received signal from a point scatterer. The echo signal of a collection of randomly distributed scatterers is obtained by summing up the individual scattering signals. If these point scatterers are shifted according to a velocity field and for every pulse emission the echo signals are calculated the records of an ultrasound flow mapping system are simulated. Please take into account that this simulation model only considers the echo displacement but not the Doppler shift of the particle motion in the received signals.

The entire simulation chain is implemented in the *MATLAB* toolbox *FieldII* provided by Jensen et al [5, 6]. All simulations are carried out using this toolbox.

3.2 Flow model

Typical flow configurations measured with the flow mapping system are vortex structures in closed vessels e.g. flows generated by traveling and rotating magnetic fields [7]. A well-suited stationary flow model for such vortex cells is the Roberts flow [8]. For simplification of this simulation approach only a two-dimensional modification is applied:

$$\begin{aligned} v_x &= -v_0 \sin x \cos y \\ v_y &= v_0 \cos x \sin y \end{aligned} \quad (1)$$

An example for a Roberts flow with 2×2 vortex cells is given in Fig. 3. Please note that there is no no-slip condition at the boundaries of the flow model; instead an infinite flow field is assumed.

The particle trajectories of the point scatterers (with their random distribution as initial condition) are determined by solving the pair of ordinary differential equations of Eq. 1 in terms of the numerical Runge-Kutta method.

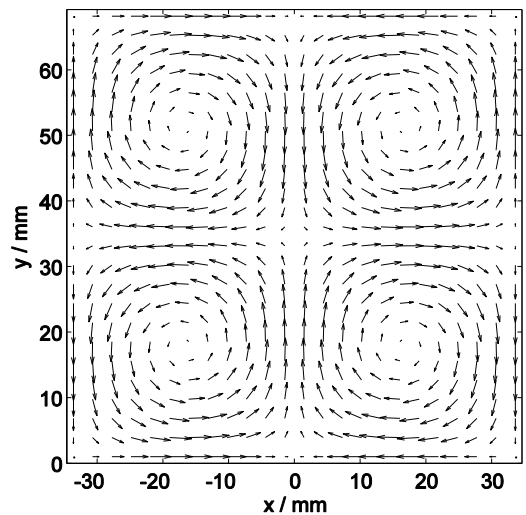


Figure 3: Velocity field of Roberts flow with 2×2 vortex cells as flow model for the ultrasound simulation

3.3 Signal processing

For accuracy reasons the simulation is carried out with a very high sampling frequency. However, for the signal

processing the echo signals are sampled down to typical sampling rates. The velocity estimation of the simulated ultrasound echoes is performed by the standard algorithm according to Kasai [9]. The matched filter is adapted to the number of cycles of the sinusoidal excitation pulse. The application of a clutter filter was dispensed with since the modelling of stationary echoes as a result of multiple wall reflexes was omitted. Since the randomly distributed point scatterers give rise to a variance of the measured flow velocities always large sets of echo data are calculated. The determined velocity data of these sets are averaged to obtain a mean velocity profile free from statistical deviations.

3.4 Simulation parameters

The simulation parameters reflect the actual measuring system: The numerical model of the transducer array complies with the real array geometry from Fig. 1. The sound velocity is chosen according to the liquid metal GaInSn usually deployed at our experiments. The edge lengths of the simulated velocity field correspond to the aperture length. The parameters of the simulation are presented in Table 1 and the sinusoidal excitation pulse is shown in Fig. 4.

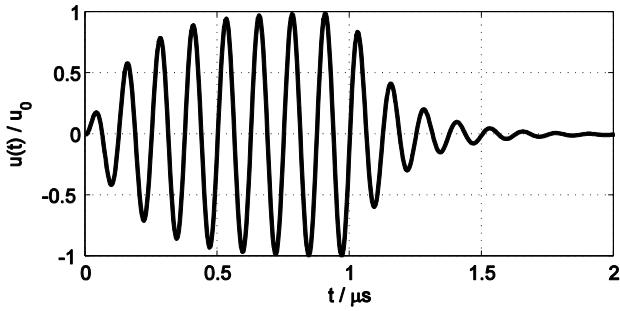


Figure 4: Excitation pulse of 8 sinusoidal cycles with bandwidth limitation to model the measurement electronics

Table 1: Simulation parameters

Parameter	Symbol	Value
Transducer frequency	f_0	8 MHz
Sound velocity (GaInSn)	c	2740 m/s
Number of cycles (excitation pulse)	N_c	8
Flow field direction 1	s_x	67.2 mm
Flow field direction 2	s_y	67.2 mm
Field thickness	s_z	20 mm
Peak flow velocity	v_0	50 mm/s
Particle density	ρ_s	0.1 mm^{-3}
Field II sampling rate	f_S	250 MHz
Echo sampling rate	f_A	25 MHz
Pulse repetition frequency	f_{PRF}	1217 Hz
Emissions per profile	N_{EPP}	50
Velocity range	v_{max}	104 mm/s
Gate distance	d_{Gates}	0.685 mm
Simulated echo signals per flow configuration	N_E	300 000

4. Results

A study with manifold parameter variations is performed focused on the analysis of the systematic error of measurement (bias) induced by the acoustic crosstalk of the multi-beam operation. Particularly the underlying flow structure of the simulation is varied with a different number of vortex cells (always same number in both field directions) within the measuring field up to 6×6 cells.

The ultrasound echo signals are simulated once for a conventional measurement with a single beam and once in multi-beam operation (see Fig. 2). A result for two different flow configurations is shown in Fig. 5. The results reveal that the acoustic crosstalk induces a significant bias of the velocity profile. Moreover the bias rises with increasing measurement depth as a result of increasing beam width induced by the beam divergence. This effect is especially exposed in flow configurations with smaller cells. Also the measured profiles of the conventional single-beam measurement exhibit a bias resulting from the limited spatial resolution capabilities of the ultrasonic pulse.

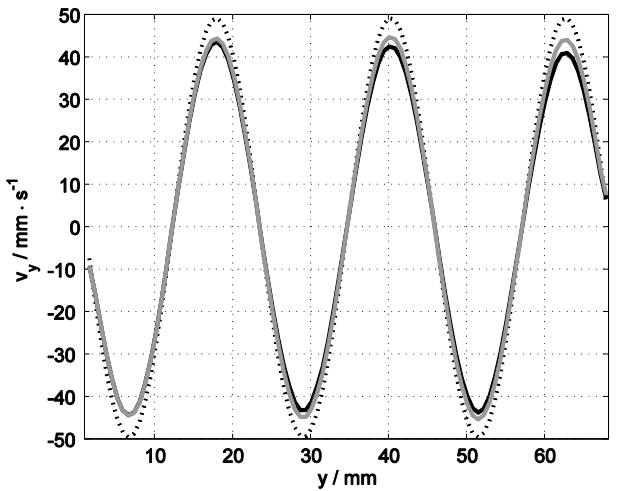
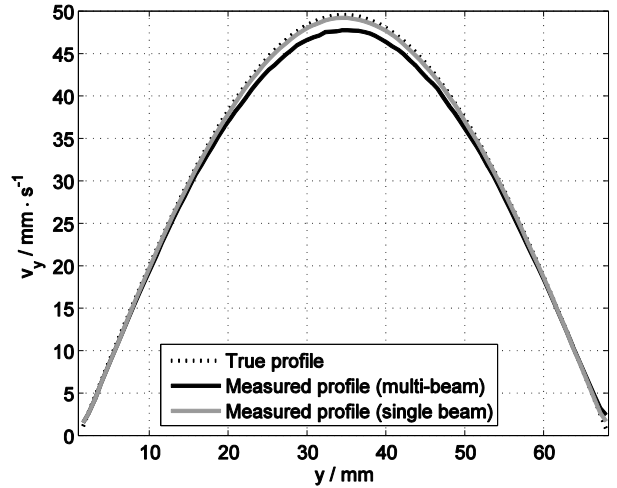


Figure 5: Averaged velocity profiles of an ultrasound simulation with 1×1 vortex cells (at the top) and 6×6 vortex cells (at the bottom). Given are the velocity profiles in multi-beam operation and in single beam operation as well as the specified true profile (legend at the bottom is the same as at the top).

The amount of the bias may vary for different measurement lines since the acoustic crosstalk may subtract or add a velocity bias depending on the velocity profiles of the neighboring ultrasound beams thereby partially compensating the bias induced by limited spatial resolution capabilities. For a better significance an error value for the entire measuring field is calculated in terms of the mean absolute error (MAE) normalized to v_0 . This also enables to compare the results of different flow configurations among each other. The equation is given by:

$$\langle e_{v,MAE} \rangle = \frac{1}{N_x N_y} \sum_{n=1}^{N_x} \sum_{m=1}^{N_y} |v(m,n) - v_{true}(m,n)| \quad (2)$$

where m, n are discrete variables for the two dimensions of the velocity field, v_{true} is the true velocity and v is the measured velocity.

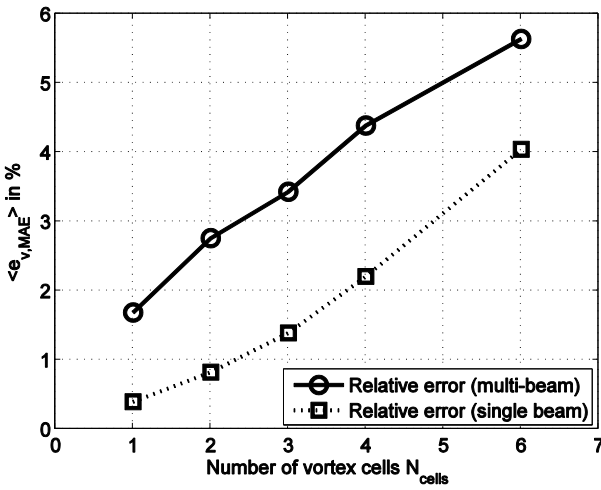


Figure 6: Normalized mean absolute error of different flow configurations.

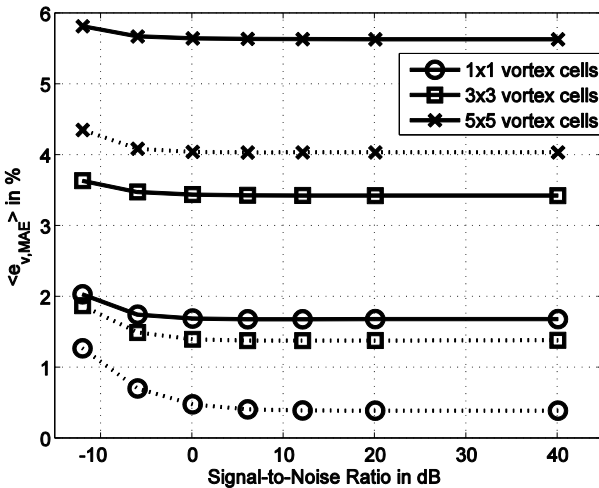


Figure 7: Error as a function of Signal-to-Noise ratio for different flow configurations. Solid lines for the error of multi-beam method and dashed lines for the single beam measurement.

In Fig. 6 the result of $e_{v,MAE}$ for different flow configuration is shown. It reveals that the bias induced by the multi-beam approach amounts around 1.3% to 2.2%.

For Fig. 7 white Gaussian noise is added to the echo signals for different flow configurations. The noise is identical for the multi-beam and single beam measurement to ensure the same measurement variance. Obviously from Fig. 7, noise has no significant influence on the crosstalk induced bias. For Signal-to-Noise Ratios (SNR) higher 0 dB the bias is almost constant.

5. Summary

A numerical model of a two-dimensional ultrasound Doppler flow mapping system is presented. It is mainly used for determining the systematic error (bias) of the measurement system, particularly the bias induced by the multi-beam approach of the system which measures with several beams simultaneously.

The calculation of the echo signals reflected from randomly distributed point scatterers moving in a defined flow field is performed by applying the system theory to linear acoustics. The simulation is carried out by the *FIELD II* toolbox for *MATLAB*. The theoretical Roberts flow is applied as flow.

Mainly, the number of vortex cells in the measuring field is varied for evaluating the bias. The received signals are calculated for the single and the multi-beam operation to compare their processed velocity data with each other. The comparison of the bias of both operation modes for different flow configuration reveals that the acoustic crosstalk increases the mean systematic error around 1.3% to 2.2% for the applied parameter set. In conclusion the error induced by the multi-beam approach is insignificant compared to the advantages (flow mapping with high frame rate and improved spatial resolution) of this measurement principle which denotes a progress for ultrasonic Doppler flow field measurements.

References

- [1] Takeda Y: Development of an ultrasound velocity profile monitor, Nucl. Eng. Design 126 (1991), 277-284.
- [2] Takeda Y & Kikura H: Flow mapping of the mercury flow, Exp. Fluids 32-2 (2002), 161-169.
- [3] Franke S, *et al.*: Two-dimensional ultrasound Doppler velocimeter for flow mapping of unsteady liquid metal flows, Ultrasonics 53 (2013), 691-700.
- [4] Franke S, *et al.*: Ultrasound Doppler system for two-dimensional flow mapping in liquid metals, Flow Meas. Instrum. 21 (2010), 402-409.
- [5] Jensen JA: Field: A Program for Simulating Ultrasound Systems, Medical & Biological Engineering & Computing 34-1 (1996), 351-353.
- [6] Jensen JA & Svendsen NB: Calculation of pressure fields from arbitrarily shaped, apodized and excited ultrasound transducers, IEEE Trans. Ultrason., Ferroelec., Freq. Contr. 39 (1992), 262-267.
- [7] Cramer, *et al.*: Local flow structures in liquid metals measured by ultrasonic Doppler velocimetry, Flow Meas. Instrum. 15 (2004), 145-153.
- [8] Kleeorin N, *et al.*: Mean-field dynamos in random Arnold-Beltrami-Childress and Roberts flows, Phys. Rev. E 79-4 (2009), 0463021-0463027.
- [9] Kasai, *et al.*: Real-Time Two-Dimensional Blood Flow Imaging Using an Autocorrelation Technique, IEEE Trans. Sonics Ultrason. 32-3 (1985), 458-464.

The signal processing of Ultrasonic reflector recognition and tracking technique

Antonin Povolny¹, Tomonori Ihara² and Hiroshige Kikura¹

¹Laboratory for Advanced Nuclear Energy, Tokyo Institute of Technology, 2-12-1 Ookayama, Tokyo 152-8550, Japan

²Department of Marine Electronics and Mechanical Engineering, Tokyo University of Marine Science and Technology, 2-1-6 Etchujima, Tokyo 135-8533, Japan

Ultrasound Reflector Recognition and Tracking Technique (URRTT) has been developed as a new technique to be applied in the measurement of bubbly two-phase flow. The URRTT measures separately the movement of each reflector, so that the difference in the behaviour of reflectors caused by their size, shape, etc. can be measured. Pulsed ultrasound is emitted into fluid and reflected by objects present in the ultrasound beam volume. The echo signal is recorded by the transducer with a certain delay (transit time) after emission of the original beam. URRTT recognizes reflectors and their positions in the echo signal and tracks reflectors from one pulse's echo to the following ones. The result of URRTT is one-dimensional (in the direction of the ultrasound beam) trajectory of each reflector. Trajectories of reflectors measured simultaneously by other transducers can be added to obtain secondary data such as reflector size, which is very important for measurement of gas bubbles in liquid. This paper focuses on the recognition and tracking algorithms of URRTT. The recognition algorithm uses assumed reflection shape to obtain points corresponding to reflectors' positions. The tracking algorithm connects those points to trajectories. A test experiment shows the performance of URRTT for bubble size measurement.

Keywords: Two-phase flow, Trajectory measurement, Signal processing, Tracking, Bubble size measurement

1. Introduction

The development of Ultrasonic reflector recognition and tracking technique (URRTT) is motivated by the development of novel simulation techniques for bubbly two-phase flow. While traditional simulation techniques (Two-fluid model) describe all bubbles using one bubble of average parameters to represent them, a technique described in [1] uses many representative bubbles to precisely simulate bubbles of sizes varying from the average. Another approach described in [2] is a direct simulation of phase interface. For further development of those techniques, proper experimental data are required.

Each individual bubble (not just averaged parameters) can be measured using video cameras and video processing. However, cameras require the optical access to the measurement position, which is often impossible due to the pipe wall or due to other bubbles blocking the way. Ultrasound measurement can overcome those limitations. Ultrasound velocity profiler (UVP) was used to measure gas bubble velocity in liquid [3-5]. While UVP provides velocity profiles of gas phase (if it can be distinguished from velocities of other reflectors), it does not distinguish between different bubbles. The attempt to do this by filtering UVP results was presented in [6] along with other methods of detecting phase interface. Simple approach without using UVP has been developed in [7] for single rising bubbles. The signal processing only includes the search for a maximum of amplitude, which corresponds to the position of the bubble surface. The transit time of this peak was recorded for each pulse repetition and then used to construct the trajectory of the bubble. It has been demonstrated that by measuring from opposite sides, bubble size can be measured and that by

parallel measurement at different positions, 2D velocities of bubbles between those two positions can be measured. The accuracy of this approach was investigated in [8]. The main drawback of this technique is that it can be applied only on single bubbles since the separation of bubbles is done only by repetitions with no bubble detected (all amplitudes lower than a threshold value). URRTT has been developed to measure the trajectory of each bubble separately while measuring more bubbles at the same time. To achieve this, completely new approach to signal processing has been applied. The signal processing of URRTT is described in this paper. The connection of trajectories from different measurement positions or directions can provide bubble size or average 2D velocity between different measurement positions. Test measurement of bubble size was performed and its results are presented in this paper to present the performance.

2. Measurement configuration

A measurement configuration used for the test measurement is shown in Fig. 1. An ultrasonic transducer (TDX) with 10 mm diameter emits beams into the fluid with bubbles. Second TDX is placed at the same measurement line (opposite direction) to obtain bubble sizes as explained in section 3.3 (Fig. 1 shows another possible configuration, which is not the focus of this paper). Pulses are generated by JapanProbe TIT-10B pulse generator and receiver device and repeated with frequency $f_{prf} = 2$ kHz. Each pulse is generated by a 1-period long wave of basic frequency $f_0 = 2$ MHz. The signal is digitised using APX-5040 AD converter (Aval data corp.) at sampling rate 140 MS/s. The AD converter enables simultaneous recording and processing of the data.

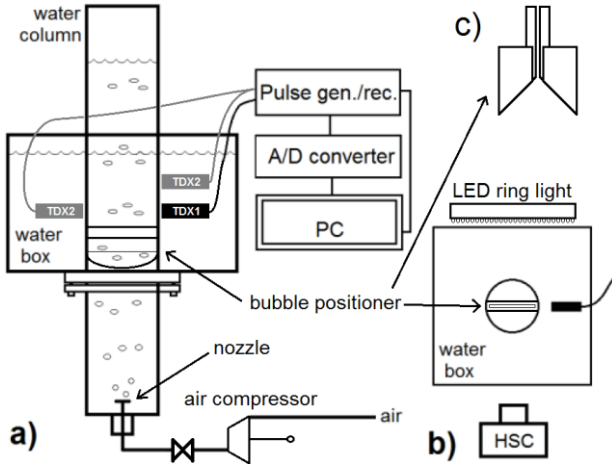


Figure 1: Experimental apparatus. a) front view, b) top view, c) side view on the bubble positioning device.

An acrylic pipe with inner diameter 51.5 mm was used with an acrylic box filled with water to enable observing the flow with a high-speed camera (HSC) Photron Fastcam MAX mounted with Micro-NIKKOR 105mm lens (with $f/4$) positioned in front of the box. A bubble positioning device (with 4 mm wide gap) is placed into the pipe just under the ultrasound beam to bring all the bubbles in the pipe to that beam and to ensure they stay in the 10 mm wide beam long enough to be detected. As a result, higher bubble number density condition was measured without bubble overlapping on the HSC footage. The video is recorded at 2,000 fps with shutter speed $1/20,000$ s and resolution $1,024 \times 256$ px. A ring LED light HPR2-150SW (CCS) illuminated the test section from behind. The HSC footage was analysed using the Computer Vision Toolbox of Matlab. The points of each bubble surface closest and furthest from the TDX were tracked in the footage to obtain trajectories of both sides of the bubble surface.

3. Signal processing of URRTT

The signal processing has been performed off-line. On-line measurement has not been attempted yet. The whole process is separated into blocks with specific purposes. First, the reflector recognition is performed on each pulse repetition echo signal. It detects all possible positions of reflectors (bubbles) using a reference signal (the assumed shape of the reflection). After that, reflector tracking is performed by joining candidate points from all pulses into chains, which should each represent one reflector. All chains are filtered to avoid noise and checked for erroneous connections of chains from more reflectors into one. Chains represent trajectories of reflector surfaces in the direction of the ultrasound beam. Chains measured by more TDXs for the same reflector (or by TDX and HSC) can be associated with each other. Associated chains can be used to compare data (if connected with HSC) or derive more data such as reflector size or average 2D velocity between two measurement lines.

3.1 Reflector recognition

First, the echo signal is filtered to get rid of any

frequency besides the basic frequency f_0 (during the test measurement, the pass-band was 1-5 MHz). Then, the echo is separated into intervals of width $1/f_0$ and the absolute value of the signal is summed over each interval to obtain the intensity of that interval. The same summation is done in preparation with no reflectors present in order to determine the background intensity for each interval. If the intensity is greater than the background intensity of the same interval, the interval is a candidate for containing a reflection. Next, cross-correlation is conducted between the reference signal (assumed reflection shape) and a piece of echo belonging to the interval and its close neighbourhood ($5 \mu\text{s}$ long in this paper). Here, it was assumed that the shape of the reflection is the same as the shape of the propagating pulse and it was measured by a TDX in the opposite direction (the reference signal was $4 \mu\text{s}$ long in this paper). The time lag T maximising the cross-correlation is a transit time of the reflector and the maximum itself corresponds to the signal strength. Since the chosen interval length was shorter than the reflection length, only the interval with the highest signal strength (among its neighbours) is chosen to be the candidate point. Each candidate point i with its time t_i (pulse emission time), transit time T_i (reflection delay inside the pulse) and signal strength M_i is recorded for further processing.

3.2 Reflector tracking

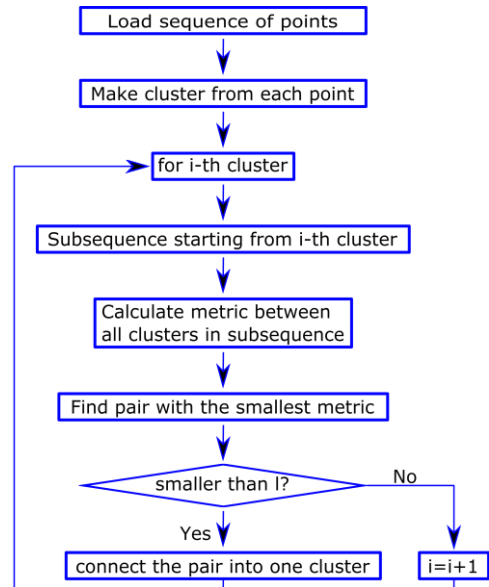


Figure 2: Simplified schematics of the tracking algorithm.

To connect all the points to chains (clusters) representing single reflectors (bubbles), a hierarchical clustering (the agglomerative approach) is employed with a modification for sorted data. All points from reflector recognition are used to create a sequence of singleton clusters sorted by time. The probability that two clusters are caused by the same reflector is described by a specific metric. Two clusters corresponding to the smallest metric value are connected into one cluster in each cycle until the smallest metric is larger than a limiting value l . The specific flow of the tracking algorithm is illustrated in Fig. 2.

The key point is the definition of the metric. It should measure the likeliness of two clusters being caused by the same bubble. The metric $D(I, J)$ between clusters I and J is calculated from the difference of time and transit time (position) of the last point i of the earlier cluster I and the first point j of the latter cluster J as

$$D(I, J) = \begin{cases} (t_j - t_i) + w|T_j - T_i| & t_j > t_i \\ l + 1 & t_j \leq t_i \end{cases} \quad (1)$$

where w is a weighting factor to weigh the importance of differences in time information t and transit time T (set to $w = 200$ in the test measurement). If metric for two clusters is higher than 1, they cannot be connected. The metric is set so that the connection can be done only if each point in the preceding cluster has been recorded earlier than all points in the latter cluster. This condition might seem unnecessary, but it is crucial since it allows keeping all clusters that could connect together and all points inside each cluster sorted by time. This enables to process the large amount of data part-by-part and thus to reduce the computational load (two points with a large difference of time cannot be connected together). It also helps to detect two separate trajectories measured at the same time close from each other. As a result of the algorithm, many chains (clusters) representing reflectors (one chain per reflector) are obtained.

This agglomerative approach works very well if the reflector number density is low. However, for higher reflector number densities, one reflector often follows a previous reflector in a similar track and it is difficult to recognize these two trailing reflectors from a single reflector. Since the signal strength corresponds to the distance between the reflector and the beam axis, each reflector passing through the field will be recorded with a characteristic shape of the signal strength as shown in Fig. 3. This information can be applied to detect trailing reflectors and separate corresponding chains. First, moving average filter is used to smooth the data. Then, peaks of signal strength are detected and they are compared to the minimum values between the peaks. In order to decide whether to separate the chain or not, some requirement (e.g. that both peaks have at least double the signal strength of the minimum) should be set.

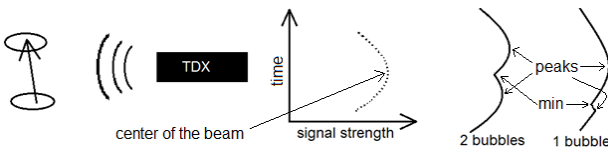


Figure 3: The signal strength corresponds to the distance between the reflector and the beam axis. The signal strength of a passing reflector has a characteristic shape (each point recorded at a different repetition), which can be applied to detect two trailing reflectors.

After a check for trailing reflectors and separation of their corresponding chains, the filter gets rid of the noise. Short chains with few points or with small signal strength are deleted. The transit time T of each chain can be used

with the speed of sound in water c to calculate the distance x between the TDX and the measured bubble surface as

$$x = \frac{Tc}{2} \quad (2)$$

and thus, the chain represents a trajectory of the reflector surface including the signal strength at each point.

3.3 Secondary data

The trajectory is a valuable information, but it is too complex to use it directly. Velocity is usually more useful. Instantaneous velocity of reflector surface (towards the TDX) can be easily calculated by taking finite differences of subsequent points of the trajectory and their times.

Results can be statistically described and compared with other measurement or used to validate some code. Comparison reflector-by-reflector is possible if chains measured by URRTT are associated with corresponding trajectories (or other data) from a different source such as HSC. The association is conducted using metric $B(I, J)$ between two sets of chains (I is from a different set than J) the chain I contains points from i_1 to i_l and the chain J contains points from j_1 to j_m . The metric is calculated as

$$B(I, J) = |t_{i_1} - t_{j_1}| + |t_{i_l} - t_{j_m}| + \left| \langle t \rangle_{i_1}^{i_l} - \langle t \rangle_{j_1}^{j_m} \right| + w' \left(|x_{i_1} - x_{j_1}| + |x_{i_l} - x_{j_m}| + \left| \langle x \rangle_{i_1}^{i_l} - \langle x \rangle_{j_1}^{j_m} \right| \right) \quad (3)$$

employing time and position from beginning and end of both chains as well as average values. The weight w' is used to scale between time and space (set to $w' = 0.1$ s/mm in the test measurement). The metric is calculated for each possible pair of chains and chains are associated with each other starting from the pair corresponding to the lowest metric value (already connected associated chains cannot be associated with some other chain).

It is possible to associate chains of URRTT results from two different TDXs as shown in Fig. 1. Metric $B(I, J)$ needs to be modified accordingly. In the case of two opposing TDXs, the difference between positions in trajectories is supposed to be a (assumed reflector size). Terms $x_i - x_j$ in Eq. 3 need to be replaced with $x_i - x_j - a$. For two parallel TDXs at different positions, assumed time delay (needed for the reflector to travel from one TDX to the other one) should be introduced. Once all trajectories are associated, the instantaneous reflector size is obtained from two opposing TDXs (using the known distance between them). For two parallel TDXs at different positions, signal strengths of associated chains can be cross-correlated to obtain the exact time delay needed to travel between those two TDXs. Average 2D velocity can be calculated using this time delay, measured trajectory data and a known distance between axes of those TDXs.

4. Example of measurement

An example of air bubble size measurement in water is introduced here. The configuration is described in

section 2 and shown in Fig. 1. Trajectories of opposite bubble surfaces were measured by two opposing TDXs. Transit time/position was measured relative to the opposing inner pipe wall (the transit time of the opposing inner pipe wall was obtained by a cross-correlation with the negative reference signal since water-acrylic boundary reflects in a phase opposite to the water-air bubble surface). The wall-to-wall distance (inner diameter of the pipe) is known, therefore trajectories can be obtained in the same coordinate system and bubble size can be calculated. Results were compared to data obtained from video processing of a HSC footage.

Two cases of measurement are presented here. In both, bubbles were spherical to ellipsoidal shape and bubble size of each bubble was calculated from the HSC footage. The mode of the horizontal size distribution was 4.1 mm and the mode of the vertical size distribution was 2.7 mm. Bubble number density was estimated from the HSC footage as well. In CASE1, the average bubble number density was 0.44 ml^{-1} (oscillating from 0 to 1.57 ml^{-1}). At the same time, there were 0 to 8 bubbles in the measurement volume (average 2.27). In CASE2, the average bubble number density was 0.19 ml^{-1} (oscillating from 0 to 0.98 ml^{-1}); 0 to 5 bubbles (average 0.98). Instantaneous bubble sizes in the horizontal direction were measured by combining URRTT results of two TDXs. Chains were also associated with HSC results so that bubble-by-bubble comparison of results is possible. For each bubble, average sizes (by URRTT and by HSC) are compared in Fig. 4 and 5. The absolute value of the difference between instantaneous bubble size measured by URRTT and HSC has been averaged over the time interval, where both methods detected the bubble. This value, the normalised bubble size error shows how well does the measurement of instantaneous bubble size agree between HSC and URRTT. Histograms of normalised bubble size errors are shown in Fig. 4 and 5.

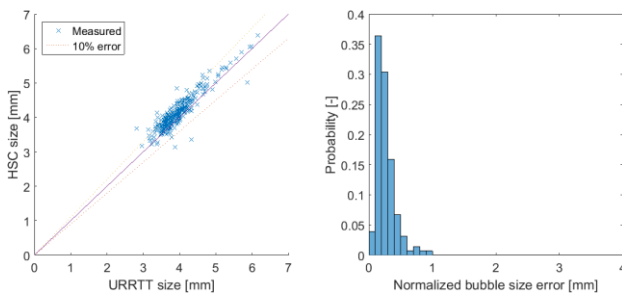


Figure 4: Measurement results for CASE1.

Results show good agreement with HSC values a little bit higher. The difference is around $200 \mu\text{m}$, which is comparable with $60 \mu\text{m}$ pixel resolution of HSC. There are also large uncertainties in the speed of sound obtained from water properties tables using measured temperature of water (speed of sound) and measurement of the inner pipe diameter (needed for calculating the bubble size in URRTT). The video processing algorithm involves the blurred bubble surface image into the bubble region and thus overestimates the bubble size. As such, results show very good agreement, especially for instantaneous bubble

sizes. Higher bubble number in CASE1 lead to a small change of accuracy. However, the reliability of the measurement (ability to detect all the bubbles and avoid erroneous trajectories) decreased.

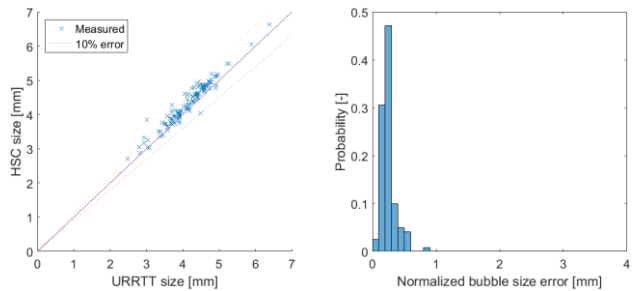


Figure 5: Measurement results for CASE2.

5. Summary

The URRTT was developed to measure the trajectory of each bubble crossing the measurement volume. This requires a new approach to signal processing, which was explained in detail. A combined measurement by more TDXs enables to obtain bubble sizes and average bubble velocities between two measurement lines. Presented results show that average bubble sizes measured by URRTT correspond well with the same value from HSC. The difference of $200 \mu\text{m}$ can be explained by the camera resolution and other measurement uncertainties.

Presented results prove the concept of URRTT as a measurement technique providing a lot of information about the movement of gas bubbles in liquid. As such, it can be applied to measure bubbly flows in many situations where the differences in bubbles sizes are of importance. However, this technique has its limitations. With more bubbles, the reliability of the method is expected to decrease. The evaluation of the range of URRTT application is the subject of future research of authors.

References

- [1] Krepper E *et al.*: Inhomogeneous MUSIG model - a population balance approach for polydispersed bubbly flows, NURETH-12, Pittsburgh, USA (2007).
- [2] Tryggvason G *et al.*: Direct numerical simulations of gas/liquid multiphase flows, Fluid Dyn. Res., 38-9 (2006), 660-681.
- [3] Aritomi M *et al.*: Measurement system of bubbly flow using Ultrasonic Velocity Profile Monitor and video data processing unit, J. Nucl. Sci. Technol., 33-12 (1996), 915-923.
- [4] Murakawa H *et al.*: Application of ultrasonic Doppler method for bubbly flow measurement using two ultrasonic frequencies, Exp. Therm Fluid Sci., 29-7 (2005), 843-850.
- [5] Murakawa H *et al.*: Application of ultrasonic multi-wave method for two-phase bubbly and slug flows, Flow Meas. Instrum., 19-3 (2008), 205-213.
- [6] Murai Y *et al.*: Ultrasonic detection of moving interfaces in gas-liquid two-phase flow, Flow Meas. Instrum., 21-3 (2010), 356-366.
- [7] Andruszkiewicz A *et al.*: Gas bubble detection in liquid metals by means of the ultrasound transit-time-technique, Eur. Phys. J. Spec. Top., 220 (2013), 53-62.
- [8] Richter T *et al.*: Measuring the diameter of rising gas bubbles by means of the ultrasound transit time technique, Nucl. Eng. Des., 291 (2010), 64-70.

Application of Partial Inversion Pulse on velocity profile and flowrate measurement using Ultrasonic Time-Domain Correlation method

Sanehiro Wada¹, Takashi Shimada¹

¹ Advance Industrial Science and Technology, National Metrology Institute of Japan, Central 3, 1-1-1, Umezono, Tsukuba, Ibaraki, 305-8563, Japan

This paper presents an application of a novel ultrasonic pulse, Partial Inversion Pulse (PIP), to the velocity profile and flowrate measurement using Ultrasonic Time-Domain Correlation (UTDC) method. In general, a measured flowrate depends on the velocity profile in a pipe, thus an on-site calibration is the only method of checking the accuracy of flowrate measurements in the fields. UTDC is a type of flow metering method that is applicable to the on-site calibration. The principle of the flowrate calculation is based on the integration of the measured velocity profile. The advantages of this method compared with the ultrasonic pulse Doppler method are the possibility of no-limitation of velocity range and applicability to flow fields without enough reflectors. Previous studies reported, however, that UTDC has also a limitation of velocity range because of the false detection. To overcome the false detection, we have developed a new waveform of pulsed ultrasound. Experimental measurements were performed at the national standard calibration facility of water flowrate in Japan. The results indicate that UTDC employing PIP can measure velocity profiles and flowrates with higher accuracy than the conventional method.

Keywords: Flowrate, Velocity profile, ultrasound, Time-domain correlation, Partial inversion pulse

1. Introduction

It is well known that the measured flowrate given by flowmeters, such as ultrasonic, electromagnetic, and turbine flow meters, generally depends on the velocity profile in a pipe. This demonstrates that the measurement accuracy of these flowmeters is influenced by the upstream pipe configuration even if flowmeters are calibrated by a calibration facility. In calibration facilities, the construction of a complete equivalent pipe layout with an actual field is often difficult, and thus an on-site calibration is the only method of checking the accuracy of flowrate measurement. An on-site calibration is a comparison test using a reference flowmeter in the fields. Although the establishment of an on-site calibration method with high accuracy is expected for actual fields, there are a few methods that realize it. For instance, Guntermann et al. [1] proposed an on-site calibration method using a laser Doppler velocimetry (LDV) system. In this method, the reference flowrate in the actual flow field is estimated using the velocity profile measured by the LDV system. However, modifications to the pipe are necessary to use the LDV system.

Mori et al. [2] have developed the flowmeter based on the ultrasonic pulse Doppler method (UDM). This type of flow metering method has a possibility of being applied to an on-site calibration. Since the basic principle of the flowrate measurement consists of measuring a velocity profile over a pipe diameter and integrating the measured profile, this method is expected to remove the necessity of modifying the existing pipe. Furuichi performed a fundamental uncertainty analysis of this flow metering method under the ideal flow condition [3] and Wada et al. reported the experimental results under disturbed flow conditions [4].

On the other hand, ultrasonic time-domain correlation method (UTDC) has been developed in the medical field to exceed the velocity range of UDM [5][6][7]. Owing to

its outstanding advantage of the high time resolution, UTDC has been applied in the engineering field [8][9]. In principal, UTDC has advantages which are a possibility of no-limitation of velocity range and an applicability to a flow condition without enough reflectors. Considering the application to actual flow fields, such as industrial facilities and power plants, these advantages are important to measure the large flowrate and to reduce the impact of reflectors on the facilities. The literature concerning the evaluation of velocity range is, however, limited. Some studies have suggested that UTDC has also a limitation of velocity range and needs an adequate threshold of cross-correlation coefficient to avoid the false detection of the sidelobe [10][11].

In this paper, we present an application of a novel pulsed ultrasound, Partial Inversion Pulse (PIP), to a velocity profile and flowrate measurement using UTDC. This method is based on the pulse compression technique [12] and has an advantage to expand the velocity range with high accuracy in comparison to the conventional UTDC. PIP can reduce the sidelobe of cross-correlation coefficient by inverting a pulsed ultrasound partially. Experimental measurements were performed and the results were evaluated at the national standard calibration facility of water flowrate in Japan.

2. UTDC

2.1 Principle of measurement

A schematic of flow velocity measurement using UTDC is illustrated in Figure 1. In general, a cross-correlation coefficient is determined by following equation,

$$R_k = \frac{\sum_{t=1}^n u_0(t) \cdot u_1(t)}{\sqrt{\sum_{t=1}^n u_0^2(t)} \sqrt{\sum_{t=1}^n u_1^2(t)}} \quad (1)$$

where, u_0 and u_1 are the detected waveforms in the

reference and search windows.

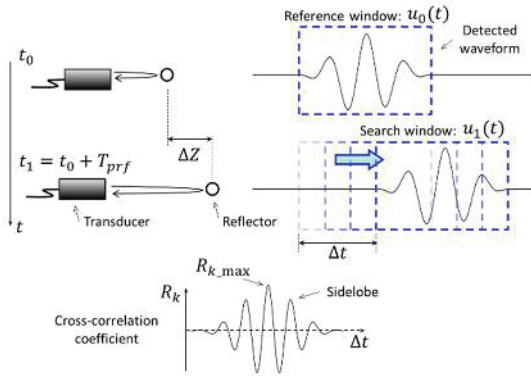


Figure 1: Schematic of flow velocity measurement using UTDC.

2.2 Partial Inversion Pulse

An input voltage signals of the normal pulse and PIP are presented in Figure 2. In normal case, a pulse with two cycles of T_0 are transmitted from a transducer and repeated with an interval of T_{prf} . Then the pulsed ultrasound is reflected on a particle and detected by the same transducer. On the other hand, PIP has a delay time of $0.5T_0$ between the two cycles. In this manuscript, we report only the case of two cycles per pulse and the delay time of $0.5T_0$. It needs to study an influence of the number of cycles and the delay time on the flow measurement in the future work.

Figure 3 shows the actual waveforms of pulsed ultrasound with the frequency of 2MHz. This figure indicates that PIP can be formed successfully. The cross-correlation coefficients of the normal pulse and PIP are illustrated in Figure 4. The coefficient of the sidelobe is approximately $R_k = 0.7$ in the normal pulse case. On the other hand, the sidelobe of PIP is reduced to approximately $R_k = 0.4$ due to the result of the inversion region.

3. Experiment

3.1 Experimental apparatus and conditions

The experiments were performed at the water flowrate calibration facility of the National Institute of Advanced Industrial Science and Technology, National Metrology Institute of Japan (AIST, NMIJ). This facility is the national standard calibration facility of water flow in Japan. The flowrate given by UTDC with PIP was evaluated with respect to the reference flowrate given by the electromagnetic flowmeter calibrated by the static gravimetric method using a tank system weighing 50 t. The uncertainty of the reference flowrate given by the 50t weighing tank system is 0.060% ($k = 2$). For the details of the system, see reference [13]. The flowrate of this experiment was $400\text{m}^3/\text{h}$, and the water temperature condition was 17.3 ± 1.0 °C. The temperature variation was within 0.1 °C during one measurement. The Reynolds number was $Re = 6.61 \times 10^5$. Figure 5 shows the schematic of the test facility and the test section. The pipe layout with the bubble generator was the same as in the previous study [3]. The flow conditioner was installed a distance of $55D$

upstream of the test section. Small bubbles that act as reflectors of ultrasound were inserted upstream of the flow conditioner [14]. The ultrasonic transducer was installed in the test pipe and placed in direct contact with the water. The incident angle of transducer was $\alpha = 19.7^\circ$ which was obtained from an actual measurement. The inner diameter of the test pipe was $D = 199$ mm.

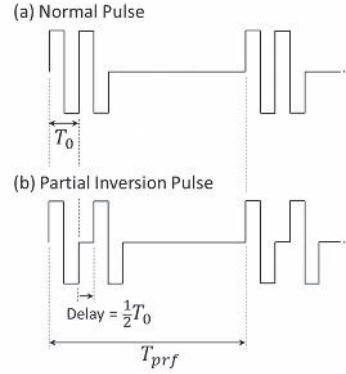


Figure 2: Input voltage signals of the normal and partial inversion pulses.

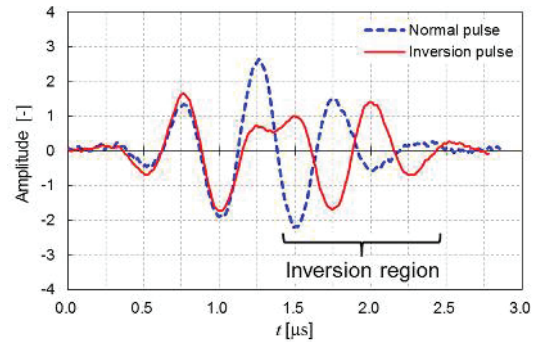


Figure 3: Waveforms of pulsed ultrasound in case of normal pulse and PIP.

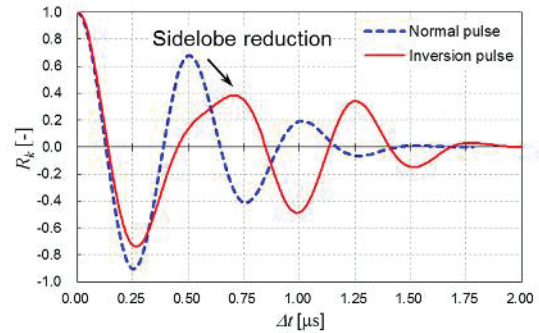


Figure 4: Cross-correlation coefficients in case of normal pulse and PIP.

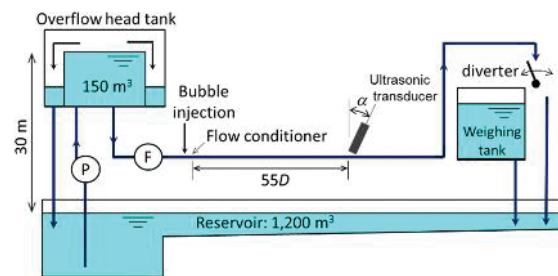


Figure 5: Experimental facility and test section.

An input voltage signal with two cycles per pulse generated by using the pulser-receiver instrument (JPR-10CN, Japan Probe Co., LTD.) was applied to the ultrasonic transducer, and a pulsed ultrasound was transmitted into water. Reflected pulses of ultrasound were detected by the same transducer and amplified by using the same pulser-receiver. These amplified signals were transferred to the digitizing instrument (NI-5122, National Instruments Co.). PIP was also generated and transmitted by the same pulser-receiver. The time interval of pulse repetition was set at 400 μs and the delay time of PIP was set at 0.25 μs . The central frequency of the ultrasonic transducer was $f_0 = 2$ MHz, and the diameter of the piezoelectric element was 10 mm. All the measurements we present were made with the same receiving gain and power amplification settings. The distance between measurement points along the ultrasonic path was 2.2 mm.

The sampling rate of the digitizing instrument was 100MHz. The width of reference and search windows were set at 3 μs to cover the entire range of the pulsed ultrasound as shown in the previous chapter. The determination of the threshold of cross-correlation coefficient is important to eliminate the false detection especially under small signal to noise ratio. The threshold was changed from 0.5 to 0.9 in this experiment.

The measurable velocity of UDM can be calculated according to the following equation,

$$v_{\max} = \frac{c}{4f_0 T_{prf} \sin \alpha} \quad (2)$$

where, c is the sound speed of water, f_0 is the center frequency of ultrasound, T_{prf} is the time interval of pulse repetition and α is the incident angle of ultrasound. Since this method can measure the both velocity directions, going away from and approaching the transducer, the velocity range is given by the equation.

$$v_{\text{range}} = 2v_{\max} \quad (3)$$

In this paper, the velocity range of UDM for $f_0 = 2$ MHz in direction of the pipe axis is approximately 2.8 m/s. Consequently, the experimental flowrate was set at 400 m^3/h to exceed the measurable velocity of UDM.

3.2 Results

An example of detected signal over the pipe region is shown in Figure 6(a). The delay time calculated by using the distance between the transducer and the inner pipe wall of the opposite side is approximately 300 μs , thus this figure demonstrates that the transducer can detect the pulses reflected on particles all over the pipe region. To confirm the shape of PIP signal, the enlarged figure is provided in Figure 6(b). PIP can be observed clearly and every detected signals have the inversion region as illustrated in this figure.

The time averaged velocity profiles at the threshold of $R_{Th} = 0.7$ are illustrated in Figure 7. The horizontal axis is the position over the pipe and the vertical axis is the normalized velocity. It is important to consider the number of particles passing through a measurement volume during

one measurement. Under the same number density of particles, the number of pulse repetition for calculating one averaged profile is better to be determined depending on the flowrate. In this paper, the number of pulse repetition is set at $N_p = 38,400$ for $Q = 400$ m^3/h . The time of one measurement is approximately 15 s. This figure indicates that the all velocities obtained using the normal pulse are smaller than the velocities using PIP. This is expected that the influence of the false detection on the velocities using the normal pulse is larger than that using PIP.

In general, the flowrate is calculated by integrating the velocity profile which is obtained in the region from $r/D = 0$ to $r/D = 0.5$ [15]. This is because that it is necessary to avoid the effect of the large stable signals occurred in the transducer or in the pipe wall near transducer. Figure 8

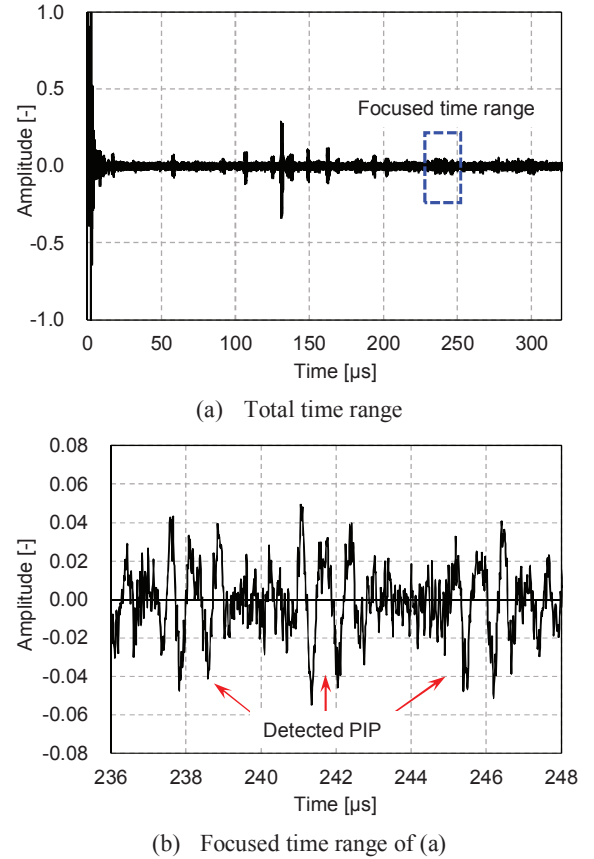


Figure 6: Snapshot of detected signal.

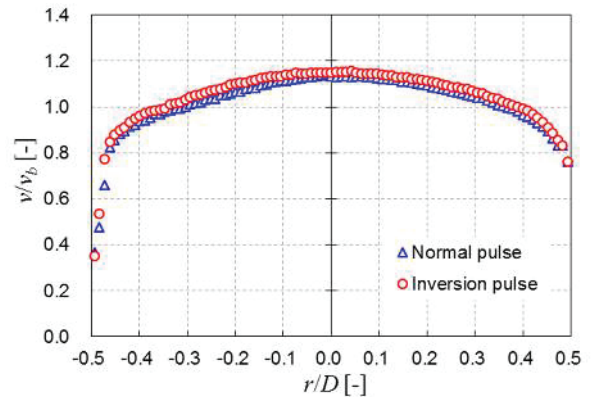


Figure 7: Mean velocity profiles at $R_{Th} = 0.7$.

shows the difference of measured flowrate between by using UTDC and by using the reference flowmeter. The difference is expressed as the equation,

$$E_Q = \frac{Q_{UTDC} - Q_{ref}}{Q_{ref}} \quad (4)$$

where, Q_{UTDC} and Q_{ref} are the flowrates measured by using UTDC and the reference flowmeter, respectively. As a result, UTDC with PIP can measure the flowrate with high accuracy under $\pm 0.3\%$ when the threshold of cross-correlation coefficient is equal to or higher than 0.7. In conclusion, UTDC with PIP allows an expansion of velocity range with a superior accuracy. It remains challenges for future research to evaluate effects of increasing number density of particles and disturbing flow condition such as downstream of an elbow or a valve.

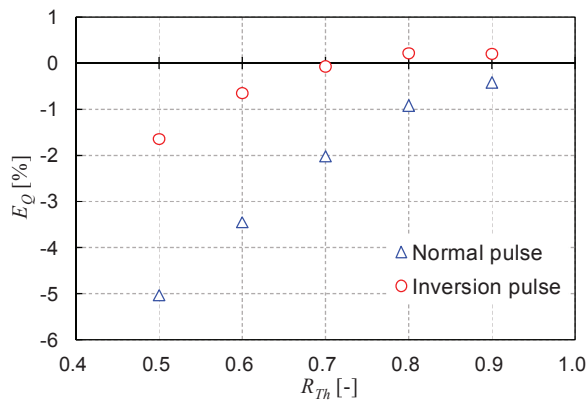


Figure 8: The differences of measured flowrate between by using UTDC and by using the reference flowmeter.

4. Conclusions

This paper presents an application of a novel ultrasonic pulse, Partial Inversion Pulse, to the velocity profile and flowrate measurement using UTDC. This method has an advantage to expansion the velocity range with high accuracy in comparison with the conventional one. PIP can reduce the sidelobe of cross-correlation coefficient by inverting a pulsed ultrasound partially. Experimental measurements were performed and the results were evaluated at the national standard calibration facility of water flowrate in Japan.

The results of the experiments show that all detected signals have a partial inversion region in a pulse. UTDC with PIP can measure the velocity profiles over the pipe diameter even if these velocities exceed the measurable velocity range of UDM. In addition, the accuracy of flowrates calculated by using the measured velocity profiles are under $\pm 0.3\%$ when the threshold of cross-correlation coefficient is equal to or higher than 0.7.

It is found that the validity of UTDC with PIP has been shown by the development of an ultrasound generator that can form PIP. It remains some challenges for future research to evaluate an influence of the increasing number density of particle, and disturbing flow condition such as downstream of an elbow or a valve.

Acknowledgment

The work was supported by JPSP KAKENHI Grant Number JP15H05566.

References

- [1] Guntermann P, *et al.*: In situ calibration of heat meters in operation, *Euro Heat and Power*, 8 (2011), pp.46–49.
- [2] Mori M, *et al.*: Development of a novel flow metering system using ultrasonic velocity profile measurement, *Experiments in Fluids*, 32 (2002), pp.153–160.
- [3] Furuichi N: Fundamental uncertainty analysis of flowrate measurement using the ultrasonic Doppler velocity profile method, *Flow Measurement and Instrumentation*, 30 (2013), pp.202–211.
- [4] Wada S and Furuichi N: Influence of obstacle plates on flowrate measurement uncertainty based on ultrasonic Doppler velocity profile method, *Flow Measurement and Instrumentation*, 48 (2016), pp.81–89.
- [5] O. Bonnefous and P. Pesque: Time domain formulation of pulsed-Doppler ultrasound and blood velocity estimation by cross correlation, *Ultrasonic Imaging*, 8 (1986), pp.73–85.
- [6] Ilmar A. Hein and William D. O'Brien JR: Volumetric measurement of pulsatile flow via ultrasound time-domain correlation, *Journal of Cardiovascular Technology*, vol.8, No.4 (1989), pp.339–348.
- [7] Ilmar A. Hein, *et al.*: A real-time ultrasound time-domain correlation blood flowmeter, *IEEE Transactions on Ultrasonics, Ferroelectrics, and Frequency Control*, vol.40, No.6 (1993), pp.768–775.
- [8] Yamanaka G, *et al.*: Velocity profile measurement by ultrasound time-domain correlation method, *5th World Conference on Experimental Heat Transfer, Fluid Mechanics and Thermodynamics*, Thessaloniki, Greece, September 24–28, (2001-9), pp.1189–1193.
- [9] Ozaki Y, *et al.*: High time resolution ultrasonic velocity profiler, *Exp Therm Fluid Sci*, 26 (2002), pp.253–258.
- [10] DW Rickey *et al.*: A velocity evaluation phantom for colour and pulsed Doppler instruments, *Ultrasound in Medicine and Biology*, 18(5) (1992), pp.479–494.
- [11] Jensen JA: Range/velocity limitations for time-domain blood velocity estimation, *Ultrasound in Medicine and Biology*, 19(9) (1993), pp.741–749.
- [12] Skoink Mi: Introduction to radar system, 2nd ed., McGraw-Hill, 1983.
- [13] Furuichi N, Terao Y and Takamoto M: Calibration facilities for water flowrate in NMIJ, *Proceedings of 7th International Symposium on Fluid Flow Measurement*, Anchorage, USA, August (2009), pp.12–14.
- [14] Tezuka K, *et al.*: Assessment of effects of pipe surface roughness and pipe elbows on the accuracy of meter factors using the ultrasonic pulse Doppler method, *J. of Nuclear Science and Technology*, 45(4) (2008), pp.304–312.
- [15] Wada S, *et al.*: Development of pulse ultrasonic Doppler method for flow rate measurement in power plant – Multilines flow rate measurement on metal pipe, *J. of Nuclear Science and Technology*, 41(3) (2004), pp.339–346.

Acoustic characterization of pulsed ultrasound sensors for improved non-invasive Pulsed Ultrasound Velocimetry through high-grade stainless steel pipes

Tafadzwa John Shamu¹, Reinhardt Kotzé¹, and Johan Wiklund²

¹ Cape Peninsula University of Technology (CPUT) PO Box 652 Cape Town 8001 South Africa

² SP Technical Research Institute of Sweden, Box 5401, SE-402 29 Göteborg, Sweden

The newly developed Flow-Viz rheometric system is capable of performing detailed non-invasive velocimetry measurements through industrial stainless steel pipes. In order to advance the current non-invasive ultrasound sensor technology; acoustic characterization tests are required. The primary purpose of this work was to evaluate the effect of different non-invasive ultrasound sensor coupling configurations, for Doppler velocimetry in stainless steel pipes. The experiments involved measuring the ultrasound beam propagation through stainless steel (316L) pipe walls. A high-precision robotic XYZ-scanner and needle hydrophone setup was utilized to measure the beam propagation after the pipe wall; using a planar measuring technique along the beam's focal axis. The output for each test was a two dimensional acoustic color map, detailing the acoustic intensity of the ultrasound beam. Critical parameters such as the: focal zone start distance, focal zone length, Doppler angle and peak focal zone intensity are presented as part of the measurement results. It was noted that variations in the measured beam properties are highly dependent on the acoustic couplants. The Flow-Viz sensor technology was for the first time acoustically characterized, through stainless steel pipes. This information will now be used to further optimise the sensor technology for advanced industrial applications.

Keywords: Non-invasive ultrasound sensor, velocimetry, acoustic characterization, PUV, PUV+PD

1. Introduction and background

Pulsed Ultrasound Velocimetry (PUV) in industrial pipe flow has now reached a high level of development, since its first application to general fluids [1]. Non-invasive PUV is an appealing flow measurement technique for several industrial applications, especially in the food processing plants where hygienic requirements impose, clean, non-intrusive and non-destructive instrumentation [2]. By using the Doppler technique as described in [1] in conjunction with pressure difference measurement, the PUV+PD technique for determining the flow properties (rheology) of fluids was developed [3]. PUV+PD is mainly used as an in-line rheometric technique for quality control purposes. Over the past 15-20 years, the PUV+PD technique has been continually optimised and evaluated for a wide range of complex industrial fluids [4]–[7]; however, no commercial in-line rheometric system was developed for industrial implementation. Most of the in-line measurement data from earlier systems was post-processed off-line in order to determine the in-line rheological properties. Recently, Flow-Viz a non-invasive industrial rheometric system based on the PUV+PD methodology was developed under collaborative research between SP – Technical Research Institute of Sweden (SP), Gothenburg and Flow Process and Rheology Center (FPRC) at Cape Peninsula University of Technology (CPUT), Cape Town. The commercially available Flow-Viz system which is able to provide rheometric data in-line, consists of three integral parts, which are the operator's panel, system software and the non-invasive sensor unit [8], [9]. The main problem which still persists, and requires more attention is related to the development of more advanced non-invasive ultrasound sensor technology for measurements in complex industrial fluids

[10]. The ideal ultrasound beam required for accurate measurements should be able to penetrate across the entire measurement depth especially in highly attenuating industrial fluids. The beam should also be as narrow as possible throughout the measurement axis, in order to achieve a higher spatial and lateral resolution [7].

Effective and efficient transmission of the pulsed ultrasound beam into the fluid under test at a predetermined Doppler angle, requires that there be an effective mechanical construction in place to hold the transducer in position, together with a suitable coupling medium to facilitate the transmission of acoustic energy [11]. The most common mounting fixtures which have been used thus far, are invasive flow adaptor designs [12]. A completely non-invasive ultrasound sensor solution which is capable of measuring through stainless steel (SS316L), was developed by Flow-Viz [10]. With the new sensors, the beam geometry is influenced by different material boundaries such as the coupling material and pipe walls, before it propagates into the fluid medium. The new non-invasive sensors require a coupling material between the sensor wedge surface and the outer pipe wall in order to maximize the acoustic energy propagating between the two material layers. The improved coupling corresponds to an increase in ultrasound transmission [11]. The resulting beam after the coupling material needs to also have a focal zone which starts at the inner pipe wall interface. This work was aimed at the acoustic characterization and evaluation of Flow-Viz ultrasound sensors for non-invasive velocity profile measurements through stainless steel pipes. None of the new sensor configurations were previously acoustically characterized. These tests investigated the propagation of the pulsed ultrasound beam from sensors, using different couplants,

wedge and transducer technologies. The focus was on comparing the effectiveness of different couplants and sensor configurations; in order to develop the next generation non-invasive ultrasound sensor technology and to maximise the effectiveness of coupling configurations for existing sensors.

2. Experimental methods

2.1 XYZ-scanning system

To determine the sensors', beam properties, acoustic characterization tests were carried out using a high-precision (1 mm) needle hydrophone (www.precision-acoustics.com/) and an advanced XYZ-scanner setup. The submersible needle hydrophone and the different acoustic sensors were immersed in the water tank at room temperature. The XYZ-scanner was used to navigate the needle hydrophone probe across a predefined scanning grid i.e., to cover the focal area where the beam was located with a spatial resolution of 1 micrometer. In this work, only two spatial dimensions were used to map out a complete acoustic map i.e., vertical (Z-axis) and lateral (Y-axis) for the tests through stainless steel. The pulser-receiver was controlled from the host computer via RS232 serial (9600 baud-rate, 8-bit data) communications. The digitizer acquired the hydrophone measurement signal for each point within the scanning grid at set times, which were determined by the Matlab® based application.

2.2 Sensors and coupling configurations

Two types of sensors were tested: (i) the new commercial black Flow-Viz sensor and (ii) the prototype sensor with separate wedge and transducer, which allows detachment of the transducer from the wedge. The new commercial Flow-Viz sensor design only requires a coupling material between the sensor unit (with wedge) and stainless steel pipe, since it contains an integrated transducer-to-wedge couplant. The new design with integrated wedge is more convenient than the prototype wedge, as it reduces the complexity of couplant installation and the uncertainties associated with determining critical measurement parameters such as the Doppler angle (θ). Three solid (solid-X, solid-Y and solid-Z) and one liquid couplant were used in different configurations: at each sensor's transducer-to-wedge (TX) and wedge-to-pipe boundaries. The thicknesses of the couplants were: solid-X is ~ 1 mm, solid-Y is ~ 2 mm and solid-Z is ~ 2.5 mm. The liquid couplant was applied as a thin film of < 1 mm. A sampling frequency of 100 MHz was used with the digitizer. Figure 1 illustrates the vertical scanning area along the beams focal axis after propagating through the half-cut stainless steel pipe spool piece. The beam propagation angle within the wedge with reference to the horizontal is α , whereas that after the inner pipe wall interface is θ . Transducers used for the tests were rated at (1.8-2.2) MHz central frequency. A pulse length of 250 ns with an excitation voltage of 100 V were applied.

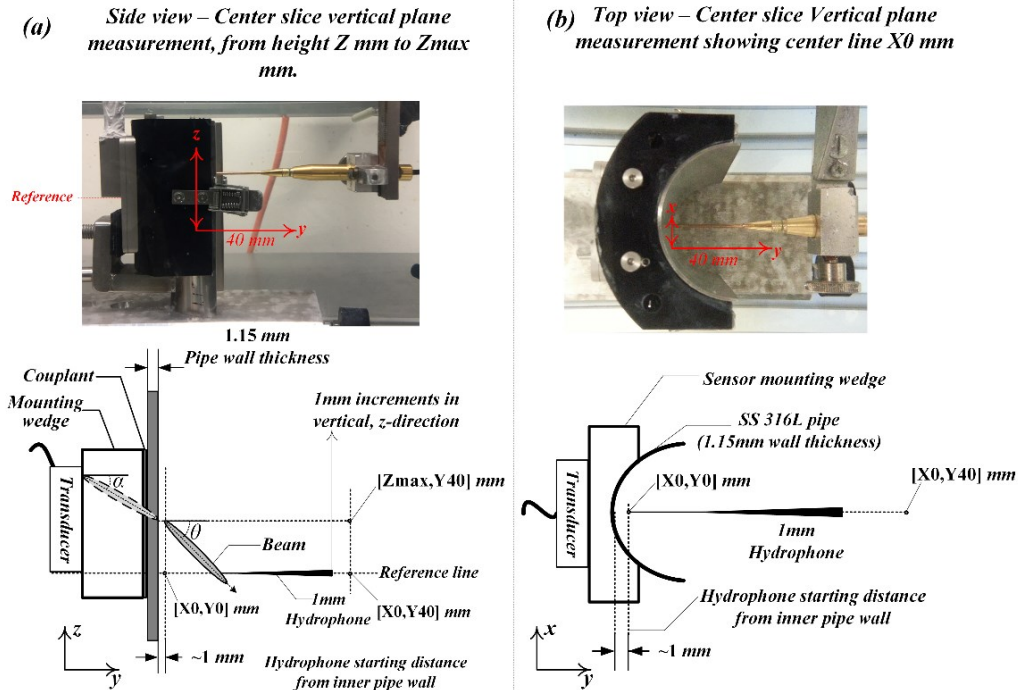


Figure 1: (a) Side view image and schematic of the vertical distance covered in the vertical direction (Z_0 to Z_{max}). (b) top-view schematic of the lateral distance covered (Y_0 - Y_{40}) along beam center line (X_0) (adapted from [9]).

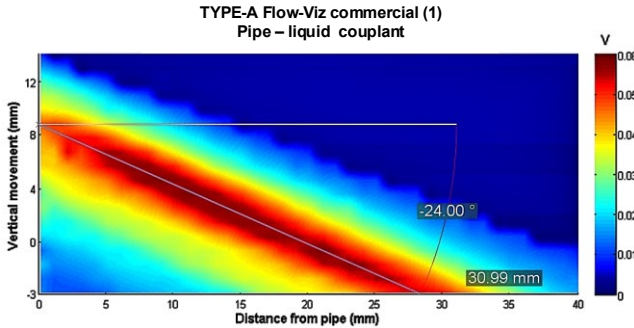
3. Results and Discussion

3.1 Flow-Viz Commercial –sensor configuration for 47.8 mm pipe

Acoustic color maps are oriented with respect to the sensor; i.e., for all pipe tests the sensor unit is positioned at the left of the acoustic map; and the 0 mm marking on the vertical movement axis is the reference position on the

physical sensor unit (see Figure 1). Four Flow-Viz transducers numbered 78, 79, 80 and 81 were used. Detailed information on these transducers can be found in [9]. Figure 2 shows the acoustic map obtained from the Flow-Viz 47.8 mm commercial sensor, pipe tests.

(a)



(b)

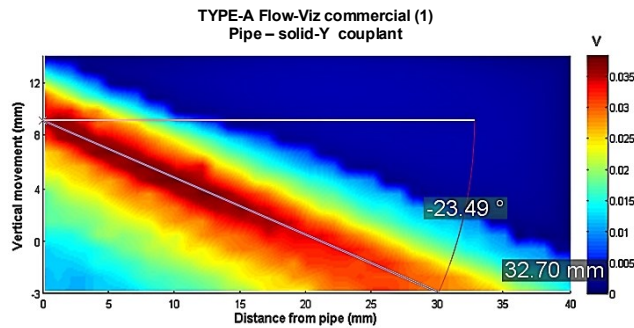


Figure 2: Acoustic maps for Flow-Viz 47.8 mm commercial sensor with (a) liquid couplant (b) liquid and solid-Y couplant at wedge-to-pipe interface [9].

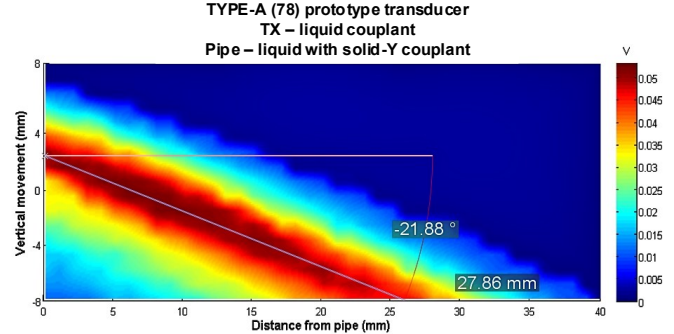
In order to test the quality and consistency of the Flow-Viz manufacturing process, two identical sensors with liquid couplant at the wedge-to-pipe boundary were tested, and similar results were obtained. One result from the sensor tests with liquid couplant is illustrated in Figure 2(a). The start of the focal zone was at a distance of ~ 5 mm away from the inner pipe wall with the liquid only couplant; however, with the solid-Y couplant the focal zone is situated close to the inner pipe wall. A focal zone starting at the pipe wall improves the near wall measurements. This is important for accurate in-line rheology as it reduces the near wall fluctuations which have been reported in literature [6]. The liquid couplant is a more effective couplant than the solid couplant when using the commercial Flow-Viz sensor unit. The solid-Y couplant in Figure 2(b), seemed to have more attenuating effects on the beam propagation. The peak focal zone voltage with the liquid couplant was 60.3 mV whereas with the solid-Y couplant it was 38.5 mV.

3.2 Prototype wedge sensor configuration for 47.8 mm pipe

Figure 3 confirmed that for the 47.8 mm prototype sensor, solid-Z resulted in the most undesirable beam of the configurations which were tested, since the focal zone length (~ 20 mm) is less than the pipe radius (23.9 mm).

The most preferable beam with regards to the length and location of the focal zone is that measured from the combined liquid and solid-Y couplant. The focal zone is both close the pipe wall and extends over half the pipe radius, similarly to the liquid only configuration in Figure 2(a), despite less focal zone peak voltages than the latter.

(a)



(b)

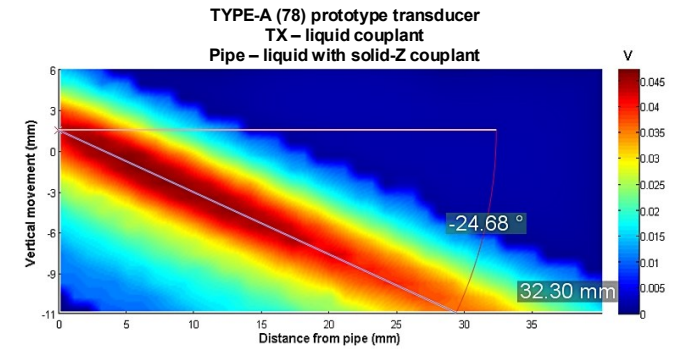


Figure 3: Acoustic maps for 47.8 mm prototype (78) sensor with liquid transducer-to-wedge couplant (TX); (a) liquid and solid-Y couplant (b) liquid and solid-Z couplant at wedge-to-pipe interface [9].

A third setup (not illustrated in Figure 3) i.e., with liquid couplant at the wedge-to-pipe interface resulted in similar beam properties to those obtained with the Flow-Viz commercial sensor in Figure 2(a). The critical Doppler angle from Figure 3 was seen to change by $\sim 3^\circ$ after changing the wedge-to-pipe couplants. This has to be taken note of since it directly affects the calculated axial velocity vectors along the pipe radius; and consequently the rheology of the fluid due to the changes in the velocity profile dependent shear rates.

3.3 Prototype wedge sensor configuration for 22.4 mm pipe

For the test in Figure 4, a different transducer-to-wedge (TX) couplant in the form of solid-X (described in Section 3) was used. The significant increase in energy observed for this test (Figure 4) is mainly attributed to the thin solid-X couplant between the transducer and wedge interface. With a solid-X couplant, the maximum voltages within the focal zone for Figure 4 (a) and (b) were ~ 127 mV and ~ 93 mV, respectively, whereas those from Figure 5 with a liquid couplant at the transducer-to-wedge were in the range of (53-55) mV. Since the high energy (peak voltage) output with solid-X was an exception, it must be pointed

out that the transducer (79) with the thin solid-X couplant had a different design compared to transducer 80, which could also be another contributing factor for the increased energy output.

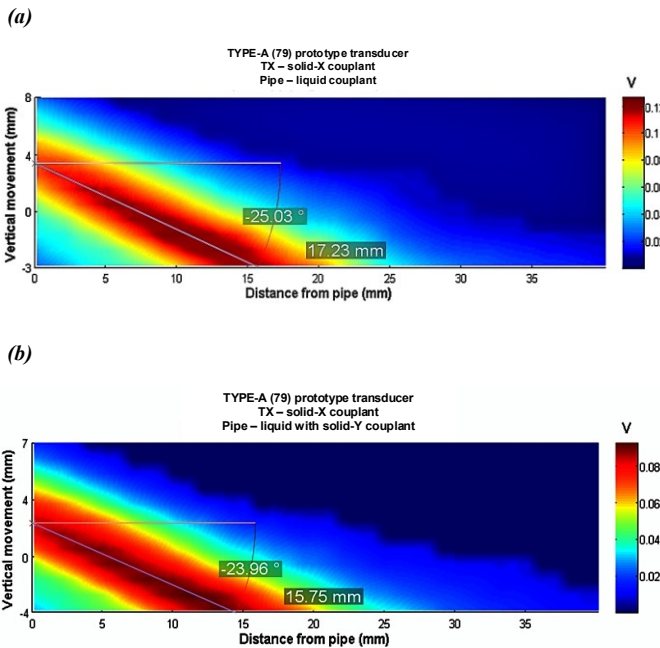


Figure 4: Acoustic maps for 22.4 mm pipe (79) sensor attached to prototype wedge with (a) only liquid couplant (b) liquid and solid-Y couplant between pipe and wedge [9].

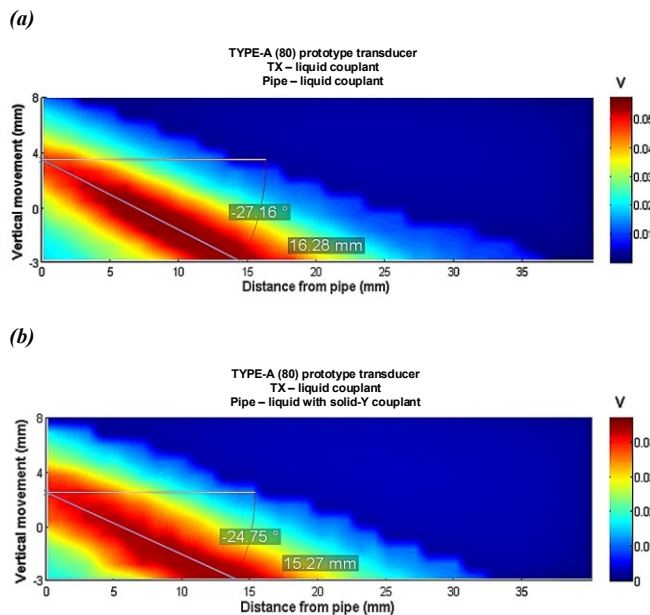


Figure 5: Acoustic maps for 22.4 mm pipe (80) sensor attached to prototype wedge with (a) only liquid couplant (b) liquid and solid-Y couplant between pipe and wedge [9].

The Doppler angle when using liquid couplant (Figure 5(a)) is reduced ($\sim 63.0^\circ$) compared to that obtained when using solid-Y couplant ($\sim 65.0^\circ$) at the wedge-to-pipe interface. This observation in Doppler angle changes is similar to that observed in Figure 4.

4. Conclusion

In this work, detailed acoustic characterization maps of the Flow-Viz non-invasive ultrasound sensors were obtained. The tests revealed that correct selection of solid and liquid couplants at different sensor interfaces is important in order to improve the overall transmitted beam properties and consequently PUV and PUV+PD measurements. As a general guideline, combining the solid-Y and liquid couplant at the wedge-to-pipe interface produced the most optimal beam properties i.e., focal zone starting distance and overall focal zone length. The next step is to conduct detailed 3-dimensional (3-D) acoustic measurements to gain more information on the entire beam geometry and to advance non-invasive sensor designs.

Acknowledgement

CPUT and SP for funding and providing the test facilities required to complete this research work.

References

- [1] Y. Takeda, "Velocity profile measurement by ultrasound Doppler shift method," *Int. J. Heat Fluid Flow*, vol. 7, no. 4, pp. 313–318, 1986.
- [2] I. Roberts, "In-line and on-line rheology measurement," in *Instrumentation and Sensors for the Food Industry*, Nestlé' Research Centre, Lausanne: Woodhead Publishing, 2001, pp. 403–422.
- [3] P. Brunn, J. Vorwerk, and R. Steger, "Optical and Acoustic Rheometers: Three Examples," *Appl. Rheol*, vol. 3, no. 1, 1993.
- [4] E. J. Windhab and B. Ouriev, "Rheological study of concentrated suspensions in pressure-driven shear flow using a novel in-line ultrasound Doppler method," *Exp. Fluids*, vol. 32, no. 2, pp. 204–211, Feb. 2002.
- [5] B. Birkhofer, S. A. K. Jeelani, B. Ouriev, and E. J. Windhab, "In-line characterization and rheometry of concentrated suspensions using ultrasound," *Proc.-4th ISUD Sapporo Jpn.*, pp. 65–68, 2004.
- [6] J. Wiklund and M. Stading, "Application of in-line ultrasound Doppler-based UVP-PD rheometry method to concentrated model and industrial suspensions," *Flow Meas. Instrum.*, vol. 19, no. 3–4, pp. 171–179, Jun. 2008.
- [7] R. Kotzé, J. Wiklund, and R. Haldenwang, "Optimisation of Pulsed Ultrasonic Velocimetry system and transducer technology for industrial applications," *Ultrasonics*, vol. 53, no. 2, pp. 459–469, Feb. 2013.
- [8] J. Wiklund, S. Ricci, Haldenwang, V. Meacci, M. Stading, and R. Kotzé, "Flow-VizTM – A fully integrated and commercial in-line fluid characterization system for industrial applications," in *9th ISUD Conference*, (Ubertone) Strasbourg, France, 2014.
- [9] T. J. Shamu, R. Kotze, and J. Wiklund, "Characterization of Acoustic Beam Propagation Through High-Grade Stainless Steel Pipes for Improved Pulsed Ultrasound Velocimetry Measurements in Complex Industrial Fluids," *IEEE Sens. J.*, vol. 16, no. 14, pp. 5636–5647, Jul. 2016.
- [10] R. Kotzé, S. Ricci, B. Birkhofer, and J. Wiklund, "Performance tests of a non-invasive sensor unit and ultrasound electronics," *Flow Meas. Instrum.*, pp. 1–8, 2015.
- [11] P. Theobald, B. Zeqiri, and J. Avison, "Couplants and their influence on AE sensor sensitivity," *J. Acoust. Emiss.*, vol. 26, pp. 91–97, 2008.
- [12] B. Birkhofer, "Doppler Ultrasound-Based Rheology," in *Practical food rheology: an interpretive approach*, I. T. Norton, F. Spyropoulos, and P. Cox, Eds. Chichester, West Sussex; Ames, Iowa: Wiley-Blackwell, 2011.

Positioning and navigation for free-fall type underwater observation system

Yoshikazu Koike¹, Hiroaki Morino¹, Etsuro Shimizu²

¹ Shibaura Institute of Technology, 3-7-5 Toyosu, Koto-ku, Tokyo 135-8548, Japan

² Tokyo University of Marine Science and Technology, 2-1-6 Etchujima, Koto-ku, Tokyo, 135-8533, Japan

In the recent years, technologies on marine development and research are strongly required and has been actively developed. However, it costs large to operate the marine apparatus, for example ROV (remote operate vehicle) or AUV (autonomous unmanned vehicle) in general. And, hence, it is difficult to increase the number of researchers or explores on the marine field. Therefore, it is necessary to develop a low cost and an easy operation system for underwater observation and exploration. In order to extend the number of which population are concerned with the underwater observation, the authors focus on the free-fall type underwater observation system(UOS) since the free-fall type UOS are realized at low cost and are easy to operate. The underwater position is required for exploration strongly although it is difficult to determine the underwater position of the free-fall type UOS due to tidal current and so on. Until now, we have developed a whole underwater circumferential observation system that is named Gyogyotto Camera. The camera system consists of the glass sphere which can be submarined at 7800m of sea depth. The observation system achieves the underwater circumferential video successfully. In this presentation, the recent free fall type UOS which recorded the world's first 3D video movie of the sea bottom at 7800m of the depth is introduced. And also the feasibility of the underwater positioning is studied using a micro electro mechanical system (MEMS) for an inertia measurement unit (IMU) inside the developed camera system.

Keywords: ocean bottom seismic observatory, underwater exploration system, inertia measurement navigation, micro-electro mechanical systems, inertia measurement sensor, whole circumferential video

1. Introduction

In the recent years, the global covering ocean observation and investigation is strongly required in order to protect sea creatures and to explore sea resource and so on.[1] A free-fall-type underwater observation systems (UOS) is often employed in order to monitor sea bed, earthquake awareness and its occurrence. Also, sea resources and creatures are often observed using the UOS. The authors are developing a low cost underwater observatory system, we call it "Gyogyotto Camera", using glass spheres like "Edokko No.1" [2-3]. The UOS we developed can monitor and record entire circumferential underwater image in real time.

For free-fall type UOS, the positioning is also required. However, a global navigation satellite system (GNSS) doesn't work under the sea because radio wave, which is a positioning signal from the satellite, reflects at the sea

surface and absorbs in the sea. Usually, inertial mass systems (IMS) or ultrasonic positioning systems like SSBL (super short baseline) are often employed. Nonetheless, SSBL takes high cost to set the ultrasonic transducer system and IMS requires a ring laser gyroscope of which cost is high and size is also large.

In this presentation, the recent free fall type UOS, "Edokko No.1" which recorded the world's first 3D video movie of the sea bottom at 7800m of the depth is introduced. And also the feasibility of the underwater positioning is studied using a micro electro mechanical system (MEMS) for an inertia measurement unit (IMU) inside the developed camera system. However, high accurate positioning is not expected completely if the cost and the size of IMS sensor is limited. Therefore, most of IMS systems has another sensor to compensate the error, for example, a Doppler Velocity Logger (DVL) [5-6] or an Acoustic Doppler Current Profiler (ADCP)[7]. The authors discuss feasibility of the employment of the IMU systems in order to determine the positioning of the free fall type UOS.

2. Free-fall type UOS

Figure1 shows a schematic explanation of the operation of the free-fall type UOS which has no propulsion system like a propeller or a thruster. Therefore, the observation system sinks to the sea bed due to the weight after the system is felt down from a ship or a boat. For a while, the system measures the data, records the video or collect the soil at the sea bed. When the system rise to the sea surface, the weight is released from the observation system due to the electrolytic corrosion.

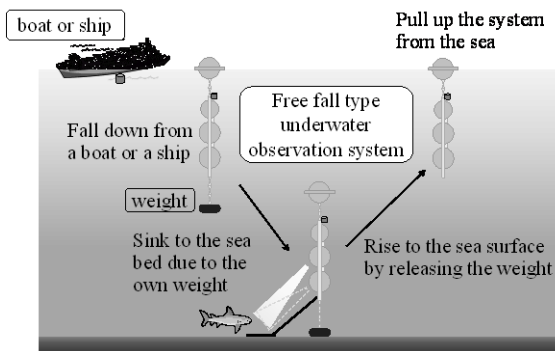


Figure 1: The operation of the free-fall type UOS.

Generally, a glass sphere is employed to contain the observation apparatus for example a camera, a light and so on. The cost of the glass sphere is too low in the comparison with the material which consists of UOV or ROV. However, the strength of the glass is enough to bear 800Mpa of hydrostatic pressure at 7800m of the depth. Recently, the project "Edokko No.1" is founded in Japan in order to realize a simple, a portable and a low-cost deep sea exploration system using glass spheres. The project members are the CEOs of the small company in Tokyo downtown districts, universities, a research institute, a bank and volunteers of an electric company. The authors are also members of the Edokko No.1 project. The free-fall deep sea exploration video system, we call "Edokko No.1", recorded 3D video of deep sea creatures at 7800m of the depth, successfully. Figure 2 shows the picture of the Edokko No.1. After the success of the Edokko No.1 project, the authors have developed the deep sea exploration system in order to make the observation system, "the Edokko No.1" easy to operate. At the next section, the new observation system we called "Gyogyotto camera" is explained.[7-8]

3. Development of GYOGYOTTO CAMERA

3.1 Constitution of the Gyogyotto camera

Figure 3 shows configuration of Gyogyotto Camera. And Table1 indicates the specification of the camera. The developed camera consists of two parts. The lower part is a glass sphere and the upper is a PVC cylindrical case. The glass sphere contains batteries, a power supply board, a Wi-Fi router, four cameras (SNC-CX600, SONY), and an IMS sensor built-in smartphone (ZenFone2, ASUSTek computer inc.). An angle of view of cameras is 120 degree in the air. In the water, the angle of view becomes narrower due to curvature of glass sphere and difference of index between glass and water. Then, the original camera lens changes into wider lens. And also, the four network camera are employed in order to record the entire circumferential image. The PVC cylindrical case contains batteries, a power supply board, a Wi-Fi router, a LED control board. Figure 4 describes the operation of the Gyogyotto camera. The camera connects with a buoy or a ship floating on the sea through a LAN or an optical fiber cable in order to deliver real time image of sea bed. The LED brightness controller using ethernet-serial converter is mounted on the power supply board. Due to the difficulty of the process against the glass, there is only one hole for depressurization on the glass sphere. For the glass sphere, the upper hemisphere put together and the lower hemisphere covered the peripheral of the contact surface by butyl rubber and plastic tape in order to prevent from sinking. The LAN cable is put through the hole on the PVC cylindrical case.

Figure 5 shows the diagram for delivering path of movie and data. The four network cameras, that is SNC-CX600, are connected to the Wi-Fi router1 in the glass sphere. As mentioned above, the Wi-Fi router2 in the PVC cylindrical case is connected to the Wi-Fi router3 on the buoy in the sea surface. The connection between the

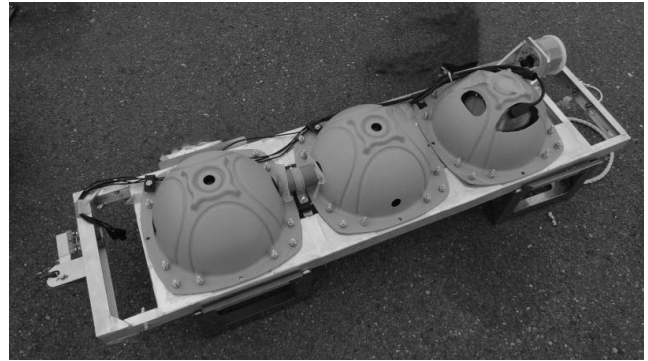


Figure 2: The whole picture of the Edokko No.1.

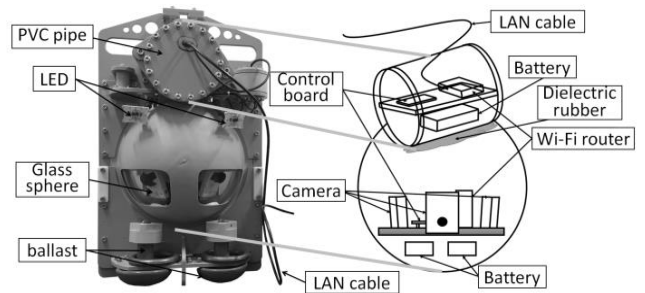


Figure 3: The configuration of Gyogyotto Camera.

Table 1: The specification of Gyogyotto Camera.

Size	
H × W × D [mm]	813 × 470 × 354
Weight [kg]	About 35
Drive time [hour]	About 4.4
Water depth[m]	About 300

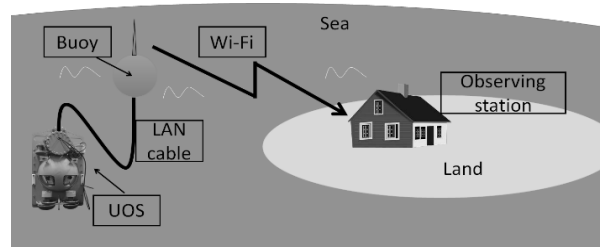


Figure 4: Schematic explanation of the operation of the Gyogyotto camera and the video delivery path.

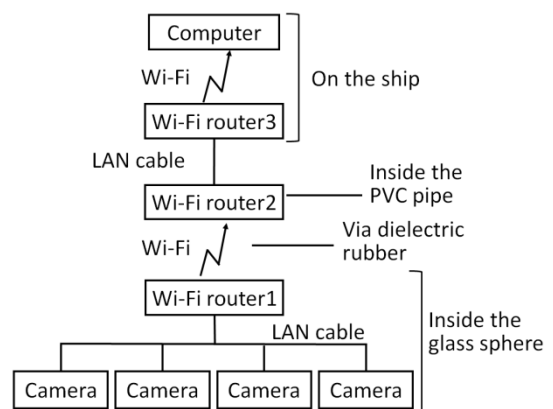


Figure 5: Diagram for delivering path of movie and data.



Fig.6 entire circumferential underwater image recorded by Gyogyotto Camera.

Wi-Fi router1 and the Wi-Fi router2 is also achieved by Wi-Fi in order to reduce the number of the process on the glass sphere and the PVC cylindrical case. As the dissipation of Wi-Fi signal becomes large, Wi-Fi is not available directly under the sea. Then, the Wi-Fi communication via dielectric rubber, which is described in [9], is employed. The dielectric rubber is installed into the contact part between the glass sphere and the PVC cylindrical case.

3.2 Underwater entire circumferential image

We conducted an experiment operation of the Gyogyotto camera at Shin-Enoshima aquarium [10]. A synthetic image from captured movie is shown in Fig.6. The images are obtained from each movie recorded by each internal camera and are stitched manually. As shown in Fig.6, the clear entire circumferential underwater image is obtained. The circumferential entire movie should help in the geomorphic investigation and creature research under the sea. For our future plan, the synthetic process is operated automatically.

4. Position estimation of the UOS

Using MEMS IMS sensor, that is accelerometer and gyroscope, built-in Zenfone2, the position of UOS is estimated. As well-known, an IMS unit produces a random walk signal. Generally, the precision of IMS sensor is characterized by the random walk signal [11]. Figure7 shows the position error by calculate the integration of the IMS sensor signal built-in the UOS when the UOS is stationary. Even if the UOS doesn't move at all, estimating position proceeds up to 800m dramatically due to the random walk signal.

The position estimation is also tried under the water. The pool as shown in Fig.8 is employed at Tokyo university of Marine Science and Technology. Figure 9 shows the estimation results. The true trajectory of the UOS measured by the laser distance measurers (DISTOTM plus, Leica Geosystems) is also indicated. On the experimentation, the UOS progress linearly by the crane in 8.1m of distance along the X direction. It took 14 seconds to progress at 0.35m/s of speed. In position estimation of the UOS, the difference between the estimation and the measurement is severe. In Fig.9, the simulation trajectory in the consideration of the Allan variance is also indicated. According the simulation results, it is confirmed that the Allan variance causes the severe difference between the estimation and the measurement. In order to reduce the error due to the

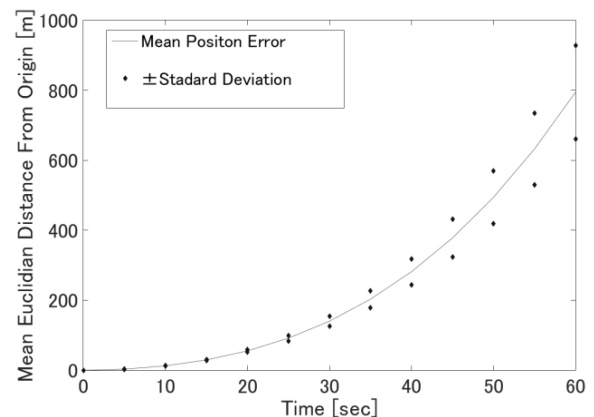


Figure 7: The UOS's stationary position error.

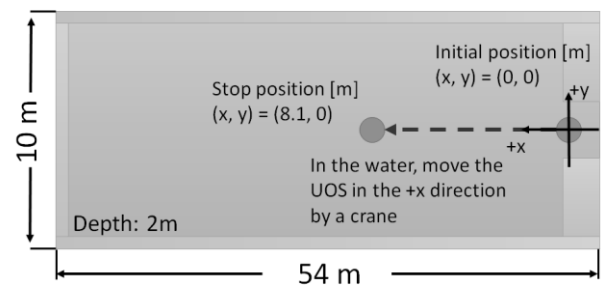


Figure 8: The setup for the position estimation experiment.

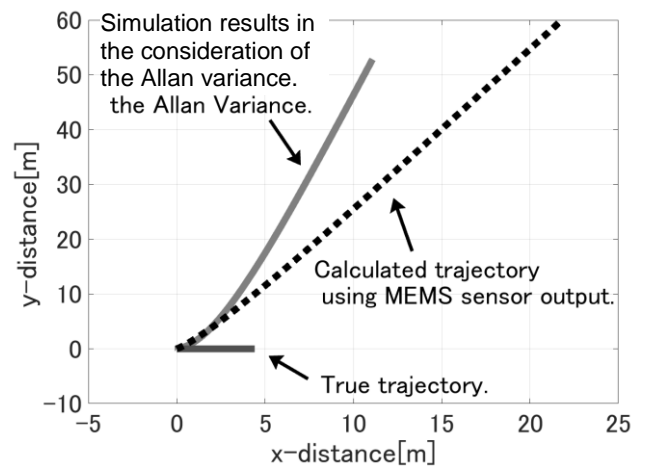


Figure 9: The UOS's trajectory under the water.

Allan variance, the filter process is generally applied. The most simple filter process is subtraction of the bias error obtained by the Allan variance from the sensor output. Figure 10 shows the results filtered by the bias error subtraction. It is confirmed to reduce the difference. However, the difference is still several meters in 14 seconds. And, hence it is difficult that only MEMS IMU sensor gives the accurate position in the condition of low velocity speed. To increase the accuracy the position estimation, auxiliary sensors like a DVL [5,13] or an ADCP [6,12] is indispensable.

5. Summary

In this presentation, the recent free-fall type UOS project is introduced. And also the developed free-fall type UOS that are able to monitor and record entire circumferential underwater image in real time is described. The position estimation under the sea using MEMS IMU sensors is also tried. A DVL or an ADCP is indispensable in order to estimate the accurate position. The authors expect to develop DVL or ADCP which can be operated under high hydro-static pressure.

Acknowledgement

This work is developed cooperatively by Mr.Sakata, the CEO of Mukojima-tech Co., Ltd., Mr.Itoi, the CEO of I2I giken Co., Ltd., Mr.Kawakami, Fukan Lab., Mr.Kurihara and Mr.Muramoto, the members of Gyogyotto camera project. We all appreciate for Mr.Miyagawa, technical officer of Tokyo university of Marine Science and Technology and the staff of Shin-Enoshima aquarium. They supported our experiment. The glass sphere is provided by Okamoto Glass Co., Ltd and the plastic cover is provided by Vacuum mold Co., Ltd. We also appreciate for them.

This work was supported by JSPS KAKENHI Grant Number JP16730101.

References

- [1] <http://www.jamstec.go.jp/sip/overview1.html> [in Japanese]
- [2] <https://en.wikipedia.org/wiki/Edokko-1>
- [3] Y. Koike, Environmental measurement of Deep Sea using Internal Physical Data of a Glass Sphere for Free-Fall Exploration System (in Japanese), IEICE Technical Report, ASN, Ambient intelligence and Sensor Networks, 114(166), 195-200, 2014
- [4] J.H.Li et al, Development of P-SURO 2 Hybrid AUV and its Experimental Study, Conference Publications: OCEANS-Bergen, MTS/IEEE, 2013
- [5] http://rdinstruments.com/product_dashboard/dvl
- [6] http://www.rdinstruments.com/product_dashboard/adcp
- [7] T.Matsumoto et al, A study of position estimation method for a free fall type underwater explorer system, IEICE Technical Report, ASN2015-105, 117-122 (2016) [in Japanese]
- [8] K.Noguchi et al, Feasibility study of positioning for free-fall type underwater observatory system using dynamic image analysis, Proc. of SEATUC, (2016)
- [9] M. Ozawa and E. Shimizu, Development of UHF Band Communication Method under the sea, Proc. Of 2012 International Offshore and Polar Engineering Conference, 472-478, 2012

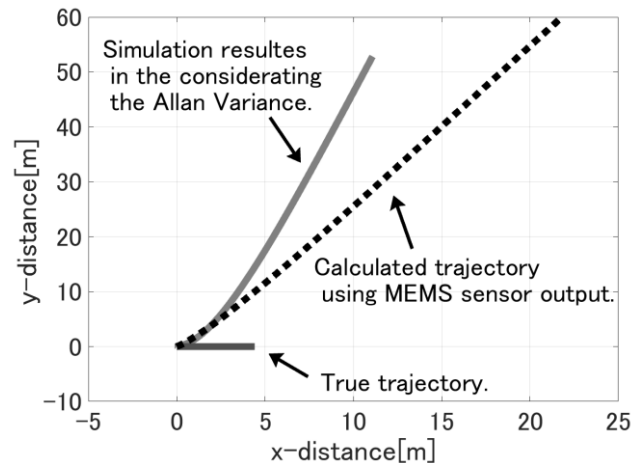


Figure 10: The UOS's trajectory under the water.

- [10] <http://www.enosui.com/en/>
- [11] Oliver J. Woodman, An introduction to inertial navigation, Technical Report, Number 696, University of Cambridge Computer Laboratory, 2007
- [12] P.M.Lee et al, Simulation of an inertial acoustic navigation system with range aiding for an autonomous underwater vehicle, IEEE Ocean Eng., 32(2), 327-344 (2007)
- [13] H.Chiba et al, Oceanographic Observations Using Shipboard CTD and ADCP In and Around Toyama Bay, Proc. of IS-GNSS 2015, 588-594 (2016)

3D interpolation in a velocity field in sewers

Sebastian Cedillo¹, Mathieu Lepot¹, Stéphane Fischer² and François H.L.R. Clemens^{1,3}

¹ TU Delft, Faculty of Civil Engineering and Geosciences, Watermanagement Department, Stevinweg 1 (Building 23), 2628 CN Delft, The Netherlands

² Ubertone, 11 rue de l'Académie, 67000 Strasbourg, France

³ Deltares, PO Box 177, 2600 MH Delft, The Netherlands

In order to propose a new sewer inspection method, a velocity/turbidity profiler (Ubertone, UB Flow) has been tested in a laboratory. A 50 m glass flume has been adapted with several lateral connections (with a range of diameter, angle, intrusions, cracks), supplied by a 1 m³ tank. Placed just below the free surface on a rotating (to scan the wet section) and translating (along the main axis of the flume) structure, velocity profiles have been recorded and accurately positioned along the reach (with data from three laser distance meters and a 3 Mpix camera): a 3D cloud of raw velocities is created. After raw data pretreatment (deduction of translation velocity, Nyquist jumps correction, low quality data removal *i.e.* with low SNR threshold and vector projection corrections), five step-interpolation (adapted from [1]) methods have been implemented and tested: *i*) data filtering, *ii*) transformation to flume coordinates velocities, *iii*) isotropic gridding, *iv*) anisotropic gridding and *v*) continuity correction. These methods aim to produce contour lines and the quantification of different streamlines in the reach.

Keywords: 3D interpolation, Lateral connection, Data treatment

1. Introduction

Sewer rehabilitation decisions are mainly taken based on data obtained from CCTV inspection, it has been shown however [1] that information from this source is subjective and not very accurate. Therefore there is a need for techniques that result in objective information on the status and/or functionality of sewer. An important defect in sewers is leakage, be it infiltration, be it exfiltration or misconnection. In this article results from lab-experiments are presented, using a velocity/turbidity profiler for detecting anomalies in the flow field due to infiltrating flows.

In order to develop a new inspection technique, the FOULC project (Fast Over-scanning of Underground and Linear Constructions) aims at the development of an amphibious drone to inspect sewers without creating disruption in the sewage service. Several sensors will be set up on this platform: laser scanning devices, infrared camera, sonar and a velocity profiler.

The velocity/turbidity profiler (Ubertone, UB Flow [2]) might be a part of the monitoring platform to construct a 3D velocity field of the inspected reach (identification of the streamlines, quantification of the lateral connections). Such a use of this probe is quite challenging: positioning, control of the moving and angular velocities, construction of the 3D velocity vector field, *etc.* This sensor has been set up on a rotating (around the horizontal axis in order to scan the full wet section) laboratory facility and tested: the present paper describes the experiments, the methods used to convert raw data to a 3D velocity distribution along a flume.

2. Materials, laboratory experiments and method

2.1 Materials

Based on a system previously designed [4], built and tested for a laser profiler, the profiler has been fixed on a rotating platform and its position and spatial orientation (x,y,z, shift, pitch, yaw and roll angles) is calculated based on measurements from three laser distance meters (Dimetix, FLS-C10) and a 3 MPix camera (Allied Vision Technology, Manta GC282C).



Figure 1: Rotation structure (up), the flume (down left) and a window with lateral connection (down right) along the flume.

This system (Fig. 1, up) has been installed on a moving platform, guided along a hydraulic flume of 50 m long (Fig. lateral connections (Fig 1, down right). The exact position (distance from the reference point, pitch, yaw and roll angles) of the profiler can be derived from the three positions of the laser dots (recorded by the camera) and the three distances (from the laser distance meters) [4].

UB-Flow is a 2D velocity vector profiler (UVP) equipped with two transducers. The velocity estimation is based on the Doppler coherent method that allows high resolution measurements. The device switches alternatively from one transducer to the other. At each switch, the instrument provides a set of space-time matrix including velocity, SNR (Signal Noise Ratio) and echo data measured on the given transducer.

2.2 Laboratory experiments

Lateral connections were supplied with tap water (cold or warm) coming from a 1 m³ tank, located just above the flume. The flow was manually controlled with a valve. The lateral connection flow was derived from the water levels (before and after the experiment), the section of the tank and the duration of the constant opening of the valve. The flow in the flume was controlled by the supply frequency of the main pump and recorded by a 600 mm diameter flow meter. Two discharges were tested in the flume: 120 and 520 l/s. In total 41 different experiments were carried out with different flume discharges, lateral connection types and discharges. Measurement have been done under stationary conditions.

2.3 Methods for data analysis

The method is divided in two parts.

The first part is devoted to the construction of a 3D velocity field from the UB Flow data and its position. With the recorded position and rotation of the profiler [3], its characteristics [2] (beam angles) and its adjustments (cell positions along the beam), measured velocities along the beams (V_1 and V_3) (coordinates of measured volume) can be placed in a 3D field. The cloud of raw data is created with velocities measured by both cells.

This second part is mainly based on the five steps method proposed by [4]: 1) data filtering to remove artefacts in raw data, 2) transformation of the velocities into the flume coordinates, 3) isotropic gridding, 4) anisotropic gridding and 5) continuity correction. Only the step 1 (data filtering) and step 5 (continuity correction) differ slightly from the one proposed by [4] (moving average). The step 2 is new, due to the specifications of the UB Flow.

Initially done with a moving average, the values of each profile have been corrected for Nyquist jumps and noisy data (low SNR) have been removed.

The SNR threshold was fixed as 0.25 and the Nyquist correction was done for the velocities outside of the range (defined by the frequencies) with Eq. 1 [3].

$$V_{k,CORR} = V_k - \frac{c \times PRF}{2 \times f_{0,k}} \quad (1)$$

1, down left), specially prepared (windows with windows including lateral

where V_k ($V_{k,CORR}$) is the velocity in m/s (corrected) for the transducer k (1 or 3), c is the speed of sound in water (1480 m/s), $f_{0,k}$ is the emission frequency for a specific transducer k (in Hz) and PRF (in Hz) is the Pulse Repetition Frequency.

The step 2 consists to the transformation (V_1, V_3) to (V_z, V_y). For this step, a 3D grid is created: measured V_1 and V_3 are calculated by the means of the measurement contained in a cell. Empty cells are fill in with the nearest neighbor interpolation method. A regular grid of $V_{1,INTER}$ and $V_{3,INTER}$ is created. V_z and V_y are calculated with equations 2 [3].

$$\begin{cases} V_z = 1.873 \times V_{1,INTER} - 1.73 \times V_{3,INTER} \\ V_y = -0.23 \times V_{1,INTER} - 0.7975 \times V_{3,INTER} \end{cases} \quad (2)$$

Those velocities (given for the coordinated system attached to the rotating UB Flow) are then converted to velocities in the flume coordinate system (V_x, V_y and V_z).

The continuity correction (Step 4) is done trough an iterative process solving two equations (Eqs. 3 and 4)

$$\nabla^2 P = \rho \frac{\nabla U}{\Delta t} \quad (3)$$

$$U_{CORR} = U - \frac{\Delta t}{\rho} \nabla P \quad (4)$$

where P is the 3D pressure field (in Pa), ρ is the water density (in kg/m³), U in the 3D velocity field (in m/s), Δt is the time step (in s), U_{CORR} is the corrected 3D velocity field (in m/s) and ∇ is the Nabla operator.

The equation system was solved with a finite difference method [5], using the scheme proposed by [6] and taking into account the Neumann boundary conditions [7]: equations (3) and (4) become (5) and (6) in a 1D scheme.

$$\frac{P^{i+2} - 2P^i + P^{i-2}}{4 \times \Delta x^2} = \frac{\rho}{\Delta t} \times \frac{U^{i+1/2} - U^{i-1/2}}{\Delta x} \quad (5)$$

$$U_{CORR,i} = U_i - \frac{\Delta t}{\rho} \times \frac{P_{i+1} - P_{i-1}}{2 \Delta x} \quad (6)$$

3. Results and discussion

3.1 Construction of the 3D cloud

Figure 2 presents a 3D cloud of the raw velocities recorded in the flume.

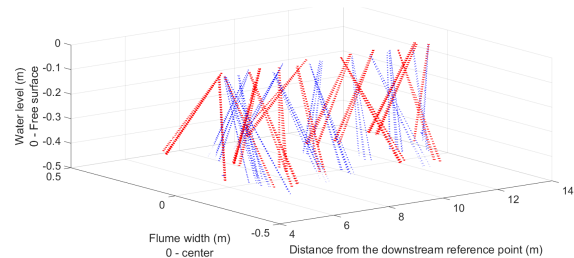


Figure 2: 3D cloud of the measurement cells (transducer 1 in blue, transducer 3 in red – both continuously moving along the virtual crest - top of each beams).

Figure 3 shows the effect of the switch [3] from transducer 1 (blue) to transducer 3 (red) during the measurement

along the flume. The flow, roughly estimated by integrating basically interpolated velocity over the wet section, seems to be non-constant: from 70 to 150 l/s instead of 120 l/s: average measured flow (125 l/s).

The fluctuations in the raw data don't seem to come from the rotation of the UB Flow or the measurement sequence on the transducer 1 and the transducer 3.

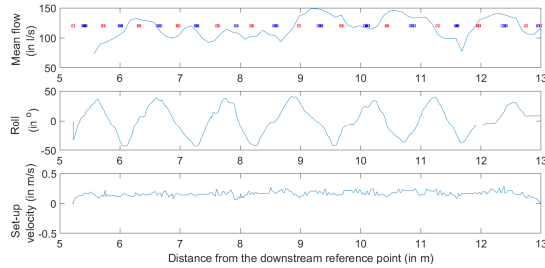


Figure 3: Fluctuations in the raw velocities (top) along the flume. Velocities (m/s) with transducer 1 (blue) and transducer 3 (red). Roll angle (middle) and set-up translation velocity (bottom).

3.2 Interpolation

Step 1. Correction of V_1 and V_3 profiles with Nyquist (if needed) and removal of low SNR value (Fig. 4).

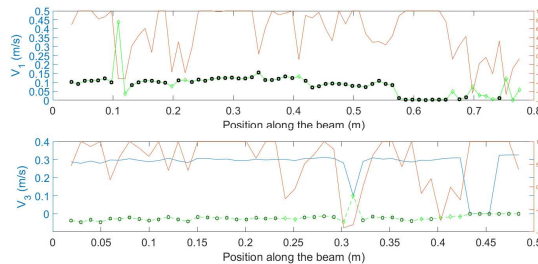


Figure 4: Raw and corrected profiles (V_1 - up, V_3 - down).

Step 2. Creation of the interpolated cloud of V (Fig. 5)_z (main axis), V_y (along the width of the flume) and V_x (along the vertical).

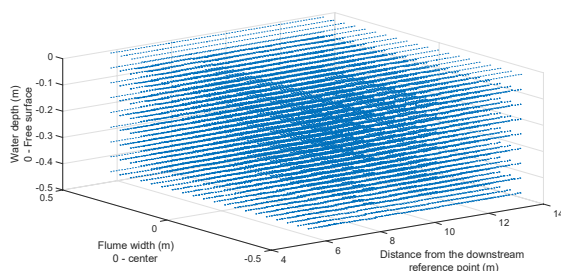


Figure 5: Quiver of velocities according to the flume coordinate system.

Step 3. The isotropic (i.e. rectangular) gridding proposed by [4] was not changed. The Figure 6-left illustrates the isotropic gridding.

Step 4. The anisotropic gridding step was not changed (Fig. 6 - right).

Step 5. The implementation of the 3D method proposed by

[4] is done in three steps, in order to check step by step the CFD code: 1D, 2D and 3D.

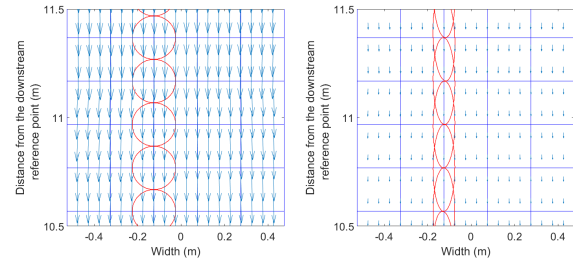


Figure 6: Gridding: isotropic (left), anisotropic (right).

For a discharge in the flume of 120 l/s, the average velocity in the wet section is supposed to be equal to 0.26 m/s (Fig. 7).

The method (in 1D) is converging (Fig. 6 bottom) but with some small instabilities (Fig.6 top).

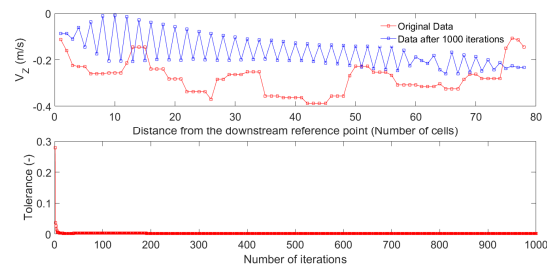


Figure 7: Effect of velocity artifacts on the convergence of the method. Top: existing data (red) and interpolated after 1000 iterations (blue). Bottom: tolerance.

The extension to the 2D methods shows the same results: the system is converging but with some punctual instabilities (Fig. 8).

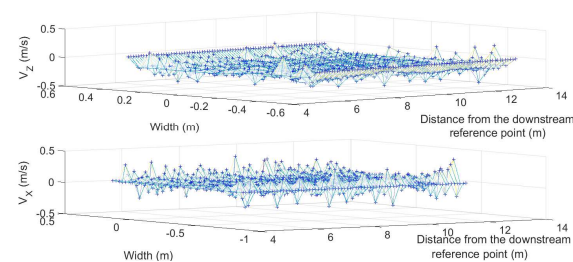


Figure 8: Result of 2D interpolation method. Top: V_z velocities. Bottom: V_x velocities.

The method will be extended in 3D in order to validate (or not) the results the preliminary conclusions and applied on data issue of CFD simulation (Coming from [8]).

4. Conclusions and perspectives

The initial goal (i.e. the reconstruction of 3D velocity fields in a sewer with a UB Flow sensor) has been realized, despite some difficulties: adjustment of the profiler (emitting frequency), no simultaneous measurement of V_1 and V_3 and the coding complexity of the fifth step.

The probe seems to deliver velocity data that are consistent with the expected average velocity in the flume. The figure

9 shows a relative small noise in the data and highlights the rotation of the UB Flow (red vertical wave on the right part of the top figure).

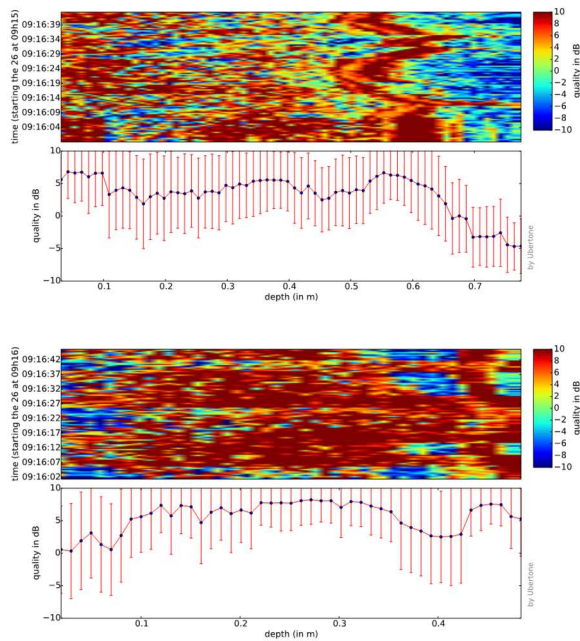


Figure 9: SNR ratios of the recorded data for the Transducer 1 (top) and the Transducer 3 (down).

Some weaknesses of the proposed method need to be highlighted. The first one is the construction of the 3D velocity clouds. The probe doesn't measure at the mean time on both beams: V_1 and V_3 need to be interpolation of the same grid to derive V_Z and V_Y . Secondly, there are few gaps in the data due to the switch between the beams: the data density (according to [4]) is around 1, instead of 3 as advised by the authors.

The UB-Flow, in its actual setting, may not be adapted for this application. In order to achieve the initial goal, improvements of the current settings have to be done in order to obtain simultaneous and continuous measurements over the two beams.

References

- [1] Dirksen, J. et al.: The consistency of visual sewer inspection data, *Structure and Infrastructure Engineering* 9(3) (2011), 214-28.
- [2] Ubertone, UB Flow user manual.
- [3] Clemens F. H. L. R., et al.: Uncertainties associated with laser profiling of concrete sewer pipes for the quantification of the interior geometry, *Structure and Infrastructure Engineering*, 11(9) (2014), 1-22.
- [4] Tsubaki R., et al.: New 3-D flow interpolation method on moving ADCP data, *Water Resources Research*, 48(5) (2012), 15p.
- [5] Ferziger, J. H., et al.: *Computational methods for fluid dynamics*. Springer Science & Business Media (2012).
- [6] Armfield, S. W., & Street, R. Fractional step methods for the Navier-Stokes equations on non-staggered grids. *ANZIAM Journal* 42 (2000), 134-156.
- [7] Gresho, P. M., et al.: On pressure boundary conditions for the

incompressible Navier - Stokes equations, *International Journal for Numerical Methods in Fluids* 7(10) (1987), 1111-1145.

[8] Sun, S. et al.: Artificial neural network modeling in simulation of complex flow at the open channel junctions based on the large data sets, *Environmental Modeling & Software* 62 (2014), 178-187.

Development of focused air-coupled ultrasound velocity profiler for steam jet flow velocity measurement

Keisuke Tsukada¹ and Hiroshige Kikura²

¹ Graduate School of Science and Engineering, Tokyo Institute of Technology, 2-12-1 Ookayama, Tokyo 152-8550, Japan

² Laboratory for Advanced Nuclear Energy, Tokyo Institute of Technology, 2-12-1 Ookayama, Tokyo 152-8550, Japan

The novel air-coupled ultrasonic velocity profiler for steam flow measurement is developed for steam jet flow velocity measurement. The steam jet is produced from the electrical boiler, and the steam pressure is 0.1 MPa G, and the average flow velocities of steam were from 190 to 380 mm/s. The steam flow velocity was measured by the developed system and the vortex flowmeter. The flow velocity measured by the developed system is comparable to the result obtained by the vortex flowmeter. The probability of the steam flow measurement by air-coupled ultrasound is revealed.

Keywords: Steam, Wetness, Jet, Ultrasonic beam focusing, Droplet.

1. Introduction

Steam is widely used in industries such as energy transportation media in thermal power plants and nuclear power plants for the electric generation, but also used in food processing and distillation process in chemical plants. The steam flowrate measurement is essential for industrial facilities because it enables us to visualize the consumption, leakage and stagnation of steam. The steam visualization can save energy and improve the operation efficiency of the plant as well. In small processing plants, the steam is under low pressurized and steam wetness is high. Conventional flowmeter such as the orifice flowmeter and the vortex flowmeter have difficulties in applying in the high wetness condition. Additionally, the invasive flowmeters cause pressure drop that is the loss of energy. Thus, the clamp-on flowmeter was developed because of its strong advantage on such points. Clamp-on flowmeter only needs to be attached on the pipe wall for the flow velocity measurement with nondestructive set-up process [1]. The clamp-on ultrasonic flowmeter based on the tuft method was developed in our group [2]. However, the tuft method is not applicable in high wetness condition, because the ultrasound is attenuated by the condensed droplets in the steam as shown in Fig. 1. This phenomenon disturbs the ultrasound reaching to the sensor. By contrast, the ultrasonic velocity profiler (UVP) can measure the flow velocity by the echo signal from the reflector. The droplets in steam are employed as reflector and the velocity profile of steam can be measured by ultrasound in high wetness condition. However, the acoustic attenuation in steam is much higher than that in water and the sound velocity in steam is lower than that in water. Thus, the air-coupled ultrasonic technique used in nondestructive evaluation field is one of the solutions to overcome this problem [3], [4]. The low frequency air-coupled ultrasound is propagated in the air and then enters into the test body. Since the air-coupled ultrasound has an efficient transmission in the steam, it can be applied at high wetness environment. Thus, the developed measurement system is evaluated by

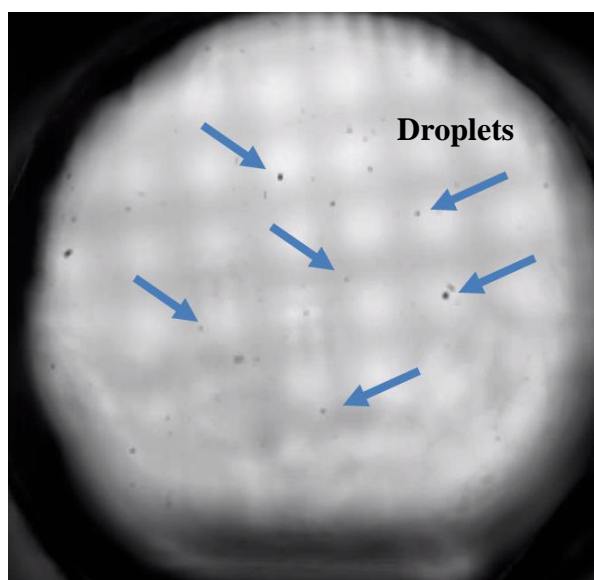


Figure 1: The condensed droplets visualized from the optical window in JIS G 3442, 100 A steam pipe pressurized at 0.3 MPaG.

measuring the flow velocity of the steam jet in the condition of high wetness.

2. UVP system for steam jet measurement

The steam has much lower acoustic impedance than that of water and other liquids. The size of droplets in steam jet is $100\ \mu\text{m} \sim 5\ \text{mm}$ and the droplets are formed when the wave length of ultrasonic is less than 1 mm. The droplets develop from the outlet. The sound velocity in steam is approximately 473 m/s in atmospheric pressure. Therefore, the ultrasonic frequency is higher than 400 kHz for the wave length which is smaller than droplets. However, since high frequency ultrasound causes attenuation during traveling in the air, the frequency of 400 kHz ultrasound is applied for the steam jet flow measurement in this study. Although 400 kHz is still low

frequency compared to the size of droplets, the high intensity ultrasonic beam is required to detect the echo signal from droplets. In order to detect the echo signal from the droplets in steam, the focused ultrasonic beam is employed [5]. The focused ultrasonic beam has high acoustic pressure in the focusing point and high pressure area is widened along the traveling direction of sound.

2.1 Focusing sensor

The air-coupled ultrasonic sensor has a matching layer on the surface. Acoustic impedance of the matching layer is about 1.5 M Rayls. The reflection of ultrasonic waves is reduced at the interface between sensor and air, thus, more ultrasonic waves can be transmitted. As shown in Fig. 2, since the sensor has a concave surface to focus ultrasonic beam, the focused ultrasonic beam has high intensity in narrow beam width that enables to detect droplets in steam jet flow. The conventional planar sensor (14 × 20 mm) is shown in Fig. 2 (A). The cross section of the ultrasonic beam of focusing sensor is enlarged to increase the amplitude and SNR of receiving signals.

In order to evaluate the developed focusing sensor, the sound pressure fields of the focusing sensor and the

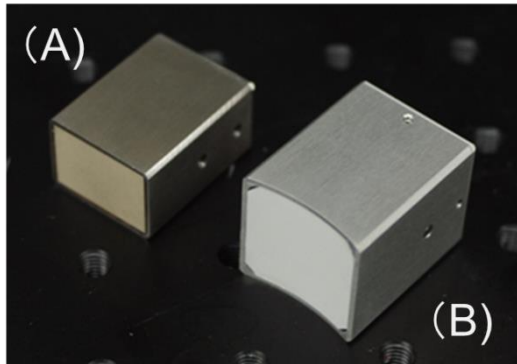
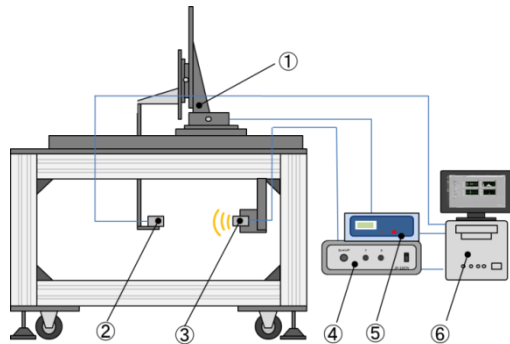
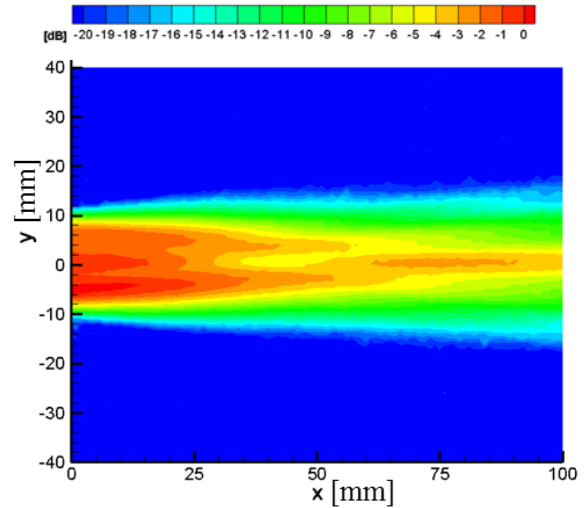


Figure 2: Air-coupled ultrasonic sensors. The conventional planar air-coupled ultrasonic sensor is shown in (A). The developed focusing sensor is shown in (B).

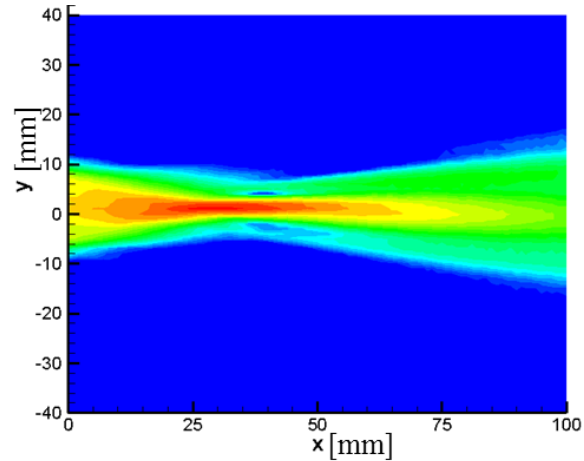


- | | |
|------------------------|----------------------|
| 1. Three axial stage | 2. Receiving sensor |
| 3. Transmitting sensor | 4. Pulsar/Receiver |
| 5. Stage controller | 6. PC with digitizer |

Figure 3: The sound field measurement apparatus. The ultrasonic sensor for evaluation is fixed and emits the ultrasound. Moving the receiving by three axial stage, sensor the sound pressure was detected.



(a) Sound pressure field of the planar sensor



(b) Sound pressure field of the focusing sensor

Figure 4: The measured sound fields by the sound field measurement apparatus. The sound pressure field of conventional planar sensor is shown in (a). The sound pressure field of developed focusing sensor is shown in (b)

planar sensor were measured. The sound field measurement experiment apparatus is shown in Fig. 3. The apparatus consists of a three axial stage, the receiving sensor, the transmitting sensor, pulsar/receiver, the stage controller and PC with digitizer. The ultrasound is transmitted by the transmitting sensor and received by the receiving sensor that is controlled by the pulsar/receiver. Receiving signals are sent to PC with digitizer and recorded. The measurement position is moved together with the three axes stage controlled by the stage controller. The measurement geometry is 100 × 80 mm in two dimension and 1 mm mesh for each direction. The sound pressure is peak to peak of received signals. The receiving sensor (Japan Probe, 0.4k20 × 14RX) has no damping material to optimize for receiving. The measured sound pressure fields are shown in Fig. 4. The sound field in the planar sensor is 22 mm in width and the beam width is slightly enlarged by propagation in Fig. 4 (a).

The sound field of the focusing sensor is focused on approximate 40 mm point and it has high amplitude compared to the result of the planar sensor at the same point in Fig. 4 (b). The high intensity of ultrasonic beam is located in the focusing point, besides the ultrasonic beam is sharpened to the travelling direction. The higher intensity is located from 25 mm to 60 mm and the beam width is roughly 10 mm. For the steam jet measurement, the ultrasonic focusing sensor was setup to detect the echo signal from droplets in the focusing area.

3. Experiment set up

The steam jet flow measurement by developed system is performed. The experiment apparatus is shown in Fig. 5. The pressurized steam is supplied from electrical boiler (MIURA Co, Ltd, ME-50). The pressure limitation was 0.59 MPa, the thermal output was 47.6 kW and the evaporation rate is 76 kg/h. The generated steam is stored in steam header to stabilize the pressure, and then the steam flows through the steam separator DC3S-10 (TLV Co., Ltd.) to remove drain. The steam flow is split into the separator and the bypath which is employed for control the steam flow rate. The steam flowing into bypath is condensed in the heat exchanger (SR-B-1.5, TLV Co., Ltd.). The main steel pipe of the test section is JIS G 3442, 15A SGP white pipe, of which outer diameter was 21.7 mm and the wall thickness was 2.8 mm. Before the test section around 0.5 m of inlet zone which is equal to 20 times of the inner diameter of pipe was prepared ahead of the test section. Vortex flow meter EF73 (TLV Co., Ltd.) was used as reference. The measurement error of the vortex flow meter was less than

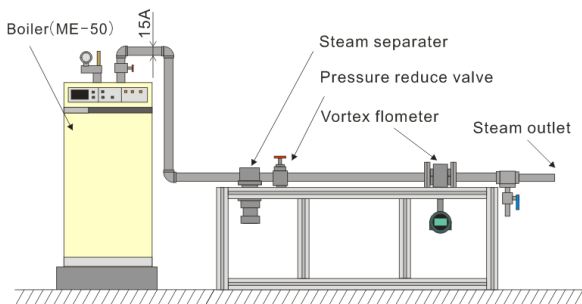


Figure 5: Experimental apparatus for the steam jet flow measurement.

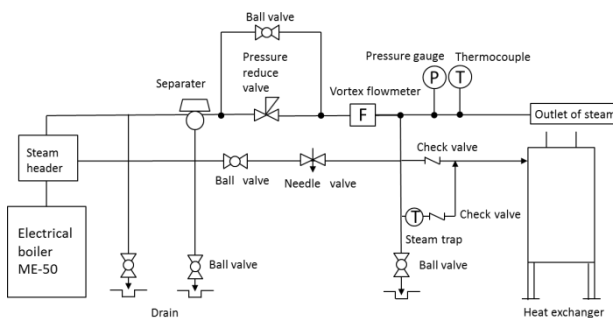


Figure 6: Schematic map of the steam line for the steam jet measurement.



Figure 7: The measurement system developed for the steam jet flow measurement.

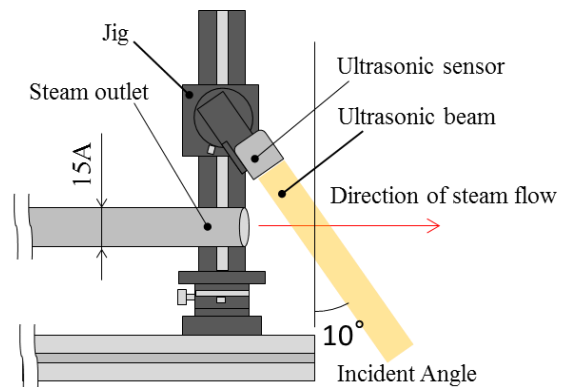
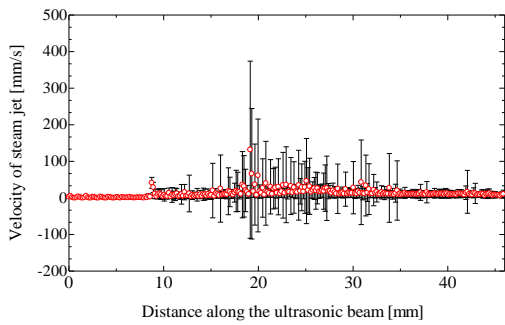


Figure 8: The location of the air-coupled ultrasonic sensor to the steam jet flow.

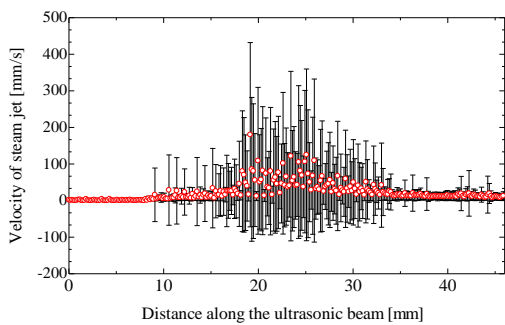
1 % in full scale. The steam pressure was observed by pressure sensor DPH-L113 (Panasonic Corp.). It was reduced to the initial pressure 0.1 MPa by pressure reduced valve DR20-6 (TLV Co., Ltd.). The temperature of steam was 120 °C and the room temperature was 24 °C. The steam pressure was kept to 0.1 MPaG and the steam flow velocity was controlled from 190 to 380 mm/s.

The measurement system is shown in Fig. 7. An Ext-amplifier is applied. Received signals at transducers are low signal-to-noise ratio. The amplifier in the receiver is influenced by noises from power supply circuit. Then, received signals are amplified outside of the receiver before noises generated. The noise filter is in the amplifier. The filter is band pass filter (BPF) that passes a certain band, and removes noise from signals. The ultrasonic sensor is controlled by the pulsar-receiver (JPR-10B, Japan Probe Co., Ltd.). Applied voltage, wave number, frequency, and pulse repetition frequency of the transmitting signal are 110V, 16 cycles, 390 kHz, 2 kHz respectively. The received signal is converted in 8-bit digitizer (NI PXI-5114) with 250 Ms/sec sampling rate. The velocity profile is calculated in personal computer.

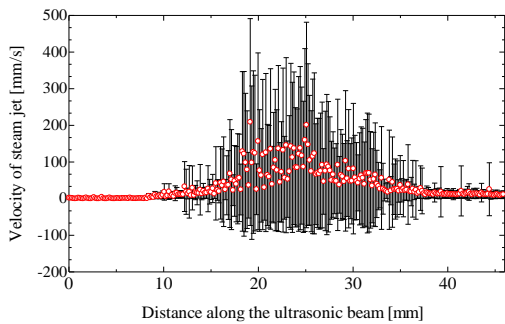
The schematic drawing of focusing sensor is shown in Fig. 8. The ultrasonic sensor is setup with 10 ° incident angle. The location of ultrasonic sensor is setup as the main steam jet which is located between 25 mm and 60 mm from the focusing sensor.



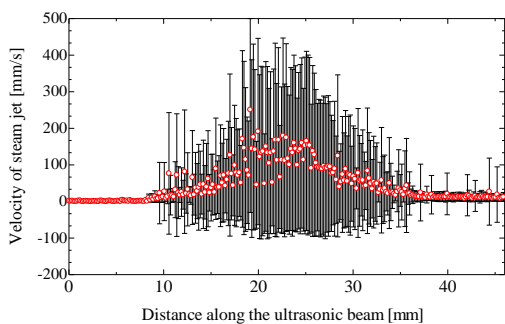
(a) Velocity profile when the average flow velocity measured by the vortex flowmeter was 190 mm/s



(b) Velocity profile when the average flow velocity measured by the vortex flowmeter was 250 mm/s



(c) Velocity profile when the average flow velocity measured by the vortex flowmeter was 330 mm/s



(d) Velocity profile when the average flow velocity measured by the vortex flowmeter was 380 mm/s

Figure 9: Velocity profile of the steam jet measured by air-coupled ultrasonic velocity profiler. The horizontal axis shows the distance from the sensor and vertical axis means the velocity. The plots show the velocity measured by developed system.

4. Result and discussion

The results of the velocity profile measured by developed focused ultrasonic steam flow velocity profiler were shown in Fig. 9. The averaged velocity with 10,000 profiles shows the flow velocity of the main steam jet from the outlet. The error bar denotes the standard deviation of each velocity. The main steam jet is observed from 10 mm to 35 mm according to the plots shown in Fig. 9 (b), (c) and (d). The size of main steam jet is developed as 25 mm from the outlet whose inner diameter is 15 mm. The velocities of steam jet increased with the flowrate, and the observed velocity boundary layers were around 15 mm and 30 mm. Moreover, vortices along the main steam jet are observed in high standard deviations around 18 mm and 25 mm. The sub flow flowing into the main steam jet is observed beyond the vortices. Hence, the focusing sensor has high intensity of ultrasonic beam in the main steam jet, and the echo signal from the droplets can be detected. However, the measurement error was occurred in the 20 mm because the ultrasonic beam is spread in 20 mm from the sensor surface. The beam spreading causes the larger spatial resolution.

5. Summary

The novel air-coupled ultrasonic velocity profiler for steam flow measurement is developed. An air-coupled ultrasonic sensor for steam flow measurement was developed. The air-coupled ultrasonic sensor has a matching layer to reduce the acoustic reflection between sensor and the air. In addition, it has a concave surface to focus ultrasonic beam. Since the focused ultrasonic beam has high intensity in narrow beam width, this enables us to detect droplets in steam by using it. For the demonstration of steam jet measurement, steam jet flow was measured by ultrasonic velocity profiler with the developed ultrasonic focusing sensor. The steam jet is produced from the electrical boiler, and the steam pressure is 0.1 MPa G. The steam flow rate was measured by the developed system and the vortex flowmeter. The flow velocity measured by the developed system is comparable to the result obtained by the vortex flowmeter. Thus, the capability of the steam flow measurement by air-coupled ultrasound is revealed.

References

- [1] R. C. Baker: Flow Measurement Handbook, Cambridge University Press, (2000), 312-356, 2000.
- [2] T. Kawaguchi, et al.: Development of the clamp-on ultrasound flow meter for steam in pipe, NUTOHS-10, (2014).
- [3] Bashford A.G: Air-coupled ultrasonic transducers for measurement of green-state ceramics at elevated temperatures, IEE Proceedings: Science, Measurement and Technology, Vol. 145, No. 5, (1998), 237-243.
- [4] L. C. Lynnworth: Ultrasonic Impedance Matching from Solids to Gases, IEEE Transactions on Sonics and Ultrasonics, Vol. su-12, No. 2 (1965), 37-48.
- [5] D.W. Schindel: Ultrasonic imaging of solid surfaces using a focussed air-coupled capacitance transducer, Ultrasonics, 35 (1998), 587-594.

Simulation of ultrasound signals for the study of velocity estimation techniques

Fabio Rizental Coutinho¹, Cesar Yutaka Ofuchi², Lucia Valeria Ramos de Arruda², Flavio Neves Jr² and Rigoberto Eleazar Melgarejo Morales³

¹ Department of Electronic Engineering, Federal University of Technology-Paraná (UTFPR) Campus Toledo-PR 85902-490 Brazil

² Graduate School of Electrical Engineering and Computer Science (CPGEI), Federal University of Technology- Paraná (UTFPR), Avenida 7 de Setembro 3165, Curitiba, Paraná, Brazil

³ Mechanical & Materials Engineering Postgraduate Program (PPGEM), Federal University of Technology- Paraná (UTFPR), Avenida 7 de Setembro 3165, Curitiba, Paraná, Brazil

In this work we demonstrate the use of simulation of ultrasound signals in the study of velocity estimation techniques. To simulate the ultrasound signals the software Field II running under the Matlab environment was used. A flat piston shaped transducer was defined to emit and receive the echoes from the reflectors. Three types of flow were simulated: turbulent, laminar and uniform velocity profile. The accuracy and limitation of the velocity profile simulated are discussed. The velocity estimation techniques used to verify the simulation were the autocorrelation and time shift methods. Effects of transducer apodization in the accuracy of the velocity profile were also evaluated.

Keywords: Simulation of ultrasound signals, ultrasound velocity estimation, velocity profile, ultrasound Doppler method

1. Introduction

Simulation of physical processes is a fundamental tool in all engineering fields. In fluid engineering, ultrasonic Doppler method for velocity profile measurement, UVP, has proved to be a valuable tool for flow study [1]. However, there are still plenty of signal processing techniques that can be studied to improve velocity estimation. Using experimental approach to test a new signal processing methodology is a complex task, because of noise and the various uncertainties related to the experimental apparatus. In this context, simulation of ultrasound flow signals can be a valuable tool because it is possible to realize an ideal experiment without noise, stationary echoes from pipe walls, transducer angle uncertainty, non-uniform particles distribution, etc. After testing a new technique in an idealized environment, it is possible to add one or more of these undesirable effects in the simulation and thus study its individual effects in the velocity profile measured. Field II is an ultrasound simulation program that has been used for several years in the medical area. Although developed for medical field, it has the potential to be also applied to fluid engineering. However, there are no reports of application of Field II in fluid mechanics. This work aims to analyze the feasibility of application of the Field II ultrasound simulation software for the study of fluid engineering. Accuracy of simulated velocity profile is analyzed through the use of an autocorrelation and a time shift estimator. Three types of flow were simulated: uniform, laminar and turbulent. The simulation of transducer apodization is also studied to show its effects in the velocity profile.

2. Ultrasound Simulation using Field II

Field II is a fast ultrasound simulation program that is based on the concept of spatial impulse response [2-4]. It uses the Huygen's principle to evaluate the impulse response as [5]:

$$h(\vec{r}_1, t) = \int_S \frac{\delta\left(t - \frac{|\vec{r}_1 - \vec{r}_2|}{c}\right)}{2\pi|\vec{r}_1 - \vec{r}_2|} dS \quad (1)$$

where $|\vec{r}_1 - \vec{r}_2|$ is the distance from the transducer at position \vec{r}_2 to the field point at \vec{r}_1 , $\delta(t)$ is the Dirac delta function, and c is the speed of sound. A large variety of transducers can be simulated, ranging from single element transducer to an array of transducers elements. This is accomplished by dividing the transducer aperture in smaller mathematical elements. In a real aperture, edges might vibrate less than the center (apodization, [6]), and this is simulated by specifying different weights for each mathematical element. Considering a pulse-echo technique, a medium with uniform density and uniform sound velocity, the voltage signal received will be [5]

$$v_r(\vec{r}_1, t) = v_{pe}(t) * f_m(\vec{r}_1) * h_{pe}(\vec{r}_1, t) \quad (1)$$

$$f_m(\vec{r}_1) = \frac{\Delta\rho(\vec{r}_1)}{\rho_0} - \frac{2\Delta c(\vec{r}_1)}{c},$$

where $v_{pe}(t)$ is the transducer excitation voltage convolved with both transducer electro-mechanical impulse response in transmit and receive, $f_m(\vec{r}_1)$ is due to scatterers that cause spatial variations in density $\Delta\rho(\vec{r}_1)$ and speed of sound $\Delta c(\vec{r}_1)$ and $h_{pe}(\vec{r}_1, t)$ is the convolution between the impulse response of the transmit and receiving aperture. The final signal for an ensemble of scatterers can be obtained as a linear sum of Eq.1 for each scatterer. Therefore, by defining the ultrasound velocity, transducer excitation voltage, transducer geometry and the position of a set of scatterers the

voltage trace for each ultrasound emission can be evaluated. Field II comprises of a set of C files that are called by Matlab m-functions. This structure makes it very flexible and easy to use.

3. Methodology

3.1 Transducer

Ultrasound transducers in Field II are treated as an aperture, i.e., only the active element should be defined. For this work, Field II was configured to use the same aperture to transmit and receive ultrasound pulses. Therefore it will simulate a pulse-echo technique. Transducer geometry used was a piston shaped aperture with 10 mm of active diameter. Aperture geometry was divided into 1.2 mm x 1.2 mm square mathematical elements (Fig. 1). With this size for the mathematical elements, Field will evaluate acoustic pressure accurately for points located 1 mm apart from the aperture. More about the rules for defining the size of the square elements can be found in [6]. Ultrasound central frequency (f_c) was configured to 4 MHz. Transducer excitation was performed by a 4-cycle sinusoidal burst. Field II also allows to simulate the effect of apodization. This effect occurs because, in real transducers, the edges might vibrate less than the center. In Field, apodization is defined by establishing coefficients for each square element. For this work a 2D hanning matrix was used to define the apodization coefficients as show in Fig. 1 (color palette). For simulations were apodization is not considered the coefficients were all set to “1”.

3.2 Pipe section

For this work, a pipe section with 30 mm of internal diameter was defined. Transducer aperture center coordinates was setup for the origin of 3-D coordinate system (Fig. 2). Pipe axis was positioned at an angle of 45 degrees with respect of z axis (Fig. 2). The number of reflectors was roughly 10 scatterers per measurement volume. Work fluid is water with sound speed defined as $c = 1480$ m/s. A 2 mm thickness was used for the pipe wall. However, the amplitude of echoes from the moving reflectors was configured to be 100 times greater than the amplitude of the echoes from the stationary reflectors. The reason for that configuration is to avoid the use of stationary filters that may introduce an additional source of errors in velocity estimation.

3.3 Simulation parameters

The simulations were performed using Field II release 3.24. This software works under Matlab environment. Matlab version used was release R2013a. The sampling frequency utilized to generate the RF voltage signal was 100 MHz. Pulse repetition frequency (f_{prf}) was set to 2 kHz. Three types of flow were simulated: uniform velocity profile, laminar flow and turbulent flow. Flow direction simulated was towards the transducer, using negative signal convention for this condition. For laminar and turbulent velocity profile the models used were

$$v(r) = V_{max} \left(1 - \left(\frac{r}{R}\right)^2\right), \quad (1)$$

$$v(r) = V_{max} \left(1 - \frac{r}{R}\right)^{1/8}, \quad (2)$$

where R is the pipe internal radius and V_{max} the maximum flow velocity. To evaluate the spatial velocity profile, 1 second of data was acquired, or 2000 ultrasound pulses. Velocity estimation were carried by a 2D autocorrelation with subsampling algorithm [8-10] and by time shift estimator based in cross-correlation technique [11,12]. No post-processing filters were used. Matlab scripts written for this work can be found at <http://dx.doi.org/10.13140/RG.2.1.1942.1046>.

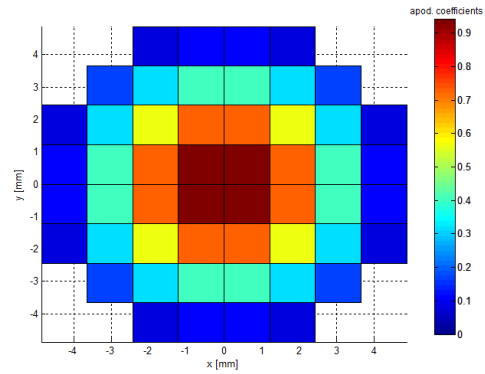


Figure 1: Transducer aperture geometry representation divided in 1.2 mm x 1.2 mm square mathematical elements. Apodization coefficients used for each element are also showed by color palette.

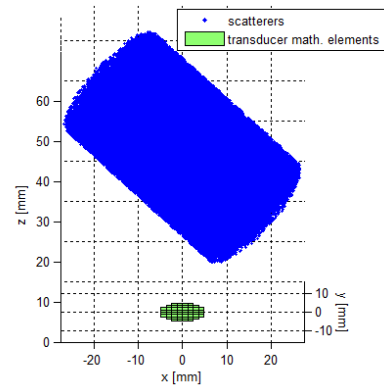


Figure 2: 3D representation of reflectors distribution with respect to the ultrasound transducer. Pipe walls were suppressed.

4. Results

4.1 Transducer apodization

To understand the effect in the spatial velocity profile measured when transducer apodization is simulated, two uniform velocity flows were simulated. In the first flow simulation, a non-apodized transducer was configured (i.e, all apodizations coefficients of Fig. 1 were set to 1). The second flow used same transducer but with the apodizations coefficients of Fig. 1. The velocity configured for the simulated flows was $0.8 v_a$, where

$v_a = cf_{prf}/4f_c$, or the maximum velocity that can be measured by the 2D autocorrelation algorithm. Spatial velocity profiles were evaluated for each flow and are shown in Fig. 3. The difference in using apodization can be notice in the extent of the spatial velocity profile. Transducer apodization effect can be observed by the narrowing of the spatial velocity profile. Without apodization the velocity profile comprise of one extra velocity profile point (to the left in Fig. 3). The ultrasound beam diameter measured using the spatial profile obtained (without apodization) was 31.2 mm. Using apodization the beam diameter became 0.95 mm narrower. Such effect occurs because apodization reduces the effective ultrasound beam radius. With a narrow beam, the first reflector echo will appear at a far point relative to the wide beam from a non-apodized aperture.

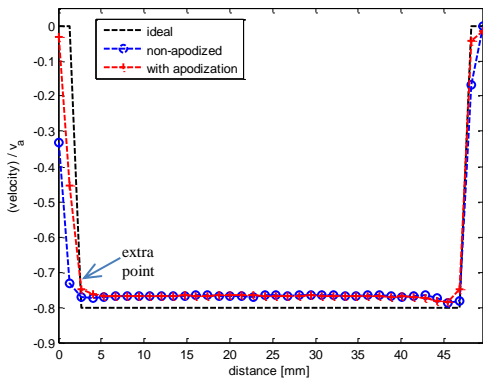


Figure 3: Comparison of velocity profile obtained from a non-apodized aperture with a velocity profile from an apodized aperture.

4.2 Accuracy assessment by Autocorrelation

Accuracy of the flow simulation was assessed by evaluating the mean flow velocity from the spatial profile measured for each type of flow simulated. For each flow, velocity profile was changed based in its maximum velocity, V_{max} (Eq. 1-2). Therefore, eight different velocity profiles were simulated where V_{max} ranged from $0.1 v_a$ to $0.8 v_a$, where $v_a = cf_{prf}/4f_c$, or the maximum velocity that can be measured by the 2D autocorrelation algorithm. The number of emissions or pulses used to evaluate each velocity was $N_{pulse}=50$. A high SNR of 50 dB was established to avoid velocity estimation errors from noise. Since the transducer was excited by a 4-cycle sinusoidal burst, velocity spatial resolution was set to 4 wavelengths (1.5 mm). To generate 1 second of acquisition data, computer simulation time took roughly 49 minutes, using an Intel Core i7-2.6 Ghz computer.

Accuracy results are summarized in Fig. 4. A comparison between measured and simulated velocity profile is shown in Fig. 5 and 6, for turbulent and laminar flow ($V_{max} = 0.8 v_a$), respectively. Mean flow spatial velocities measured were underestimated for all velocities and all flows (left axis, Fig. 4). For uniform flow, the relative mean spatial velocity error (right axis, Fig. 4) do not vary significantly, ranging between -3.92% to -3.95%. For turbulent flow, mean spatial velocity error

also remains almost constant varying from -13.08% to -13.12%. However, turbulent flow relative error is roughly 3 times higher than the relative error from uniform flow. Such increase in error relatively to the uniform profile is due to the curvature of the turbulent velocity profile (Fig. 5). The mean velocity error is proportional to the intersection area between the measured and the simulated velocity profiles from Fig. 5. Since spatial velocity profile from turbulent flow has a large intersection area than uniform velocity profile, the mean velocity error of the former is expected to be higher than the last. For laminar flow, mean velocity error also maintains a stable behavior, ranging from -20.8% to -21.3% (Fig. 4, right axis). The mean velocity accuracy for this condition is worse than the turbulent velocity and the uniform velocity profile. Such error increase can be explained by the increase in the area between the two profile curves (Fig. 6). In laminar flow the profile curvature is greater than turbulent flow. Therefore is expected a greater mean flow velocity error for laminar flow.

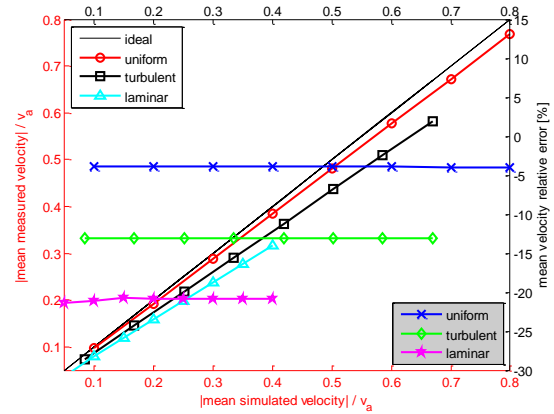


Figure 4: Left axis: Mean spatial measured velocity (autocorrelation) versus mean spatial simulated velocity, both normalized by the maximum velocity of the autocorrelation method, v_a . Legend at top left. Right axis: mean velocity relative error for each flow and each simulated velocity. Legend at bottom right.

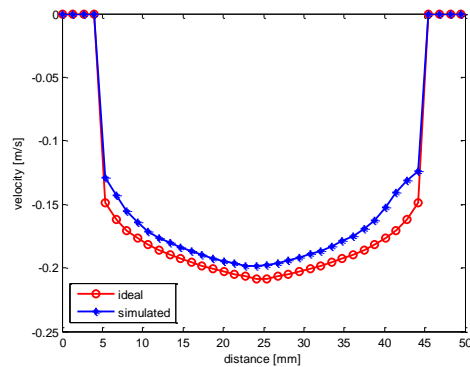


Figure 5: Spatial velocity profile measured versus spatial velocity profile simulated for turbulent flow where $V_{max} = 0.8 v_a$, SNR=50 dB, $N_{pulse}=50$.

The mean velocity errors of Fig. 4 indicate a systematic behavior, where velocities estimated from the three flows

are all underestimated. Since this error occurs systematically in every velocity tested, most of it can be suppressed by a simple calibration procedure.

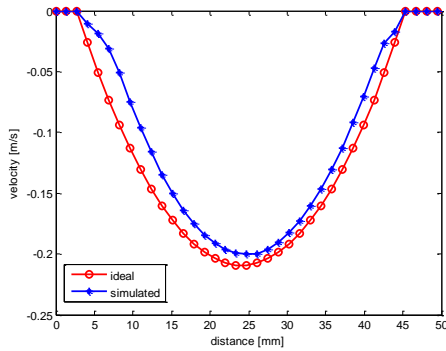


Figure 6: Spatial velocity profile measured versus spatial velocity profile simulated for laminar flow where $V_{max} = 0.8 v_a$, SNR=50 dB, $N_{pulse}=50$.

4.3 Accuracy assessment by Cross-correlation

The underestimation observed in the measurement of the simulated data by the autocorrelation method motivates the use of another velocity technique to confirm the results obtained. The cross-correlation technique was chosen because most works published related to Field II only use this technique. The accuracy evaluation was performed using the same configuration described in section 4.2. Results obtained are summarized in Fig 7. Accuracy results of Fig. 7 also show that all velocities measured are underestimated for every flow tested (left axis). Turbulent and laminar mean velocity error presented larger error for low velocity values (Fig.7 right axis). However after these larger error values, the relative error remains roughly constant. Thus, the result obtained corroborates with the underestimation observed in the results obtained using the autocorrelation algorithm.

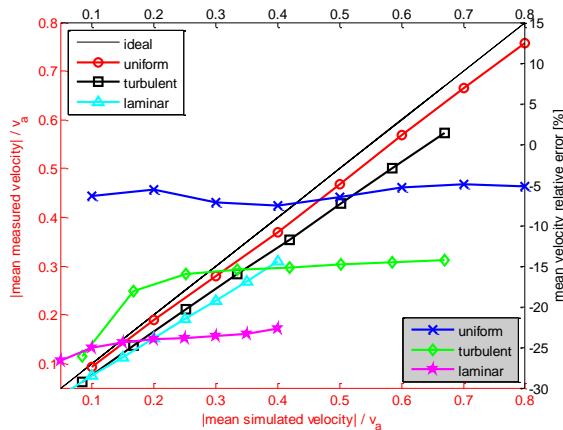


Figure 7: Left axis: Mean spatial measured velocity (cross-correlation) versus mean spatial simulated velocity, both normalized by the maximum velocity, v_a . Legend at top left. Right axis: mean velocity relative error for each flow and each simulated velocity. Legend at bottom right.

5. Conclusions

Some more work still need to be carried on in order to

fully deploy Field II as an accurate simulation tool for fluid engineering study. At this stage, ultrasound flow signals simulation using Field II may only be used for the study of velocity estimation techniques if a prior calibration step is performed. The reason for the underestimation of velocities in the simulations results could lie in several factors. The discretization of the spatial impulse response, the division of the transducer in square mathematical elements, sampling frequency, can be responsible for the low velocities obtained. It is possible to change the simulation parameters mentioned to obtain an accurate result, however simulation time can increase considerably. Effects in velocity profile measured due to transducer apodization were also analyzed. Including transducer apodization in the simulation will incur in a narrow ultrasonic beam and thus will consequently generate a narrow velocity profile.

6. Acknowledgments

This work was carried out with the support of following Brazilian agencies: Fundação Araucária (grant 06A/2014) and Secretaria de Estado da Ciência, Tecnologia e Ensino Superior do Paraná (SETI). The authors are grateful for their support.

References

- [1] Takeda Y: Velocity profile measurement by ultrasonic Doppler method, *Exp. Fluids*, 10 (1995), 444-453.
- [2] Tupholme G E: Generation of acoustic pulses by baffled plane pistons. *Mathematika*, 16(1969),209-224,
- [3] Stepanishen P R: The time-dependent force and radiation impedance on a piston in a rigid infinite planar baffle. *J. Acoust. Soc. Am.*, 49(1971), 841-849.
- [4] Stepanishen P R: Transient radiation from pistons in an infinite planar baffle. *J. Acoust. Soc. Am.*, 49(1971), 1629-1638.
- [5] Jensen J A: Simulation of Advanced Ultrasound Systems using Filed II. *Proceedings of the IEEE Int. Symp. on Biom. Imag. Washington* (2004), 636-639.
- [6] Jensen J A & Svendsen NB: Calculation of pressure fields from arbitrarily shaped, apodized, and excited ultrasound transducers. *IEEE Trans. Ultrason., Ferroelec., Freq. Contr.* 39(1992), 262-267.
- [7] Jensen J A: A program for simulating ultrasound systems. *Med. Biol. Eng. Comp.*, 10th Nordic-Baltic Conf. on Biom. Imag., Vol.4, Supplement 1, Part1 (1996b), 351-353.
- [8] Loupas T *et al.*: Experimental evaluation for ultrasound blood flow imaging, by means of a two-dimensional autocorrelation approach. *IEEE Trans Ultrason., Ferroelec., Freq. Control* 42(1995), 689-699.
- [9] Loupas T *et al.*: An axial velocity estimator for ultrasound blood flow imaging, based on a full evaluation of the Doppler equation by means of a two-dimensional autocorrelation approach. *IEEE Trans Ultrason., Ferroelec., Freq. Control.* 46(1995), 672-688.
- [10] Hoek A P G *et al.*: Subsampling volume processing of Doppler ultrasound signals. *Ultrasound Med. Biol.* 20(1994), 953-965.
- [11] Bonnefous O and Pesqué P.: Time domain formulation of pulse-Doppler ultrasound and blood velocity estimation by cross-correlation, *Ultrasound Imag.* 8(1986), pp. 73-85.
- [12] Jensen J A.: Implementation of ultrasound time-domain cross-correlation blood velocity estimators, *IEE Trans. Biomed. Eng.*, 40(1993), pp. 468-474.

Non-intrusive flow velocity measurements in pressurized pipe with orifice

Nicolas J. Adam¹, Giovanni De Cesare¹ and Anton J. Schleiss¹

¹Laboratory of Hydraulic Constructions, Ecole Polytechnique Fédérale de Lausanne, 1015 Lausanne, Switzerland

Orifices are hydraulic devices producing pressure drops or head losses in pipes ways. Flow velocity measurements at the upstream of orifices allow understanding the effect of given flow field on head losses, while downstream measurements provide information of orifice jet stability. The placement of an UVP sensor in the flow disturbs the surrounding velocities and thus the results. The research therefore focuses on the implementation of a non-intrusive velocity measurement using an UVP sensor located outside the pipe. A seeding method is needed to improve the signal quality and accuracy using hydrogen bubbles produced by electrolysis of the flowing water. Firstly, this research shows the flow velocities in the orifice jet, at the upstream and downstream of the orifice. Logically, the average jet velocities are higher than upstream or far downstream flow velocities. Then, pressure recordings show the asymmetry behavior of head losses for the tested orifice. Finally, the power spectra analysis of the pressure and kinetic energy at the same location are compared and show a slightly higher decrease of energy for kinetic energy. The results highlight that further experiments should be performed with higher acquisition frequency.

Keywords: Orifice, non-intrusive velocity measurement, pressurized pipe

1. Introduction

Orifices are hydraulic structures used to produce head losses [1] or to evaluate the discharge flowing through [2]. They can be used to throttle surge tanks in high head power plants to manage extreme water level during mass oscillations [3]. A better understanding of these structures involve identifying main geometry parameters and their effect on the head losses produced by the orifice and the orifice jet flow.

Flow field measurements could highlight flow natural frequencies. Furthermore, the power spectra analysis of pressure and kinetic energy are compared showing discrepancies and giving feedbacks of used acquisition parameters. This research shows preliminary tests of a bigger experimental campaign. The main goal of these studies is to have a better understanding of velocity fields around an orifice and their consequences on the produced head losses.

At end, the knowledge improvement of relation between head losses and flow field should lead to decrease the design duration of an orifice geometry for a given pair of head losses (in flow directions AB/BA shown in Figure 2).

2. Laboratory installation

2.1 Experimental set-up

The experimental set-up at the Laboratory of Hydraulic Constructions (LCH) in Lausanne is shown in Figure 1. The main part of the set-up, where an orifice (Figure 2) is placed at the middle, has an inner diameter, D , equal to 0.216 m and a length of 4 m while the water supply and restitution of the set-up have a diameter of 0.150 m.

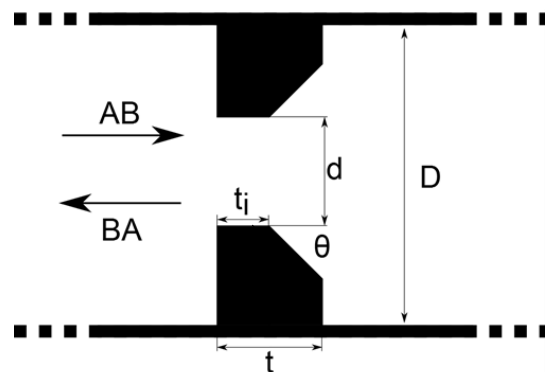


Figure 2: Tested orifice whose geometrical parameters are $d/D = 0.5$, $t/D = 0.4$, $t_i/D = 0.2$ and $\theta = 45^\circ$

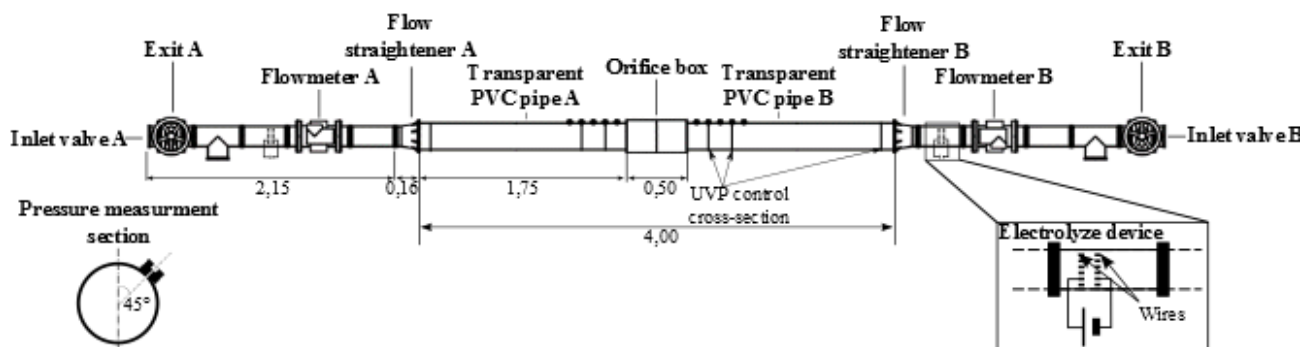


Figure 1: Physical set-up

2.1 Measuring instrument

Pressure are recorded in one point tilted 45 degrees to the pipe top (Figure 1) using 6 piezo resistive pressure sensors (Keller - series 25 with an acquisition rage between -0.1 to 0.5 bar). The acquisition frequency is 500 Hz and number of sample is 262'144 (2^{18} samples). It allows performing frequency analysis from low-frequency to high-frequency (until 250 Hz). Three discharges are tested to evaluate the pressure drop through the orifice: 10, 20 and 30 l/s.

Flow velocity profiles are evaluated by using ultrasound. For each flow direction, 1 upstream cross-section and 3 downstream cross-sections are tested (2 in the orifice jet and 1 at the end of the 0.216-meter pipe. A 20-degree angle with the vertical is introduced in order to evaluate longitudinal velocity. The UVP transducer (emitting frequency 2 MHz) is placed outside the pipe avoiding any perturbations of the flow by the transducers (Figure 3). The number of sample is 16'384 (2^{14} samples) for the same duration as pressure acquisition. The sampling frequency is 22 Hz. Only one discharge is tested for the velocity profile measurements, 20 l/s.

The discharge is recorded with two electromagnetics flowmeters: ENDRESS-HAUSER – PROMAG 50 W.

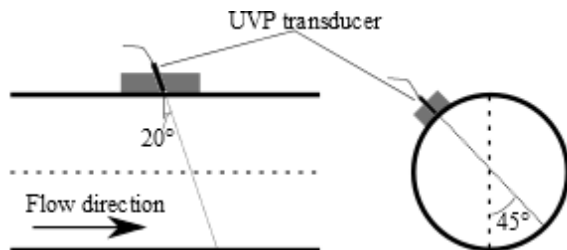
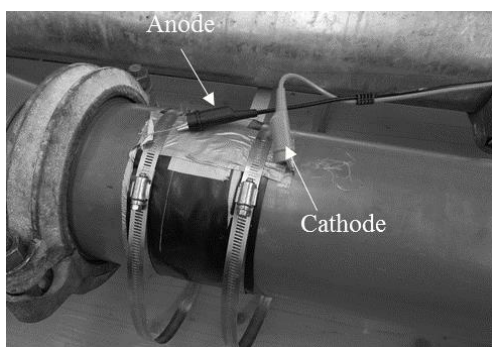


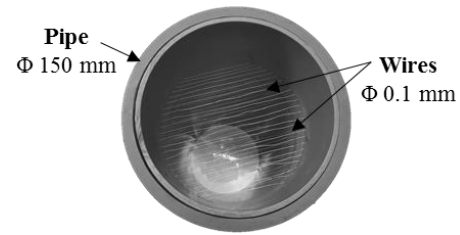
Figure 3: Installation of UVP Transducer (Longitudinal and cross-sectional view)

2.2 Non-intrusive seeding

The quality of the signal is improved by introducing hydrogen seeding with an electrolyze device in the upstream pipe (Figure 1). The hydrogen is created by electrolysis of water between two racks of wires (whose diameter is 0.1 mm) connected with a DC electrical power source (Figure 4). A steady 30-volt voltage is applied between the anode and cathode (Figure 4). As discharges, from 10 l/s to 30 l/s, flow through the experimental set-up, the characteristic flow velocities are between 0.55 and 1.75 m/s in the upstream pipe.



(a)



(b)

Figure 4: Electrolyze device (a) Inner device with two racks of wires; (b) Electrical connections outside of the pipe

3. Velocity profile

Velocity profiles are evaluated for a discharge of 20 l/s on different cross-sections as shown in Figure 1.

According to Figure 5, the following observations can be made:

- The upstream velocity profile is disturbed and asymmetric showing that upstream flow conditions are not optimal.
- This high velocity core decreases along the pipe axis (1.35 m/s at +1.97 D and 0.76 m/s at 2.89D). Far away the orifice, the velocity profile recovers standard turbulent profile for pipe flow.
- There is a trough in the jet mean velocity profiles. Further experiments should be performed to confirm or reverse this behavior.

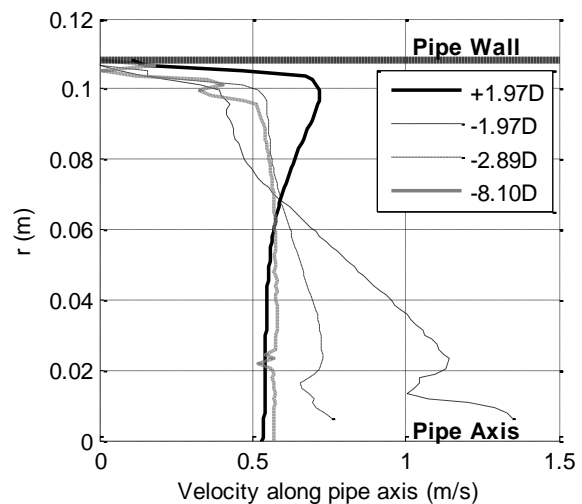


Figure 5: Flow velocity fields along the pipe axis on the half upper section of the pipe for BA flow directions

4. Pressure drop through orifice

According to [4,5], the pressure drop is proportional to the kinetic energy of the flow in the pipe. Turbulent head losses, which are independent of Reynolds number, are ensured if the Reynolds number in the pipe is higher than 10^4 . This condition is satisfied for the lower discharge (1.2×10^4). Note that the downstream pressure is set artificially to 0 mH₂O in order to compare pressure for all

discharges. Figure 6 and Table 1 show that the pressure drop increase with a higher discharge. In the same time, the pressure drop in the jet increase as well. While the discharge is three times larger, the global pressure drop is almost seven times larger.

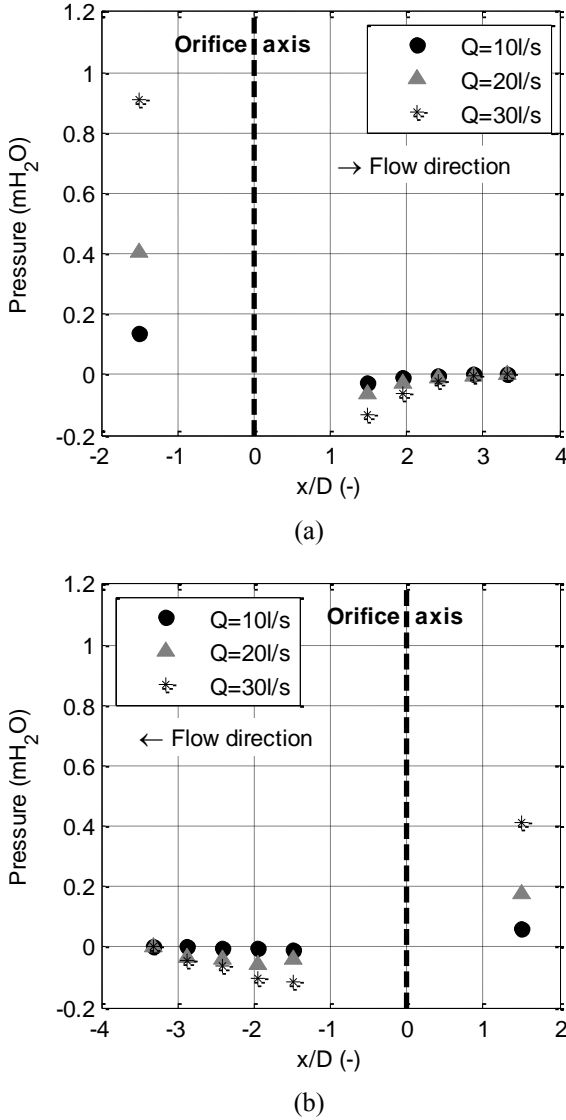


Figure 6: Pressure drop across the orifice (Figure 2) for three discharges for (a) AB and (b) BA flow directions

Table 1: The global pressure drop, ΔP , between upstream and downstream of the orifice and the additional pressure drops due to the high velocities jet, ΔP_{jet} , with the downstream pressure

Q (l/s)	AB		BA	
	ΔP_{jet} (mH ₂ O)	ΔP (mH ₂ O)	ΔP_{jet} (mH ₂ O)	ΔP (mH ₂ O)
10	-0.131	0.908	-0.113	0.414
20	-0.063	0.407	-0.040	0.180
30	-0.025	0.135	-0.011	0.060

Figure 7 shows that the global pressure drop is proportional to the kinetic energy in the pipe. Furthermore, the global pressure drop is almost 55%

smaller when the streamlines are contracted with a slope approach (Figure 2 and flow direction BA). The head loss coefficients (which is the ratio between the global pressure drop and the kinetic energy in the main pipe) is 27.4 for AB flow direction and 12.2 for BA flow direction.

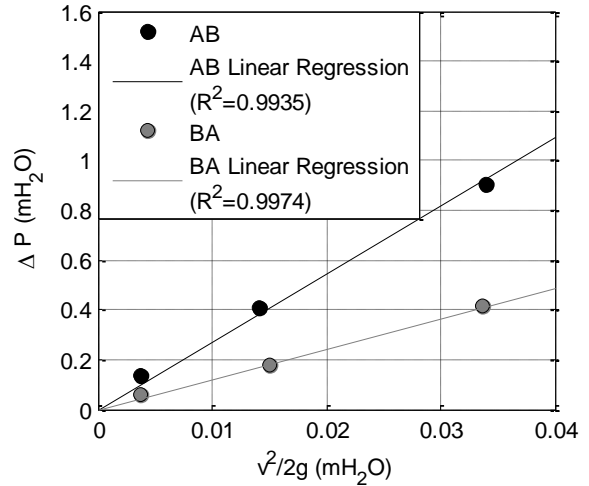


Figure 7: Pressure drop across the orifice (Figure 2) as a function of the kinetic energy in the main pipe

5. Power Spectrum Analysis

The power spectral densities for pressure and velocity fluctuations are determined using Welch utilities. For both pressure and velocity power spectrum analysis, the window length is equal to 1024 samples. Thus, there are 16 windows for the velocity power spectrum and 256 for the pressure. A similar comparison between powerspectral densities for pressure and velocity fluctuations has been performed in [6].

5.1 Kinetic energy

Figure 8 (a) shows the power spectrum of the velocity 5 mm away from the pipe wall while Figure 8 (b) shows the power spectrum on the pipe axis. These observations can be made:

- The energy of kinetic energy fluctuations increases after flowing through the orifice. At the end of the downstream pipe, the energy of fluctuations decreases to the same level as upstream the orifice.
- In the orifice, a natural frequency seems to appear at 0.2 Hz. However, the recording duration was not sufficient to cover accurately this frequential area.
- The energy cascade slope of kinetic energy near the wall is smaller than the typical turbulence slope of $-5/3$. However, this difference is higher in the jet area than upstream of the orifice (+1.97D) or further downstream (-8.1 D).
- The energy cascade slope of kinetic energy on the pipe axis is more or less equal to the typical turbulence slope $-5/3$.

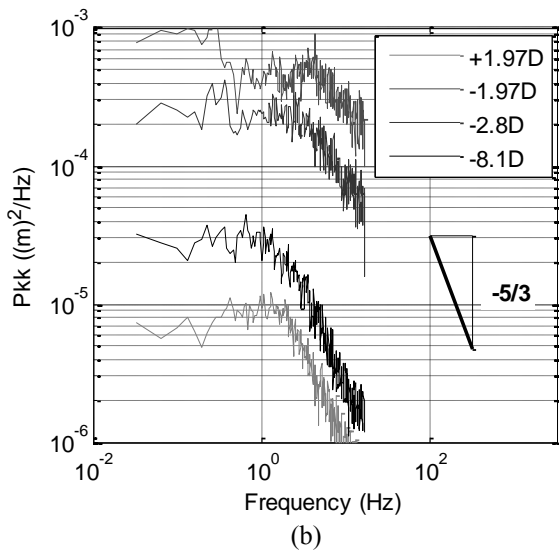
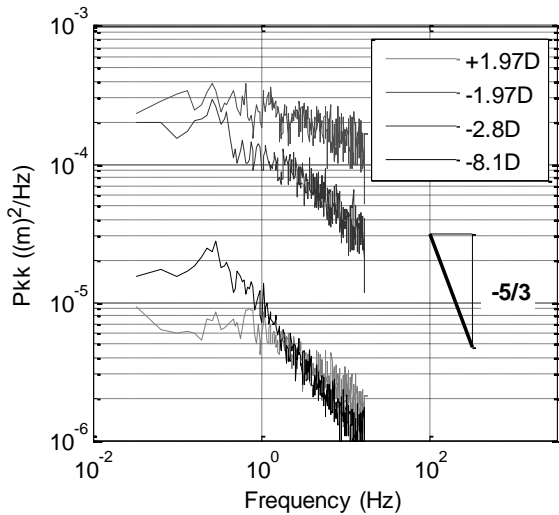


Figure 8: Power Spectrum using welch tools for the kinetic energy upstream and downstream of the orifice for flow direction BA: (a) 5 mm away from the pipe wall; (b) on the pipe axis

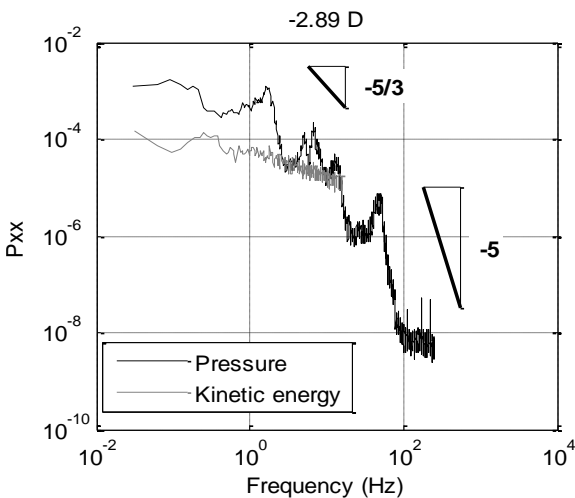


Figure 9: Comparison between power spectra of velocity and pressure at the downstream of the orifice ($x = -2.89 D$) for flow direction BA (5 mm away from the pipe wall)

5.2 Comparison with pressure power spectrum

Figure 9 compares the power spectra of the kinetic energy close to the pipe wall and the pressure recorded as detailed in Figure 1. The decrease of energy is smaller for the kinetic energy. The average slope of the pressure energy cascade is in good agreement with the theory. However, there are at least two big steps of energy in the pressure power spectrum (13 Hz and 48 Hz).

6. Conclusion

Orifices are useful to throttle surge tank. A better understanding of the flow behavior produced by different geometry would allow to shorten the duration of the design step during a refurbishment of a high head power plant.

The pressure drop produced higher head losses when the section restriction is sudden than when the restriction is progressive with an angle introduction.

Finally, the power spectra of kinetic energy and pressure show different behaviors. The slope of energy cascade is slightly higher for the kinetic energy. Further experiments should be performed with a higher acquisition frequency for the velocity recording in order to increase the accuracy for high frequencies.

The orifice seems to produce a jet core where velocities are higher than in the surrounding areas. Furthermore, it seems to have a characteristic frequency close to the pipe wall.

References

- [1] F. Hachem, C. Nicolet, R. Duarte, G. De Cesare, and G. Micoulet, "Hydraulic Design of the Diaphragm's Orifice at the Entrance of the Surge Shaft of FMHL Pumped-storage Power Plant," *Proc. 35th IAHR World Congr.*, 2013.
- [2] B. Standard, "Measurement of Fluid Flow by Means of Pressure Differential Devices Inserted in Circular Cross-Section Conduits Running Full," *Part*, vol. 2, pp. 5167–2, 2003.
- [3] J. Giesecke, S. Heimerl, and E. Mosonyi, *Wasserkraftanlagen: Planung, Bau und Betrieb*, 6., aktualisierte und erw. Aufl. Berlin: Springer Vieweg, 2014.
- [4] R. D. Blevins, "Applied fluid dynamics handbook," *N. Y. Van Nostrand Reinhold Co*, vol. 1, p. 568, 1984.
- [5] I. Idel'cik, "Mémento des pertes de charges singulières et de pertes de charges par frottement [Handbook of singular and friction head losses]," *Eyrolles Paris*, 1969.
- [6] M. Pfister, R. Duarte, M. Müller, and G. De Cesare, "Cavitation risk estimation at orifice spillway based on UVP and dynamic pressure measurements," in *Proc. of the 8th International Symposium on Ultrasonic Doppler Methods for Fluid Mechanics and Fluid Engineering*, 8th ISUD, 2012, pp. 137–140.

Flow rate measurement after 90 degrees bended pipe using multi-path ultrasound shift method

Kei Kuramoto, Tatsuya Kawaguchi, Isao Satoh and Takushi Saito

School of Engineering, Tokyo Institute of Technology, 2-12-1 Ookayama, Meguro-ku, Tokyo 152-8552, Japan

High precision management and control has been important issue in energy plant or reaction device using such gaseous fluid as vapor and air. The objective of the study is to improve the accuracy of the ultrasound flow rate measurement after bended pipe. Firstly, the radial velocity profile after 90 degrees bended pipe was calculated by commercial CFD software. By using the result of calculation, the suitable estimation methods of flow rate in distorted velocity profile were examined and resulted that the three parallel measurement paths enable to determine the resultant flow rate even in distorted velocity profile. Inner diameter of pipe was 160 mm and the diameter of bend was 240 mm. The flow rate was varied from 2.0 m/s to 9.0 m/s. The frequency of ultrasound was 40 kHz. The test section was located after 90 degrees bended pipe. The estimated error was 5 % by numerical simulation and the value was 20 % in the actual measurement.

Keywords: Flow rate, Ultrasound flow meter, Ultrasound shift method, Signal processing

1. Introduction

High precision management and control has been important issue in energy plant or reaction device using such gaseous fluid as vapor and air. Accurate flow rate measurement generally requires a long straight section in order to stabilize the velocity profile. However, the space saving flow metering method that has low pressure drop and high reliability is desired. The ultrasound flow metering has the significant advantages that the pressure drop is negligible. Conventional transit-time method or sing-around method, however, have difficulties in measuring the flow rate of conduit flow with distorted velocity profile due to the secondary flow. The objective of the study to improve the flow rate measurement that can be applied to the distorted velocity profile with ultrasound shift method proposed by the authors^[1,2]. In this method, the displacement of sound pressure distribution due to conduit flow is determined by the sensor array. The method could be extended to the multi-path measurement for the distorted flow velocity profile. In this paper, the amount of the flow rate modulation due to the velocity profile distortion after 90 degrees bended pipe was firstly obtained by CFD that is followed by the experimental validation of the measurement accuracy.

2. Theory of ultrasound shift method

In the ultrasound shift method flow rate is calculated from the displacement of sound pressure distribution due to conduit flow. Figure 1 shows the schematics of the ultrasound shift method. Ultrasound beam is shifted due to the flowing gas while transmitting perpendicularly to the main stream. Displacement of sound pressure distribution, S , can be calculated by the equation 1 as follow:

$$S = \int_0^D \frac{U(y)}{c} dy \quad (1)$$

Where c is sound speed, D is internal diameter of pipe, $U(y)$ is velocity distribution of gas flow. The average flow velocity, v , as

$$v = \frac{S \cdot c}{D} \quad (2)$$

and flow rate Q is given by equation 3.

$$Q = v \frac{\pi D^2}{4} = \frac{S \cdot c \pi D^2}{D \cdot 4} \quad (3)$$

Equation 3 describes the flow rate with certain flow condition such as fully developed conduit flow. When the flow is distorted, especially nearby a bend or an elbow.

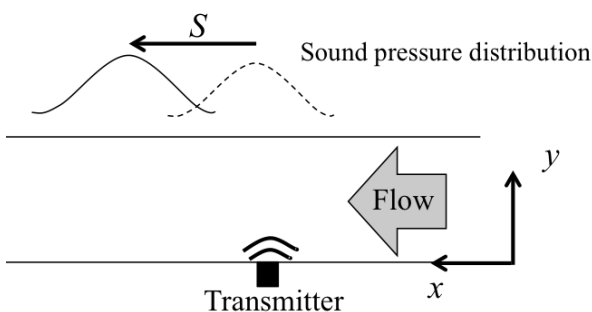


Figure 1: Schematics of ultrasound shift method

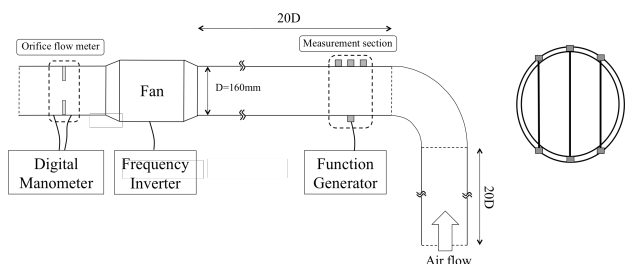


Figure 2: Experimental rig and location of test section

3. Experiments and results

Figure 2 shows the experimental setup. The internal diameter of pipe is 160 mm. A centrifugal fan is installed downstream the measurement section and it is powered with frequency-controlled inverter to generate the airflow in the way of suction. There are $20D$ length of flow pipe installed upstream and downstream of the centrifugal fan respectively. 90 degrees bended pipe is installed upstream of measurement section to generate distorted velocity profile. Measurement section is located at 220 mm from the exit of the bended pipe. 40 kHz transmit/receive dual-purpose ultrasound transducers are selected for the experiment. The ultrasound transducer for transmitting ultrasound is located wall of pipe. And the transducer for receiving ultrasound is located opposite wall of transmitting transducer. There are 3 parallel measurement paths. One measurement path is through the center of the pipe. Others are located at intervals of 45 mm.

For the acquisition of sound pressure distribution, the peak positions of sound pressure distribution were measured at every flow rate. Therefore, the resultant accuracy to the flow measurement with ultrasound shift method rely on the accurate determination of sound pressure distribution and the degree of shift. In order to determine the peak position of sound pressure distribution, the reconstruction method of sound pressure distribution was used^[3]. In this method, 3 transducer located pipe wall were used for measuring the sound pressure. These measurements were used to reconstruct the sound pressure distribution fitting function $f(x)$, which were assumed to be as same shape as Gaussian distribution:

$$f(x) = \frac{1}{\sigma\sqrt{2\pi}} e^{-\frac{(x-\mu)^2}{2\sigma^2}} \quad (4)$$

Where x is measuring point position in longitudinal direction of pipe, σ and μ is standard deviation and median of $f(x)$ respectively, which means μ is the peak position of sound pressure distribution. Assumed that x_1, x_2, x_3 are positions of 3 transducer and acoustic

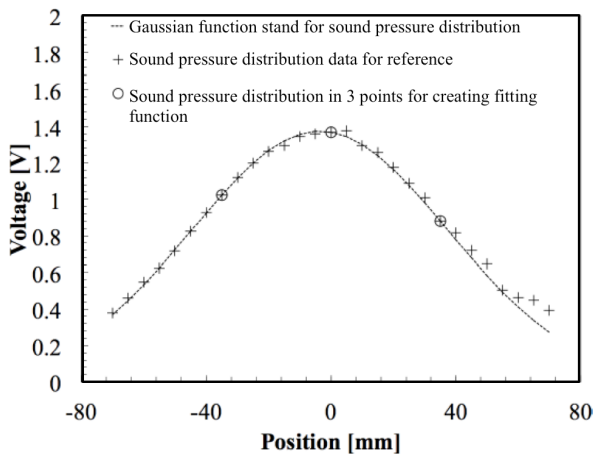


Figure 3: Sound pressure distribution

intensity measurements are y_1, y_2, y_3 , sound pressure peak position μ can be calculated as follow:

$$\mu = \frac{(x_2^2 - x_3^2) \ln \frac{y_1}{y_2} - (x_2^2 - x_1^2) \ln \frac{y_3}{y_2}}{2 \left[(x_2 - x_3) \ln \frac{y_1}{y_2} - (x_2 - x_1) \ln \frac{y_3}{y_2} \right]} \quad (5)$$

By using this method, the sound pressure distribution can be determined and the peak position can be determined. Figure 3 shows the measured result of sound pressure distribution and fitting curve.

Equation 3 describes the flow rate with the certain flow condition such as fully developed flow. However, the flow is distorted, especially nearby a bend or an elbow. It becomes difficult to assume the axisymmetric velocity profile, and therefore the accuracy will decrease compared with the single path. In contrast, the multi-path measurement is effective in the accurate flow rate determination in distorted velocity profile. In this study, 3 parallel paths are used for flow rate determination. The distribution of shift (displacement of sound pressure distribution) is approximated by using results of 3 parallel paths measurements. Since the amount of shift is equal to the line integral of velocity on measurement path, flow rate is calculated as integral of distribution of shift. Figure 4 shows the velocity profile after 90 degrees bended pipe. The dimension of pipe used simulation and simulation condition are shown in Figure 5 and Table 1. The distributions of shift are shown in Figure 6. There are 2 types of the directions of three-parallel paths shown in figure 6 (horizontal and vertical). Using the shift of three

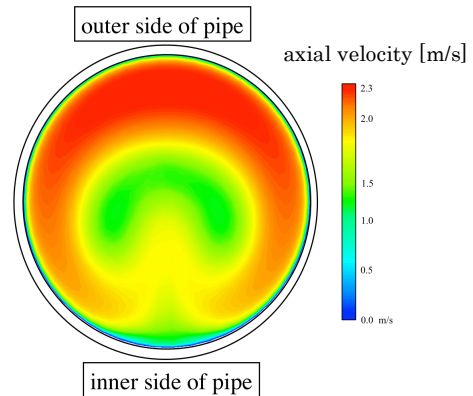


Figure 4: Result of simulation

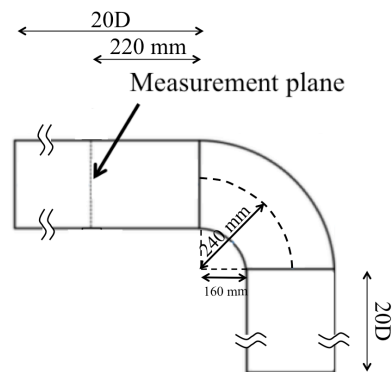


Figure 5: Dimension of bended pipe

Table 1: Simulation conditions

Software	ANSYS Fluent ver.16.2
Turbulent model	$k-\epsilon$ model
Boundary condition (inlet)	Uniform velocity
Boundary condition (outlet)	Uniform gauge pressure (0Pa)
Working fluid	air

measurement paths, the curve shown in figure 3 was estimated by the 4th polynomial approximation. The plots in figure 6 represent the measured quantity of shift, S , and the solid curve represents the estimated distribution of S . The flow rate could be obtained by integrating the curve.

The error, E , of flow rate was defined by equation 6.

$$E = \frac{Q_{ref} - Q}{Q_{ref}} \quad (6)$$

where Q_{ref} is reference flow rate by Orifis, Q is measured flow rate by the preset method. The error by horizontal paths was -2.2 %, and by vertical paths was -0.5 %. From this result, the error of horizontal paths was less than vertical paths. So horizontal paths are more suitable for flow rate measurement after 90 degrees bended pipe than vertical paths.

Figure 7 compares the degree of shift of the direction of three-parallel path. The trend of the distribution of shift

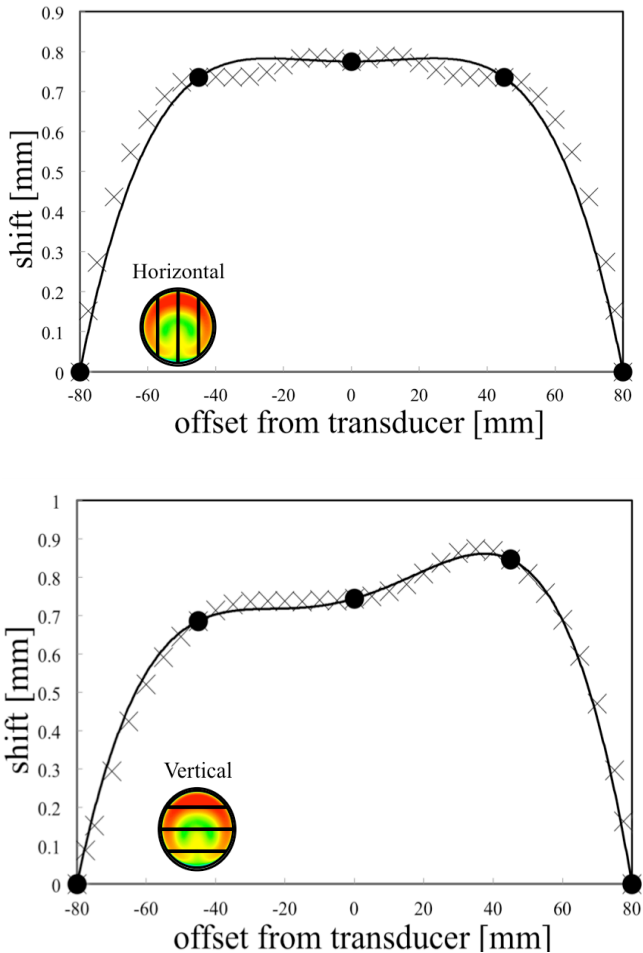


Figure 6: The distribution of shift by simulation

was agreed with the result of numerical simulation. Figure 8 compare the measured flow rate by Orifice and present method. The error by vertical paths was 21.6 % and horizontal paths was 17.6 %. This error is due to the measurement uncertainty of shift values. The error by single path^[4] which through the center of pipe was varied from 7.3 % to 30.5 % depending on directions of

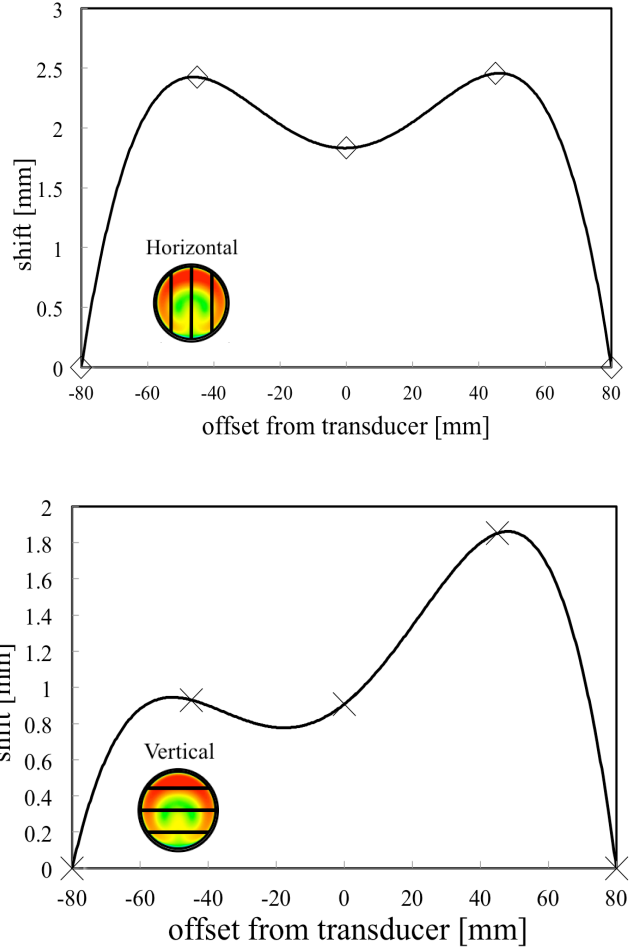


Figure 7: The distribution of shift by experiments

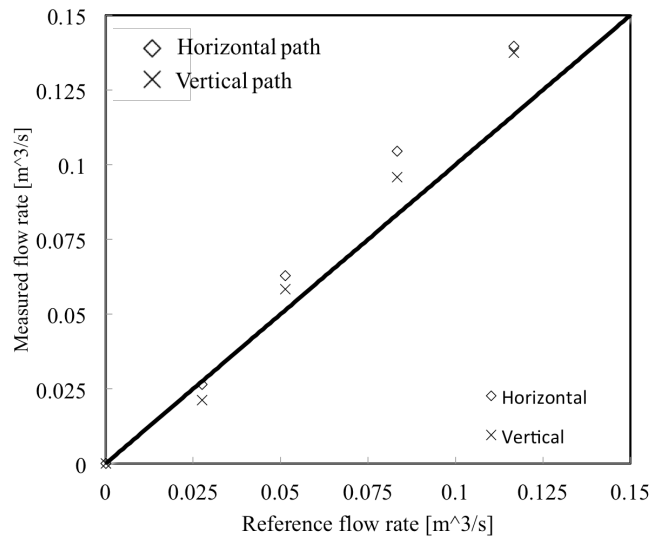


Figure 8: Flow rate versus reference flow rate

measurement paths. The arithmetic mean error of the radial four-path^[4] which radical beams was 23.5 %. By comparing the various methods, three-parallel paths measurement could reduce the measurement error in distorted velocity profile.

5. Conclusions

The flow rate measurement after bended pipe using parallel path ultrasound shift method was developed. The axial velocity profile after 90 degrees bended pipe was firstly calculated by commercial CFD software. From the result of calculation, the measurement error by three-parallel paths was estimated to 5 %. By the experiments, it was confirmed that the measurement error of the flow rate was below 20 % even by a distorted velocity profile.

References

- [1] T. Abe, T. Kawaguchi, T. Saito and I. Satoh, Development of new gas flowmeter by ultra sound tuft method, *Proc. 49th HTSJ Symp.* Vol. I + II , SP27, p123, 2012.
- [2] I. Satoh, T. Saito and T. Kawaguchi, Development of new gas flowmeter by ultra sound tuft method, *Chemical Engineering*, Vol.58, No.2 123-139, 2013.
- [3] Z. Yang, T. Kawaguchi, T. Saito and I. Satoh, Flow metering of distorted pipe flow by means of multi-path ultrasonic shift method, *FLUCOME2013*, 2013.
- [4] K Kuramoto T. Kawaguchi, T. Saito and I. Satoh, Verification of flow rate measurement using ultrasound shift method after bended pipe, *The National Symposium on Power and Energy System*, 2015.

Low Velocity Measurement on The Joule-Heating Flow by Ultrasound Velocity Profiler Method

Jiaju Zhou¹, Tomonori Ihara², and Hiroshige Kikura¹

¹ Tokyo Institute of Technology, 2-12-1 Ookayama, Tokyo 152-8550, Japan

² Tokyo University of Marine Science and Technology, 2-1-6 Etchujima, Tokyo 135-8533, Japan

A development ultrasound velocity profiler method was tested on the Joule-heating flow in a cubic cavity. The Joule-heating flow was observed in simplify cubic model and also observed in a real glass melter model by UVP method. However, due to velocity resolution of the time repetition method is low, the very slow velocity flow was difficult to measure. A new UVP method named phase difference method was developed for very slow velocity measurement. In this study, the new method was tested on the Joule-heating flow in a cubic cavity for the validation. The Joule-heating cavity is accomplished by passing an alternative current employing a pair of plate electrodes immersed on a facing plane of the liquid in order to generate internal heat source by connecting them with a constant voltage (65V). The electrode surfaces are assumed to be iso-potential and the rest of the boundaries are treated as electrically and thermally insulated. Test section is located in the middle plane between two electrodes. One-dimensional continuous velocity profiles are observed by UVP. As a result, although there are several problems of the phase difference method, the phase difference method can be applied for Joule-heating flow measurement.

Keywords: UVP, Phase difference, Joule-heating, Chaotic flow, Low velocity measurement.

1. Introduction

High-level radioactive waste (HLW) is already produced in all over the world as a waste from nuclear power plants, and the method to reprocess HLW becomes an important issue to solve. In the reprocessing, HLW is dissolved into High-Level Radioactive Liquid Waste (HLLW), and HLLW is poured into molten borosilicate glass in a glass melter to make stable mixture of HLLW and glass for geological disposal. In Japan, Liquid Fed Ceramic Melter (LFCM) type glass melter (Fig. 1) is being developed for the reprocessing.

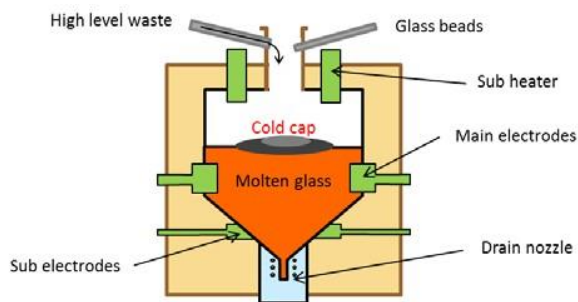


Figure 1: LFCM glass melter.

The glass melter is composed of an upper cubic part and a lower pyramid-shape part. The glass melter applies Joule-heating to generate molten glass, and the melter can mix HLLW and molten glass by convective flow mainly induced by Joule-heating. These volumetric heating in lower part and cooled in the upper part make continuous chaotic flow behavior, named as ‘chaotic steady state.’ [1] In fact, the chaotic flow behavior in the glass melter is difficult to understand, and the melter operation sometimes aborted when an accident is observed in the melter. Understanding the chaotic flow behavior is important for the effective melter operation, however,

there are many effects on the flow behavior: those are electrode cooling, cold cap, platinum group, foaming reagent, etc. Thus, former studies about the chaotic flow behavior was executed using a simple cubic cavity shown on Fig 3. For simplification.

However, the flow behavior depends on the shape of the cavity, it is also important to observe the actual flow in the cavity which has similar shape to the real glass melter. The flow behavior in the sloping bottom cavity was different from the flow behavior in the cubic cavity under several conditions. [2] The most important change from cubic cavity to sloping bottom cavity was the flow in the bottom parts of the cavity. In the sloping bottom cavity, the non-flow area can be observed by 2-D visualization, the flow in this area was very slow. As the velocity resolution of the time repetition method is not enough, the flow in the bottom of the cavity is difficult to measure. Ihara et al developed new UVP method named phase difference method for very low velocity field. [3] To apply the phase difference method, Ihara also developed new system by LabVIEW. [3] However, the Joule-heating flow is affected by thermal field, electromagnet field and flow field. These three field lead flow is completed and the echo of ultrasound signal is difficult to receive. In this paper, phase difference method was tried to apply in the Joule-heating flow and compare with previous study.

2. Principle of Phase Difference Method

UVP measurement system inherits advantages of ultrasonic measurement methods such as non-intrusive, applicable for opaque flow and time-series velocity measurement, especially for the unstable flow measurement. On the other hand, this technique has some difficulties such that the ultrasonic velocity depends on the temperature along the measurement line. The UVP

method is based on echo signal analysis of ultrasonic pulses reflected by particles suspended in the fluid of each position in the measurement axis and deriving instantaneous velocity. The working principle is depicted in Fig.2.

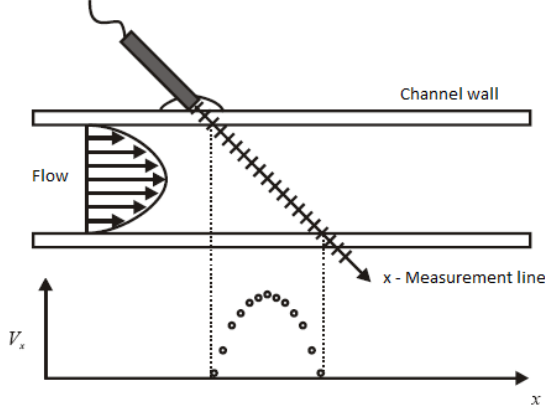


Figure 2: Principle of UVP method.

The transducer emits a pulse and receives the echo signal reflected from the particle suspended in the liquid. The information of position in each channel is extracted from the time delay τ_{prf} or pulse repetition frequency f_{prf} as following:

$$x = c \frac{\tau_{prf}}{2} \quad (1)$$

For the determination of the Doppler frequency, the peak frequency of the spectrogram was chosen. Considering the calculation load and stability, FFT (fast Fourier transform) technique [4] was used for comparison. The echo signal is modeled by the following equation.

$$E(t) = \sin 2\pi f_0 t + A_f \sin 2\pi(f_0 + f_f)t + A_b \sin 2\pi(f_0 - f_b)t \quad (2)$$

where the second term is the forward flow component and the third is the backward component. Stored echo signal is demodulated digitally and Doppler sequences of in-phase and quadrature phase are yield in a repetition order. In the demodulation, a finite impulse response (abbr. FIR) filter is used as a low-pass filter. The length and the repetition interval of the sequences determine the frequency resolution in the spectra. To derive the spectra from these sequences, FFTs are carried out for each channel, and forward and backward power spectra are obtained by the following equation.

$$P_f = (R_e[X_I] - I_m[X_Q])^2 + (R_e[X_I] + I_m[X_I])^2 P_b \quad (3a)$$

$$P_f = (R_e[X_I] + I_m[X_Q])^2 + (R_e[X_I] - I_m[X_I])^2 P_b \quad (3b)$$

where P_f and P_b are power spectra of forward direction and backward direction respectively. After merging these spectra, the spectrogram is obtained. As the device is based on digitized time domain, this corresponds to the minimum detectable velocity, namely a velocity threshold, which is expressed as

$$V_{\min,DS} = \frac{f_{PRF}}{N_j f_0} c \quad (4)$$

Practically, in order to improve the velocity resolution, the peak of the spectrum is interpolated using a three-point Gaussian curve fit. Nevertheless, this V_{\min} could be attributed to a velocity threshold. For example, when a 4 MHz signal is emitted in water at 2 kHz repetition frequency, 128 repetitions yield 5.9 mm/s as the velocity threshold. Although this technique offers high stability, there is a trade-off between time and velocity resolution depending on N_j . The time resolution can be expressed as

$$\Delta T_{DS} = \frac{N_j}{f_{PRF}} \quad (5)$$

For a single measurement volume in the fluid and when the emission signal contains only one frequency component, the echo signal from tracer particles can be expressed as

$$E(t) = \sin(2\pi f_0 t + \theta) \quad (6)$$

where θ is the average phase in the measurement volume. For the second emission, the echo signal is represented using a slightly different value of phase, which reflects the motion of tracer particles inside the measurement volume. Therefore, the main idea of this method is to detect the mean particle displacement from a difference of the phase of two successive signals as

$$\Delta x = \frac{c}{2\pi f_0} \Delta \theta \quad (7)$$

Therefore, the velocity could be estimated using a pulse repetition period T

$$V = \frac{\Delta x}{2T} = \frac{f_{PRF}}{2} \Delta x = \frac{f_{PRF}}{4\pi f_0} c \Delta \theta \quad (8)$$

then the velocities for multiple volumes along the ultrasonic beam axis can be used to form a velocity profile.

The echo signal received and digitized by the receiver is stored in matrix d_{ijk} . This echo signal is described by Eq. (6) substituting

$$t = \bar{t} + \frac{j}{f_{PRF}} + \frac{k}{f_s} \quad (9)$$

in order to determine the echo phase, a (windowed) fast Fourier transform of d_{ijk} ($k=1, \dots, 128$) is calculated, denoted by X_{ijs} . The phase difference is obtained from the $X_{ijs} X_{ij-1s}^*$ as

$$\angle(X_{ijs} X_{ij+1s}^*) = \theta_{ijs} - \theta_{ij-1s} \quad (10)$$

The flow velocity V_{ij} can be calculated using Eq. (7) where the frequency index s is selected as it corresponds to the ultrasonic basic frequency f_0 .

Since this technique estimates a velocity from two successive repetitions of echo reception, the minimum temporal resolution is given by

$$T_{PD} = \frac{2}{f_{PRF}} \quad (11)$$

The maximum velocity that can be detected, V_{max} , is the same as for the Doppler method because the range of $\Delta\theta$ remains between $-\pi$ and π . Numeric simulations suggest that the velocity threshold of the phase difference method can be affected by quantization error. However, its practical performance has not been investigated.

3. Experiment Apparatus

The dimension of cavity is shown as Fig. 3. Two carbon electrode plates are placed on opposing side wall. The cubic cavity is used in former study.

In this experiment, the work fluid was 80wt% glycerin-water solution, and 0.5wt% LiCl was added into the fluid to lead fluid possess the conductivity. After the glycerin-water solution mixed, nylon powder was added into the fluid as a reflected powder. About 1.3 kg fluid was used in the experiment.

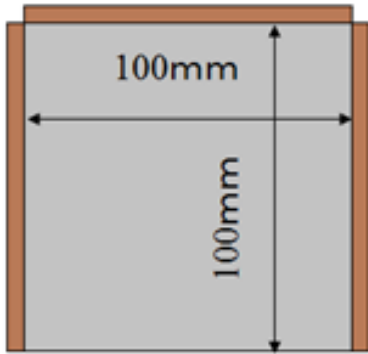


Figure 3: Joule-heating cavity in experiment.

The room temperature was kept at 20°C. The initial temperature of the fluid was also 20°C. Cooling temperature of the top surface was 20°C as the room temperature by using copper heat sinks and a water circulator at top surface. The electrodes side was adiabatic condition. The experimental apparatus is shown on Fig. 4. AC power was applied in the experiment to generate Joule-heating. A chiller was connected to the heat sink and keep the cooling temperature. UVP transducer was set at the bottom of the cavity. The UVP measurement was shown as Fig. 5. It is composed of three hardware components: an ultrasonic pulser/receiver, a digitizer and a personal computer (PC). The pulser/receiver (JPR-10CN, Japan Probe Co., Ltd.) drives an ultrasonic transducer with square burst signal whose pulse-width corresponds to the transducer frequency. Both of them were connected to the PC and the specialized software control each other. Applied voltages, frequency, burst cycle and PRF (pulse repetition frequency) are controlled by the PC through a USB interface. A low noise preamplifier (PR-40A, Japan Probe Co., Ltd.) is used with the pulser/receiver, and compensates for the attenuation of the ultrasound in the fluid; its gain is +40 dB. To improve the signal-to-noise ratio (SNR), a band-pass filter is integrated into the

amplifier. The echo signal is acquired by a 12-bit digitizer (PXI-5105, National Instruments Inc.) and stored in its 128 MB onboard memory. 1-D velocity profile of the Joule-heating flow in the cubic cavity was measured by this system.

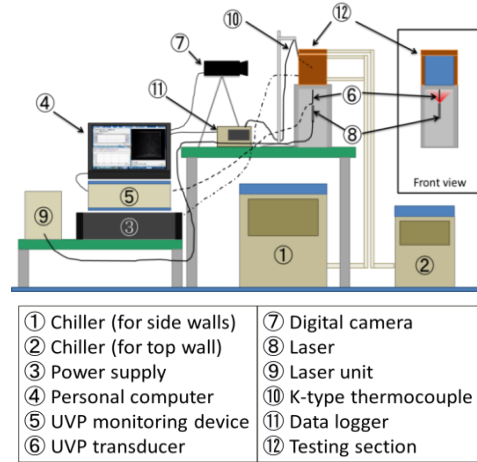


Figure 4: Experimental apparatus.

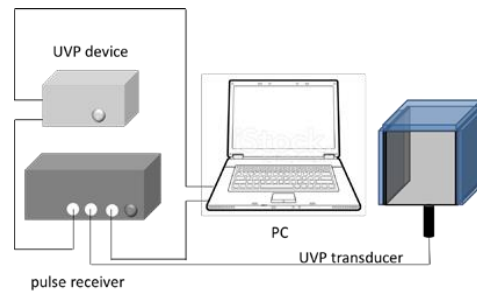


Figure 5: Structure of pulse receiver UVP.

The experiment was started when voltage was applied between the electrodes, it leads Joule-heating occurring in the cavity. After sufficient time from heating started and when the temperature tended to a stable state.

4. Verification of Phase Difference Method

Considering if the electrodes surface was cooling, the flow in the bottom was difficult to measure, the electrodes surface changed to adiabatic. Therefore, just the top surface of the cavity was cooling, and the other surface were adiabatic. Under this condition, the chaotic flow occurred in the whole cavity. Therefore, the reflect powder won't be decreased during the experiment and easy to catch the echo from the ultrasound signal.

The flow profile in the cubic cavity was measured by phase difference method and compare with the time repetition method. The flow behavior in the center line of cubic cavity measured by phase difference method is shown as the Fig. 6(a), and the Fig. 6(b) shows the data was measured by the time repetition method. The similar chaotic flow can be observed in almost whole of the cavity. The chaotic flow occurred almost in the whole cavity. However, in the bottom of the cavity, the phase difference method shows more noise than time repetition

method. In the time repetition method, the bottom parts just show no flow. However, in the phase difference method, the flow in the bottom parts is complete and difficult to analyze. To know the flow profile in the cavity, 30s average data is shown in Fig. 7.

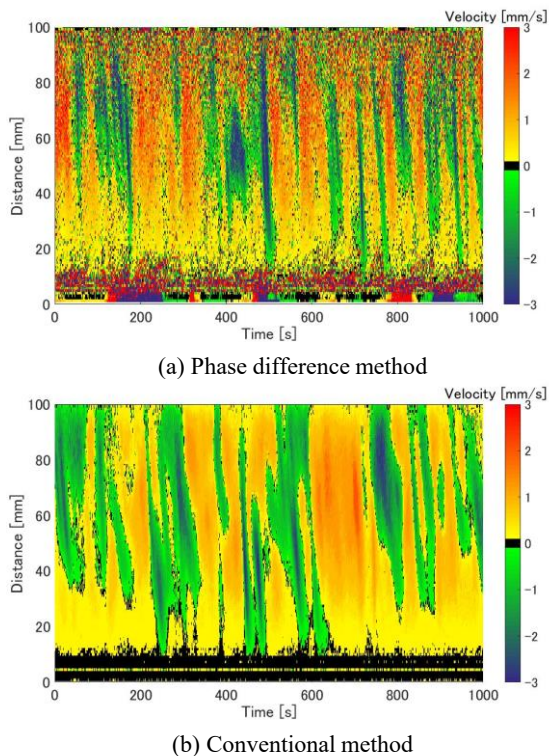


Figure 6: Flow behavior at the center line.

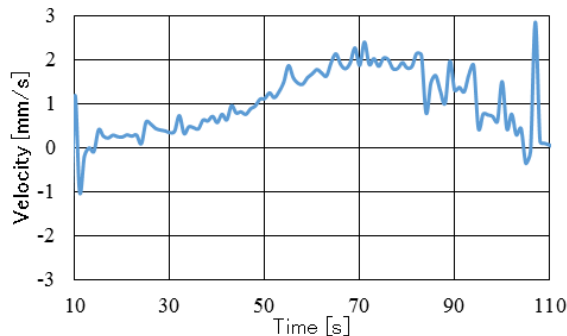


Figure 7: 30s average profile of phase difference method.

It can be found that flow measurement was not started at 0mm position, the noise observed by the phase difference method was the echo from wall. The phase difference method was easy to be affected by the noise near the transducer. However, in the cavity, the echo of ultrasound signal from reflect powder can be recognized well, the chaotic Joule-heating flow was observed by the phase difference method clearly. Therefore, the phase difference method can be applied for the Joule-heating flow measurement. The flow measurement in the bottom of the sloping bottom cavity, which the velocity was very low almost no flow can be expected. 2013

5. Conclusion

A new UVP measurement method, phase difference method was developed for low velocity measurement. New soft system and phase difference method was tested for applying to the Joule-heating flow measurement. The Joule-heating flow in a simple cubic cavity was measured by the phase difference method. The electrodes surface under the cooling condition was applied to test the new system, and the electrodes surface under the adiabatic condition was applied to test the phase difference method. The result of phase difference method measurement was compared with the time repetition method. The following conclusions were carried out by the experiment.

The new UVP system can be applied in the Joule-heating flow. When the repetition number of high, few reflect powder field is difficult to measure. However, the velocity profile can be observed by the average data. In addition, if the reflect powder can keep in a high amount, the low flow field can be measured.

The phase difference method has noise near the wall, however, the flow in the cavity can be measured by the phase different method.

The phase difference method can be considered apply in the sloping bottom cavity to observe the flow behavior in the sloping bottom part.

References

- [1] Tsuzuki N, *et al.*: The numerical analysis on unsteady flow in the cavity with Joule-heating, 48th Heat Transfer Symposium of Japan, Volume III, 727-728 (2011).
- [2] Zhou J, *et al.*: Effect of Cavity Shape on Chaotic Flow Behavior by Joule-Heating, ISFMFE2014, No. 90196 (2014).
- [3] Ihara T, *et al.*: Ultrasonic velocity profiler for very low velocity field, Flow Measurement and Instrumentation, 34 (2013), 127-133.
- [4] Chihara K, *et al.*: The microcomputer-based ultrasonic pulsed Doppler flowmeter system, IEICE Transactions, 63 (1980), 351-352.

Development of Two-dimensional Vector UVP with Phased Array Technique

Hiroshige Kikura¹, Ari Hamdani¹, and Tomonori Ihara²

¹ Tokyo Institute of Technology, 2-12-1, Ookayama, Meguro, Tokyo 152-8550, Japan

² Tokyo University of Marine Science and Technology, 2-1-6, Etchujima, Koto-ku, Tokyo 135-8533, Japan

Phased array ultrasonic velocity profiler is developed in this study. Phased array ultrasonic technique is widely used in nondestructive evaluations and medical applications. Phased array technique requires multi-channel transducer and pulser receiver. According to geometry arrangement of the transducer, ultrasonic pulser apply pulse excitation with certain time delays to focus ultrasonic beam to the designated angle. This electric scanning is performed in different steering angles. Consequently, two dimensional measurement can be performed without changing the transducer installation. For each measurement lines, two velocity profiles are measured simultaneously. Whole elements are used for ultrasonic excitation and selected two elements are used as receiver. Since two elements are placed in different position, measured velocity profiles are different as well. Therefore, two-dimensional vector can be reconstructed by solving the geometry matrix. Engineering application for fluid flow measurement is demonstrated successfully using the developed system.

Keywords: Ultrasound, Phased Array, Flow Mapping, CFD, Swirling Flow

1. Introduction

Ultrasonic Velocity Profiler (UVP) method can be used for flow mapping in channel flow. In UVP method, instantaneous velocity profiles of fluid on measurement line can be obtained by analyzing echo signals, which are reflected from particles in the fluid [1]. In addition, UVP can be applied in opaque channel and it is non-intrusive measurement method. Takeda and Kikura [2] investigated velocity field of the mercury flow using UVP. Flow mapping was accomplished either by using multiple transducers (at least 24 transducers was needed for velocity field measurements in order to get good spatial resolution [3]), which were arranged in different positions, or by using single transducer which was moved mechanically through multiple positions and set to multiple angles. However, by using those two techniques, the measurement system becomes larger as the number of transducers increase. Furthermore, the spatial accuracy becomes lower if the transducer is moved mechanically. Three-dimensional velocity flow mapping also can be accomplished by UVP method. The concept and the idea of velocity field flow mapping by UVP was proposed by Lemmin, U. [4] and later developed by Ohbayashi, H. [5]. Measurement system consists of a central emitter, symmetrically surrounded by three receivers, R1 to R3. An ultrasonic pulse is emitted into fluid from the emitter, and the surrounding receiver receives the echo reflected from tracer particles. By analyzing these received echo waves, three directional velocity components can be obtained in the same manner as in the conventional UVP for each receivers and three-dimensional velocity vector can be formed. Recently, velocity vector measurement using phased array sensor had been developed by Hamdani [6].

This paper presents the development of two-dimensional

velocity vector using phased array sensor. To overcome such problems in conventional UVP (multiple sensors and mechanical movement), an array sensor, which has multiple ultrasonic elements, can be used. By using the array sensor, velocity profiles on multiple measurement lines can be obtained with only one sensor. This technique is applied in pipe flow with twisted-tape inserted for investigating the velocity field in single-phase swirling flow. In addition, the measurement technique is used for CFD validation in swirling flow.

2. Sensor and Phased Array UVP

2.1 Hardware and Software

Phased array sensor has 8 elements with basic frequency 4 MHz and it is shown in Fig 1. Those elements are individually excited by electric pulses and it is controlled by 8-channel pulser/receiver (JPR-10C-8CH, Japan Probe Co., Ltd.) with specific delay times. The steering angle and focal point of ultrasonic beam can be changed by controlling the time delay. The beam steering principle is used to control the ultrasonic beam direction. Figure 2 shows the pattern of ultrasonic beam. When the excited element emits rectangular ultrasonic wave, the interference of wave fronts was occurred. Thus, the pattern of the interference depends on the time delay. The steering angle θ and the time delay Δt is related with the speed of sound in a medium c and inter-element spacing d as:

$$\theta = \sin^{-1} \left(\frac{c\Delta t}{d} \right) \quad (1)$$

Figure 3 shows a phased array UVP system. The phased array UVP consists of eight elements linear array sensor, 8-channel pulser/receiver (JPR-10C-8CH, Japan Probe Co., Ltd.), A/D converter (NI PXI-5114, National Instruments) and PC. The 8-channel pulser/receiver is

used to control the pulse emission from the array sensor. This pulser/receiver generates a rectangle pulse wave signal (measurement volume is, width = 0.74 mm and length = 3.95 mm), and can set these parameters to each element: basic frequency, impressed voltage, wave cycles per pulse, gain, time delay, usage of high-pass and low-pass filter. The digitized signal is transferred to the PC through a PXI system (PXI-1033 National Instruments Inc.), where all signal processing is performed digitally using LabVIEW™ 2011. The spatial and temporal resolution of phased array UVP is 0.74 mm and 32 ms.

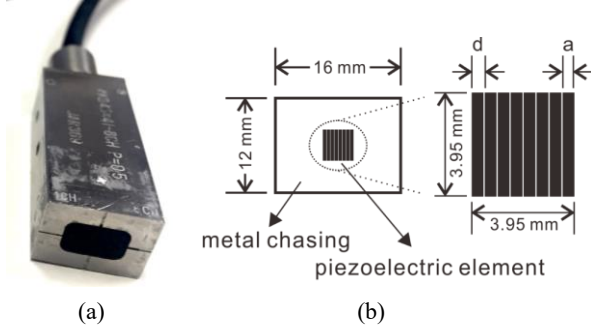


Figure 1: (a). Phased array sensor, 4 MHz and 8 elements. (b). Geometry of phased array sensor ($d = 0.5$ mm, $a = 0.45$ mm).

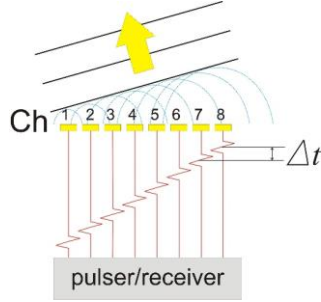


Figure 2: Beam steering technique by emitting pulse on each element with time delay (Δt).

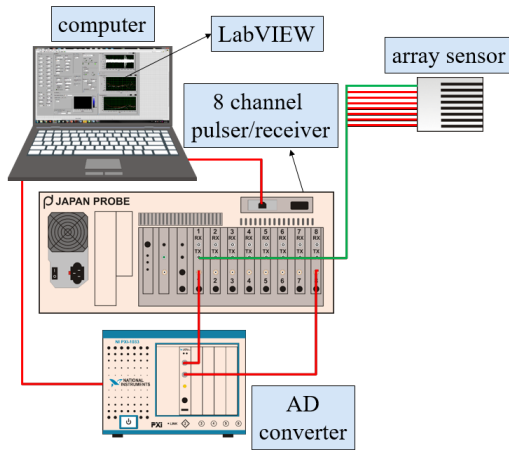


Figure 3: Phased array UVP system.

2.2 Vector Reconstruction

Schematic of the velocity vector reconstruction method with one linear array sensor is shown in Fig. 4. Ultrasonic pulse is emitted from array sensor and each element in the array sensor receives the echo reflected from the surface of particle in the measurement line. The Doppler

frequency observed at each element is described as:

$$f_{Di} = \frac{f_0}{c} (\vec{e}_e + \vec{e}_i) \cdot \vec{V} \quad (2)$$

where f_{Di} is the Doppler frequency which is observed at i_{th} -channel element \vec{e}_e is the unit vector in the opposite direction to the emitted beam, \vec{e}_i is the unit vector in the direction from particle to i_{th} -channel element and \vec{V} is the particle velocity. From equation (2), the Doppler shift frequency, which is observed in each element, is different due to the difference of element position.

Using reflections recorded by 1st and 8th elements, as shown in Fig. 4, the particle velocity can be obtained as follows:

$$\vec{V} = \frac{c}{f_0} \begin{bmatrix} \vec{e}_e \\ \vec{e}_e \end{bmatrix} + \begin{bmatrix} \vec{e}_1 \\ \vec{e}_8 \end{bmatrix}^{-1} \begin{bmatrix} f_{D1} \\ f_{D2} \end{bmatrix} \quad (3)$$

Therefore, velocity vector in measurement point can be calculated by analyzing the echoes received by different elements in array sensor. Moreover, velocity vector distribution on measurement line can be obtained using this processing at each measurement point. Applying the phased array technique, flow mapping can be conducted with only one array sensor.

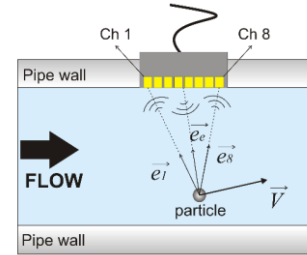


Figure 4: Velocity vector reconstruction with a linear array sensor.

2.3 Doppler Shift Frequency Estimation

The Doppler-shift frequency is calculated by using autocorrelation method. One velocity profile is obtained from several echo signals. The quadrature detection is applied to the received echoes. The signals, which contain Doppler shift frequency, pass the low pass filter, and the information of Doppler-shift frequency remains in the signal because the Doppler-shift frequency is small enough to be separated from the original signal by the low pass filter. The complex envelope signal $z(\tau)$ after the low pass filter is expressed as:

$$z(\tau) = I(\tau) + jQ(\tau) \quad (4)$$

where $I(\tau)$ and $Q(\tau)$ are the in-phase signal and the quadrature phase signal with the received signal respectively. The autocorrelation function R is expressed as:

$$\begin{aligned} R(T_{prf}, \tau) &= \int z(\tau) \times z^*(\tau - T_{prf}) d\tau \\ &= R_x(T_{prf}, \tau) + jR_y(T_{prf}, \tau) \end{aligned} \quad (5)$$

where T_{prf} is the time between two subsequent pulse emission, $z^*(\tau)$ is the conjugate complex signal of $z(\tau)$, and R_x and R_y are the real and imaginary parts of R , respectively. The phase difference φ between consecutive echo signals is expressed as:

$$\varphi(T_{prf}, \tau) = \tan^{-1} \frac{R_y(T_{prf}, \tau)}{R_x(T_{prf}, \tau)} \quad (6)$$

Doppler shift frequency f_D is obtained as follows:

$$f_D = \frac{1}{2\pi T_{prf}} \tan^{-1} \frac{R_y(T_{prf}, \tau)}{R_x(T_{prf}, \tau)} \quad (7)$$

Thus, a velocity profile can be obtained by analyzing the echo and calculating instantaneous frequencies at each instant.

3. Measurements in Swirling Flow and CFD Validation

To demonstrate the capabilities of Phased Array UVP (PAUVP), a single-phase swirling flow is prepared. Figure 5 shows a simplified measurement set up in pipe with inner diameter 20 mm and twisted tape inserted with twist ratio 3. The measurement of 2D velocity field is performed in different Reynolds number at same position. Phased array sensor is installed perpendicular to the flow and there is no gap, between sensor and liquid, as shown in Fig. 6, in order to measure tangential velocity.

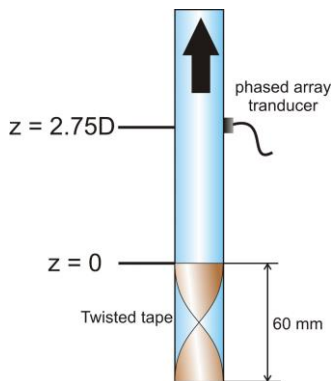


Figure 5: Simplified measurement set up in single-phase swirling flow.

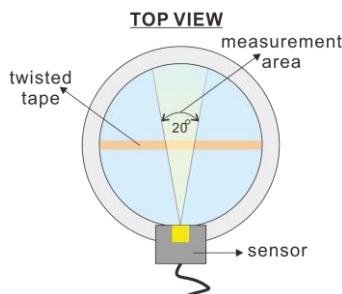


Figure 6: Set up of phased array transducer for tangential velocity measurement.

The numerical simulation is performed with the model geometry scaled to the size of the experimental model. The structure grid for computational domains is

generated by using commercial software GAMBIT v.2.2.30 as shown in Fig 7. The test section geometry with 20 mm diameter and 620 mm in length. Twist ratio of twisted tape is three, 420 mm in length and 1 mm thickness. Two model of twisted is made; symmetric and asymmetric model. For asymmetric model, 5° inclination of twisted tape is modelled.



Figure 7: Model domain with twisted tape inserted.

Three-dimensional Reynolds-averaged Navier-Stokes (RANS) equations are solved by commercial CFD code FLUENT® v.14.5. Simulations are carried out on Windows 7, Intel® Core™ i7 3.40 GHz with RAM memory 8 GB.

Two-dimensional velocity field visualization for different Re (10000, 14000, and 18000) is done at $z/D=2.75$. Figure 8 presents the velocity field comparison between experiment (top images) and simulation (bottom images) results. Swirling core position both experimental and numerical does not change for different Reynolds number. Numerical results show that swirling core position is located in the center. On the other hand, experimental results show that swirling core position is not located exactly in the center. It is due to unsymmetrical geometry of twisted tape leads to unsymmetrical flow.

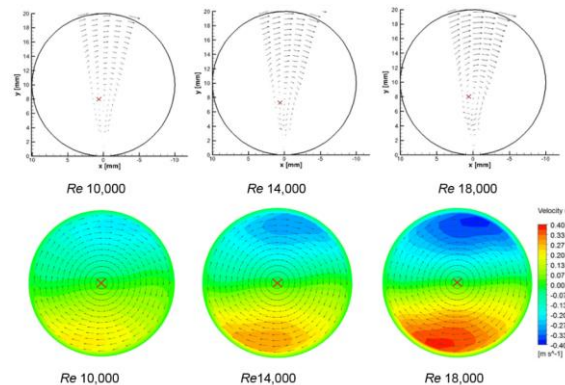


Figure 8: 2D tangential velocity field experiment and CFD at different Re .

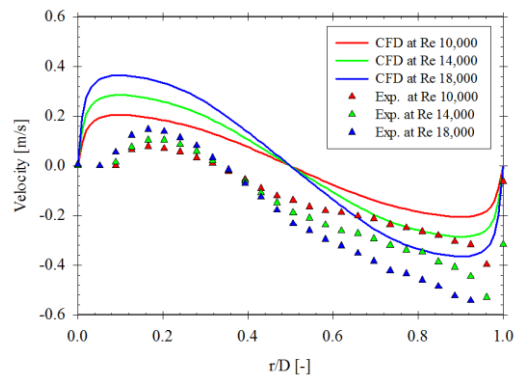


Figure 9: Tangential velocity experiment and CFD at different Re .

Quantitative comparison between experiment and CFD is done for tangential velocity at different Reynolds number, as shown in Fig 9. The qualitative comparison of tangential velocity between experiment and CFD, at different Reynolds number shows no good agreement. Therefore, qualitative comparison is needed in case different location of swirling core position.

The discrepancy between numerical and results might be due to the unsymmetrical geometry in experimental apparatus (twisted tape) as shown in Fig. 10. To analyze this problem, unsymmetrical geometry with 5° (same as experiment) and 20° are made in CFD model. Figure 11 shows the comparison of swirling core position between CFD and experiment at different axial position for Re 14,000. It can be seen that it is very difficult to get same core position in CFD. As a result, qualitative comparison is done by shifting the core position in CFD result to core position in experiment result. The swirling core position which is detected by PAUVP measurement is used for shifting the data in CFD. A good agreement between CFD and experiment is achieved when CFD data is shifted as shown in Fig. 12, Fig. 13 and Fig. 14.

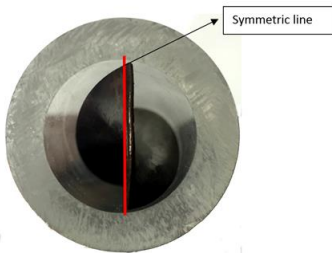


Figure 10: Unsymmetrical geometry of twisted tape (experiment).

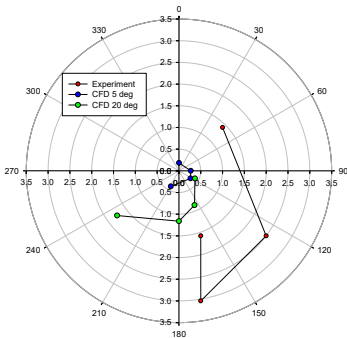


Figure 11: Swirling core position CFD vs experiment.

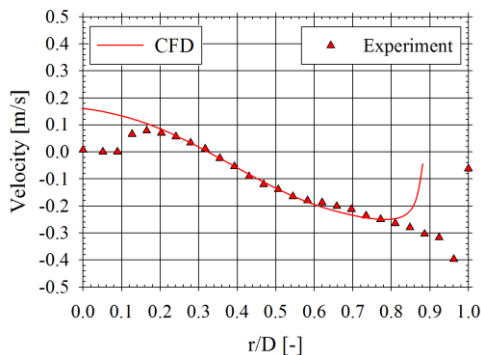


Figure 12: Tangential velocity for Re 10,000 at 2.75D (CFD vs experiment).

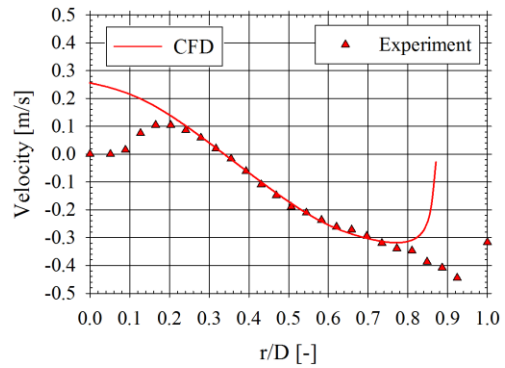


Figure 13: Tangential velocity for Re 14,000 at 2.75D (CFD vs experiment).

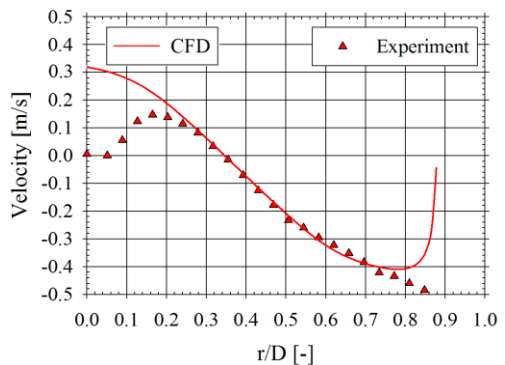


Figure 14: Tangential velocity for Re 14,000 at 2.75D (CFD vs experiment).

4. Summary

Two-dimensional velocity field measurement has been successfully developed using phased-array technique. This measurement technique has been tested for measuring 2D velocity field in swirling pipe flow. Experimental data are used for validation commercial CFD code FLUENT in single-phase swirling flow. It is concluded that swirling core position in experimental data is needed for a correction in CFD investigation.

References

- [1] Takeda Y: Measurement of velocity profile of mercury flow by ultrasound Doppler shift method, Nucl. Technol. 79 (1987), 120-124.
- [2] Takeda Y & Kikura H: Flow mapping of the mercury flow, Experiments in Fluids, 32(2) (2002), 161-169.
- [3] Liu JN, *et al.*: Ultrasonic tomographic velocimeter for visualization of axial flow fields in pipes, Flow Measurement and Instrumentation, 41 (2015), 57-66.
- [4] Lemmin U: High Resolution 3-D Acoustic Doppler Velocity and Sediment Flux Profiling in Laboratory and Environmental Studies: Potential and Limits, 3rd International Symposium on Ultrasonic Doppler Method for Fluid Mechanics and Fluid Engineering, (No. LHE-CONF-2002-003), 3(2002), 145.
- [5] Ohbayashi H, Yamaguchi K, & Takeda Y: Fundamental Study for Development of Vector-UVP, 4th International Symposium on Ultrasonic Doppler Method for Fluid Mechanics and Fluid Engineering, 4 (2004), 125-128.
- [6] Hamdani A, Ihara T, & Kikura H: Experimental and numerical visualizations of swirling flow in a vertical pipe, Journal of Visualization, 19(3) (2016), 369-382.

Ultrasonic characterization of 3-D thermal turbulence confined by moderate aspect ratio box

Megumi Akashi¹, Yuji Tasaka¹, Yuichi Murai¹, Takatoshi Yanagisawa²

¹Laboratory for Flow Control, Hokkaido University, Sapporo 060-8628, Japan

²Department of Deep Earth Structure and Dynamics Research, Japan Agency for Marine-Earth Science and Technology (JAMSTEC), Yokosuka 237-0061, Japan

Ultrasonic velocity profiling was performed in a square Rayleigh-Bénard (RB) cell confined by a moderate aspect ratio box using water as working fluid. Rayleigh number, Ra , was in a range from 8.8×10^5 to 1.3×10^7 and the regime of thermal turbulence were expected. Spectra of velocity were calculated to capture transition of spatiotemporal characteristics. Velocity maps show that cellular flow vanishes, and instead large scale flow arises from coalescence of transient plumes and drifts in a direction at $Ra = 2.4 \times 10^6$. As reached $Ra = 1.3 \times 10^7$, this large scale flow is divided to several pieces and their arrangement change temporally. Spectra also represent modification of shapes by the transition. The energy spectrum obtained at $Ra = 8.8 \times 10^5$ has a clear gap of energy between large and small scales of flow unlike that the others have simple decrease of the energy from large to small scales. The power spectrum obtained at $Ra = 1.3 \times 10^7$ shows a clear peak at much lower frequency in addition to oscillations corresponding to behaviors of local structures. This represents the temporal characteristic of 3-D motions in large scale flow and it may be considered to be unique to RB convection confined by a moderate aspect ratio box.

Keywords: Natural convection, Thermal turbulence, Large scale flow, Flow reversal

1. Introduction

Rayleigh-Bénard convection in fluid layers heated from below is the most fundamental thermal convection and has been a preferred subject for the study of turbulence. In this system, cellular convection with horizontal length scale comparable to the layer depth occurs for small enough values of the Rayleigh number. As the Rayleigh number is increased, cellular flow vanishes and is replaced by a random array of transient plumes and the regime achieves thermal turbulence. In further increase, these plumes coalesce and drift in a direction near the bottom and in the opposite direction near the top of the layer. In the case of water having Prandtl number $Pr = 7.0$, this large scale flow is formed around Rayleigh number $Ra = 2.4 \times 10^6$ in the experiment [1]. At high Rayleigh number conditions, plumes separating from the thermal boundary layer interact with the mean shear flow. The interactions tilt the plumes, generate a Reynolds shear stress and maintain the large scale flow against viscous dissipation. Even with considerations of such high Rayleigh number effects, there is a room for discussions, for example, why such transition occurs and how the direction of the large scale flow is determined. The investigation of the behavior of large scale flow mostly has been limited to convection confined by boxes of aspect ratio close to unity. And spontaneous flow reversals of the large scale flow were detected and analyzed in the particular case of the two-dimensional (2-D) rectangular geometry [2]. The occurrence of flow reversals sensitively depends on the aspect ratio, because the lateral wall of box is decisive for the large scale flow. Therefore, much interest centers to investigate the behavior of large scale flow in 3-D thermal turbulence confined by a moderate aspect ratio box from both points of view in engineering and

geophysics.

Point measurements have been employed to investigate the behavior of thermal turbulence, e.g. thermocouples and a laser doppler anemometer, and have detected statistic features of thermal turbulence [3,4]. In the present report, ultrasonic velocity profiling (UVP) is used to visualize the behavior of large scale flow in thermal turbulence confined by a moderate aspect ratio box as time-space velocity maps. Besides, we obtain spatiotemporal characteristics of thermal turbulence quantitatively by calculating spatial spectra and power spectra from the time-space velocity maps using discrete Fourier transform. Less effort has been made to investigate transition of spatiotemporal characteristics of 3-D thermal turbulence as increasing Rayleigh number experimentally. And it is important to understand how large scale flow occurs and how the structure of large scale flow changes as increasing Rayleigh number. In this study, a range of Rayleigh numbers from 8.8×10^5 to 1.3×10^7 is investigated.

Rayleigh-Bénard convection in this system is described by two non-dimensional numbers; Rayleigh number ($Ra = g\beta\Delta TL^3/\kappa\nu$) indicating the balance between buoyancy and viscous force and Prandtl number ($Pr = \kappa/\nu$), where g and ΔT are gravitational acceleration and vertical temperature difference of the fluid layer, β , κ , and ν are bulk modulus, thermal diffusivity and kinematic viscosity of the test fluid, respectively.

2. Experimental apparatus and method

2.1 Apparatus

Figure 1 shows illustrations of the experimental setup. The fluid layer has a horizontal cross section of $200 \times 200 \text{ mm}^2$ and the height is $L = 40 \text{ mm}$, giving an

aspect ratio five. The working fluid is water with a mean temperature of 22 °C, having $Pr = 6.8$. The upper and bottom plates of the fluid layer are made of copper with the temperature of each plate are maintained by circulating water. The experimental conditions regarding temperature are listed on Table 1. Here T_c and T_h mean the temperatures at the top and bottom plate, respectively, and the vertical temperature difference of the fluid layer is $\Delta T = T_h - T_c$. The Rayleigh number is controlled by ΔT in a range from $Ra = 8.8 \times 10^5$ to 1.3×10^7 , where thermal turbulence regime is expected and large scale flow occurs as reached $Ra = 2.4 \times 10^6$. The side walls of the fluid layer are 10 mm thick Teflon block providing good thermal insulation. In addition, the outside temperature is kept at a mean temperature of the test fluid by air conditioning in the room.

Table 1: Experimental conditions regarding temperatures

	$T_h(^{\circ}\text{C})$	$T_c(^{\circ}\text{C})$	$\Delta T(^{\circ}\text{C})$	Ra
Exp.(a)	22.5	21.5	1	8.8×10^5
(b)	23.5	20.5	3	2.6×10^6
(c)	26	18	8	7.0×10^6
(d)	30.5	15.5	15	1.3×10^7

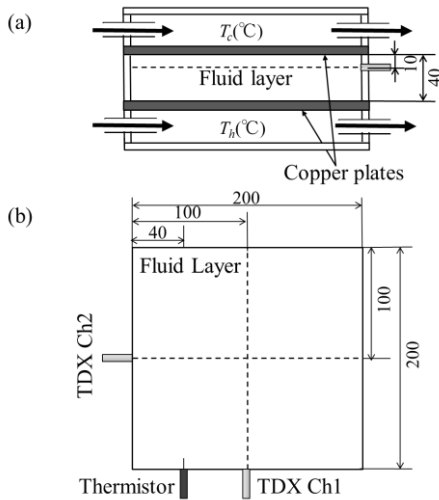


Figure 1: (a) Side view of the setting of the experiment. The dimensions are in mm. (b) Top view of the fluid layer. Dash lines show an ultrasonic beamline of the transducer.

2.2 Measurement method

UVP was used to measure the velocity field of the flow in thermal turbulence. The equipment for velocity measurement was a UVP-Duo (Met-Flow S.A); the basic frequency and effective diameter of the ultrasonic transducer are 4 MHz and 5 mm. Two transducers (TDX Ch1, TDX Ch2) were set in holes on the sidewalls and had direct contact with the fluid to improve transmission of ultrasonic wave as shown in Fig. 1. Each transducer was located with its center 10 mm away from the upper plate. With this condition,

UVP has the velocity resolution of 2.7×10^{-1} mm/s, the spatial resolution of 9.7×10^{-1} mm and the temporal resolution of 2.1 s. The flow velocities were measured along two beamlines from those transducers which cross perpendicularly at the center of the fluid layer. Therefore, it was possible to deduce 3-D structure of thermal turbulence with their time variations. Also spatial-temporal characteristic of the thermal turbulence were captured quantitatively by calculating spatial spectrums and power spectrums of the velocity fluctuations from time-space velocity map through DFT. As ultrasonic reflection particles, HP20SS, were suspended in the fluid. The particles have 63-153 μm in diameter and about 1.01 in specific gravity. To measure temperature oscillations simultaneously, a thermistor probe was installed in the fluid layer close the sidewall as shown Fig.1 with setting height 10 mm below the top plate. Besides, two thermistor probes were also installed to monitor the temperatures of top and bottom plates. The sampling rate and temperature resolution on the measurements are 2.0 Hz and 0.01 °C, respectively

3. Results

3.1 Multiple-scale flow patterns in thermal turbulence

Figure 2 shows time-space velocity maps of the flow for 1000 s observed by the UVP at four Rayleigh numbers, (a) $Ra = 8.8 \times 10^5$, (b) 2.6×10^6 , (c) 7.0×10^6 and (d) 1.3×10^7 . The horizontal axis is the time and the vertical axis is the distance from the respective transducers. The UVP measures horizontal velocity along the ultrasonic beamlines, and the direction and magnitude of the horizontal flow velocity are displayed in gray scale: White (minus) indicates flow toward the transducer and black (plus) indicates flow away from the transducer. Time-space velocity maps obtained by the transducers are in the velocity range and show similar patterns at each Rayleigh number. This suggests that the flow structure is almost isotropic (no dependence on sides of the box). We, therefore, display the velocity maps obtained from one transducer in Fig. 2.

In the case of (a) $Ra = 8.8 \times 10^5$, there are relatively clear boundaries of positive and negative velocity component area on the velocity map and each velocity band is in size of 50 – 100 mm. This suggests that a 3-D cellular structure remains with indistinct boundaries. The cells are organized by transient plumes and the boundaries are fluctuating. Positions of the cells are kept for about several hundred seconds.

In the case of (b) $Ra = 2.6 \times 10^6$ and (c) $Ra = 7.0 \times 10^6$, positive and negative velocity parts move on the map mainly toward the transducer through measurement lines. The parts have around 50 mm in size and may correspond to local convection structure organized by transient plumes. The direction is kept the same throughout measurement time and this carrier flow indicates large scale flow in thermal turbulence. In comparison with condition (b), the velocity map for condition (c) has smaller structures, but takes common

characteristics of motions of the local structures.

As reached (d) $Ra = 1.3 \times 10^7$, unlike other cases, motion of the local structure is not uniform. The large scale flow seems to be divided in to two or three pieces and corresponding flow direction changes temporally. A comparison of the velocity maps through the conditions from (a) to (d) indicates that the magnitudes of flow velocities become larger at higher Rayleigh number, while the sizes of local structures become smaller and the fluctuations of flow velocity have shorter periods. To characterize variations of these scales, in the next section, spatial spectrum and power spectrum calculated from time-space velocity maps and temperature fluctuations are investigated.

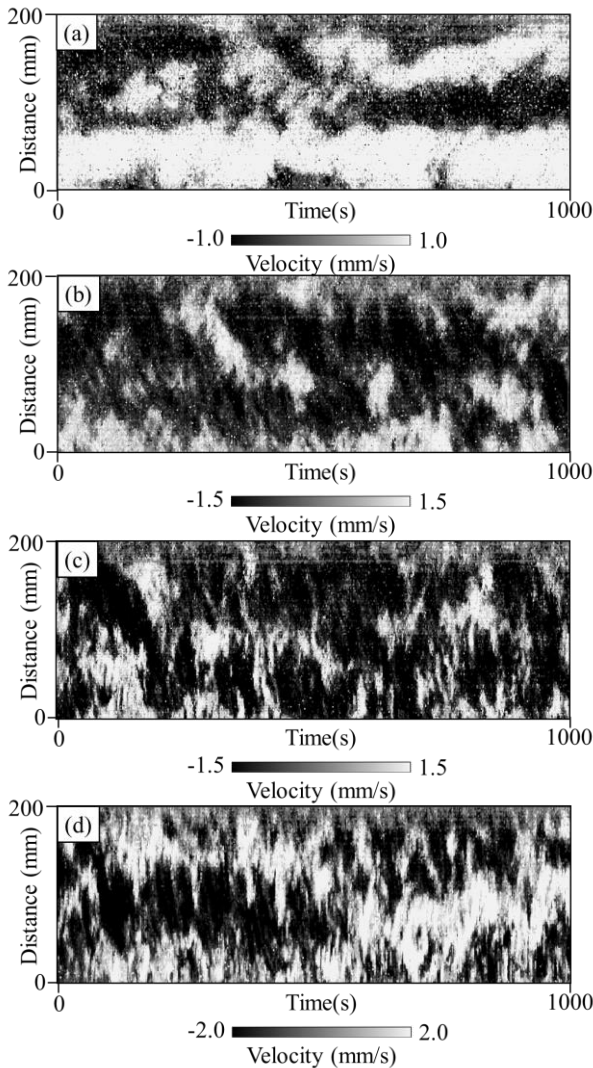


Figure 2: Time-space velocity map of the horizontal flow velocities measured by Ch1 for 1000 s at (a) $Ra = 8.8 \times 10^5$, (b) 2.6×10^6 , (c) 7.0×10^6 and (d) 1.3×10^7

3.2 Time-space characteristics of thermal turbulence

Spectral analysis is the most straightforward tool to understand complex structures of thermal turbulence. Figure 3(A) shows time-averaged energy spectral density, average of energy spectra obtained at each time

step, at each Rayleigh number. The spectra show continuous variation indicating feature of thermal turbulence. These are classified into two shapes, the spectrum obtained at (a) $Ra = 8.8 \times 10^5$, and the ones for larger Ra conditions. The former has a peak at the wave number of 0.01 mm^{-1} whose wavelength is 100 mm and indicates the sizes of 3-D cells observed in the time-space velocity map in Fig. 2(a). Also it has inflection point around 0.07 mm^{-1} while the other spectra show almost simple decreases. The latter has the maximum energy at the longest wave number of 0.005 mm^{-1} whose wavelength is 200 mm. This corresponds to size of the large scale flow and these agree with observations in the velocity map shown in Fig. 2.

To elucidate instantaneous features of scale of flows, Fig. 3(B) shows comparison of instantaneous energy spectral densities at (a) $Ra = 8.8 \times 10^5$ and (c) $Ra = 7.0 \times 10^6$. The spectra at (a) show peaks at the wavelength of about 100 mm corresponding to the 3-D cells. Besides, they have several spectral peaks at higher wave numbers and these indicate the sizes of transient plumes. The spectra at (c) $Ra = 7.0 \times 10^6$ have an additional peaks at the wavelength of about 50-100 mm that correspond to local structures. These sizes of local structures have deviation and change every moment. Thus the corresponding peaks disappear in the time averaged spectrum. Besides, the spectrum at $Ra = 7.0 \times 10^6$ has several peaks at higher wave numbers describe transient plumes as well as energy spectrum density at (a) $Ra = 8.8 \times 10^5$. But the variation of energy has clear difference between them. The former ones have clear threshold to separate larger and smaller structures, but the latter shows continuous envelope as also mentioned at the averaged spectra.

Velocity fluctuations observed in the velocity map (Fig.2) with low frequencies are consistent with the previous studies [3]. In thermal turbulence, they are caused by a thermal boundary layer instability triggered

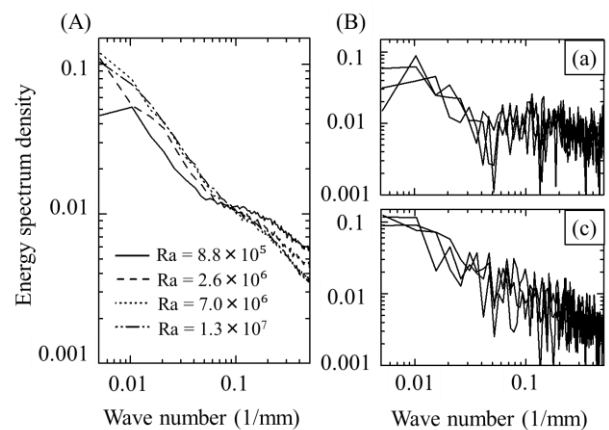


Figure 3(A): Average of energy spectral densities obtained at each time step, at each Ra . $Ra = 8.8 \times 10^5$ (solid line), 2.6×10^6 (dash line), 7.0×10^6 (dot line) and 1.3×10^7 (dash dot dash line). (B): Temporal energy spectrum densities at 264s, 500s and 764s at (a) and at 250s, 500s and 750s at (c).

by incoming transient plumes which are transported in

fluid layers [4]. In this study, velocity and temperature fluctuations with frequencies in the order of 10^{-3} Hz have some spectral peaks at each Rayleigh number as shown in Figure 4 (A). It indicates the fluctuation by a thermal boundary layer instability in the point of the order. In addition to these fluctuation, the spectrum at $Ra = 1.3 \times 10^7$ has a dominant peak at much lower frequency 0.0014 Hz .

Figure 4 (B) shows the periods of these oscillations plotted, τ , normalized by thermal diffusion time, L^2/κ against Rayleigh number, where the open symbols represent periods corresponding to dominant peaks in power spectrum of velocity map, and solid symbols periods calculated from frequencies of temperature fluctuations. A solid line indicates the variation of periods extrapolated from the previous study with temperature measurements in the time dependent flow regime at which cellular convection emerges [3]. The obtained period agree with the extrapolation at $Ra = 8.8 \times 10^5$, and the periods obtained at larger Ra numbers have large gap against the extrapolation. This is because that large scale flows emerge and transport transient plumes all around the box for $Ra \geq 2.6 \times 10^6$: behaviors of the thermal plumes are dominated by large scale circulation, not by thermal boundary layer instability and the periods become longer. Variation of the periods tends to decrease as increasing Rayleigh number for $Ra \geq 2.6 \times 10^6$, because the magnitude of velocity of transient plumes become larger. Therefore, the fluctuation with a much longer period $\tau\kappa/L^2 = 0.069$ (0.0014 Hz in frequency) at $Ra = 1.3 \times 10^7$ seems isolated and is not a kind of ones by transient plumes. To characterize such long-term fluctuations observed at $Ra = 1.3 \times 10^7$, a long-term recording is performed as detailed in the next section.

3.3 Fluctuation of large scale flows

Figure 5 shows the time-space velocity maps of the flow for 4000 s measured by the Ch2 at $Ra = 1.3 \times 10^7$. As re

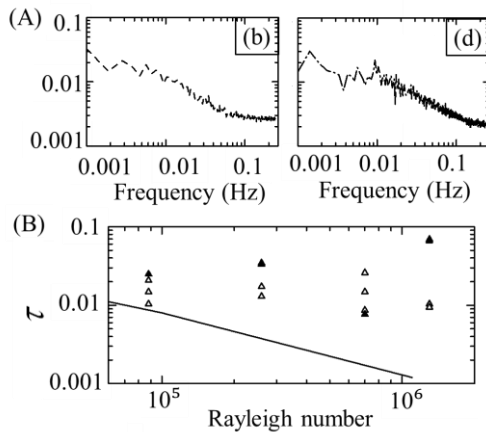


Figure 4: (A) Power spectrum density at (b) $Ra = 2.6 \times 10^6$ and (d) $Ra = 1.3 \times 10^7$ (B): The periods against Rayleigh number. (open symbols) periods corresponding to dominant peaks in power spectrum of velocity map. (solid symbols) periods calculated from frequencies of temperature fluctuations. (a solid line) the extrapolation from previous studies [3].

ported in the section 3.1, there are separated large scale flows and drift local structures organized by transient plumes for each direction. Advections of the local structures are represented by thinner stripes on the velocity map and these have a fluctuation with a period $\tau\kappa/L^2 = 0.01$ (0.01 Hz in frequency). In addition to this, there are thicker band on the map and it fluctuates with a period $\tau\kappa/L^2 = 0.09$ (0.001 Hz). This motion of large scale flow is considered to be affected by the lateral wall of moderate aspect ratio box. Characterizing this meandering motion is ultimate goal of this study.

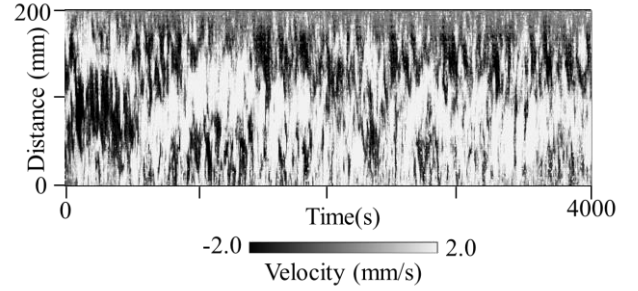


Figure 5: Time-space velocity map of the horizontal flow velocities obtained by Ch2 for 4000 s at $Ra = 1.3 \times 10^7$

4. Conclusion

The spatiotemporal velocity maps obtained by UVP at four Rayleigh numbers were investigated to elucidate transition of spatiotemporal structures of thermal turbulence confined by a moderate aspect ratio box. In the case of $Ra = 8.8 \times 10^5$, 3-D cellular structures are indistinctly organized by transient plumes. At $Ra = 2.6 \times 10^6$ and 7.0×10^6 , local structures are carried in a direction and it indicates the emergence of large scale flow. As reached $Ra = 1.3 \times 10^7$, large scale flow is divided to several pieces and their arrangement changes in time. A comparison of spectra represents the transition as the change on spectral shape. The spatial spectra at the smallest Ra have clear gaps of energy between large and small scales of the flow. The others have almost simple decrease of the energy from large to small scales with several peaks representing local structures. In addition to the consistent oscillation, the much longer term fluctuation is dominant in power spectrum at $Ra = 1.3 \times 10^7$. It indicates the motion of large scale flows at the long-term recording and it is considered to be the effect of the lateral walls of a moderate aspect ratio box.

References

- [1] Krishnamurti R & Howard LN: Large-scale flow generation in turbulent convection, Proc Natl. Acad. Sci. USA, 78 (1981)
- [2] Sugiyama K, *et al.*: Flow Reversals in Thermally Driven Turbulence, Phys. Rev. Lett, 105(2010)
- [3] Krishnamurti R: On the transition to turbulent convection. Part2. The transition to time-dependent flow, J. Fluid Mech., 42(1970)
- [4] Qiu X-L *et al.*: Large-scale coherent rotation and oscillation in turbulent thermal convection, Phys. Rev. E, 61(2000)

Appearance of 3D structures on quasi-2D convection rolls in a Rayleigh-Bénard convection imposed by horizontal magnetic field

Wataru Ishimi¹, Tobias Vogt², Yuji Tasaka¹, Takatoshi Yanagisawa³,
Ataru SAKURABA⁴, Yuichi Murai¹ and Sven Eckert²

¹ Laboratory for flow control, Hokkaido University, Sapporo, 060-8628, Japan

² Helmholtz-Zentrum Dresden-Rossendorf, 01314 Dresden, Germany

³ Department of Deep Earth Structure and Dynamics Research (D-EARTH), Japan Agency for Marine-Earth Science and Technology (JAMSTEC), Yokosuka 237-0061, Japan

⁴ Department of Earth and Planetary Science, University of Tokyo, Tokyo 113-0033, Japan

We investigate the development of 3D structures on quasi-2D convection rolls of Rayleigh-Bénard convection in a liquid metal layer with an imposed horizontal magnetic field using UVP. Measurement lines arranged parallel to the magnetic field effectively represent 3D structures on the convection rolls. As the fundamental 3D structure, existence of horizontal circulations parallel to the axis of convection rolls was elucidated. Scale estimation suggests that the circulation is caused by Ekman pumping due to increase of rotation speed of the rolls and thinning of velocity boundary layer on the side wall perpendicular to the magnetic field as typical MHD effects. On the four-roll state that is observed in a parameter region where the Lorentz force against the buoyancy is relatively weak, couple of thinner vortices wrapping around the primary convection rolls and advection along the horizontal circulation was observed. Oscillating motion of the main rolls is modulated by these advectons. Parameter region for the appearance of this 3D structure is very close to that for the flow reversals and it may have importance to determine the appearance of the flow reversals.

Keywords: Ultrasonic flow visualization, MHD, Rayleigh-Bénard convection, Flow instability

1. INTRODUCTION

The application of a horizontal magnetic field to the liquid metal Rayleigh-Bénard convection stabilizes complex three-dimensional motions into quasi-two dimensional convection rolls because of the effect of Lorentz force. This MHD-Rayleigh-Bénard convection is governed by three non-dimension parameters, Rayleigh number ($Ra = \beta g \Delta T L^3 / \kappa \nu$) indicating the balance between buoyancy and viscous force, Chandrasekhar number ($Q = \sigma B^2 L^2 / \rho \nu$) indicating the balance between Lorentz and viscous force, and Prandtl number ($Pr = \kappa / \nu$, 2.3×10^{-2} in GaInSn), where β , ν , κ , σ , ρ are respectively, bulk modulus, kinematic viscosity, thermal diffusivity, electric conductivity, and density of a test liquid metal, and g , ΔT , L , and B are respectively, gravity acceleration, vertical temperature difference, height of the fluid layer, and intensity of the magnetic field.

In a recent paper [1], we reported the regime diagram of the convection patterns including the rolls-number dependence for Rayleigh number and Chandrasekhar number in a square vessel of aspect ratio five. In cases of moderate intensity of the magnetic field, various flow patterns appear depending on a balance between Lorentz force due to the applied magnetic field and the buoyancy. With decreasing intensity of the magnetic field, the quasi-2D convection rolls arrange parallel to the magnetic field assumes considerable 3D structures. Our group represented regime transitions including characteristics phenomena termed ‘flow reversals’ with Ra and Q [2]. This phenomenon might be caused by oscillatory instability and skewed varicose instability on quasi-two

dimensional rolls. There is, however, still very small knowledge about 3D development of the flow structures.

In this report, we provide detailed representation of the 3D development by investigating transitions on spatiotemporal maps of flow velocity component parallel to the magnetic field reflecting 3D modifications of structures by ultrasonic velocity profiler (UVP), which is a good tool to visualize flow patterns in opaque fluids like liquid metals. Doing that in addition to velocity profile measurements perpendicular to the magnetic field by UVP, the development of 3D structures on quasi-2D convection rolls of Rayleigh-Bénard convection can be observed.

2. APPARATUS AND METHOD

Figure 1 shows the setting of the experimental container that has the same geometry as in the previous study [1]. The test section has dimensions of 200 mm \times 200 mm \times 40 mm leading to an aspect ratio of 5. The top and bottom plates are made of copper. The temperature of each plate was kept constant by circulating water via a thermostatic bath. The container was filled with the gallium-indium-tin alloy (GaInSn) of which melting point is -19 degree of Celsius, and thus it is in liquid state at room-temperature, is commercial liquid metal alloy composed of 67% of gallium, 20.5% of indium and 12.5% of tin. The fluid temperature was constant during each parameters. A DOP2000 velocimeter (Signal Processing SA) was used to measure the fluid velocities. The device is connected to 8 MHz transducers which are set in holes in the side wall made of polyvinyl chloride and are in direct contact with the test fluid. The velocity

components perpendicular to the magnetic field were measured by two transducers (ch1, ch2), while the velocity components parallel to magnetic field were measured by six transducers (ch3-8). The UVP measures the projected flow velocity along each line, and thus the present arrangement of the transducers provides two velocity components, parallel and perpendicular to the magnetic field. The temperature fluctuations were measured by thermocouples at three points (Fig. 1). The head of each thermocouple was located 3 mm below the top surface of fluid layer. A magnetic generator consisting of a pair of rectangular shaped coils creates quasi-uniform horizontal magnetic field with an intensity of 300 mT as the maximum.

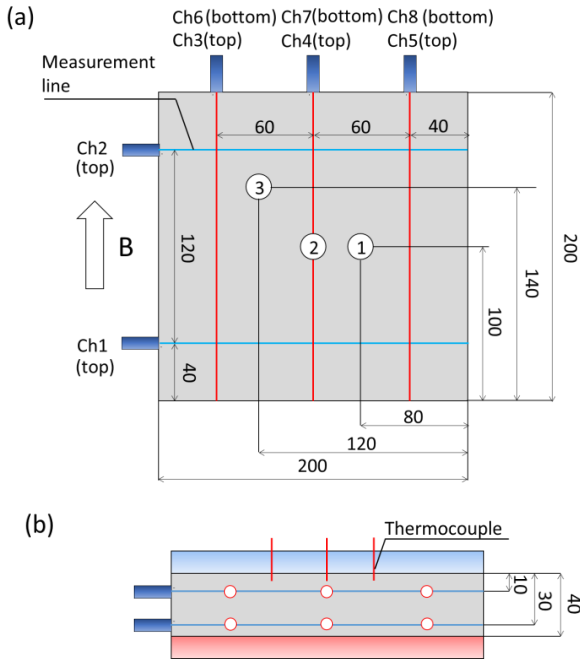


Figure 1: Geometry of the experimental container; (a) top view of the vessel and UVP measurement lines, and (b) side view and locations of each sensor

3. RESULTS AND DISCUSSION

3.1 Flow structure parallel and perpendicular to magnetic field in 5 roll configuration

Spatio-temporal velocity distributions perpendicular and parallel to the magnetic field were measured at $Ra = 1.26 \times 10^4$ and $Q = 3.38 \times 10^3$. Figure 2 shows the velocity distribution along the four measurement lines (Ch1, Ch6-8) for 2000 s. The distribution at Ch1 confirms that five-roll structure arranged parallel to the magnetic field exists stably. In the direction parallel to the magnetic field, the velocity distribution is separated into two regions having opposite flow directions at the middle of measurement distance in Ch6-8. In comparison with the velocity field perpendicular to the magnetic field, the magnitude of velocity component parallel to the magnetic field is smaller, but not negligible, around 1/5. Though the flow achieves a highly quasi-two dimensional structure shown by Ch1 accompanied by a weak structure in the direction parallel to the magnetic field.

The flow direction shown in Fig. 2 is opposite between Ch6, Ch8 and Ch7. Checking the arrangement of transducers (Fig. 1) against arrangement of rolls (Fig. 2 Ch1), Ch6 and Ch8 are placed near the edge of a convection roll, while Ch7 is placed at the center of a convection roll. These results indicate that two horizontal circulations exist inside the roll structure. Figure 3 shows the illustration of this circulation expected from the velocity profile measurements. This circulation is directed from the wall to the center of the vessel at the center of rolls and the opposite direction at the outside of roll structure. This circulation may be caused by the formation of Ekman pumping inside the Hartman layers: In MHD flows, existence of electrically-insulated walls perpendicular to the magnetic field makes velocity boundary layers thinner because of induced electric current in the fluid layer (Hartman layer) [3]: Ekman pumping induces fluid motion perpendicular to walls by the conversion of divergence at a boundary layer in a rotating flow field. The order of flows due to Ekman pumping is estimated to compare with the horizontal circulation observed. Induced velocity component normal to the wall, w_e driven by Ekman pumping is estimated by thickness of boundary layer δ and normal vorticity component against the wall at the surface ω_z defined as, $w_e = 1/2 * \delta \omega_z$. Assuming that the roll structure takes rigid body rotation according to the isothermal core of usual Rayleigh-Bénard convections and roll size ($D \sim 40$ mm) is diameter of the rigid body, characteristic velocity U is defined as rotation speed of the roll. This is defined as $\delta_H = (\rho\nu/\sigma B^2)^{1/2}$ which depends only on the

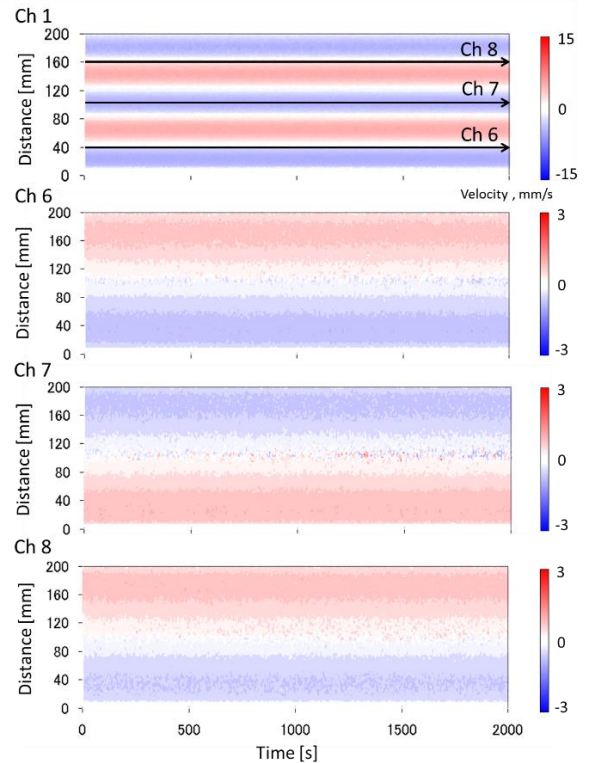


Figure 2: Spatio-temporal velocity distribution measured by UVP at each transducer; Ch1 perpendicular to the magnetic field; Ch6-8 parallel to the magnetic field ($Ra = 1.26 \times 10^4$ and $Q = 3.38 \times 10^3$)

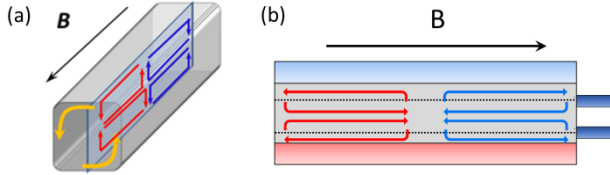


Figure 3: Schematic views of the horizontal circulation with five rolls; (a) the flow direction in the roll structure with quasi-two dimensional convection, (b) the overall view of horizontal circulation inner roll structure at side view

fluid property and the strength of the magnetic field [4]. According to this formula, thickness of the Hartman layer is estimated as $\delta_H = 6.89 \times 10^{-1}$ mm. The vorticity is $\omega_z = O(U/D)$, so the velocity due to Ekman pumping is estimated as $w_e = O(10^{-1})$. The magnitude of time-averaged velocity parallel to the magnetic field is 0.49 mm/s and assents to the estimated order of Ekman pumping.

3.2 Appearance of 3D structure in four roll

Velocity distributions displayed in Fig. 4 show the results of the measurement at $Ra = 1.2 \times 10^4$ and $Q = 5.12 \times 10^2$, where a four-roll structure is emerged. The result at Ch2 perpendicular to the magnetic field confirms formation of the four rolls with small oscillations. In the results of Ch6-8 parallel to the magnetic field, characteristic small scale flow structures appear, while the roll structures are maintained (Fig. 4 Ch6-8). These small structures are advected from the center to the side-walls of the vessel and are superimposed with small fluctuations. These small fluctuations might be caused in connection with the oscillation of the roll structure. Comparing the signals of the transducers placed at the bottom and the top of fluid layer, it seems that these flow structures span around the entire convection roll circumference.

To characterize the roll and small scale structures, Fig. 5 shows the results of two-dimensional Fourier transform calculated from spatiotemporal velocity distributions at Ch2 and Ch8, where the vertical axis represents wavenumber k , the horizontal axis represents frequency f . Here the sampling time is 2.4 s and the spatial resolution is 1.37 mm. It is observed that two peaks appear on the spectra of Ch2 and Ch8 at $f = 0.003$ and 0.03 Hz. The former frequency indicates the cycle of emitted vortex generations. The period corresponding to this frequency is about 330 s. This agrees with the period observed on the spatiotemporal velocity distributions.

The latter frequency indicates the frequency of the short time oscillation on the roll structures, because the corresponding period, about 33 s, agrees with the circulation time with considering elliptic shape for the rolls, 31.4 s (e.g. [3]). For the estimation we assumed that length of circulation on a roll is $\sim 2\pi \times 10$ mm, where 10 mm equals the displacement of the measurement line from the center of the rolls, and the typical flow velocity is around 4 mm/s. This oscillation of roll structure affects the advective vortices, because the vortices move along the horizontal circulation created by the primary rolls. In comparison with the spatiotemporal map shown in Fig. 4,

the former frequency component corresponds to the cycle of the vortex behaviour, generation at the center of vessels, advection along the horizontal circulation, and disappearance at the side wall. The corresponding wave number k on the spectrum of Ch2 is $k = 0.019$ mm $^{-1}$, this value shows the size of roll structures. It is assumed that the oscillation of the former frequency at each roll is influenced by the appearance of these vortices.

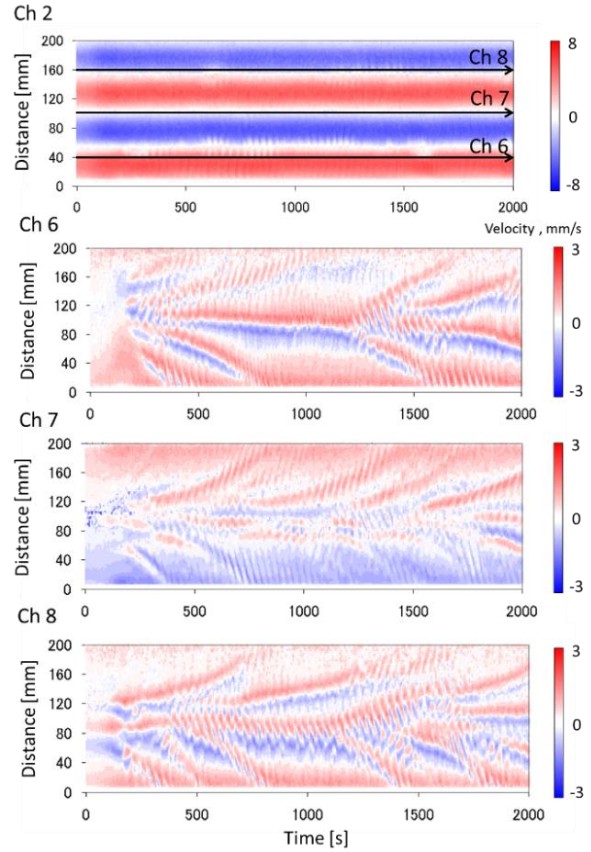


Figure 4: Spatio-temporal velocity distributions in the four roll structure ($Ra = 1.2 \times 10^4$ and $Q = 5.12 \times 10^2$), Ch2 perpendicular, Ch6-8 parallel to the magnetic field

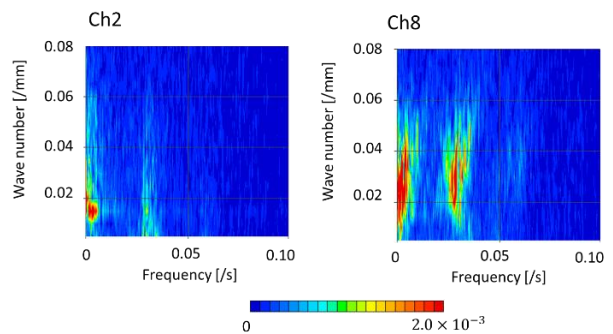


Figure 5: Two-dimensional Fourier transform of the spatiotemporal velocity distribution of Fig. 4 at Ch2 and Ch8, where the horizontal axis represents frequency f the vertical axis represents wavenumber k .

We may be able to find the corresponding flow structure in results of numerical simulations previously done by our group to reproduce the experimental results [5]. Figure 6 shows examples of the simulations, (a) $Ra = 1.0 \times 10^4$ and $Q = 1.0 \times 10^3$, (b) $Ra = 3.0 \times 10^4$ and $Q = 1.0 \times 10^3$. The setting parameters do not agree completely with the experiments, but each result qualitatively represents flow structures expected from Fig. 2 and Fig. 4, respectively; Fig. 6(a) shows five-roll condition, where the rolls stably exist; Fig. 6(b) shows, primary four rolls and secondary fine vortices around primary ones. It is assumed that transducers mounted parallel to the magnetic field detected these thinner vortices.

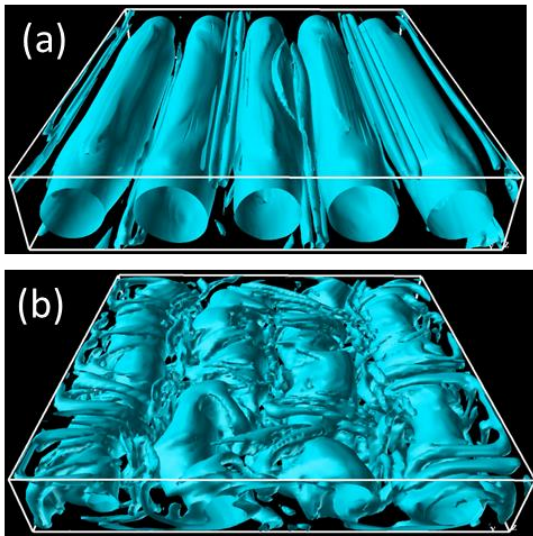


Figure 6: Appearance of secondary vortices around primary convection rolls observed in numerical simulation; (a) $Ra = 1.0 \times 10^4$ and $Q = 1.0 \times 10^3$, (b) $Ra = 3.0 \times 10^4$ and $Q = 1.0 \times 10^3$ [5]

Appearance of these thinner vortices suggests that secondary instability occurs. The mechanism behind this instability is explained as follows. In the laminar state, the flow in the convection vessel is composed of the main convection rolls, aligned along the direction of magnetic field. In addition to this, there are much smaller rolls located at the vessel corners and between neighbouring rolls (see figure 6(a)). The axis of these smaller vortices is parallel to the primary convection rolls. If the rotational speed of the primary convection rolls exceeds a certain threshold, the smaller corner vortices are entrained and wind around the primary rolls. The consequence is a counter rotating vortex pair that spans around the perimeter of the primary convection rolls and whose visual appearance looks similar to Taylor-Görtler vortices [6].

Previous work indicated that the regimes taking different number of rolls can be organized by Ra/Q on the $Q - Ra$ plane [1]. The fraction of Ra/Q is a measure for the ratio of the buoyancy to the Lorenz force. This flow structure with thinner vortices appears at $Ra/Q \sim 10$ that corresponds to the region of Ra/Q to observe the flow reversals [1]. Appearance of these 3D structures may be

connected to the flow reversals, especially restriction of the range of Ra/Q and hysteresis.

4. CONCLUSION

Appearance of 3D structure on quasi-2D convection rolls with imposed horizontal magnetic field was investigated by the measurement of velocity profiles parallel to the direction of magnetic field. As the fundamental 3D structures, horizontal circulation along the roll axis aligned parallel to the magnetic field, was observed through the experiments. The magnitude of this circulation is about 1/5 of speed of rotation of the rolls. Assuming that the roll structure takes rigid body rotation like a circular cylinder and applying some parameters in the formula of Ekman pumping, estimated velocity of wall-normal flows is comparable to the measurement results of circulation velocity. It suggests that this circulation is caused by Ekman pumping with increasing the rotation speed and thinning the velocity boundary layer on the side wall perpendicular to the magnetic field.

Additional 3D flow structures appear as couple of thinner vortices advecting along the horizontal circulation. Appearance of the vortices modulates the behaviour of primary convection rolls with a frequency that is about one order lower as the oscillation frequency of the rolls. The existence of the vortices is related to smaller vortices aligned parallel to the primary convection rolls. These vortices become unstable at a certain Ra/Q threshold and wind around the convection rolls. The range to observe this vortical structure on Ra/Q is very close to that for the flow reversals, $Ra/Q \sim 10$, appearance of the structure may restrict the appearance of the flow reversals.

Acknowledgement

This work was supported by JSPS KAKENHI Grant No. 24244073. Visiting of WI at HZDR was supported by CEED/Hokkaido University. The authors express thanks for these supports. The authors from HZDR acknowledge the financial support in the framework of the Helmholtz alliance “LIMTECH.”

References

- [1] Yanagisawa T, *et al.*: Convection patterns in a liquid metal under an imposed horizontal magnetic field, Phys. Rev. E 88(2013), 063020.
- [2] Tasaka Y, *et al.*: Regular flow reversals in Rayleigh-Bénard convection in a horizontal magnetic field. Phys. Rev. E. 93 (2016)
- [3] Sommeria J and Moreau R.: Why, how, and when, MHD turbulence become two dimensional. J., Fluid Mech. 118, (1982)
- [4] Yanagisawa T., Hamano Y., and Sakuraba A.: Flow reversals in low-Prandtl-number Rayleigh-Bénard convection controlled by horizontal circulation. Phys. Rev. E, 92, (2015)
- [5] Vogt T, *et al.*: On the formation of Taylor-Görtler vortices in RMF-driven spin-up flows. Exp. Fluids. (2011)

Ultrasonic Doppler Velocimetry Experiment of Lead-Lithium Flow

Yoshitaka Ueki¹, Yuya Noguchi¹, Juro Yagi², Teruya Tanaka², Takehiko Yokomine³,
Masaru Hirabayashi⁴, Kuniaki Ara⁴, Tomoaki Kunugi³, Akio Sagara²

¹ Mechanical Engineering, Osaka University, 2-1 Yamadaoka, Suita, Osaka 565-0871, Japan

² National Institute for Fusion Science, 322-6 Oroshicho, Toki, Gifu 509-5292, Japan

³ Nuclear Engineering, Kyoto University, Kyoto-Daigaku Katsura, Nishikyoku, Kyoto 615-8540, Japan

⁴ Fast Reactor Technology Development Department, Japan Atomic Energy Agency, Oarai, Ibaraki 311-1393, Japan

The lead-lithium eutectic alloy (PbLi) is a promising coolant for nuclear fusion reactors. Although PbLi flow and heat transfer in a nuclear fusion reactor condition needs to be comprehended, no velocity profile measurement techniques have been developed yet. Since PbLi is a high-temperature liquid metal, ultrasonic Doppler velocimetry (UDV) is a promising method. In the present paper, a series of investigations regarding the UDV measurement of PbLi flows are overviewed, and a UDV experiment of a laminar PbLi circular pipe flow is described. One of new findings is that naturally-contained particles as flow tracers differs by their alloying processes, and this difference influences the PbLi UDV measurement.

Keywords: Lead-lithium, high-temperature liquid metal, ultrasonic Doppler velocimetry

1. Introduction

A liquid metal is expected to be in use as a coolant since it has a low value of Prandtl number. For an example, a nuclear fusion reactor is expected to employ a liquid metal as a coolant. One of liquid metal candidates for the fusion reactor is lead-lithium eutectic alloy (PbLi) [1]. In a magnetic confinement fusion reactor, a plasma confining magnetic field exists even in a blanket region. Because of this, a liquid metal flow, such as PbLi flow, is reconstructed by the strong magnetic field, which is known as magnetohydrodynamic (MHD) flow. In order to design a fusion energy conversion system of the fusion reactor, we need to comprehend a complex fluid flow in a fusion reactor environment, where the lead-lithium flows under an influence of a magnetic field. The fluid flow needs to be known if the heat and mass transfer in the blanket has to be evaluated. Although, no flow velocity profile measurement techniques had been developed. Therefore, we employ ultrasonic Doppler velocimetry (UDV) in the present study.

Since the UDV was developed by Takeda [2], it was successfully applied to various kinds of liquid metals, such as mercury (Hg) (e.g., [2,3]), gallium-indium-tin eutectic alloy (GaInSn) [4,5], and molten gallium (Ga) [6] by using a regular transducer. Molten sodium (Na) [7], molten lead-bismuth eutectic alloy (PbBi) and molten bronze (CuSn) were measured by using an acoustic wave-guide [8]. As just described, the UDV is capable of measuring flow velocity profiles of room-temperature liquid metals and high-temperature liquid metals.

The UDV requires the following prerequisites:

- 1) Sound speed in a target fluid; generally, a sound speed depends on medium temperature.
- 2) Ultrasonic transmission at an interface between a tip material of a transducer and the target fluid. When the target fluid is a high temperature liquid metal, wettability

influences the interfacial ultrasonic transmission. Besides, acoustic impedances determine ultrasound reflection and transmission at the interface.

- 3) Ultrasound reflecting particles dispersed in the target fluid. They play a role as flow tracer particles.

Sometimes the technology and knowledge which solve problems of one liquid metal cannot be applied to another liquid metal. In other words, each liquid metal needs each research and development. It is because different liquid metals have quite different physical and/or chemical properties. For an example, although PbLi and PbBi have majority content of Pb in themselves, corrosion behaviors are quite different. PbBi corrosion is an oxidation-type, but PbLi corrosion is a dissolution-type [9]. It is empirically known that liquid metal corruptions influence the interfacial ultrasonic transmission [10, 11]. Based on this, to comprehend characteristics of the target liquid metal is necessary for successful UDV measurement. Studies of the prerequisites for PbLi are described in the following chapters.

2. Acoustic Properties of PbLi

The sound speed in the target fluid is necessary for UDV, since it is necessary for evaluating depth of each of interrogation volumes that UDV examines, and flow velocity of each of the interrogation volumes. Another physical property related to UDV is acoustic impedance. The acoustic impedance, Z , is a product of sound speed in a medium, C , and density of the medium, ρ . This physical property characterizes ultrasound transmission, reflection, and refraction at a medium interface.

Ueki et al. experimentally evaluated the sound speed in PbLi as a function of temperature [10]. Figure 1 is a plot of measured values of the sound speed in PbLi, together with those in Pb, PiBi [12], and Li [13] From this figure, it can be noticed that Li content in PbLi hardly contributes to determine the sound speed in PbLi. It is valid since the

weight percent of Li in PbLi, which is less than 5 wt%. Table 1 is a summary of acoustic properties of PbLi, PbBi, Pb, Li, and Ti. Ti is a wetting material of the transducer employed for the present study.

Table 1: Sound speeds and acoustic impedances.

	C (10^3 m/s)	Z (10^6 kg/m ² s)
PbLi (at 300°C)	1.785	16.9
PbBi (at 300°C)	1.739	18.3
Pb (at 330°C)	1.773	18.9
Li (at 300°C)	4.48	2.3
Ti (room temperature)	6.070	27.3

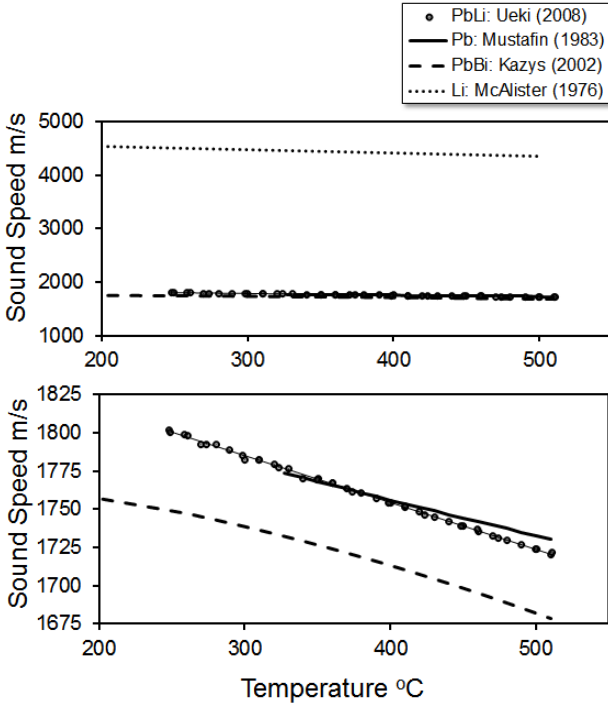


Figure 1: Sound Speed in molten PbLi, PbBi, Pb, and Li.

3. Ultrasonic transmission at interface

The ultrasonic transmission at the interface between the tip material of the transducer and the PbLi needs to be high for successful UDV measurement. We employ high-temperature transducers, the tips of which are made of Ti. The transducers (JAEA-type transducer) are capable of working up to at 500°C. Hereafter, the ultrasonic transmission at the interface between Ti and PbLi is discussed.

In general, ultrasonic transmission at an interface is expressed by the following relation:

$$TE = \frac{2Z_2}{Z_1 + Z_2} \quad (1)$$

Here, TE is the transmission coefficient that is the ratio of the pressure amplitude of a transmitted wave over that of an incident wave. Z_1 is the acoustic impedance of a medium of the incident wave, and Z_2 is that of the transmitted wave. Calculated from Table 1, TE of Ti and PbLi at 300°C is 0.765. Based on this, ultrasound transmission is dominant over reflection, and Ti is

considered to be a suitable material for PbLi.

It was experimentally observed that the ultrasonic transmission at the interface is sensitive to an oxygen concentration of an inert cover gas in contact with the PbLi. In case that the oxygen concentration is low enough, that is less than 1 ppm, the ultrasonic transmission is high enough for the successful UDV [10,14]. On the other hand, in case that the oxygen concentration is not low enough, that is tens of ppm, the ultrasonic transmission is almost zero. Under this condition, the Ti interface changes from its pure material, which is speculated to be oxidation (see Figure 2 left and center photograph). Gibbs free energy can explain the Ti oxidation in contact with the PbLi [11]. Based on them, it is concluded that the oxygen concentration sufficiently low of less than 1 ppm is necessary to have sufficient ultrasonic transmission at the Ti-PbLi interface.

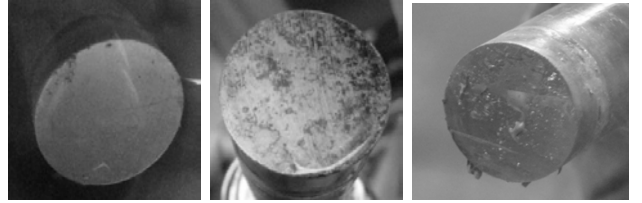


Figure 2: Photographs of transducer tip: (left) after initial immersion at oxygen concentration of tens ppm; (center) approximately 290 hours after the initial state; (right) after 1-hour immersion at oxygen concentration of less than 1 ppm [11].

4. Flow tracer particles for PbLi

Ultrasound reflecting particles, which plays a role as flow tracer particles in the target fluid, are necessary for UDV. Some liquid metals contain natural oxide particles. The particles may play a role as the flow tracer. However, it was unknown whether or not PbLi contains oxides. X-ray diffraction analysis was performed for PbLi. The analysis showed that PbLi in a bulk region contains lead-oxide (PbO) [15]. X-ray photoelectron spectroscopy also detected PbO in the PbLi [16]. PbO has high melting point of 886°C, and density close to PbLi. Based on them, PbO particles are expected to work as the flow tracers.

In order to confirm that naturally-contained particles work as flow tracers in PbLi, a swirl flow experiment was performed in the Ar-gas glovebox where the oxygen concentration was maintained to be less than 1 ppm [14]. It is known that suitable tracer particle size is 1/4 -1/2 of the ultrasound wavelength, that is approximately 100-200 μ m in the present study. PbLi ingots employed for this experiment were from Atlantic Metals and Alloys, Inc. A UDV instrument used was UVP Monitor Model X-1 from Met-Flow SA. Mean velocity profiles measured in the experiment were speculated to be valid since each interrogation volume gave continuous velocity profiles. This result indicated that reflected ultrasounds from each of the interrogation volumes was sufficiently high for evaluating flow velocities. Under a condition similar to the above, it was confirmed that another kind of UDV instrument, that is DOP2000 from Signal-Processing SA, also successfully worked as well as the Met-Flow instrument.

5. UVP experiment in PbLi loop

The swirl flow experiment was suitable for investigating the flow tracers in PbLi. However, its flow field was 3-dimensional, and complicated. Because of this, the experiment configuration was not suitable for evaluating UDV measurement accuracy. A simple flow field serves for the measurement accuracy evaluation. A steady circular pipe flow is employed in the present study.

Figure 3 illustrates a schematic drawing of a test-section employed in the present study. A main part of the test-section is a straight circular pipe, 1900 mm in length, 41.2 mm in the inner diameter, and made of SUS304. In downstream side of the main circular pipe, the transducers which are the identical model employed in the previous experiments described in Chapter 5. High-temperature pressure sensors are mounted on the test main pipe to measure PbLi gauge pressures. The distance between the upstream pressure sensor and the transducers is more than $40D$, where D is the inner diameter of the main part. That is long enough compared to a flow fully-developed length. Because of this, the PbLi flow is expected to be fully-developed in the region where UDV detects flow velocities.

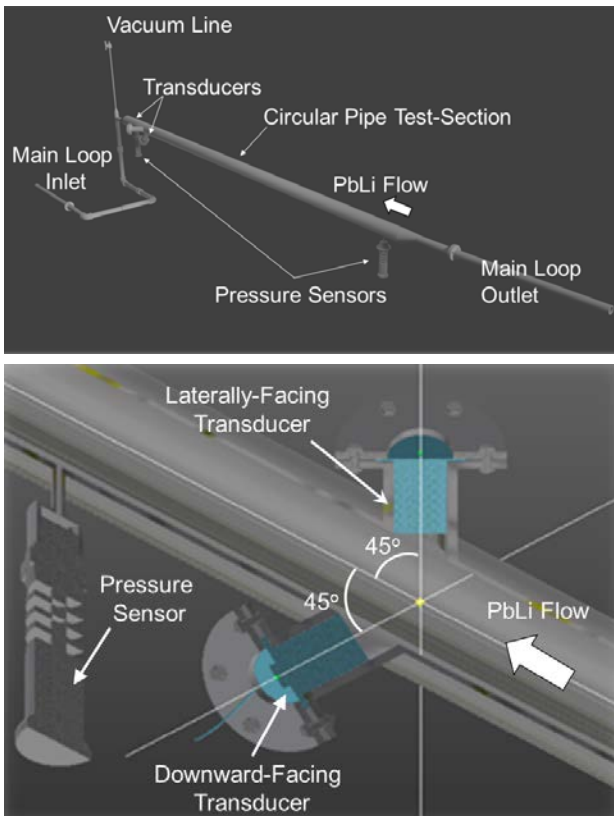


Figure 3: Schematic drawing of test-section; (top) overview; (bottom) Transducer region.

Two transducers (JAEA-type transducers) are mounted on the main pipe of the test-section on its downstream side. One of the two is downward-facing, and the other is laterally-facing, as shown in Figure 3. Those acoustic beam lines cross the straight pipe axis at an angles of 45° with respect to the pipe axis. With this configuration, two velocity profiles are expected to be measured in the fully-developed region. The test-section is installed on a PbLi

thermofluid loop, named as Orosshi-2 loop, at the National Institute for Fusion Science in Japan [17]. The UDV instrument employed in the present study is UVP-DUO from Met-Flow SA. Echo signals of the UDV instrument are monitored and recorded by a digital oscilloscope connected to the UDV instrument.

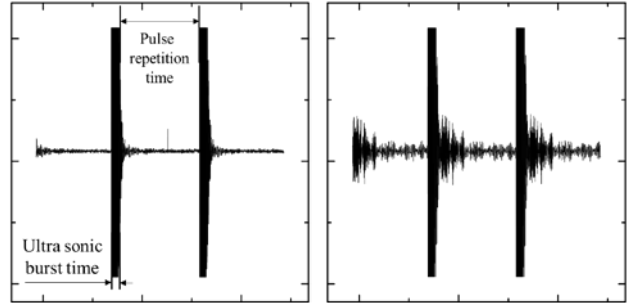


Figure 4: Echo waveforms measured by downward-facing transducer (left); by laterally-facing transducer (right).

Figure 4 is plots of echo waveforms of repeatedly-pulsed ultrasounds measured by the transducers. The left waveform shows that the transducer membrane damping is favorably rapid. On the other hand, the right waveform shows that the damping is slow and not sufficient. These results indicate that the downward-facing transducer is in a well contact with the target fluid, but the laterally-facing one is not. We speculate that the poor damping resulted from that Ar-gas bubbles might have been trapped on the laterally-facing transducer. Hereafter measurement with the downward-facing transducer is described.

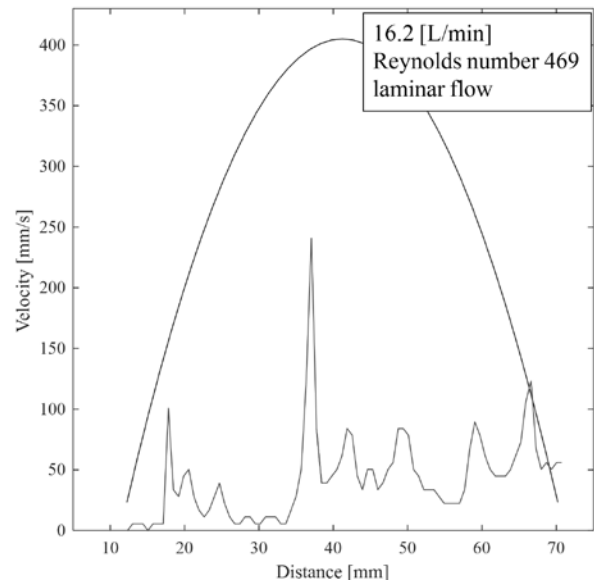


Figure 5: Measurement result of spontaneous velocity profile of PbLi pipe flow, and expected laminar flow velocity profile; it is speculated that insufficient amount of tracer particles arises the flow profile detection deterioration.

The ultrasound frequency is 4 MHz, the number of cycles is 32, and the number of repetitions is 1024. Figure 5 is a measurement result of a spontaneous velocity profile of the PbLi pipe flow when the flow rate is 16.2 L/min, which correspond to Reynolds number of 469. Therefore, the flow regime is laminar. The Hagen-Poiseuille flow is expected to be developed in the transducer region. The

Hagen-Poiseuille flow velocity profile calculated from the flow rate is depicted as well in Figure 5 for the purpose of comparison.

The velocity profile measured with UDV under the above mentioned condition is underestimated with respect to the theoretical prediction. The other result obtained is that the flow velocity profile fluctuates in time, although the flow regime is laminar. We speculate that it is because an amount of flow tracer particles contained in PbLi is insufficient for a successful UDV measurement. Although in the previous measurement described in Chapter 4, an amount of the naturally-contained particles was sufficient. What makes this difference is speculate to be PbLi purity. The PbLi employed in the previous study was from Atlantic Metals & Alloy, that was alloyed in an atmospheric condition [18]. However, the PbLi employed in Oroshhi-2 loop was alloyed in the Ar-gas glove box where an oxygen concentration was extremely low of less than 1 ppm, and also made from high-purity lead and lithium. Based on this process, the PbLi in the Oroshhi-2 loop is expected to have less amount of oxides particles than the commercial PbLi.

UVP-DUO is based on a time-domain algorithm to evaluate a Doppler shift from detected pulsed ultrasounds. Therefore, it is expected that the insufficient amount of the flow tracers results in lack of waveform information in the time-domain algorithm, and then the flow velocity profile underestimation occurs.

Conclusions

In the present paper, a series of investigations regarding the UDV measurement of PbLi flows are overviewed, and a UDV experiment of a laminar PbLi circular pipe flow is described. One of new findings is that naturally-contained particles as flow tracers differs by their alloying processes. In the UDV experiment with the PbLi loop, the flow velocity profile is underestimated, and also fluctuates timewise. From this, it is indicated that the amount of flow tracers in the PbLi employed in Oroshhi-2 loop is insufficient for PbLi UDV measurement. In order to stabilize the measurement, seeding some artificial tracer particles suitable for PbLi is favorable.

Acknowledgement

YU acknowledges the financial support by JSPS KAHENHI Grant number 16K18334, and Osaka University Career Boost Program for Early Career Researchers. This work is performed with support and under auspices of the NIFS Collaboration Research program (NIFS15KERF026).

References

[1] Abdou M, *et al.*: Blanket/first wall challenges and required R&D on the pathway to DEMO, *Fusion Engineering and Design*, 100 (2015), 2-43.
[2] Takeda Y: Development of an Ultrasound Velocity Profile Monitor, *Nuclear Engineering and Design*, 126 (1991), 277-284.
[3] Takeda Y & Kikura H : Flow Mapping of the Mercury Flow, *Experiments in Fluids*, 32 (2002), 161-169.
[4] Cramer A, *et al.*: Local Flow Structures in Liquid Metals

Measured by Ultrasonic Doppler Velocimetry, *Flow Measurement and Instrumentation*, 15 (2004), 145-153.

[5] Andreev O, *et al.*: Application of the Ultrasonic Doppler Velocity Profile Method to the Mapping of Liquid Metal Flows under the Influence of a Non-Uniform Magnetic Field, *Experiments in Fluids*, 46 (2009), 77-83.
[6] Brito D, *et al.*: Ultrasonic Doppler Velocimetry in Liquid Gallium, *Experiments in Fluids*, 31 (2001), 653-663.
[7] Eckert S & Gerbeth G: Velocity Measurements in Liquid Sodium by means of Ultrasonic Doppler Velocimetry, *Experiments in Fluids*, 32 (2002), 542-546.
[8] Eckert S, *et al.*: Velocity Measurements at High Temperatures by Ultrasound Doppler Velocimetry using an Acoustic Wave Guide, *Experiments in Fluids*, 35 (2003), 381-388.
[9] Takahashi M & Kondo M: Compatibility of Reduced Activation Ferritic/Martensitic Steel in Pb-17Li, *Journal of Plasma and Fusion Research*, 86 (2010), 413-416 (in Japanese).
[10] Ueki Y, *et al.*: Acoustic properties of Pb-17Li for ultrasonic Doppler velocimetry, *Fusion Science and Technology*, 56, (2009), 846-850.
[11] Ueki Y, *et al.*: Oxygen influence on ultrasonic Doppler velocimetry of lead-lithium flow using titanium transducer, *Fusion Engineering and Design*, 89 (2014), 77-81.
[12] Sobolev V: Thermophysical properties of lead and lead-bismuth eutectic, *Journal of Nuclear Materials*, 362 (2007), 235-247.
[13] McAlister SP, *et al.*: The Effect of Isotopic Mass on the Velocity of Sound in Liquid Li, *Journal of Physics F: Metal Physics*, 6 (1976), 1415-1420.
[14] Ueki Y, *et al.*: Velocity profile measurement of lead-lithium flows by high-temperature ultrasonic Doppler velocimetry, *Fusion Science and Technology*, 60 (2011), 506-510.
[15] Ueki Y, *et al.*: Contact angle measurement of molten lead-lithium on silicon carbide surface, *Fusion Engineering and Design*, 86 (2011), 2297-2300.
[16] Ueki Y: Development of high-temperature ultrasonic Doppler velocimetry for lead-lithium flow, *Kyoto University Ph.D dissertation*, (2012).
[17] Sagara A, *et al.*: First Operation of the Flinak/LiPb Twin Loop Orosh2i-2 with a 3T SC Magnet for R&D of Liquid Blanket for Fusion Reactor, *Fusion Science and Technology*, 68 (2015), 303-307.
[18] Smolentsev S, *et al.*: Construction and initial operation of MHD PbLi facility at UCLA, *Fusion Engineering and Design*, 88 (2013), 317-326.

Transition of patterns in liquid metal convection under a horizontal magnetic field

Takatoshi Yanagisawa¹, Yuji Tasaka², Ataru Sakuraba³, Takehiro Miyagoshi¹ and Yozo Hamano¹

¹ Department of Deep Earth Structure and Dynamics Research (D-EARTH), Japan Agency for Marine-Earth Science and Technology (JAMSTEC), Yokosuka 237-0061, Japan

² Laboratory for Flow Control, Division of Energy and Environmental Systems, Hokkaido University, Sapporo 060-8628, Japan

³ Department of Earth and Planetary Science, University of Tokyo, Tokyo 113-0033, Japan

We performed both laboratory experiments and numerical simulations of Rayleigh-Bénard convection of an electrically conductive low-Prandtl-number fluid under a uniform horizontal magnetic field. The flow pattern is constrained, as the axes of convection rolls tend to align in the direction of the horizontal magnetic field. Ultrasonic measurement of flow velocity profile is suitable for this setting of liquid metal convection, because it can grasp quasi-two-dimensional structure with its time variations. Transitions of flow structure such as repetition of reversals of flow direction occur when the intensity of the magnetic field is in a limited range for a given Rayleigh number. By analyzing both the laboratory experiments and numerical simulations, we clarified the process of transitions as well as their mechanism. The process can be regarded as an interaction between aligned convection rolls and global-scale mean flow. The occurrence of global circulation bends the aligned rolls in a style of the skewed-varicose instability and induces roll number reduction. On the other hand, transitions can be regarded as a competition between two flow modes having different roll numbers and variations of their relative intensities in time.

Keywords: Rayleigh-Bénard convection, liquid metal, magnetic field, flow regimes

1. Introduction

To elucidate the way to turbulence is one of the most important topics in fluid dynamics. A typical setting to study transitions to turbulence is thermal convection in a layer driven by a vertical temperature gradient, that is, Rayleigh-Bénard convection (RBC). Many studies have been made on RBC (recent reviews in [1, 2]). Behaviors of thermal convection strongly depend on the Prandtl number (Pr) of the working fluid, and low Pr fluids such as liquid metals tend to be turbulent just after the onset of convection because of their low viscosity. On the other hand, liquid metals are electrically conductive fluids, and applying magnetic field to the system can control the transition to turbulence. When a magnetic field is imposed on liquid metals, it enhances two-dimensionality and creates anisotropic flow structures with suppressing turbulence, depending on the direction and intensity of the field [3].

The controlling non-dimensional parameters in a RBC system under an imposed uniform magnetic field are the Rayleigh number (Ra), and the Chandrasekhar number (Q) [4]. In RBC of low Pr fluid like liquid metals, the region where two-dimensional (2D) rolls remain steady in the wave number-Rayleigh number space (the Busse balloon) is limited by the Eckhaus instability on the smaller wave number side, by the skewed-varicose instability on the larger wave number side, and by the oscillatory instability on the higher Ra values [5]. With a uniform horizontal magnetic field imposed, the Busse balloon extends by the increase of the onset Ra of oscillatory instability [6], and the values of Ra for further

transitions to turbulence also increase. These are confirmed by earlier experiments [7,8]. The delays of transitions are convenient for the study of the way to turbulence, because the larger flow velocity at higher Ra makes it easier to observe the structure of the flow. It also means that transitions are controllable by the intensity of the magnetic field, while the value of Ra is fixed.

We conducted laboratory experiments on RBC of a liquid metal with observing the flow velocity by an ultrasonic velocity profiling method. We also performed a series of numerical simulations of RBC with electrically conductive low-Prandtl-number fluid under a uniform horizontal magnetic field. We reproduced flow structures and their time variations by numerical simulations that is consistent with observations in laboratory experiments. Based on these results, we can clearly grasp a route from a laminar flow with 2D rolls to a turbulent state.

2. Method

2.1 Laboratory Experiments

The vessel we used has a square geometry with aspect ratio five (Figure 1(a)) [9-11]. The horizontal scale of the vessel is 200 mm, and the thickness is 40 mm. The top and bottom plates are made of copper, and the temperature of each plate is maintained by circulating water. Liquid gallium is used as the working fluid. Transducers for the Ultrasonic Velocity Profiler are set in holes in the Teflon sidewalls, and are in direct contact with the liquid gallium. We are using UVP-Duo (Met-Flow S.A.), with the basic frequency of 4 MHz. The flow velocities of the gallium were measured along four lines from the transducers. The UVP measures the projected

flow velocity along each line. We used a Helmholtz coil, or coils with large yoke to apply a uniform magnetic field (Figure 1(b)). The direction of magnetic field is horizontal in this study, and its intensity is controlled by an electric power supply. The maximum intensity of the magnetic field is 120 mT. The spatial variance of field intensity is within 2 % around the vessel. Refer [9] for more details of the setting and method of these laboratory experiments.

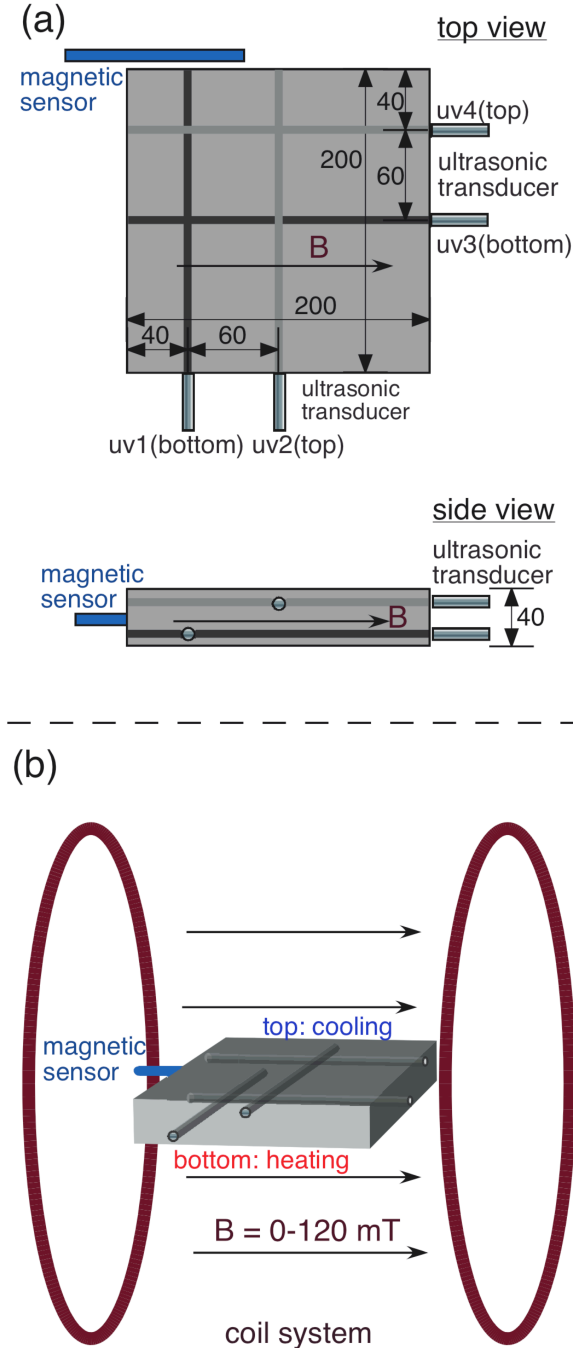


Figure 1: (a) Geometry of the vessel and ultrasonic beam lines for flow velocity measurement. Liquid gallium is filled in the vessel. The numbers are the dimensions in mm. (b) The vessel in a coil system. A uniform magnetic field B is applied in the horizontal direction.

2.2 Numerical Simulations

We performed numerical simulations for the same setting as laboratory experiments, with horizontal magnetic field imposed on the vessel of no-slip velocity boundaries. A set of magnetohydrodynamic equations are solved by a finite difference method with a uniform grid interval. We used realistic low value of Prandtl number for liquid metals (0.025). Refer [12] for the details and evaluation of the code.

3. Results

We identified several flow regimes depending on Ra and Q , between steady 2D laminar flow states and fluctuating large-scale flows with turbulence. We report here transitions on the decrease in Q , at a fixed Ra .

3.1 Time variations by Laboratory Experiments

Typical examples of the flow are shown in Figure 2, in a style of time-space map of horizontal flow velocity measured by the uv2 of Figure 1(a). All the panels show time variations for 2000 s. The intensity of the magnetic field, that is Q , is decreasing from top to bottom in this figure.

Figure 2(a) shows a laminar flow structure that has 5 rolls, with the roll axis parallel to the direction of the magnetic field. The flow parallel to the magnetic field is very weak in this case. Very small amplitude of oscillation is observed. It comes from a periodic horizontal movement of the rolls, while the pattern keeps 2D state. This represents a typical flow regime under a strong horizontal magnetic field.

In Figure 2(b), the pattern keeps roll-like structure with dominant flow velocities perpendicular to the magnetic field, but repetitions of roll number transitions mainly 5–4 rolls are observed. Reversals of the flow direction in the rolls occur accompanied by the transitions.

Figure 2(c) is a state of oscillating convection, where the pattern shows large amplitude of oscillations with keeping a 4-roll state. The axes of rolls are winding in this oscillation. The period of oscillation is nearly equal to the circulation time of the flow for a roll.

Figure 2(d) shows a state after a transition to turbulence occurred, where whole- or half- vessel scale flows exist with short time fluctuations, and the magnitude of the velocity is similar in both directions perpendicular and parallel to the magnetic field. There are no roll-like structures, though the experiment is conducted with a horizontal magnetic field imposed. The behavior is similar to that without a magnetic field.

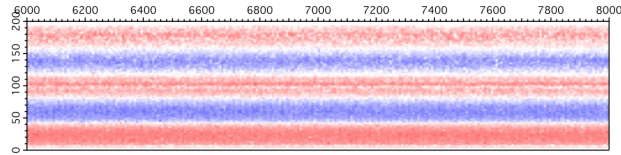
These results indicate that the number of rolls decreases with decrease in Q , from 5 to 1 or 2. The amplitude of spacial fluctuation increases in accordance with the decrease of the roll number, and continues to the fully developed turbulent state.

3.2 Flow structures by Numerical Simulations

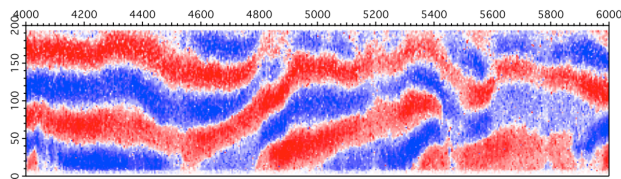
In our numerical simulations, we first confirmed that both the time averaged number of rolls and their time

variations are consistent with those observed in laboratory experiments. We present here 3D structures of flow in the whole vessel in Figure 3, by showing the isosurface of the Q_{3D} , that is the second invariant of the velocity gradient tensor. Though the values of the Chandrasekhar number Q are not exactly same as those in Figure 2, each of the regime of flow shown in Figure 3 corresponds to (a-d) of Figure 1.

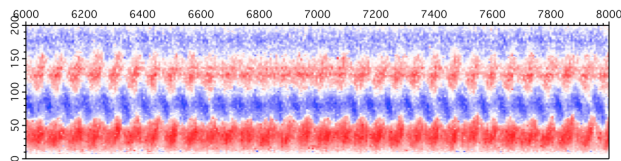
(a) $Ra=3\times 10^4$ and $Q=8\times 10^3$: five rolls, 2D oscillation



(b) $Ra=3\times 10^4$ and $Q=1\times 10^3$: roll number transitions



(c) $Ra=3\times 10^4$ and $Q=7\times 10^2$: four rolls, 3D oscillation



(d) $Ra=3\times 10^4$ and $Q=8\times 10^1$: no rolls, fluctuating cell

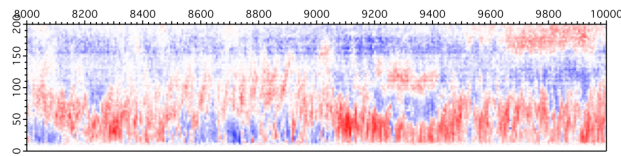


Figure 2: Typical examples of flow regimes. Time-space maps of the horizontal flow velocity are displayed for the measurement line at the center of the vessel, perpendicular to the applied magnetic field. The duration of time is 2000 s. The direction and magnitude of the velocity are shown in the color scale, red is away from the transducer (located at distance=0) and blue is toward it.

Figure 3(a) is a laminar 5-roll structure with the roll axis fixed in the direction to the magnetic field. Small amplitude of horizontal oscillation of the rolls are also reproduced. As shown in the figure, in addition to the main 2D rolls, smaller secondary circulations exist between the rolls near the top or bottom boundary.

Figure 3(b) is a snapshot from a regime of roll number transition. A typical process of roll number transition is as follows. A 5-roll structure bends horizontally, and a roll at a sidewall is shrinking to make a 4-roll structure. Then, reconnection of the rolls between front and back occurs; Figure 3(b) shows just before the timing of a reconnection. A new roll is growing along a sidewall, and 5-roll structure is reproduced. In this process, the key mechanism is an emergence of a global circulation in the

horizontal plane. The horizontal circulation is related to the skewed-varicose instability of two-dimensional roll structure aligned in the direction of the magnetic field. This process of roll number transition can be thought as a repetition of two states those have different roll numbers.

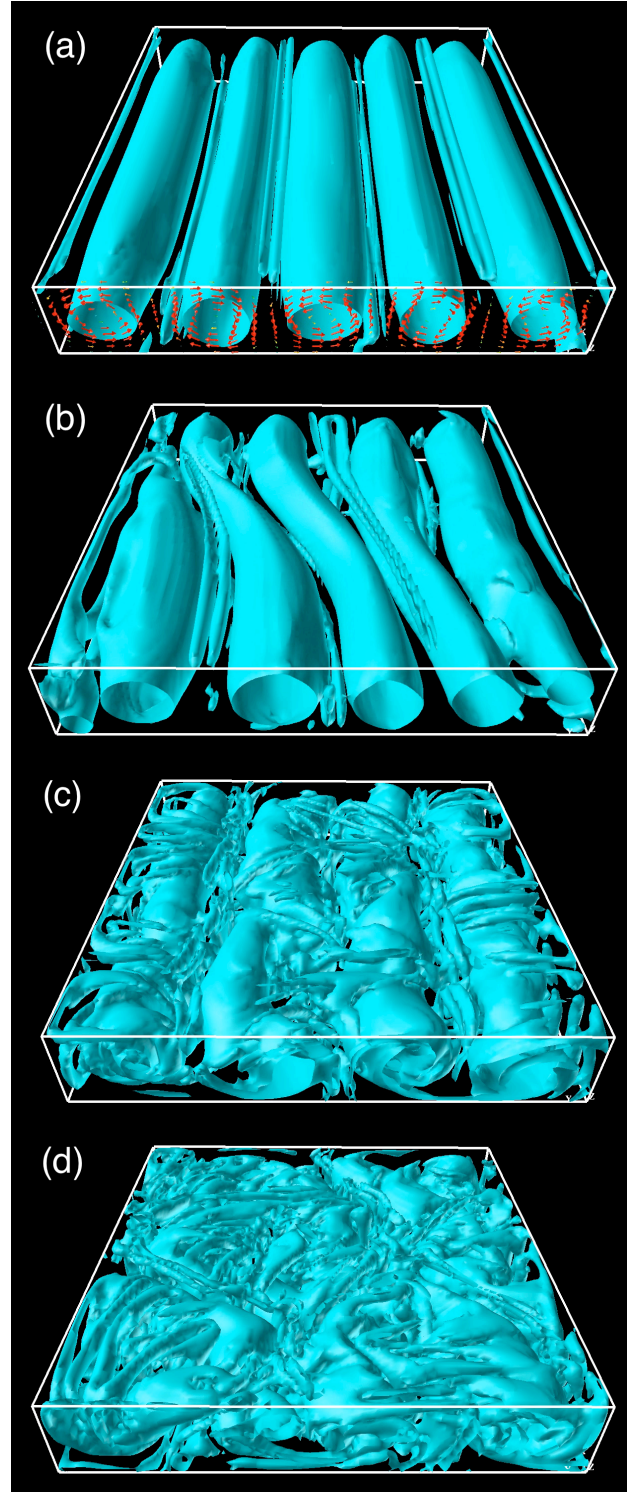


Figure 3: Typical examples of flow structures obtained by numerical simulations. The isosurfaces of $Q_{3D}=0$ are shown. A uniform magnetic field is applied from front to back; its intensity corresponds to (a) $Q=6\times 10^3$, (b) 3×10^3 , (c) 7×10^2 , and (d) 1×10^2 . Ra is fixed as 3×10^4 .

Figure 3(c) is a snapshot of 4-roll oscillation. The axes of rolls are winding and the amplitude of horizontal movement is large. A remarkable feature of this case is that many secondary vortices are accompanied by the oscillation of main rolls.

Finally, Figure 3(d) is a snapshot of a flow under a weak magnetic field. There are no distinct roll structure, but the flow shows large-scale isotropic features in average. Many secondary vortices are drifting with rise and fall on vessel-scale circulations.

4. Summary

Several transitions of flow pattern were identified in RBC of a liquid metal under a uniform horizontal magnetic field. In a decreasing way of the intensity of the magnetic field, these transitions are from (a) laminar 2D roll convection, to (b) roll number transitions, to (c) large amplitude of oscillatory rolls, and to (d) turbulent state with fluctuating large-scale circulations. In this process, the horizontal scale of the structure decreases with losing distinct rolls. The dominant flow in (a) is in the vertical plane perpendicular to the magnetic field (that is rolls), while the magnitude of circulations in the horizontal plane gets larger with decrease in Q . In the state (d), the power of horizontal circulations is as intense as that of vertical circulations.

References

- [1] Ahlers G et al.: Heat transfer and large scale dynamics in turbulent Rayleigh-Bénard convection, *Rev. Mod. Phys.* 81 (2009) 503-537.
- [2] Chilla F & Schumacher J: New perspectives in turbulent Rayleigh-Bénard convection, *Eur. Phys. J. E* 35 (2012) 58.
- [3] Davidson PA: *An Introduction to Magnetohydrodynamics*, Cambridge University Press, Cambridge (2001).
- [4] Chandrasekhar S: *Hydrodynamic and Hydromagnetic Stability*, Oxford University Press, New York (1961).
- [5] Clever RM & Busse FH: Large wavelength convection rolls in low Prandtl number fluids, *J. Appl. Math. Phys.* 29 (1978) 711-714.
- [6] Busse FH & Clever RM: Stability of convection rolls in the presence of a horizontal magnetic field, *J. Theor. Appl. Mech.* 2 (1983) 495-502.
- [7] Fauve S et al.: Horizontal magnetic field and the oscillatory instability onset, *J. Phys. Lett.* 45 (1984) L101-L105.
- [8] Burr U & Müller U: Rayleigh-Bénard convection in liquid metal layers under the influence of a horizontal magnetic field, *J. Fluid Mech.* 453 (2002) 345-369.
- [9] Yanagisawa T, *et al.*: Spontaneous flow reversals in Rayleigh-Bénard convection of a liquid metal, *Phys. Rev. E* 83 (2011) 036307.
- [10] Yanagisawa T, *et al.*: Convection patterns in a liquid metal under an imposed horizontal magnetic field, *Phys. Rev. E* 88 (2013) 063020.
- [11] Tasaka Y, *et al.*: Regular flow reversals in Rayleigh-Bénard convection in a horizontal magnetic field, *Phys. Rev. E* 93 (2016) 043109.
- [12] Yanagisawa T, *et al.*: Flow reversals in low-Prandtl-number Rayleigh-Bénard convection controlled by horizontal circulations, *Phys. Rev. E* 92 (2015) 023018.

Measurements of a three-dimensional flow in a cube by means of an ultrasound array Doppler velocimeter (UADV)

Vladimir Galindo¹, Richard Nauber², Sven Franke¹, Dirk Rübiger¹, Lars Büttner², Norman Thieme², Hannes Beyer², Jürgen Czarske², and Sven Eckert¹

¹ Helmholtz – Zentrum Dresden – Rossendorf, Dresden, Germany

² Technische Universität Dresden, Germany

Velocity measurements were carried out in a cube filled with the liquid metal GaInSn using a dual plane, two-component ultrasound array Doppler velocimeter. It provides flow instrumentation at frames rate of typ. 11 Hz over long measurement durations (>1h) using an FPGA based signal processing, which enables capturing transient flow phenomena with nondeterministic onsets. The liquid metal was suddenly exposed to an azimuthal body force generated by a rotating magnetic field (RMF). The measurements show a similar flow structure compared to the case of the RMF-driven flow in a cylindrical container, in particular the so-called initial adjustment phase followed by an inertial phase which is dominated by inertial oscillations of the secondary flow. The interest was especially focused on the onset of unsteady flow regimes. The transition from the steady double vortex structure of the secondary flow to an oscillating regime was detected at a magnetic Taylor number of $Ta > 1.3 \times 10^5$. A detailed analysis of the flow structure was done by means of the Proper Orthogonal Decomposition (POD). Corresponding numerical simulations were performed showing an excellent agreement with the experimental data.

Keywords: Rotating magnetic field driven flow, Ultrasound velocity measurement, Spin-up, OpenFOAM, Proper orthogonal decomposition”

1. Introduction

In the last years a broad study about the flow in closed circular cylindrical container under the action of a rotating magnetic field was performed, paying special attention to the transition from a steady to a time-dependent flow regime [1]. The authors tried to find a critical non-dimensional magnetic Taylor number Ta (cf. Eq. 3) for the onset of the instabilities using different direct numerical simulation methods. Most recently, Grants and Gerbeth [2] conclude that the rotating-magnetic field driven flow in a circular cylinder becomes unstable first to non-axisymmetric, azimuthally periodic perturbations at diameter-to-height aspect ratios $AR=D/H$ between 0,5 and 2. In this paper we present an experimental and numerical study of the flow in a closed cubic container driven by a rotating magnetic field. We focused our interest in the transient behavior of the flow and the characterization of the transition from a steady state below the critical magnetic Taylor number ($Ta < Ta_{cr}$) to oscillatory states and then, for a considerable high Ta , to a completely unsteady state.

2. Experimental setup

The experimental setup consists of the eutectic metal alloy GaInSn, which is liquid at room temperature, enclosed in a cubic container with an edge length of $2L = 67,5$ mm. The container is centered in the MULTIMAG (MULTI purpose MAGnetic field) facility, which is capable of generating different types of magnetic fields with varying strength and frequency [3].

In the current study the investigations were focused on the spin-up process, this means that the experiments were started with the fluid being at rest. The liquid metal

(GaInSn) was suddenly exposed to an azimuthal body force generated by a rotating magnetic field (RMF) with a frequency of 50 Hz. Due to the electromagnetic force action and the presence of walls, a vortex develops in the horizontal plane (primary flow) as well as a secondary flow in the meridional plane. Both planes are instrumented simultaneously with the ultrasound array Doppler velocimeter (UADV) [4, 5] as shown in Fig. 1. In the given configuration, the UADV employs four linear arrays.

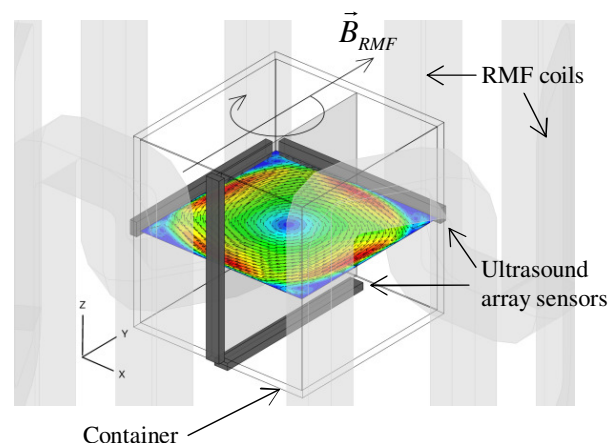


Figure 1: Measurement configuration: cube instrumented with four ultrasound array sensors.

An array consists of 25 transducers with the dimensions $2,5 \times 5$ mm² resulting in a total sensitive length of 67,5 mm (cf. Fig. 2). A pairwise driving of neighboring transducers results in an active surface of 5×5 mm², which leads to a sound beam width of approximately 3 mm in GaInSn.

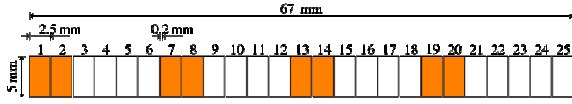


Figure 2: Geometrical dimensions of the used ultrasound array sensor.

By arranging the sensor arrays orthogonally in a single plane and combining the data two components velocity fields can be obtained. The excitation signal is eight periods of a sine wave at 8 MHz resulting in an axial resolution of about 1.4 mm [4]. The acoustical impedance of the transducers is matched to PMMA (3.4 MRayl), which allows reliable measurements through the container walls. The frame-rate is increased over a simple sequential scan by using a parallelized time division multiplexing (TDM) scheme. In this way a measurement frame rate of up to 33 Hz can be achieved. To avoid crosstalk between the sensor arrays, all four arrays are driven mutual exclusively. The velocity information is extracted from the amplified and digitized US echo signals via the Kasai autocorrelation method. A typical mean bandwidth after digitalization is 1.2 GB/s, which is beyond the limit that can be acquired and stored continuously with common PC-hardware. A real-time data compression is performed by offloading parts of the signal processing to a field-programmable gate array (FPGA, NI PXIe-7965R). The pre-processing reduces the amount of data by 10:1 and enables a continuous streaming for a practically unlimited duration. This approach allows for the study of long-term transient flows.

3. Governing equations

Let us consider the flow of an electrically conducting fluid with kinematic viscosity ν , density ρ and electrical conductivity σ in a cubic container with an edge length $2L$ driven by a uniform magnetic field of induction B_0 rotating in a horizontal plane (around the z -axis) with a constant angular frequency ω . In the scope of the low-induction approximation (very small magnetic Reynolds number $Rm = \mu_0 \omega u_0 L \ll 1$) the electromotive field $\vec{u} \times \vec{B}$ can be neglected compared to the induced electric field E within the Ohm's law $\vec{j} = \sigma(\vec{E} + \vec{u} \times \vec{B})$. Here is μ_0 the magnetic vacuum permeability and u_0 is a characteristic velocity of the flow. The simulations of the electromagnetic field and the fluid flow can be conducted separately. Hence, a quasi-analytical expression for the over one period time-averaged electromagnetic force density $\vec{f} = \langle \vec{j} \times \vec{B} \rangle_T$ acting on the liquid metal in the cavity can be derived [6]:

$$\vec{f} = \sigma \omega B_0^2 / 2 \{ (-\partial_z b + y) \vec{e}_x + (-\partial_z a - x) \vec{e}_y \} \quad (1)$$

The functions a and b are solutions of the Laplace equation under special boundary conditions [6]. The numerical simulation of the liquid metal flow is performed using the open code library OpenFOAM. The flow was computed solving the incompressible Navier Stokes equation which in a dimensionless form, with L ,

L^2/ν and $\rho(\nu/L)^2$ being the distance, time and pressure scale, respectively, is given by

$$\partial_i \vec{u} + (\vec{u} \cdot \nabla) \vec{u} = -\nabla p + \nabla^2 \vec{u} + Ta \vec{f}_{EM} \quad (2)$$

together with the incompressibility condition $\nabla \cdot \vec{u} = 0$. The last term is the non-dimensional electromagnetic force density and

$$Ta = \frac{\sigma \omega B_0^2 L^4}{2 \rho \nu^2} \quad (3)$$

denotes the magnetic Taylor number, a ratio between the electromagnetic and the viscous force acting on the liquid metal.

Boundary conditions for the calculation of the flow field have been the no-slip condition $u = 0$ at the solid container walls. For the upper surface either $u = 0$ or the conditions for a stress-free, non-deformable surface $u_n = 0$ and $\partial u_i / \partial n = 0$ were used depending on whether the melt flow was evaluated in an open or in an enclosed container. A computational grid with at least one million volume elements was used depending on the boundary layer thickness. A second-order discretization scheme was used for the convective term in Eq. 2.

4. Results

In order to estimate the critical Taylor number Ta_{cr} for the transition from steady to oscillatory flow regime, we examine the time evolution of the velocity field. Fig. 3 shows the velocity component u_x at the monitoring point with the coordinates $x = 0,9L$; $y = 0$; $z = 0,1L$ for different values of Ta as a function of time. The transition to a time-dependent flow regime appears to occur for a value of the magnetic Taylor number in the range $1,3 \times 10^5 < Ta_{cr} < 1,4 \times 10^5$. The corresponding critical value for the case of a finite circular cylinder of aspect ratio 1 is $Ta_{cr} = 1,232 \times 10^5$ (Grants et al. [2]).

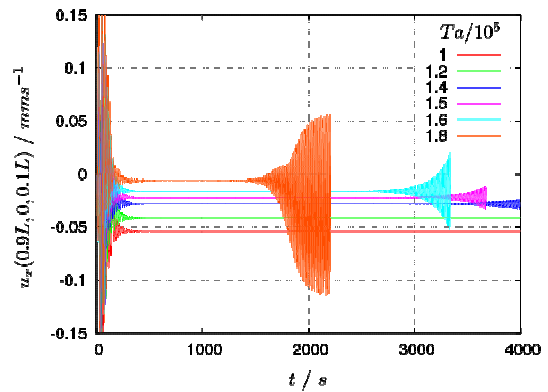


Figure 3: Time evolution of u_x at a monitoring point for different values of the magnetic Taylor number Ta .

The secondary flow reaches the maximal values near the top and the bottom of the container. Due to saturation effects, the measurement system yields no valid velocity measurements near the walls and therefore the measurement volume does not include these regions.

Fig. 4 shows a comparison of the flow pattern in the meridional plane ($x=0$) for $Ta = 10^5$. In the top part, the values from the numerical simulation are shown. We can observe at the bottom part of this figure that the maximal velocity magnitudes are found outside of the measurement volume of the ultrasound instrumentation. This fact shows the importance of the numerical simulation in order to resolve boundary layers correctly in near wall regions. On the other hand side, the experimental approach in combination with proper flow instrumentation can yield data in the high Ta regime, which is not accessible through direct numerical simulation (DNS) yet.

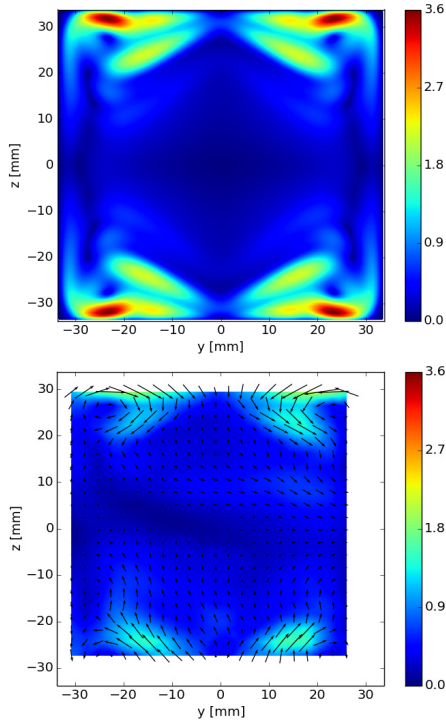


Figure 4: Mean velocity of the secondary flow in mm/s for $Ta = 10^5$ (top: computed from the numerical simulation, bottom: measured mean velocity distribution)

Complex flow time-dependent structures can be described using a model reduction because such flows are often dominated by low-dimensional dynamics. Such a one is the proper orthogonal decomposition (POD) technique, which decomposes the flow velocity vector field into orthogonal spatial modes and time-dependent amplitudes.

Fig. 5 depicts the time evolution of the amplitudes of the leading modes $a_1(t)$, $a_3(t)$, $a_4(t)$ and $a_6(t)$. The upper diagram demonstrates the exponential growth of the modes whereas the evolution of the kinetic energy $a_m(t)^2$ of the modes $m=1,2,\dots,7$ can be seen in the bottom graph. More details will be shown in a subsequent paper that will be published elsewhere.

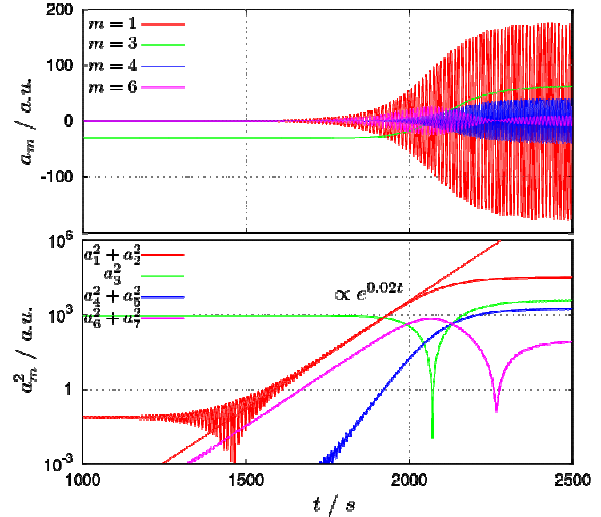


Figure 5: POD of the primary flow (numerical simulation for $Ta = 1,7 \times 10^5$) - Time evolution of the amplitude of the most important modes $a_m(t)$; $m = 1, 3, 4, 6$ (top) and of the kinetic energy of the modes $m = 1, \dots, 7$ (bottom).

4. Conclusions

We present a semi-analytical expression for the induced electromagnetic force density in an electrically conducting medium contained in a square cavity in the presence of a rotating magnetic field. This allows a direct numerical simulation of the flow. We found the transition from the steady state to time dependent flow structures to occur for $Ta > 1,3 \times 10^5$. Velocity distributions in two perpendicular planes were measured using a two-component ultrasound array Doppler velocimeter for a large time interval for the first time. The mean flow structures and the evolution of the flow in time in experiments and numerical simulation are in very good agreement.

Acknowledgements

Financial support for this research from the German Helmholtz Association in frame of the Alliance ‘‘Liquid Metal Technologies (LIMTECH)’’ is gratefully acknowledged.

References

- [1] L. M. Witkowski et al., Physics of Fluids 11 (1999) pp. 1821 - 1826.
- [2] I. Grants et al., Journal of Fluid Mechanics 463 (2002) pp. 229 - 239.
- [3] J. Pal et al., Flow Measurement and Instrumentation 20 (2009) pp. 241 - 251.
- [4] S. Franke et al., Ultrasonics 53 (2013) 3, pp- 691-700.
- [5] R. Nauber et al., The European Physical Journal 220 (2013) pp.43 - 52.
- [6] Galindo et al., Proceedings of the 8th International Conference on electromagnetic processing of materials, Cannes, France (2015) pp. 227-230

On Some Influences of the Geometry of a Simplified Flip-Flop Jet Nozzle

Hiroyuki Ota¹, Kazuki Umemura¹, Tatsuya Inoue¹,
Hirochika Tanigawa² and Katsuya Hirata¹

¹Department of Technical Engineering, Doshisha University, Kyoto 610-0321, Japan

²National Institute of Technology, Maizuru College, Maizuru 625-8511, Japan

We experimentally investigate a self-excited oscillatory phenomenon of a confined jet entering a rectangular cylinder as a downstream obstacle using ultrasonic velocity profile UVP, particle-image velocimetry PIV and hot-wire anemometer HWA, focusing on two geometry effects such as its aspect-ratio effect and the effect of a streamwise target size a . Furthermore, we conduct two-dimensional numerical analyses. As a result, we reveal a good agreement between experiments and computations, which suggests that the present phenomenon is intrinsically two-dimensional. And, we confirm that the dominant jet's frequency f_D detected by the UVP can be approximately predicted by the proposed empirical formula (Hirata *et al.*, 2011), whenever the jet stably oscillates. The effect of a/b upon the occurrence of stable jet's oscillation is not negligible at $a/b \geq 10$, where b denotes the breadth of a primary nozzle. Besides, the first and the second POD modes are almost dominant in the present flow.

Keywords: Flip-flop jets, Flowmeter, Fluidic logic, Fluidics, Flow-induced vibration

1. Introduction

A confined jet sometimes becomes unstable and causes self-induced oscillation of flow, due to the existence of a downstream obstacle [1, 2]. The knowledge of this phenomenon is useful for many applications in various aspects, like flip-flop jet nozzles, flowmeters, oscillatory components of fluidics, mixers, chemical reactors and so on.

In the present study, we deal with the self-excited oscillatory phenomenon of a two-dimensional confined jet with a rectangular cylinder as a downstream obstacle, which is similar to the flowmeter reported by Yamasaki *et al.* [3]. More specifically, we experimentally investigate this phenomenon using velocimetry, namely, (1)ultrasonic velocity profile UVP [4, 5], (2)particle-image velocimetry PIV and (3)hot-wire anemometer HWA, focusing on two geometry effects such as the aspect-ratio effect and the effect of the streamwise target size a .

The UVP has proposed and developed by Takeda (1986) [4] and Takeda *et al.* (1992) [5]. The UVP gives us a smaller number of instantaneous information, but its accuracy is higher. We may consider alternatives to the UVP, such as a hot-wire velocimetry (HWV), a laser-Doppler velocimetry (LDV), a particle-image velocimetry (PIV) and a tracking velocimetry (PTV). The HWV has high reliability and high accuracy, but it disturbs flow by its probe. The LDV has high responsibility and high accuracy, but it is often sensitive to the condition of tracer particles. As both of the HWV and LDV give us the information at only one point in space, we are required to select the point carefully, especially for unknown complicated flows. Tracer-particle concentration should be kept high and homogenous for the LDV. The PIV and the PTV give us neither the ping-point nor the one-dimensional information,

but the two-dimensional information on the basis of flow-visualised photographs [6].

Furthermore, we conduct two-dimensional numerical analyses based on vorticity ζ and stream function ψ using a finite-difference discretization method. Two-dimensional numerical analysis is suitable to examine the two-dimensionality of the phenomenon than three-dimensional one.

2. Experimental Method

Figure 1 shows the present model of a simplified flip-flop jet nozzle, together with the present coordinate system. A jet is emitted from a primary nozzle exit into the flip-flop jet nozzle with an inlet spatially-averaged velocity U_{in} at the nozzle exit. Such a confined jet sometimes oscillates at a dominant frequency f_D in the presence of a downstream target, which has one of the simplest geometries like a rectangular-cross-section cylinder in the present study. Concerning this model, we consider seven geometric parameters as a, B, b, c, D, d and h , as shown in Fig. 1.

We should suppose U_{in} , fluid density ρ and viscosity μ in addition to the seven geometric parameters as the dimensional governing parameters for the present model.

Through the present study, we simply choose U_{in}, ρ and b as characteristic scales. Therefore, it is necessary to induce seven non-dimensional parameters to specify the model's condition. The Strouhal number is a non-dimensional form of f_D , which is defined by $St = f_D b / U_{in}$. When we consider f_D , we get $St = \phi(Re, a/b, B/b, c/b, D/b, d/b, h/b)$. Here, ϕ denotes an arbitrary function.

Among the non-dimensional governing parameters, D/b is to a constant: 47 and 40 in all the water and air experiments, respectively, being approximated to be large enough to ignore D/b effect. As well, Re is 500 and 5000

in all the water and air experiments, respectively. We can ignore the Re effects upon both St and the occurrence condition for $Re > 200$ [2].

Figure 2 shows the details inside the model, in order to show the measuring points for the jet's oscillation frequency by the UVP in water and by the HWA in air. Tracer particles and other main experimental conditions are the same as Funaki *et al.* [7].

3. Results and Discussion

3.1 Velocity fluctuation

Figure 3 shows its corresponding spectrum and a sample raw data of the flow-velocity fluctuation measured on the points indicated in the figure using UVP [1]. Specifically speaking, the inserted figure denotes the x -component u of a velocity vector at $Re = 500$, $a/b = 2.5$, $B/b = 15$, $c/b = 2.5$, $d/b = 9$ and $h/b = 10$ in water. Inserted figure represents a time history, and the main figure represents

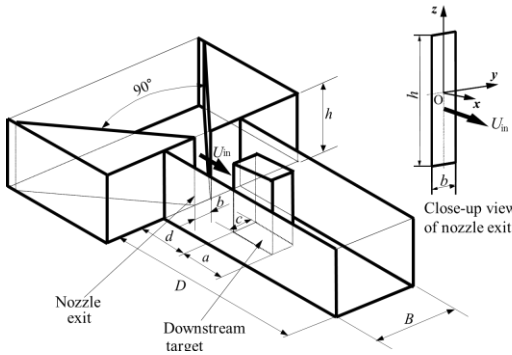


Figure 1: Model (a simplified flip-flop jet nozzle), together with coordinate system.

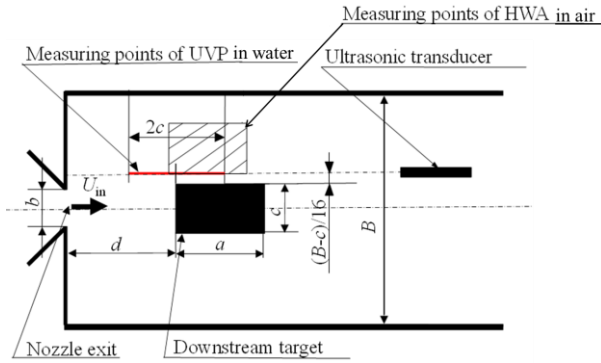


Figure 2: Measuring points for jet's velocity.

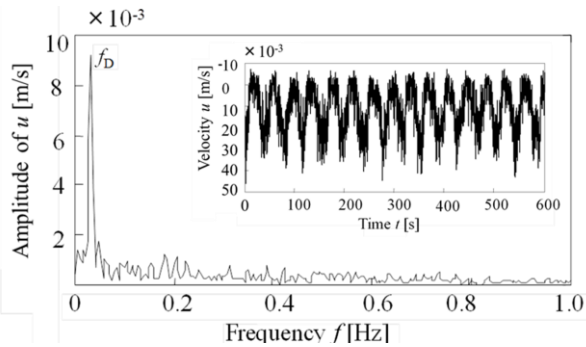


Figure 3: Velocity fluctuation, at $Re = 500$, $a/b = 2.5$, $B/b = 15$, $c/b = 2.5$, $d/b = 9$ and $h/b = 10$ using UVP in water (Hirata *et al.* 2009) [1].

its corresponding spectrum using a fast-Fourier-transform (FFT) algorithm. In the inserted figure, we can see a distinct and stable periodicity, together with higher-frequency random fluctuations due to flow turbulence. In the main figure, we can see a clear dominant frequency f_D of about 1/40 Hz in the spectrum, which corresponds to the oscillation period of about 40 s. As shown by flow visualisation in our previous study [1], f_D is related with a 'stable' jet's oscillation inside the flip-flop jet nozzle. The 'stable' means that where the jet's oscillation is periodic at any time, and the 'less-stable' condition means that where the oscillation is almost non-periodic and sometimes periodic.

3.2 Influence of aspect ratio

Figure 4 shows the present experimental results using the HWA, together with the experimental results using the UVP at $Re = 500$ and the HWA at $Re = 500$ [1, 2]. In the figure, St is plotted against d/b . We should note that all the data points at $St = 0$ represent such a condition as the jet's oscillation is not 'stable' but 'less-stable.'

Two vertical chained lines in the figure represent the stability boundaries proposed by [1]. That is to say, in order to predict the occurrence condition for the stable jet's oscillation, Hirata *et al.* have proposed a pair of the following empirical criteria:

$$3/2 \leq B/d \leq 4, \quad (1)$$

and

$$1/10 \leq c/d \leq 2/5. \quad (2)$$

Concerning the first criterion Eq. (1), it is supposed to be inherent for the stable jet's oscillation that the two recirculating areas should exist on both the sides in the upstream of the square cylinder at any time. Therefore, B/d is a primarily-important geometric parameter to secure the spaces for the two re-circulating areas. Concerning the second criterion Eq. (2), it is supposed to be inherent for the stable jet's oscillation that the spacial relationship should be adequate between the jet's shear layers and the downstream-target edges. A chained line at $d/b = 6.3$ represents such an equation as $c/d = 2/5$, and another chained line at $d/b = 10$ represents such an equation as $B/d = 3/2$. Of course, in a zone at $d/b = 6.3 - 10$ in the figure, both of the criteria Eqs. (1) and (2) are satisfied.

In addition, a dashed line in the figure denotes the empirical formula to predict the stable jet's oscillation frequency by [2]. This formula is given by

$$St = ke^{\alpha(a/b)}(B/b)^\beta(c/b)^\gamma(d/b)^\delta, \quad (3)$$

with such experimental constants as $k = 0.5$, $\alpha = -0.2$, $\beta = -0.7$, $\gamma = 1.0$ and $\delta = -1.5$.

We can see that, for all the experimental results including [1, 2], the empirical criteria for occurrence conditions and the empirical formula for dominant jet's oscillation frequency are valid in spite of wide parameter ranges of Re and h/b . That is to say, the jet's oscillation is stable at $d/b = 7 - 10$ in agreement with Eqs. (1) and (2). Also, St is well predicted by Eq. (3); namely, all the values of St

are in the order of 10^{-3} tending to decrease with increasing d/b . Strictly speaking, St is somewhat smaller than Eq. (3) at $h/b \leq 5$. Moreover, we have confirmed the h/b effect [1]. The degree of the scattering in experiment suggests that the oscillating phenomenon could be sensitive not only to the supposed governing parameters like Re , a/b , B/b , c/b , D/b , d/b and h/b , but also to some other factors such as noise, geometric imperfections, etc.

Moreover, Fig. 4 shows computational results together with experimental ones. As a result, we can observe that the stable jet's oscillation occurs in a closely-wider zone than that between the boundaries with $d/b = 6.3 - 10$. And, whenever the jet stably oscillates ($St \neq 0$), St is not close to but qualitatively similar to the empirical formula. Then, regarding these two facts, we can conclude that the two-dimensional computation can simulate the experiments, from a qualitative point of view. This suggests the two-dimensionality of the phenomenon.

In summary, we have revealed a good agreement in experiment and computation with various Re and h/b . This suggests that the present phenomenon is intrinsically two-dimensional, and that the influences of Re and h/b are negligible from a qualitative point of view at $Re > 500$ and $h/b > 3$. Then, we discuss the phenomenon only by the two-dimensional computation at $Re = 500$ and $h/b = \infty$ or the water experiment at $Re = 500$ and $h/b = 10$.

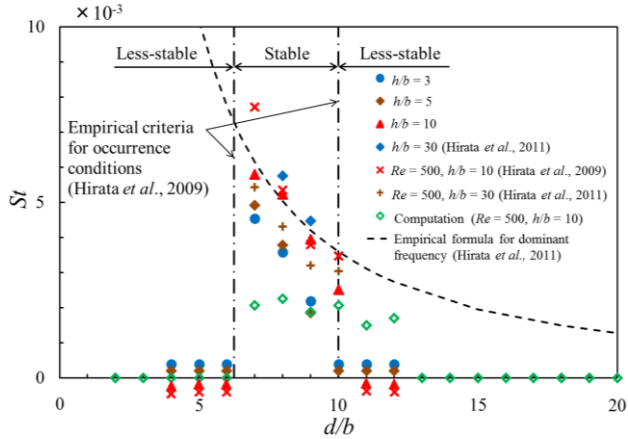


Figure 4: Strouhal number St against the distance d from a nozzle to a target, at $Re = 5000$, $a/b = 2.5$, $B/b = 15$ and $c/b = 2.5$ using HWA in air.

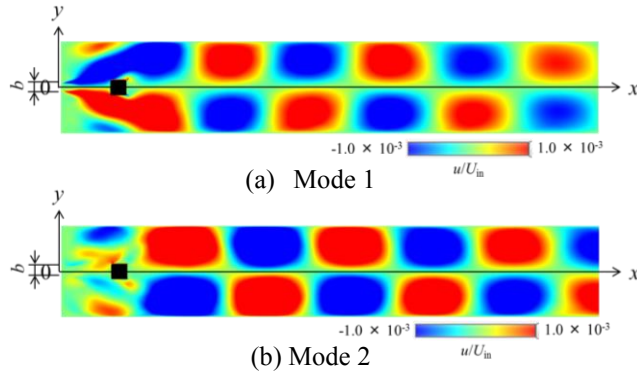


Figure 5: The first two POD modes (at $n = 100$): eigenfunctions of the x -component velocity u at $Re = 500$, $B/b = 15$, $c/b = 2.5$, $d/b = 8$ and $h/b \equiv \infty$ by computation.

3.3 Flow visualisation

In order to explain the physics of problems, flow visualisations often give us useful information. The proper orthogonal decomposition (hereinafter, referred to as POD) is another alternative. Figure 5 is an example analysed by the POD technique. More specifically, the figure shows the first two POD modes (at a snapshot number $n = 100$); namely, eigenfunctions of the x -component velocity u at $Re = 500$, $B/b = 15$, $c/b = 2.5$, $d/b = 8$ and $h/b = \infty$ by computation. Because the first and the second POD modes are almost dominant in the present flow, we can clearly see the downstream travelling of a spatially-staggered periodic pattern.

3.4 Influence of streamwise-target dimension

In this section, we discuss the influence of the target's shape upon the flow. More specifically, we consider the effect of one geometric parameter a non-dimensional streamwise target size a/b upon both the dominant frequency and the occurrence of stable jet's oscillation.

Figure 6 shows St plotted against a/b for several values of d/b , at $Re = 500$, $B/b = 15$, $c/b = 2.5$ and $h/b = 10$ using the UVP. Dashed lines in the figure denote the empirical formula proposed by [2], for reference. The results for $St = 0$ represent the flow with less-stable jet's oscillation as well as Fig. 4. Whenever the jet stably oscillates, St can be approximated by the formula (3). On the other hand, the oscillation tends to suppress at $a/b \geq 10$, in addition to such an empirical criterion with $d/b < 7$ or $d/b > 9$.

In order to examine the above a/b effect concerning the occurrence/suppression of stable jet's oscillation, Figs. 7 to 9 show the stable-oscillation domain on the a/b - d/b plane, at $Re = 500$, $B/b = 30$, $c/b = 2.5$ and $h/b = 10$ using the UVP. In the figures, dots represent the 'stable' condition where the jet's oscillation is periodic at any time as shown in Fig. 3, and crosses represent the 'less-stable' condition where the oscillation is almost non-periodic and sometimes periodic. Then, a red solid line denotes the boundary of the stable-jet-oscillation domain.

Two chained lines in each figure denote the stability boundaries proposed by [1]; namely, the upper and lower ones represent such equations as $B/b = 3/2$ and $c/b = 2/5$, respectively. We can observe using PIV that the stable jet's oscillation occurs in a zone between the two boundaries with $d/b = 6.25 - 10$ in Fig. 7, with $d/b = 6.25 - 13.3$ in Fig. 8 and with $d/b = 7.5 - 20$ in Fig. 9, whenever the jet stably oscillates.

However, even inside the zone between the two chained lines, the stable jet's oscillation does not always occur. That is to say, we cannot observe any stable jet's oscillation at $a/B > 4/5$ (a blue solid line in each figure). Then, we now get an additional criterion for the occurrence condition of the stable jet's oscillation, as follows.

$$0 < a/B \leq 4/5. \quad (4)$$

We can confirm the effectivity of this criterion in a range of $B/b = 15 - 30$, as shown in Figs. 7 - 9.

This new criterion is not enough, as shown in the figures.

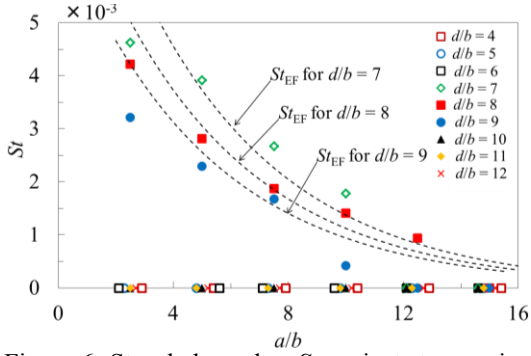


Figure 6: Strouhal number St against streamwise length a of a target for several values of d/b , at $Re = 500$, $B/b = 15$, $c/b = 2.5$ and $h/b = 10$ using UVP in water. Dashed lines denote the empirical formula proposed by Hirata *et al.* (2011) [2].

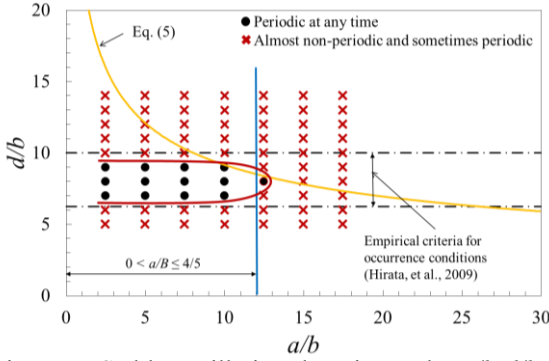


Figure 7: Stable-oscillation domain on the a/b - d/b plane, at $Re = 500$, $B/b = 15$, $c/b = 2.5$ and $h/b = 10$ using UVP in water.

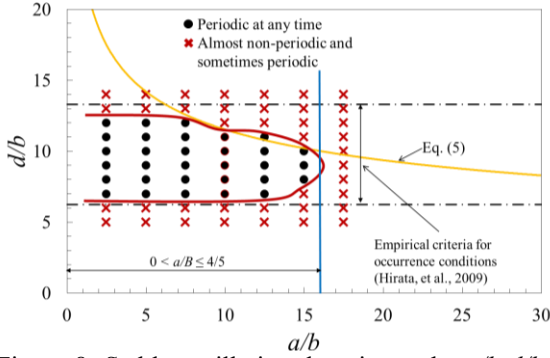


Figure 8: Stable-oscillation domain on the a/b - d/b plane, at $Re = 500$, $B/b = 20$, $c/b = 2.5$ and $h/b = 10$ using UVP in water.

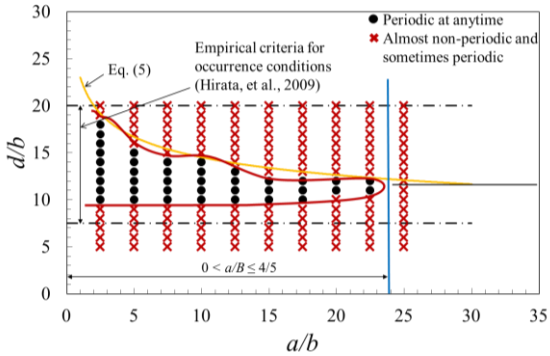


Figure 9: Stable-oscillation domain on the a/b - d/b plane, at $Re = 500$, $B/b = 30$, $c/b = 2.5$ and $h/b = 10$ using UVP in water.

So, we propose another additional criterion. This criterion is given by the following equation.

$$d/b \leq 23 (a/b)^{-6/(B/b)}. \quad (5)$$

A yellow solid line in the each figure denotes this criterion. We can see a good agreement between the criterion and the boundary of the stable-jet-oscillation domain. Of course, we can confirm the effectivity of this criterion in a range of $B/b = 15 - 30$, as well. On the present stage, the mechanism of this a/b effect upon the occurrence/suppression of stable jet's oscillation is not obvious yet, being expected to be solved in future.

4. Summary

We have experimentally investigated a self-excited oscillatory phenomenon of a two-dimensional confined jet with a cylinder as a downstream target using velocimetries, namely, (1)ultrasonic velocity profile UVP, (2)particle-image velocimetry PIV and (3)hot-wire anemometer HWA, focusing on two effects of the geometry such as an aspect-ratio effect and a streamwise-target-size effect. Furthermore, we have conducted two-dimensional numerical analyses based on vorticity ζ and stream function ψ using a finite-difference discretisation method.

As a result, we have revealed (1) a good agreement between experiments and computations, which suggests that the present phenomenon is intrinsically two-dimensional, and (2) the importance and the complexity between the upstream and the downstream target. Concerning (2), we have confirmed on the basis of UVP's measurements that the dominant jet's frequency f_D can be approximately predicted by the proposed empirical formula [2], whenever the jet stably oscillates at various values of the non-dimensional streamwise target size a/b where b denotes the length scale of the jet's breath. The effect of a/b upon the occurrence of the stable jet's oscillation is negligible at $a/b < 10$. Then, the occurrence can be predicted by the proposed empirical formula [1]. On the other hand, at $a/b \geq 10$, the effect of a/b is not negligible. Besides, we conduct the proper orthogonal decomposition POD, where the first and the second POD modes are almost dominant in the present flow.

References

- [1] Hirata, K., Matoba, N., Naruse, T., Haneda, Y. and Funaki, J.: On the Stable-Oscillation Domain of a Simple Fluidic Oscillator, *JSME Journal of Fluid Science and Technology*, Vol. 4, No. 3 (2009), 623-635.
- [2] Hirata, K., Inoue, T., Haneda, Y., Miyashita, N., Tanigawa, H. and Funaki, J.: On Dominant Oscillation Frequency of a Simplified Fluidic Oscillator, *JSME Journal of Fluid Science and Technology*, Vol. 6, No. 4 (2011), 534-547.
- [3] Yamasaki, H., Takahashi, A. and Honda, S., A New Fluidic Oscillator for Flow Measurement, *Proc. FLUCOME (1988)*, 16-20.
- [4] Takeda, Y., Velocity Profile Measurement by Ultrasonic Doppler Shift Method, *International Journal of Heat Fluids Flow*, Vol. 7 (1986), 313-318.
- [5] Takeda, Y., Fischer, W. E., Kobayashi, K. and Takeda, T., Spatial Characteristics of Dynamic Properties of Modulated Wavy Vortex Flow in a Rotating Couette System, *Experiments in Fluids*, Vol. 13 (1992), 199-207.
- [6] Hirata, K., Shintani, A., Kawaguchi, R., Inagaki, K., Nagura, T., Maeda, T.: 3D-PTV Measurement Verified by UVP for Unsteady and Three-Dimensional Flow inside a Suction Sump, *JSME Journal of Fluid Science and Technology*, in press.
- [7] Funaki, J., Matsuda, H., Inoue, T., Tanigawa, H. and Hirata, K.: UVP Measurement on Periodic Flow in a Flip-Flop Jet Nozzle, *JSME Journal of Fluid Science and Technology*, Vol. 2, No. 2 (2007), 359-367.

A novel design of ultrasonic spinning rheometry

Yuji Tasaka¹, Taiki Yoshida¹, and Yuichi Murai¹

¹Laboratory for Flow Control, Hokkaido University, N13 W8, Sapporo 060-8628, Japan

We introduced grand design of ultrasonic spinning rheometry that utilizes velocity profile measurement by UVP in rotating cylinder flows of complex fluids including multiphase media to overcome problems on common spinning rheometry. Multiple schemes dealing with physical relations through physical values reflecting rheological properties allow evaluation of multiple rheological properties by single measurement. Rheometry along the design was demonstrated on bubble suspension, and effective Newtonian viscosity near the cylinder wall, where the bubbles are largely elongated, and linear viscoelasticity on little inner region were evaluated. Additionally, a novel scheme utilizing Fourier transform for higher frequency spinning tests were proposed.

Keywords: Rheometry, Effective viscosity, Viscoelasticity, Rotating flow, Spatio-temporal velocity data

1. Introduction

Accurate and rapid evaluation of rheological properties of fluids has great importance in scientific, engineering and industrial fields for multiple purposes. For example, in manufacturing processes dealing with fluid materials, correct estimation of the properties allows accurate control and improvement of the process. Conventional, rotational rheometers that assume ideal Couette flow in a narrow gap between concentric cylinders, a cone and a plate, or concentric disks have satisfied the demands by robustness on the results. But recent broadening demands have exceeded areas covered by the conventional rheometers and have required novel rheometry. One of typical examples is rheometry for multiphase media. If the size of the dispersed phase of a multiphase medium is considerably large in comparison with the test gap of conventional rheometers, assumption of ideal Couette flow is not realized, and thus the measurement results would be unstable. Existence of shear banding and local yield area cause similar problems on the evaluation. To overcome this problem, simultaneous measurement of velocity profiles of fluids filled in wider gaps was performed [1]. Velocity profile measurement also makes possible to evaluate local shear dependent viscosity of flowing material in a pipe [2]. The literatures show that velocity profile measurements have great potential on rheometry for complex fluids.

Our group has developed a novel rheometry utilizing velocity profile measurement by ultrasonic velocity profiling (UVP) and functional oscillation of a cylinder as a vessel of the test media, this is termed ultrasonic spinning rheometry (USR). With USR we performed; (a) rapid estimation of shear dependent viscosity of yoghurt [3]; (b) evaluation of effective viscosity of dispersed bubbly liquid in unsteady shear flows [4]; model-free rheometry for evaluation of rheological properties of unknown media and also for avoiding errors due to miss-selection of rheological model [5, 6]. Attempts to evaluate time-dependent rheological properties of thixotropic fluids are also ongoing [7]. In the individual projects of application of USR introduced above, suitable information of flows is

extracted from spatio-temporal velocity distributions measured using UVP to evaluate different rheological properties. In this study, we would like to propose assembled form of USR to evaluate its applicability and discuss rising problems to be solved for further evolution of the methodology.

2. Ultrasonic spinning rheometry

2.1 Configuration of equipment

Measurement configuration, equipment and definition of coordinates for USR through the experiments are explained. Figure 1 shows an illustration of the test cylinder made of acrylic resin with 145 mm in diameter filled with test fluids. The cylinder motion is controlled by a stepping motor and thus functional oscillatory rotations can be realized. The measurement line of UVP is located parallel to the center line of the cylinder with off-center displacement $\Delta y = 15$ mm; this value is determined empirically to consider both incidence of the ultrasonic wave into the test fluid and reduction of amplification of the measurement error due to inverse projection of velocity vectors. An UVP monitor model Duo (Met-Flow S.A.) was adopted with alternative use of 2 MHz or 4 MHz ultrasonic transducers depending on the attenuation of ultrasonic wave in test media.

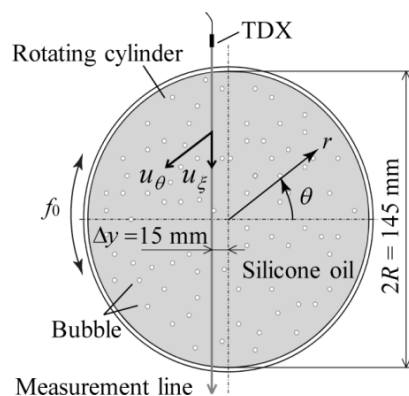


Figure 1: Illustration of a test cylinder, measurement configuration and coordinate system adopted for ultrasonic spinning rheometry [4]

With periodic oscillations of the cylinder, flows inside the cylinder can be assumed as axisymmetric. And conditions with frequency of 0.5 Hz to 2.0 Hz and amplitude 90 degrees, it was confirmed that flows of a viscous silicone oil agree with ideal one-directional flow driven by cylinder rotation in comparison between exact solution with assumption of the one-directional flow and spatio-temporal velocity distributions measured UVP [4]. The velocity component along the measurement line, u_ξ , can therefore be assumed as projection of the azimuthal velocity u_θ and thus u_θ is simply calculated from u_ξ at each radial position with Δy (hereafter we remove θ from u_θ for simplicity). For measurements, quasi-neutrally buoyant particles with $O(10 \mu\text{m})$ were dispersed into the test fluid as tracer particles.

2.2 Assembled design of USR

Figure 2 shows block diagram of design of USR by assembling previous attempts for various test fluids, where italic words represent rheological properties evaluated by USR from analysis on spatio-temporal velocity distributions $u(r, t)$ via different process. Words in the boxes indicate physical values or physical relations reflecting the rheological properties. The parameters that can be set are oscillation speed U and frequency ω for sinusoidal oscillation cases, and type of functions for the cylinder motion, steady rotation, rapid start and sudden stop are chosen depending on the purpose. The individual schemes to evaluate the rheological properties are summarized below.

Shear dependent viscosity and Flow curve: Radial velocity profile of fluid having shear-dependent viscosity against steady rotation of the cylinder takes a shape depending on the viscosity. Fitting the velocity profile estimated from ‘‘suitable’’ rheological model, for example power law,

$$\tau = k\dot{\gamma}^n = k\left(\frac{\partial u}{\partial r} - \frac{u}{r}\right)^n \quad (1)$$

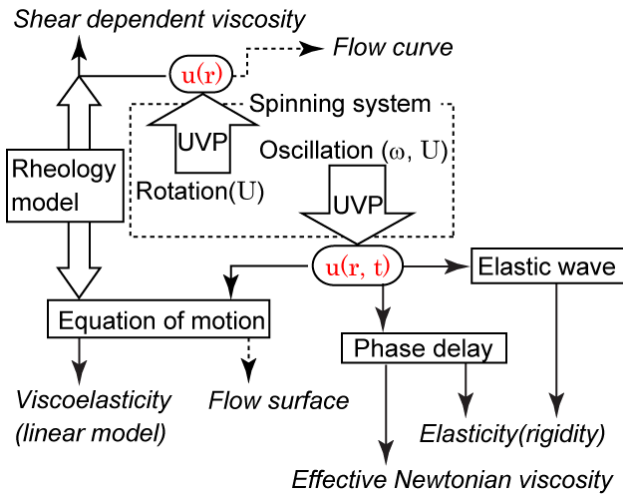


Figure 2: block diagram of assembled design of ultrasonic spinning rheometry: italic words represent rheological properties that can be evaluated and words in boxes indicate physical values or physical relations to extract the properties utilizing spatio-temporal velocity data, $u(r, t)$

where k and n represent the properties, then we can evaluate the viscosity. This scheme was already established well [1] and we do not mention details of this.

Combination with torque measurement allows having general relation between shear stress and strain rate, so-called flow curve. This does not require rheological model and achieves model-free rheometry [5].

Effective Newtonian viscosity: Assuming Newtonian viscosity on test fluids, propagation of the cylinder oscillation into the fluid has to be described by phase delay $\phi(r)$ of the azimuthal velocity against the cylinder wall in the radial direction. With comparing the phase delay obtained from $u(r, t)$ with that of ideal exact solution for representative viscosity [4], we can estimate the viscosity of the test fluid. This scheme is applicable to liquid with dispersion phase because of relatively large measurement volume of UVP, and thus ‘effective’ viscosity in the measurement volume is obtained [4].

Elasticity (rigidity): Two different schemes were proposed for elasticity analysis. One is from propagation of elastic wave dominated by equation of waves,

$$\frac{\partial^2 \Theta}{\partial t^2} = c^2 \frac{\partial^2 \Theta}{\partial r^2}, \quad c = \sqrt{\frac{G}{\rho}}, \quad (2)$$

where $\Theta(r, t)$ represent azimuthal oscillation of media and c speed of elastic wave. Sudden start of the rotation, for example, induces the elastic wave in viscoelastic bodies and calculating c from $u(r, t)$ as propagation speed of waves tells us modulus of rigidity G . Another scheme assumes situation where the quasi-viscous body connects continuously viscoelastic body. At positions nearby the boundary, phase lag of the velocity fluctuation due to the cylinder oscillation $\phi(r)$ is affected by elasticity and is decreased from pure viscous body with δ as

$$\phi(r + \Delta r) = \phi(r) + \left. \frac{d\phi}{dr}(\mu) \right|_r \Delta r - \left. \frac{d\delta}{dr}(E, \mu) \right|_r \Delta r \quad (3)$$

where $r + \Delta r$ is neighboring measurement volume for r . The 2nd term represents increase of the phase lag due to the original viscous effect. Assuming linear viscoelasticity, δ is estimated as influence of elasticity relative to the viscosity. Then it is represented with storage modulus G' and loss modulus G'' by

$$\frac{\pi}{2} - \delta = \tan^{-1} \frac{G''}{G'} = \tan^{-1} \frac{E}{\omega\mu} \quad (\text{for Maxwell model}) \quad (4)$$

Here we adopted Maxwell model for linear viscoelasticity. According to Eq. (4), elasticity E is obtained from δ and viscosity μ .

Viscoelasticity and flow surface: If the strain on the fluid motion is small enough, we can evaluate linear viscoelasticity as rheological properties of viscoelastic bodies. Assuming axisymmetric one-directional flow in the cylinder, equation of motion of fluids is reduced into

$$\rho \frac{\partial u}{\partial t} = \frac{\partial \tau}{\partial r} + \frac{2\tau}{r}. \quad (5)$$

Measured $u(r, t)$ has to satisfy this equation. And

adopting Maxwell model to represent ‘linear’ viscoelasticity,

$$\tau + \frac{\mu}{E} \frac{\partial \tau}{\partial t} = \mu \left(\frac{\partial u}{\partial r} - \frac{u}{r} \right), \quad (6)$$

viscosity and elasticity can be evaluated as values minimizing cost function

$$\begin{aligned} \min_{\tau, \mu, E} \int_r \int_t \left[\tau + \frac{\mu}{E} \frac{\partial \tau}{\partial t} - \mu \left(\frac{\partial u}{\partial r} - \frac{u}{r} \right) \right] dt dr, \\ \text{s.t.: } \rho \frac{\partial u}{\partial t} - \frac{\partial \tau}{\partial r} - \frac{2\tau}{r} = 0. \end{aligned} \quad (7)$$

In difference form, it is described as

$$\begin{aligned} \min_{\tau, \mu, E} \sum_i \sum_j \left[\tau_{i,j} + \frac{\mu}{E} \frac{\tau_{i+1,j} - \tau_{i,j}}{\Delta t} - \mu \left(\frac{\partial u}{\partial r} \Big|_{i,j} - \frac{u_{i,j}}{r_j} \right) \right]^2, \\ \text{s.t.: } \rho \frac{\partial u}{\partial t} \Big|_{i,j} - \frac{\tau_{i,j+1} - \tau_{i,j}}{\Delta r} - \frac{2\tau_{i,j}}{r_j} = 0. \end{aligned} \quad (8)$$

Similar to the flow curve explained above, relation of stress, strain, and strain rate can represent general viscoelastic properties without adopting rheological model. This representation is not restricted in linear regime, and is termed ‘flow surface’ by our group as a novel model free rheometry [6]. Obtaining this relation requires additional torque measurement simultaneously with velocity profile measurement by UVP.

3. Demonstrations and results of USR

The USR is demonstrated on evaluation of rheology of bubbly liquid. Evaluation of the effective viscosity on bubbly liquid has long history and some evaluation schemes were proposed for steady [8] and unsteady shear flows [9]. But the scheme still has imperfection for general situations.

Figure 3 shows pictures of bubble deformations in the oscillating cylinder with difference conditions, (a) steady, oscillation with (b) 0.5 Hz and 2.0 Hz in frequency, where the amplitude of oscillation is 90 deg. for the both cases and volume fraction of bubbles is $\alpha \sim 2\%$. The bubbles are largely deformed near the cylinder in oscillation conditions, and seem to keep original spherical shape at the inner part. It is suggested that the surface

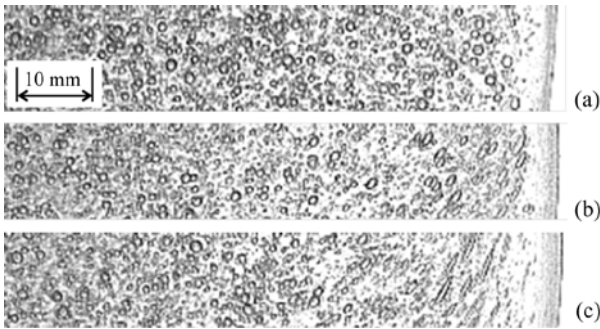


Figure 3: Pictures of bubble deformations in the oscillating cylinder; (a) stationary, (b) 0.5 Hz and (c) 2.0 of the cylinder oscillation

tension of bubbles that is origin of elasticity on bubbly liquid is already lost in the former case and still effective in the latter case. So rheology in the former case would be able to be evaluated as effective Newtonian viscosity and one in the latter as linear viscoelasticity.

3.1 Effective Newtonian viscosity

Effective Newtonian viscosity analysis is thus adopted in near wall region of the cylinder. As mentioned in Sec. 2.2, effective Newtonian viscosity is estimated from phase lag of the velocity fluctuations against the cylinder wall, where the phase is calculated from Fourier analysis of the velocity fluctuation at each radial position as phase of the most dominant frequency component. Figure 4 shows profiles of the phase lag measured from 1000 cSt silicone oil without/with bubbles, where the profile estimated from analytical solution for 1000 mm²/s in the kinematic viscosity is displayed for comparison [4]. The variation for the pure oil seems to follow that of the analytical solution. On the other hand, the variation in bubble suspension has displacement from the analytical solution and it becomes wider toward the cylinder center. We evaluated gradient of the phase delay $\Delta\phi/\Delta r$ at each radial position to estimate local effective viscosity and averaged them in a range of 0.1R to reduce the noise. Comparing the $\Delta\phi/\Delta r$ of bubble suspension with that of analytical solution with various value of the kinematic viscosity, the local effective viscosity ν^* is determined as a viscosity providing most similar value of $\Delta\phi/\Delta r$.

Table 1 summarizes results of the estimation of effective Newtonian viscosity μ^* for different frequency condition and at $r/R = 0.95$ and 0.85, where the viscosity is in style of relative viscosity against the original viscosity of silicone oil μ ,

$$\eta = \frac{\mu^*}{\mu} = (1 - \alpha) \frac{\nu^*}{\nu}. \quad (9)$$

The relative viscosity larger than unity means increase of viscosity by bubble dispersion and vice versa. Near the cylinder wall, the viscosity increases for 0.5 Hz and decreases for larger frequencies. As shown in Fig. 3(c), bubbles near the wall for 2.0 Hz are largely elongated and have very small effort on the momentum propagation. This is reason why the viscosity decreases, and value of

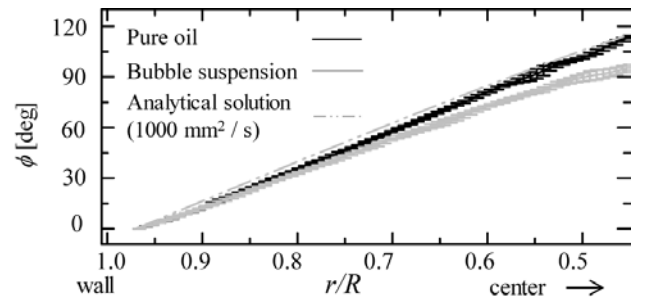


Figure 4: Phase lag of the velocity fluctuation against the cylinder oscillation for pure oil, bubble suspension and estimated value from analytical solution for 1000 mm²/s in kinematic viscosity [4]

the decrease, around 17 %, is much larger than estimation from the previous schemes [9]. In the inner block at around $r/R = 0.85$, the viscosity increases with 10 %. This is also considerably larger than the evaluation according to the previous scheme [9].

Table 1: Estimated relative effective viscosity for different frequency condition and at $r/R = 0.95$ and 0.85 [4]

Frequency [Hz]	η at $r/R = 0.95$	η at $r/R = 0.85$
0.5	1.109	1.169
1	0.979	1.154
2.0	0.831	1.062

3.2 Linear viscoelasticity analysis

We performed linear viscoelastic analysis according to the scheme detailed in Sec. 2.2. As a preprocessing, we performed POD (proper orthogonal decomposition) filtering on the original spatio-temporal velocity distribution (Fig. 5(a)) to reduce measurement errors that are largely enhanced by process of differences in calculation of Eq. (8). Figure 5(b) shows the results constructed from 1st and 2nd POD modes and the distribution seems to smooth enough. Evaluated value of viscosity and elasticity for 1.0 Hz at $r/R = 0.7$ are $\mu = 1.05$ Pa·s and $E = 69.40$ Pa. Corresponding absolute value of complex viscosity,

$$|\mu^*| = \frac{\mu}{\sqrt{1 - (\omega\mu/E)^2}} \quad (10)$$

is 1.045 Pa·s.

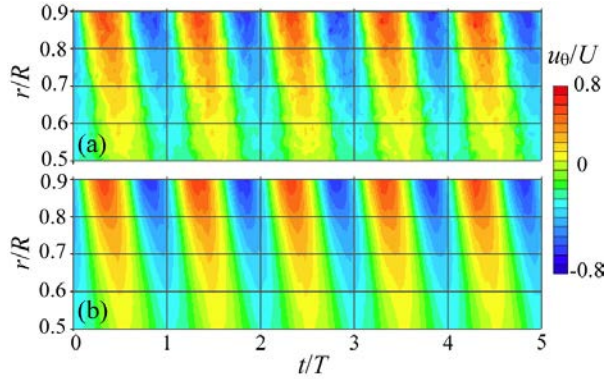


Figure 5: Spatio-temporal distribution of azimuthal velocity component for 1.0 Hz in the oscillation frequency; (a) raw data and (b) filtered data by POD, where 1st and 2nd modes are used

4. Ongoing attempts

Each scheme in the assembled design has not been fully optimized yet and has area to be improved. Here we introduce ongoing attempts to reduce calculation noise on linear viscoelastic analysis.

For high frequency testing on USR, sampling frequency of UVP would become insufficient to resolve fluid motion. And it may enhance measurement error in the process of differences of spatio-temporal velocity distribution for viscoelastic analysis. To overcome this

problem, we propose frequency domain analysis using Fourier transform. Applying Fourier transform converts Eqs. (5) and (6) into

$$\hat{\tau} + i\omega \frac{\mu}{E} \hat{\tau} = \mu \left(\frac{\partial \hat{u}}{\partial r} - \frac{\hat{u}}{r} \right), \quad (11)$$

$$\hat{\tau}(r, \omega) = \mathcal{F}[\tau(r, t)], \hat{u}(r, \omega) = \mathcal{F}[u(r, t)].$$

$$i\omega \rho \hat{u} = \left(\frac{\partial}{\partial r} + \frac{2}{r} \right) \hat{\tau}. \quad (12)$$

The problem is converted into minimizing cost function,

$$G(r; E, \mu) = \int_0^\Omega \left[i\omega \rho \hat{u} - \left(\frac{\partial}{\partial r} + \frac{2}{r} \right) \hat{\tau} \right]^2 d\omega, \quad (13)$$

where

$$\hat{\tau}(r, \omega) = \mu \left(\frac{\partial \hat{u}}{\partial r} - \frac{\hat{u}}{r} \right) \left(1 - i\omega \frac{\mu}{E} \right) \left[1 + \left(\omega \frac{\mu}{E} \right)^2 \right]^{-1}. \quad (14)$$

Applicability of this scheme has not evaluated yet, but the equations tell us it can avoid temporal differences in the calculation.

6. Summary

We proposed assembled desing of ultrasonic spinning rheometry for wider use of the methodology on general complex fluidss. According to the design we can evaluate same rheological properties by different schemes and to increase robustness of the estimated value. The design is still in progress and also each scheme still requires improvement. The present methodology has great potential and demonstration on analysis of bubble suspension was performed.

References

- [1] Derakhshandeh B and Vlassopoulos D.: Thixotropy, yielding and ultrasonic Doppler velocimetry in pulp fiver suspensions. *Rheol. Acta* 51 (2012) 201–214.
- [2] Ouriev B and Windhab E.: Novel ultrasound based time averaged flow mapping method for die entry visualization in flow of highly concentrated shear thinning and shear-thickening suspensions, *Meas. Sci. Technol.* 14 (2003) 140–147.
- [3] Section 5.2.1.2 Spinning Flow Rheometry in Takeda Y ed.: *Ultrasonic Doppler velocity profiler for fluid flow*, Springer, Germany (2012).
- [4] Tasaka Y, *et al.*: Estimating the effective viscosity of bubble suspensions in oscillatory shear flows by means of ultrasonic spinning rheometry, *Exp. Fluids*, 56 (2015), 1867.
- [5] Shiratori T, Tasaka Y, Oishi Y and Murai Y: Ultrasonic velocity profiling rheometry based on a widened circular Couette flow, *Meas. Sci. & Technol.* 26 (2015) 085302.
- [6] Shiratori T, Tasaka Y and Murai Y: Rapid rheological characterization of a viscoelastic fluid based on spatiotemporal flow velocimetry, *Exp. Thermal & Fluid Sci.* 71 (2016) 1-13.
- [7] Yoshida T, Tasaka Y, Murai Y: Quantitative evaluation of rheological properties for complex fluids using ultrasonic spinning rheometry, *Proc. ISUD10* (2016)
- [8] Frankel NA, Acrivos A: The constitutive equation for a dilute emulsion, *J. Fluid Mech.* 44 (1970) 65-78.
- [9] Llewellyn EW and Manga MJ: Bubble suspension rheology and implications for conduit flow, *Volcanology and Geothermal Res.* 143 (2005) 205-217.

Determining the thermal flow structure inside fermenters with different shapes using Ultrasonic Doppler Velocimetry

Heiko Meironke¹, David Kasch¹, Richard Sieg¹

¹ University of Applied Sciences Stralsund, School of Mechanical Engineering,
Zur Schwedenschanze 15, 18435 Stralsund, Germany

In this work the experimental investigations of the flow and the temperature field in fermenters are presented. The investigated tank is used for fermentation and storing of beer. The flow stability and the fermentation process are affected of the height/diameter ratio and the bottom shape of the fermenter. The modern cylindroconical tanks are generally equipped with sharp conical bottom (60° to 70° cone angle). Various studies have shown that a hemispherical bottom offers advantages in terms of the fermentation process. In the presented study, a tank with two different shapes of bottom (classic conical with 60° angle and hemispherical bottom) have been used in the laboratory, which were equipped with special design features. The velocity fields are measured by means of Ultrasound Doppler Velocimetry. Furthermore temperature measurements are conducted to analyze the interrelationship between the heat transfer and flow structure. In the course of our research the experiments have been performed with model fluid and it is intended to be measure in real turbid fermentation fluid (wort).

Keywords: Ultrasound Doppler Velocimetry, flow field measurements, fermentation, multiphase flow

1. Introduction

The process steps of fermentation, maturation and storage following the wort production have a decisive influence on the efficiency and product quality in beer production. In particular, the fermentation and maturation have complex interactions between the exothermic yeast metabolism and the resulting convection in the fermenter. The description of the thermo-fluid-dynamical processes and the economic benefit of this knowledge have despite increasing scientific and technological progress in this field, still innovative potential especially in the structural design of the fermenter and in the effective control of the cooling zones.

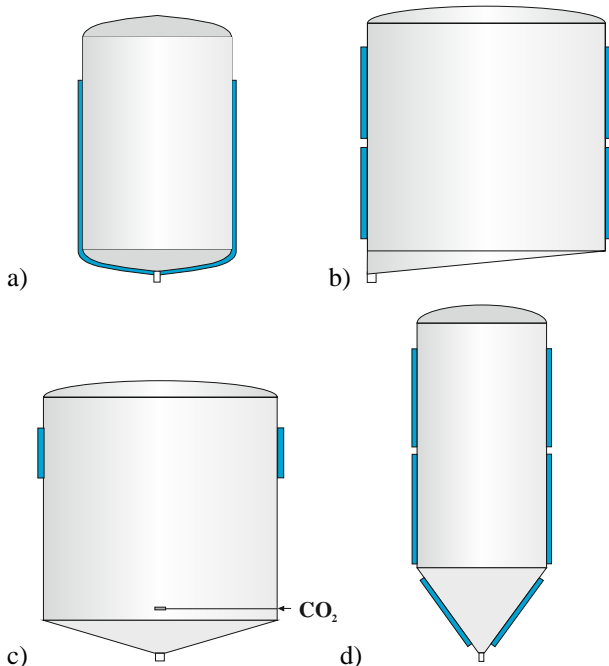


Figure 1: Fermenting tanks: a) Nathan-tank, b) Asahi-tank, c) Uni-tank, d) Cylindroconical tank [1]

In the course of the last century, various fermentation vessels have formed starting out from the open fermenting vat to closed fermenting tanks. One of the oldest method of performing the fermentation, maturation and storage in closed fermenting tanks represents the Nathan method. Nathan [2] developed in 1902 in connection with his quick method of brewing a cylindrical and multi-functional closed tank (Hansena apparatus) made of cast iron with a conical bottom part (Fig. 1a). This cylindroconical tank had a maximum volume capacity of 30,000 liters at a height to diameter ratio of 4. Lindner [3] conducted a series of studies to these tanks. Since the mid-1960s the accelerated development and the industrial mass production of closed fermenting tanks took place worldwide. The Japanese Asahi - Brewery developed the Asahi-tank under the global effort of the tank developments in the brewing industry (Fig. 1b). One special feature is the flat inclined bottom (about 10%) [4]. Due to a special suction device inside the tank, the finished green beer always has the same content of CO₂. An advancement of the Asahi-Tanks carried out in the early 1970s by Knudsen and Vacano [5] of the American "Rainier Brewing Company" with the development of the Uni-tanks (Fig. 1c). The Uni-tank could be used in one-Tank process, while fermentation, maturation and storage are carried out successively in this tank. The tank has a flat conical bottom (155° cone angle) and approximately the same height to diameter ratio. The special feature of this tank is a nozzle ring which is located in the lower cone area and CO₂ can be injected through the ring. With the rediscovery and introduction of cylindroconical tanks in the mid-1960s, production times could be reduced and the tank capacity in the brewing industry can be increased significantly [6].

The cylindroconical tank (CCT) is nowadays the preferred shape of the tank in a modern European brewery and has an acute conical bottom (60°-70° cone

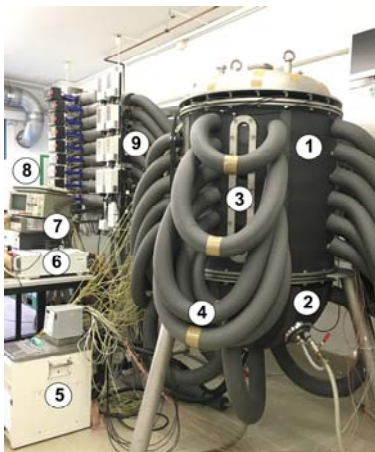
angle) as well as an upper torispherical or semi-ellipsoidal head (Fig. 1d). In outdoor tanks height to diameter ratios of up to 6 are realized, whereby in particular in indoor tanks from the mid-1980s, the trend towards a height to diameter ratios of 2 [7]. In many breweries in the indoor area of buildings because of technical reasons smaller height to diameter ratios (e.g. 1 or 0.8) are installed.

Due to strong turbidity of wort, the advantages of the Ultrasonic Doppler Velocimetry (UDV) are used for comprehensive studies of the convection flow in real wort during the last years in several projects [1, 8]. These provided measurements of the velocity fields in opaque fluids for any time during the fermentation. In these previous experimental studies of flow fields, mainly the cylindrical part was investigated. In this work the entire tank, especially the lower part (cone area) is in the focus. For the current studies, a new modular tank was developed.

2. Experimental Setup

2.1 Experimental Arrangement

For the experimental investigation of flow phenomena and temperature fields an existing experimental setup with a cylindroconical tank (270 liter) has been enhanced with a new modular tank which can be equipped with different bottoms (Fig. 2). In the present studies, the tank is equipped with a conical bottom (60°) and a hemispherical bottom with a total capacity of 350 liter respectively 375 liter.



- 1 - cylindrical part
- 2 - modular bottom
- 3 - optical access
- 4 - tube connection cooling panels
- 5 - bottom heating
- 6 - UDV – System
- 7 - data acquisition
- 8 - 10 kW cooling aggregate
- 9 - heating tubes and temperature control

Figure 2: Test rig with modular tank

Several openings in the new tank enable the integration of sensors for the temperature and flow measurement technology (Fig. 3). The modular tank was equipped with six separately controlled heating or cooling zones in the cylindrical part and one in the bottom part.

For the control of test facility, a program was created based on the software tool "LabView", to implement the automated continuous data acquisition of temperature and flow rates during operation of the test rig. Two operation modes are possible, the one is the simulated fermentation

by means of a model fluid and the other, the real fermentation operation.



Figure 3: Cylindrical Part of the new modular tank with the temperature measuring grid and the arrangement of transducers

2.2 Implementation of the temperature measurement

The temperature detection inside the tank is carried out by a conventional temperature measuring method in a grid array of 57 temperature sensors (RTD). The grid is installed in cross-section of the tank and will be adjusted accordingly for the two bottoms. Calibrations of all sensors are performed by comparison against a thermometer with a high accuracy.

2.3 Implementation of UDV

For the measurement of the flow fields, the Ultrasound Doppler Velocimetry is used, because in the planned experiments it is intended to be measure in real turbid wort (Table 1). The measurement of the flow field is carried out by means of the Ultrasonic Velocity Profile Monitor System UVP-XW-PSi from Met-Flow S.A.. The system was enhanced to a two dimensional diagnostic system for investigations of convection flow inside fermenters. The main principle is the combination of the measurements of the ultrasound echo time delay and the Doppler frequency. The basic feature of this system is the ability to establish the velocity in 128 separate points along measurement axis. For two dimensional measurements of velocities it is necessary to measure two velocity components at one spatial point in order to form a vector. Due to the fact that a two-dimensional measurement system is used, the array is aligned in the cross section of the tank. Here a certain degree of rotational symmetry of the flow is assumed. As the measurements have shown, however, the fluid movements are not symmetrical and fluctuate strongly.

The measuring array in the cylindrical part is rectangular and consists of 10 horizontal and 10 vertical transducers arranged (Fig 4 left). The vertical transducers are immersed in the fluid and the horizontal transducers measure through the wall (acrylic glass). In order to measure the velocities in the conical bottom, the 10 vertical transducers are lowered and 7 transducers are aligned orthogonal to the surface of the cone (Fig 5 right). In this study these transducers measure

through the bottom wall (stainless steel). This results in a corresponding angular orientation of the measuring array. The installation of the transducers on the hemispherical bottom is much more complicated because of the rounding there is a constant change of the angle (Fig 5 left). In a first arrangement, 7 transducers are mounted horizontally at the bottom. Due to the strong refraction angle a nearly radial distribution of the measuring lines is generated. This leads to non-uniform distribution of the intersection points in one half of the hemispherical bottom.

Table 1: Properties of the Measuring fields

Measuring fields	cylindrical part	conical bottom	hemispherical bottom
Transducer (4 MHz)	20	17	17
Intersection points	100	38	35

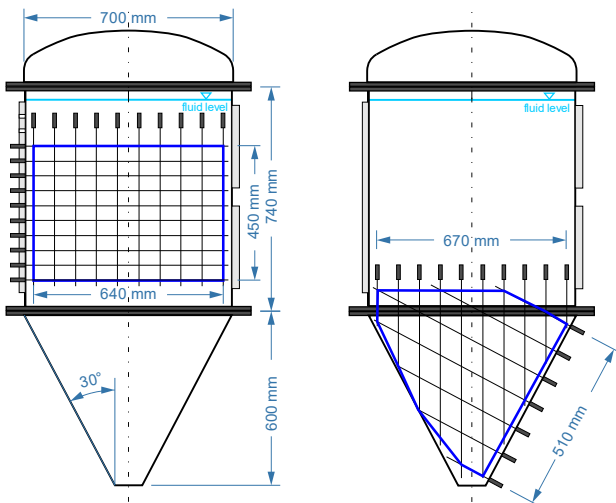


Figure 4: Measuring arrays (blue line) for the velocity measurement in the cylindrical part (left) and in the cone (right)

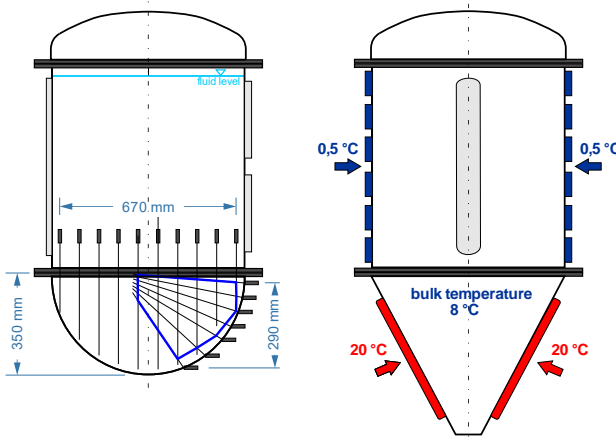


Figure 5: Measuring array for the velocity measurement in the hemispherical bottom (blue line) Figure 6: Thermal boundary condition for example in the cylindroconical fermenter

For the present experiments water is used as a model fluid, because water is very close with its properties on

the fermenting liquid. In the studies the cold fermentation was simulated used at a bulk temperature of 8°C. For simulation of the fermentation heat the bottom is heated at a temperature of 20°C. This temperature corresponds approximately to the resulting from the yeast metabolism fermentation heat. The steady state was achieved by removing the heat with the cooling zones (0.5°C) in the cylindrical part (Fig 6).

3. Results and Discussion

3.1 Measurement of temperature fields

The temperature field was measured continuously every ten minutes during the steady state of the simulated fermentation. The temperature field inside the cylindrical tank with conical bottom (Fig. 7 left) is about 0.5 K warmer than the tank with hemispherical bottom (Fig. 7 right) in the same boundary condition. The reason may be due to better mixing behavior in the cylindroconical tank. The temperature field in the upper part of this tank is determined by means of a large warm region in the middle. The lower tank area is determined by means of the cooled fluid, which sinks down to the cone due to the supporting effect of downward going flow in the boundary layer at the wall. Remarkable is the fact that there is a small temperature difference during the process of maximum of about 1°C, if the temperature gradient in the small wall region and the lowest cone is neglected. This small temperature difference is caused by the wide mixing zone with turbulent flow in the largest part of the tank. The cool area in the lower part of the tank with hemispherical bottom has a greater extension.

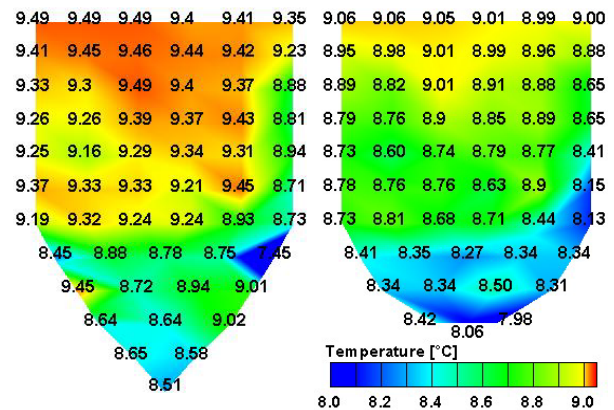


Figure 7: Temperature fields of the steady state inside the cylindrical tank with conical bottom (left) and hemispherical bottom (right)

3.1 Measurement of flow fields

The flow field in the upper area of the cylindroconical tank (Fig. 8) is determined by means of a large vortex in the middle. In the upper part of the tank with hemispherical bottom a large vortex could be detected close to the cooling zone (Fig. 9). Both vortices are driven by the rising warm fluid from the heating bottom. The fluid flows in the direction of the cooling zones and

sinks down at the border area of the tank towards the cone. The radial flow of this vortex was measured with velocities up to 20 mm/s. In general, the measured velocities are low but mostly between 2 mm/s and 10 mm/s. In the cone area no significant flow pattern can be detected with the present measurement configuration.

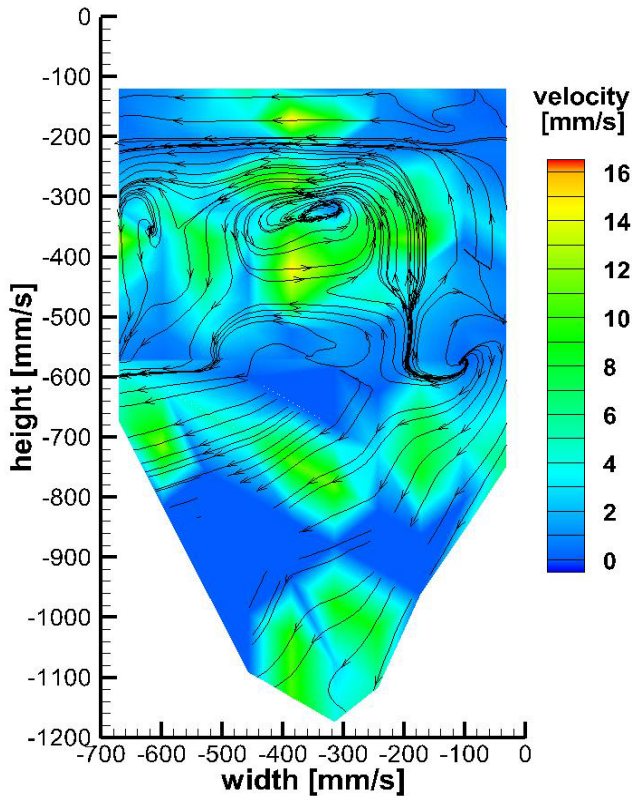


Figure 8: Velocity field and streamlines in the cylindrical tank with conical bottom

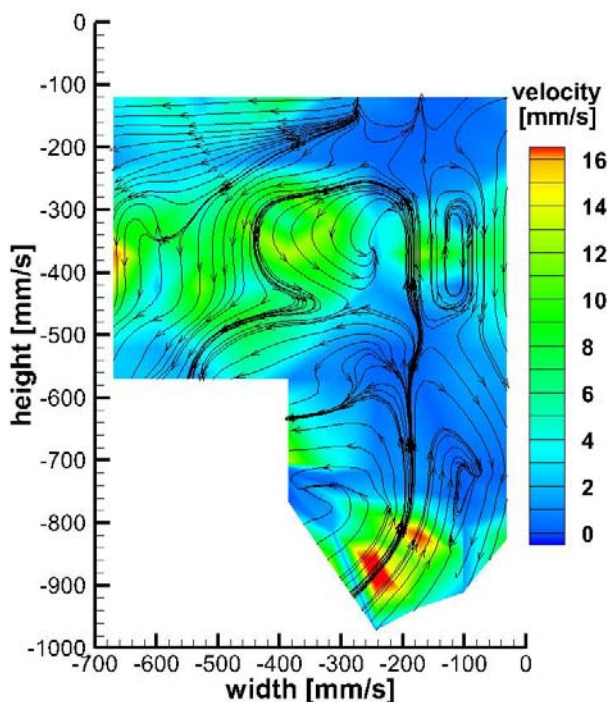


Figure 9: Velocity field and streamlines in the cylindrical tank with hemispherical bottom

4. Conclusion

In this study the temperature and velocity fields are described in a fermenter with two different bottoms. The selected thermal boundary conditions are used to simulate in the model fluid the fermenting wort during the real fermentation. The investigations have shown that, in particular the coupling of the transducers in the conical and hemispherical bottom turns out to be complicated. This relates to the measurement through the tank wall which is affected by the refraction, and the large difference in acoustic impedance. Another problem is the combination of the measurement fields, since the measuring depth of the transducers is limited.

Basically, the flow field is driven into the tank at the present boundary conditions by natural convection phenomena and thus is subject to very high fluctuation movements at very low velocities. These strong fluctuating movements to a low average velocity are also a challenge for the data acquisition.

In further tests, sensors with lower frequencies (2 MHz) will be used to detect a higher measuring depth or higher velocity range. In this context, the coupling of sensors will be optimized in both bottoms. Corresponding to this study, it is planned to investigate the flow and temperature fields during a real fermentation in this modular tank, especially focused on the lower tank area in different bottoms.

Acknowledgements

The authors gratefully acknowledge financial support from the "European Union Funds for Regional in different bottoms.

References

- [1] Meironke H: Charakterisierung des Impuls- und Wärmetransports in zylindrokonuschen Tanks während der Gärung, Reifung und Lagerung mittels laseroptischer und Ultraschall-Messtechniken, Dissertation, University of Rostock, Verlagshaus Monsenstein und Vannerdat, Münster (2007)
- [2] Nathan L: Nathan's Bierbereitung, Wochenschrift für Brauerei, Nr. 40, (1902), 597-599.
- [3] Lindner P: Das Nathan'sche Bierherstellungsverfahren im „Hansena“ Apparat, Wochenschrift für Brauerei, Nr. 28, (1901), 354-356.
- [4] Amaha M, *et al.*: Some experiences in the "one-tank" process with Asahi large-capacity tanks, Proceedings of EBC Convention, (1977), 545-560.
- [5] Knudsen F B & Vacano N L: Uni-Tanks - Grundideen, Betriebserfahrungen, Wirtschaftlichkeit, Brauwelt Vol. 113, Heft 9, (1973), 158-166.
- [6] Bellmer H-G, Knoepfel K H: Technik und Technologie zylindrokonuscher Großraumtanks, Brauwelt, Vol. 120, Heft 30, (1980), 1069-1073.
- [7] Narziß L: Abriss der Bierbrauerei, 7. aktualisierte und erw. Auflage, Wiley-VCH Verlag, Weinheim, (2005)
- [8] Meironke H, Böttcher K: Experimental Investigation of Parameters, Influencing velocity fields during beer fermentation, in: Progress in Mechanical Engineering and Technology, Vol. 597 (2014), 37-44.

Bubbly Flow Measurement in High Temperature Molten Salt

Tomonori Ihara¹, Keisuke Tsukada², Hiroshige Kikura², and Horst-Michael Prasser³

¹ Department of Marine Electronics and Mechanical Engineering, Tokyo University of Marine Science and Technology, 2-1-6 Etchu-jima, Koto-ku, Tokyo 135-8533, Japan

² Laboratory for Advanced Nuclear Energy, Institute of Innovation Research, Tokyo Institute of Technology, 2-12-1 Ookayama, Meguro-ku, Tokyo 152-8550, Japan

³ Laboratory for Nuclear Energy, Swiss Federal Institute of Technology Zurich, Sonneggstrasse 3, Zurich 8092, Switzerland

Ultrasonic velocity profiler (UVP) was applied for the measurement of bubbly flow in high temperature molten salt. Buffer rod technique was used to transmit ultrasound into the melt. Trailing echo is a typical problem of buffer rod, which cause measurement error in UVP. Customized signal processing technique was presented to suppress noises due to trailing echoes. In addition to the signal processing, post-processing techniques were employed to extract bubbly flow from noisy measurement result. Obtained velocity profile was reasonable result, and it was proven that data processing approach presented was useful to improve measurement quality in UVP with buffer rod.

Keywords: Bubbly flow, Doppler signal processing, Noise suppression, Buffer rod, Post-processing

1. Introduction

Molten salt nuclear reactor is one of advanced reactor systems considered in the generation IV international forum [1]. Nuclear fuel is dissolved in molten salt and circulated in the core and heat exchanger system. Many conceptual designs were presented elsewhere (for example, [2,3]). Fluoride molten salt is used under high temperature (for example, 750 °C) and atmospheric pressure. One of the attractive features of molten salt reactor is online reprocessing; fission products (FPs) can be separated from fuel liquid. Separation of FPs is very important from the safety aspect since inventory of volatile FPs (such as cesium, xenon, etc.) can be reduced from a reactor core, which is recognized as a missing function in the existing light water reactors especially after the Fukushima Daiichi NPP accident. Helium bubbling can be utilized to separate some FPs. From the inlet of the reactor core, small amount of helium is injected as with fuel dissolved molten salt and it is collected at the outlet. Volatile FPs are captured by bubble and are then separated from salt mixture. Noble metal FPs are also captured, which may cause plating on inner structure and then lead damage of the core due to decay heat and high radiation. Optimization of bubble injection is an important task for the realization of helium bubbling. CFD and experimental works have been performed for this purpose [2,4].

Due to very high temperature, radioactivity and corrosive property, measurement and instrumentation techniques are limited [5], Ultrasonic velocity profiler (UVP) has a high potential for the bubble monitoring. The biggest difficulty lies on the emission of ultrasound into high temperature molten salt. We have proposed the buffer rod technique for the application of UVP to high temperature molten glass (up to 1200 °C) [6-7]. One of the drawbacks of the buffer rod technique is noise issue of trailing echoes, which are due to reflection and refraction inside buffer rod. Since trailing echoes overlay on echoes of

interest, erroneous velocities are measured in UVP. By optimizing the buffer rod, trailing echoes can be mitigated to a certain level [6,8-10]. Yet, trailing echoes are also amplified and remain as with the signals of interest due to high gain setup of UVP. Consequently, some noise suppression technique should be implemented for the measurement with a buffer rod. There would be two solutions to realize such a noise suppression. First solution is to reject trailing echoes with a standing wall filter. Since trailing echoes are located in the same position like static walls in measurement region, those echoes can be ideally eliminated using a DC filter toward repetition order. This procedure must be implemented before the velocity estimation. Second solution is to distinguish significant velocities in post-processing. Such a procedure can be realized by a statistical approach. Noise suppression techniques are needed to be optimized for buffer rod considering characteristics of trailing echoes. In this paper, signal processing is specially arranged to realize the measurement. Then, bubbly flow measurement in high temperature molten salt is demonstrated using buffer rod.

2. Signal processing

2.1 Phase Difference Method

Velocity profile estimation is performed using phase difference method [7,11]. Demodulation is implemented using complex FFT. Let the output sequence for a repetition i be X_i , then average phase difference $\Delta\theta$ can be calculated among certain repetitions N_i .

$$\Delta\theta = \arg \sum_{i=0}^{N-1} (X_i - \hat{X})^* \cdot (X_{i+1} - \hat{X}) \quad (1)$$

Mean value is firstly subtracted and then conjugate products are calculated. This subtraction procedure works as a DC filter (standing wall filter). Averaging is required to increase possibility to capture significant echo signals within one velocity profile estimation and to improve

signal-to-noise ratio. Velocity is then estimated as follows.

$$V = \frac{f_{\text{PRF}}}{4\pi f_0} c \cdot \Delta\theta \quad (2)$$

Doppler amplitude A can be also calculated by the following equation.

$$A = \frac{1}{N_i - 1} \text{abs} \sum_{i=0}^{N_i-1} (X_i - \hat{X})^* \cdot (X_{i+1} - \hat{X}) \quad (3)$$

Doppler amplitude means amplitude of varying signal during the repetition period since DC component is already rejected from the sequence.

While the DC filter is implemented as described above, erroneous signal practically remains. One of the reasons is a jitter issue due to triggering delay and different clock domains between a pulser and a digitizer. Another reason is the stability issue of an amplifier in a receiver. In addition to those issues, temperature variation in buffer rod may cause a variation of transit time from transducer end to measurement end. As a result, trailing echoes are not eliminated completely. A high-pass filter (HPF) toward repetition order will be one approach to solve this issue. Nevertheless, a filter with a sharp frequency response and a high time response is not available. Under a small number of repetition parameter, low velocity component might be also attenuated and distorted when a HPF is applied. For this reason, a HPF was not employed in this study.

2.2 Velocity Offset

For example, velocity of the measurement end of buffer rod should be always zero since it is a static wall. However, zero velocity cannot be found in some measurements due to jitters and other factors discussed above. In order to solve this problem, offset velocity is introduced. Offset velocity is calculated by averaging velocities among different channels which should be zeros. Then, it is subtracted through a velocity profile to collect the bias.

2.3 Amplitude Filter

Even if trailing echoes are varying in time, they are more or less stable when they are observed in long measurement time. Erroneous velocity also inherits this characteristic from trailing echo, and they may dwell in almost the same place in velocity and amplitude domains. While a prior information about velocity is unavailable, information about amplitude is clear; amplitude of bubble should be larger than the noise level. Therefore, bubble velocities can be extracted in post processing. Amplitude data is obtained together with velocity data with Eq. (3). Mean μ and standard deviation σ of amplitude for each channel are calculated among long measurement result sequence. By removing velocities whose amplitude is less than $\mu + z\sigma$, significant velocities can be extracted in velocity profiles. In this procedure, one should select an appropriate confidence interval z . Assuming the Gaussian distribution, $z=1.28$ and 2.33 will lead the data validities of 1% and 0.1%, respectively. In case amplitude are not

following the Gaussian distribution, data validity will be different.

3. Bubbly Flow Measurement

3.1 Buffer Rod

Design of a buffer rod is very important since it coarsely define trailing echoes and signal-to-noise ratio. It was found that conical shape is simple and efficient to suppress trailing echoes [6]. In this study, buffer rod with conical shape is used. Considering the bore diameter of the experimental setup described later, diameter of the buffer rod is decided to 27.5 mm. A transducer with efficient diameter of 20 mm was used to transmit ultrasound into the buffer rod. Therefore, designed diameter of measurement end is 20 mm to avoid inadequate diffraction in buffer rod. Overall length is 300 mm. The rod has a straight section of 50 mm and the rest section (250 mm) is tapered to 20 mm. Stainless steel was used to fabricate the buffer rod since stainless steel showed high durability against the molten salt mixture in our preliminary test. On the conical surface of buffer rod, ceramic adhesive was coated to decrease trailing echo level. Echo response from the buffer rod is shown in Figure 1. Rod end echo can be seen at 110 ms. Small echoes are following the rod end echo, which are trailing echoes. Amplitude ratio is 28dB in this figure.

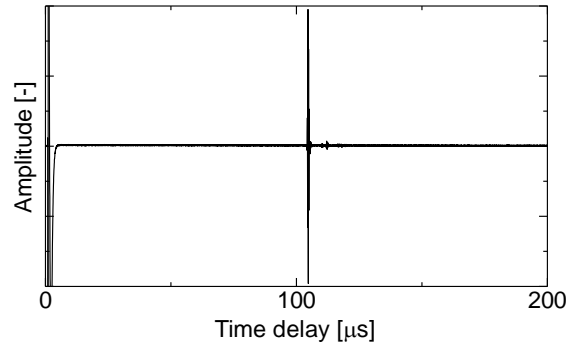


Figure 1: Echo response from the stainless buffer rod used in this study. Trailing echoes can be seen after the rod end echo.

3.2 Experimental Setup and Procedure

Experimental setup is shown in Figure 2. Chloride salt was selected instead of fluoride salt for ease of handling in the laboratory. Salt mixture (56wt% KCl and 44wt% LiCl) was melted in the stainless tube whose inner diameter is 78.1 mm and thickness is 5.5 mm. Approx. 3 kg of salt was stored and the depth of the melt was around 450 mm. Two branch pipes are welded on the tube with the angle of 20 deg. Inner diameter of the branches is 27.2 mm. Buffer rod and thermocouple are installed from each branch pipe. Inside the main pipe, baffle plates are placed to divide the flow section into a raiser section (between baffle plates) and a down comer section. Bent pipe (diameter of 6 mm) is used to inject helium gas from the bottom of the melt. Rising bubbles which cross the ultrasonic beam path are observed with the buffer rod technique. A transducer (center frequency of 4 MHz and efficient diameter of 20 mm) is fixed on

the buffer rod. The transducer is connected to the signal processing setup. The setup consists of a pulser/receiver (JPR-600C; Japan Probe Co., Ltd.) and a digitizer (APX-5040; Avaldata Corp.) installed in the signal processing PC. 20 cycle burst pulse was repeated at the frequency of 4 kHz. Echo signal is amplified by the gain of +25dB. RF signal is sampled at the speed of 40 MS/s. Channel width of signal processing was 250 ns. Sound velocity of this mixture was 1930 m/s in 500 °C. Subsequently, channel distance was 0.24 mm along beam path and $0.083 (= 0.24 * \sin(20))$ mm in radial direction. Velocity and amplitude profile set is measured from the end of the buffer rod to 30 mm in radial direction due to the restriction of signal processing system, which will be solved in the future. 8 repetitions (N_i) are used to estimate one profile set. Longer wave cycle and shorter channel width are used to increase the possibility of capturing weak echo signal from bubble. Molten salt mixture was kept at the temperature of 500 °C for two hours before the experiment. Helium gas was injected at the rate of 12.5 ml/s. Measurement was started after a few minutes later the injection starts so that temperature and bubble are stabilized. 200,000 profile sets were acquired in the experiment. Temperature variation during the experiment was less than 10 °C.

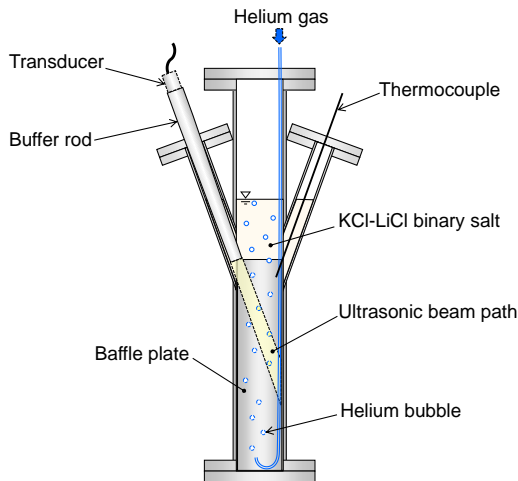


Figure 2: Schematic of helium bubbling experiment apparatus. Chloride salt mixture was melted in the setup. Helium gas was injected through the bent pipe.

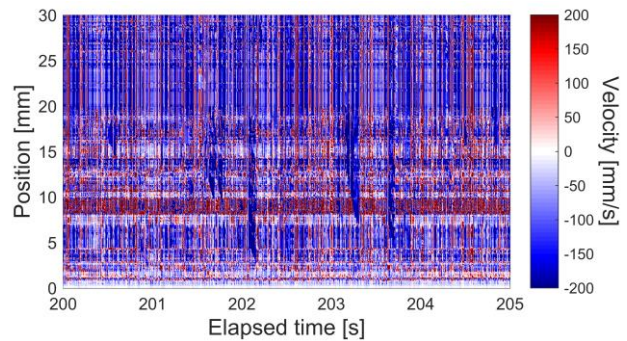
4. Result and Discussions

Spatio-temporal velocity plots for a certain time are shown in Figures 3(a). In raw velocity data plot, sign of the velocities are changing randomly. Around 202 and 203 s in elapsed time, there seems to be significant velocities. Velocity offset and amplitude statistics were calculated from the raw data, and offset rejection and amplitude filter were applied. Processed data is shown in Figures 3(b). Velocities mentioned above are successfully extracted in the plot. Confidence factor was set to three in this paper.

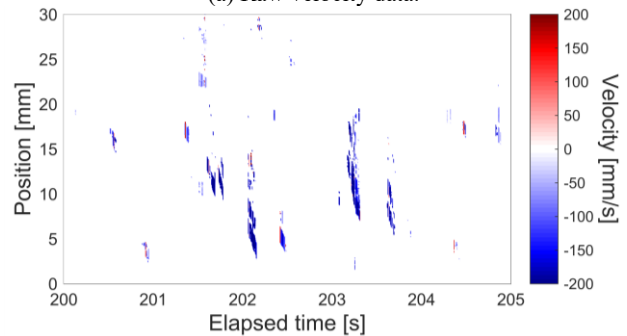
Probability density function (PDF) and mean value of velocities are shown in Figures 4. In raw data, mean velocities do not have a meaningful shape due to withstanding trailing echoes. On the contrary, erroneous

velocities are successfully rejected in the processed data while the intensity of PDF dropped in two order of magnitudes. Boundary layer around the wall can be observed. Velocities are not completely continuous where there are strong trailing echoes, for example, around 20 mm in radial position. Nevertheless, high velocity continued toward the end of the measurement depth (30 mm).

Figure 5 shows mean amplitude profiles. Raw amplitudes are indicated by black circle symbols and processed amplitudes are indicated by red square symbols. Raw amplitude profiles outline the trailing echo level. Even after the post-processing, the shape of trailing echo remains in the amplitude profile. Processed velocities (Figures 4(b)) are distorted as well where trailing echo level is higher than its neighboring points (for example, 5 mm in radial position). It means that erroneous velocities are not eliminated perfectly. This velocities cannot be removed by increasing the confidence factor. Amplitude of bubbly flow is almost flat by 20 mm. Strong trailing echoes disturb measurement and amplitudes increased around 20 mm. After 22 mm, amplitudes are decreasing. Number of extracted data points are plotted as data validity in Figure 6. It can be seen that validities after 20 mm are significantly low. It is because of remaining trailing echoes. As confidence interval was set to three, data validity would be 0.13% assuming the Gaussian distribution. However, experimental results are far larger than this value. It can be predicted that amplitude may follow bimodal distribution once a large enough data set is obtained. Therefore, there will be a possibility to extract significant data by applying an advanced filter and adjusting the parameter automatically.

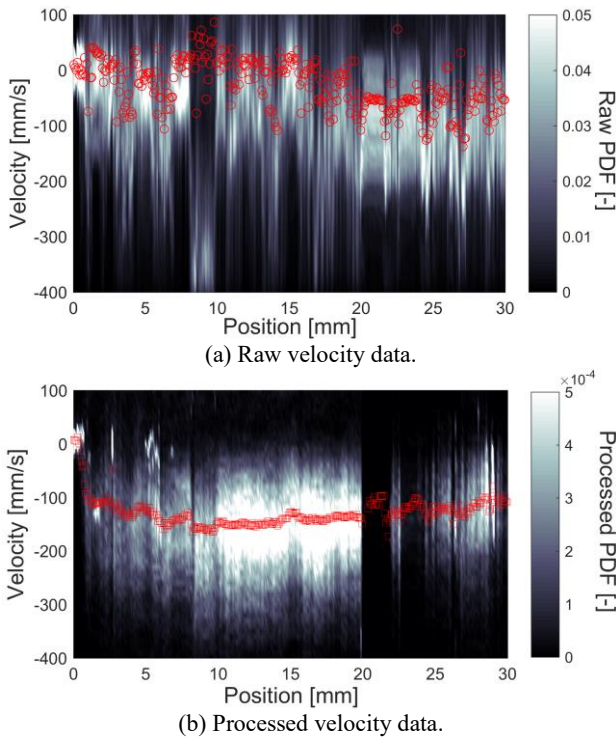


(a) Raw velocity data.



(b) Processed velocity data.

Figures 3: Spatio-temporal velocity plots of bubbly flow in molten salt.



Figures 4: Probability density function and mean velocity (red circle symbols) among 200,000 profiles.

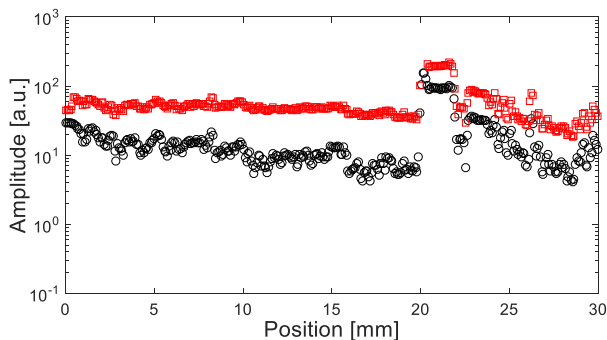


Figure 5: Mean amplitude profiles of raw data (black circle symbols) and processed data (red square symbols).

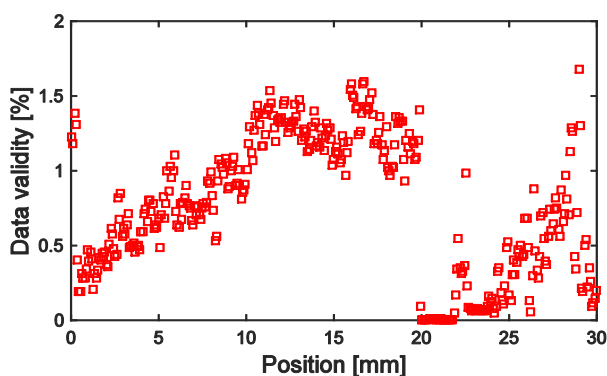


Figure 6: Data validity profile after the post-processing.

6. Summary

Signal processing and post-processing techniques are presented for UVP measurement with buffer rod. Bubbly

flow in molten salt was measured at the temperature of 500 °C. Trailing echoes are inevitable problem with buffer rod measurement. Considering the characteristics of trailing echoes, DC filter was applied to eliminate the standing wall echo signal. Phase difference method was applied to estimate velocity and amplitude profiles. Jitter problem was observed due to triggering error, temperature variation and other factors. Offset velocity was introduced to compensate the jitter problem. In order to extract bubble velocities from noisy measurement result, amplitude filter was used. Velocities with higher amplitude than mean amplitude are extracted. Confidence factor was set to three. Data validity was higher than the value, which can be predicted by the Gaussian distribution assumption. Measured velocity profile was reasonable result considering the experiment condition. It is proven that those procedure was useful to realize UVP measurement with buffer rod even if only classical approaches were used in this study. It was seen that error velocities are not yet rejected completely. Further improvement of post-processing will be required in the future work.

References

- [1] Generation IV International Forum, 2014 annual report.
- [2] Rouch H, *et al.*: Preliminary thermal–hydraulic core design of the molten salt fast reactor (MSFR), *Annal. Nucl. Energy* 64 (2014), 449–456.
- [3] Serp J, *et al.*: The molten salt reactor (MSR) in generation IV: Overview and perspectives, *Prog. Nucl. Energy*, 77 (2014), 308-319.
- [4] Kedl RJ: The migration of a class of fission products (noble metals) in the molten-salt reactor experiment, Technical Report of Oak Ridge National Lab. (1972), ORNL-TM-3884.
- [5] Tallackson JR, *et al.*: Instrumentation and controls development for molten-salt breeder reactors, Technical Report of Oak Ridge National Lab. (1967), ORNL-1856.
- [6] Ihara, T, *et al.*: Development of the ultrasonic buffer rod for the molten glass measurement, *Prog. Nucl. Energy*, 82 (2015), 176-183.
- [7] Ihara T, *et al.*: Application of ultrasonic Doppler velocimetry to molten glass by using broadband phase difference method, *Flow Meas. Inst.*, 48(2016), 90-96.
- [8] Sather A: Ultrasonic buffer-rod technique for the high-temperature measurement of the elastic moduli of short specimens, *J. Acoust. Soc. Am.* 43 (1968), 1291-1294.
- [9] Jen CK, *et al.*: Fabrication and characterization of continuously cast clad metallic buffer rods, *J. Acoust. Soc. Am.*, 91 (1992), 3565-3570.
- [10] Lynnworth LC, *et al.*: Extensional bundle waveguide techniques for measuring flow of hot fluids, *IEEE Ultrason. Ferro. Freq. Cntl.*, 52 (2005), 538-544.
- [11] Ihara T, *et al.*: Ultrasonic velocity profiler for very low velocity field, *Flow Measurement and Instrumentation*, 34 (2013), 127-133.

Study of the rheological properties of the retropulsive jet build by the antral contraction wave in a simplified artificial stomach

Damien Dufour¹, Franz X. Tanner², Kathleen Feigl², Yasushi Takeda¹, Stéphane Fischer³, and Erich J. Windhab¹

¹ Laboratory for Food Process Engineering (FPE), Swiss Federal Institute of Technology Zurich, Zurich 8092, Switzerland

² Department of Mathematical Sciences, Michigan Technological University, Houghton, MI 49931-1295, U.S.A.

³ Ubertone SA, 67000 Strasbourg, France

The digestion of food is a process composed of different phases. A better knowledge of the entire process allows to design tailor made foods. This study is focused on the retropulsive jet generated by the contractions of the stomach and the impact of this flow field to the disintegration of the food. The antral contraction wave is moving at a constant speed toward the pylorus and shrinks at the same time. A prototype of a stomach was built to mimic the displacement of these contractions, in a simpler way. The flow field in the prototype was measured by UVP and compared with numerical simulations. Then, the simulations were used to compute the local stress applied on the fluid. Experiments with Newtonian fluids and two contractions with relative occlusions (RO) of 0.6 and 0.75 shown good agreement with the simulations. The elongation rate was higher with a RO of 0.75. A higher translation speed of the contraction (RO=0.6) allowed to increase the elongation rate.

Keywords: Artificial stomach, Retropulsive jet, UVP, ACW, Non-Newtonian fluid

1. Introduction

The digestion of food in the gastro-intestinal tract is a long process, going through many steps [1]. The mouth and the stomach are the major actors in the disintegration of food. Then, the different sections of the intestine ensure the final break down and the absorption of the nutriments. The disintegration of food in the stomach is a combination of two different actions [2]. First, the chemical action (e.g. saliva, gastric juices and enzymes) helps to soften the ingested food. The second action is mechanical, the stomach produces antral contraction waves (ACW) [1,3], which have different functions. One role is the transportation. From the storage part of the stomach, called the corpus, a small part of the bolus (ingested food) moves toward the antrum. In the antrum, the ACW shrinks and produces a retropulsive jet. This jet helps the chemical reaction by mixing the content of the stomach. Finally, at the end of the antrum, a small part of the chyme is transferred to the intestine, through the pylorus, to start the next digestive step. On top, the retropulsive jet induces high elongation and shear stresses in the fluid. This stress is transferred to the solid particles and break when the threshold value of the particle is reached.

The chemical action in the stomach is well known. Few prototypes of artificial stomachs were created [6-7]. These reproduce the chemical conditions happening in the stomach. Some of them simulate a mechanical action but it is often over simplified [8]. In the last few decades, the field of computational fluid dynamics made a lot of improvements and it is now able to compute complex systems like a human stomach. Several models were developed, in 2D and 3D, which shown the action of the ACW on the flow field [4,5]. These studies proved the

impact of the rheological properties of the fluid on the shape of the jet, i.e. the stress applied to the particles. However, due to the lack of accurate *in vivo* measurement of the retropulsive jet, direct comparisons with simulations are impossible. Only ultrasonography or MNR imaging are allowed on humans [9-11], which do not provide a sufficient resolution of the flow field.

A device imitating the dynamic flow of the stomach, will have two benefits. It will help to build a more elaborate artificial stomach, which is able to reproduce the chemical environment and the flow field of the stomach. In addition, such device can reproduce flows of the stomach and can be used to validate results from simulations. This study aims to better understand the retropulsive jet created by the displacement of the ACW. To this end, a prototype of an artificial stomach was made. The dimensions are close to a real stomach, and large enough to allow the insertion of the UVP sensors. The prototype was tested with Newtonian and non-Newtonian fluids. The velocity along the center line in the antrum part was measured by UVP and compared with simulations.

2. Material and method

2.1 Prototype of stomach

The artificial stomach developed for this study was made of Plexiglas, as shown on Fig. 1b. It was built by the workshop of the FPE laboratory. The main part is a cuboid, which stands for the corpus of the stomach. The cuboid has a squared base of 120*120mm² and 150mm height. This is connected to a cylinder of diameter D and length L, representing the antrum. The cylinder was pierced in a 60mm squared rod. On Fig. 1a are represented two hollow pistons, which are used to reproduce the ACW. The pistons were 3D printed

(Sculpteo, Paris, France). The dimensions are detailed in Table 1. The cross section is a parabolic shape. Two distinct inner diameters, D_i , allow to reproduce different states of contraction of the ACW [7]. The relative occlusion (RO) is calculated according to Eq. (1). One piston is placed in the cylinder and driven with two stainless steel rods, going through the back wall of the tank. These rods are moved by a stepper motor and a screw-nut system. The outer diameter of each piston is 0.2mm smaller than D , to avoid friction with the cylinder. The pylorus (left side on Fig. 1b) is drilled to insert the UVP sensors (Tr1), aligned with the central-axis of the cylinder. In addition, a target (8mm diameter PVC cylinder) was placed in the tank, to measure the sound speed in the fluid.

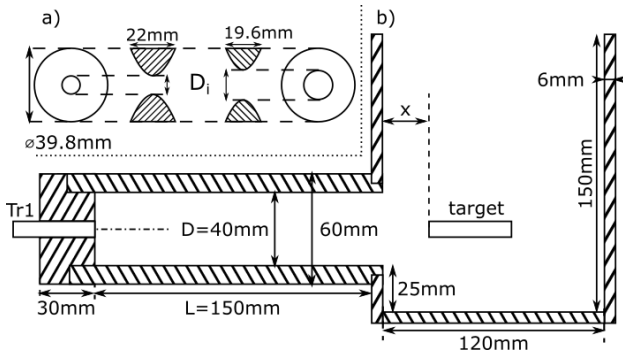


Figure 1: (a) Schematic of the axisymmetric contractions used in the artificial stomach. The inner diameters D_i are specified in Table 1. (b) Schematic of the artificial stomach used for the experiments. The system used to translate the contractions is located on the right-hand side of the prototype (not shown here).

The average human stomach is about 0.94L, ranging from 0.25L to 1.7L [7]. The nominal volume of the prototype is 1.5L, which corresponds to 90mm of fluid in the tank. The ACW are formed roughly 150mm away from the pylorus [7,8]. The length of the artificial antrum is also 150mm, which is long enough to reach the steady flow of the jet. The inner diameters of the contractions were limited by the diameter of the ultrasound beam, to reduce interception with the piston ($D_i \geq 10\text{mm}$). Due to the maximal RO we studied (0.75), the diameter D of the cylinder was constrained to 40mm.

$$RO = 1 - \frac{D_i}{D} \quad (1)$$

Table 1: Dimensions of the hollow pistons used as ACW.

D_i (mm)	Outer dia. (mm)	Width (mm)	RO
10	39.8	22	0.75
16	39.8	19.6	0.6

2.2 Simulations

A numerical 2D model of the cylinder was done, with a mesh size of 213 x 32 x 1 cells. The mesh describes half of the cylinder. The result of the simulation is equivalent to a 3D cylinder due to an axisymmetric computation.

The ACW was modelised as a progressive wave, by deforming the wall. The velocity on the walls is null everywhere except at the surface of the contraction. In this case, the boundary velocity equals to the translation speed of the contraction. The simulations were made by F. Tanner and K. Feigl from the Michigan Technological University.

2.3 UVP measurement

The UVP device is a UB-lab from the Ubertone company (Strasbourg, France). The transducers are from Imasonic (Besancon, France). Two types of transducers were used, which are described in Table 2.

Table 2: Characteristics of the ultrasound sensors used for the experiments. The half opening angle is given at -6dB of beam amplitude and goes up to 5.2° when the amplitude is null.

Central frequency (MHz)	Active element dia. (mm)	Outer dia. (mm)	Half opening angle (°)	Near field (mm)
4	5	8	2.2	17
8	2.5	8	2.2	8.5

2.4 Newtonian fluid

The Newtonian fluid used was a glycerin solution, with a 27% volume concentration. Glycerin was added to tune the buoyancy of the particles used as acoustic reflectors. These particles were from Metflow (Lausanne, Switzerland). The density was 1.07kg/L and the diameter range from 80μm to 200μm. A small amount of these particles were added to the solution (<0.5%). The viscosity of the final solution (27% glycerin + particles) was 3.2mPa.s and the sound speed was 1645m/s.

2.5 Shear thinning fluid

Two non-Newtonian solutions were prepared with guar gum, at 0.5% and 1% mass concentration. No acoustic reflectors were added and the sound speed was around 1485m/s. The shear viscosity of the solution was measured with a MRC-300 rheometer (Anton Paar, Ostfildern, Germany). The viscosity was measured over 5 decades of shear rate, from 10⁻² to 10³s⁻¹, and after a pre-shear at 100s⁻¹ for 10s. A Bird-Carreau model, defined by Eq. (2), was fitted on the viscosity data. The results in Table 3 were used to compute the simulation.

$$\eta(\dot{\gamma}) = \eta_{\infty} + (\eta_0 - \eta_{\infty}) \left(1 + (\lambda \dot{\gamma})^2 \right)^{\frac{n-1}{2}} \quad (2)$$

η_{∞} is the infinite shear viscosity and η_0 is the null shear viscosity. λ is the relaxation time and n is the power-law index. As the solution was water based, the infinite viscosity was set to 1mPa.s.

Table 3: Results of the Bird-Carreau fit from guar solutions.

Guar con. (%)	η_0 (Pa.s)	λ (s)	n	R ²
0.5	0.247	0.188	0.523	0.993
1	6.18	1.10	0.355	0.954

2.6 Experimental

Tr1 was inserted at the pylorus. While the stomach was filled, large air bubbles were flushed from the cylinder. The stomach was placed on the bench and the contraction was connected to the screw-nut system to control the displacement. The target was inserted in the tank and the x distance, on Fig 1b, was measured. The sound speed was calculated, with an error below 1%. The contraction was set to the initial position and halted 10 seconds to stabilize the flow in the stomach. The contraction started moving with the defined speed. The velocity of the fluid was recorded by UVP over time, using one setup from Table 4. The Doppler spectrum was computed from the I and Q Doppler data. The center line velocity was extracted from the Doppler spectrum using a threshold on the intensity of the spectrum [12]. Due to a broad range of velocities in the repulsive jet, the threshold T was kept low (e.g. 2dB) to only select the higher velocities (i.e. center line velocity). The velocity was calculated, for each position (cell), according to the Eqs. (3) and (4).

$$v_{fft} = \frac{c}{2f_0} \frac{\sum f_i S(f_i)}{\sum S(f_i)} \quad (3)$$

$$S(f_i) = \begin{cases} S(f_i), & \text{for } 10\log_{10}\left(\frac{S_{max}}{S(f_i)}\right) \leq T \\ 0, & \text{otherwise} \end{cases} \quad (4)$$

Where c is the speed of sound in the fluid, f_0 is the emission frequency. f_i and $S(f_i)$ are respectively the frequency i of the Doppler spectrum and the spectral density associated to this frequency. S_{max} is the maximum of the spectral density, for a given cell. An offset of $1e-20$ is added to $S(f_i)$ to avoid divisions by zero.

Table 4: Two configurations of the UVP device used for the experiments. The amplification was fixed at 60dB over all cells. The 4.17MHz setup was used with the 4MHz transducer and the 7.5MHz setup, with the 8MHz transducer. The distances are given for a sound speed of 1480m/s.

f_0 MHz	PRF kHz	Sam- ples	Pulse mm	1 st cell mm	Δ cell mm	N cells
4.17	0.73	128	0.79	80.2	0.355	100
7.5	1.1	128	0.79	40.2	0.355	90

The 2D velocity vector measurement is not shown here because of challenges induced by the contraction. An echo on the piston creates a strong shift on the Doppler spectrum which completely biased the 2D reconstruction. Similar effect appends on the 10mm case, on Fig. 2. A filtering of the Doppler data is needed to erase this echo.

3. Results and Discussion

3.1 Glycerin solution

The first experiments were done with the 4MHz transducer. The 10mm contraction was running at 2.5mm/s, the 16mm contraction was tested at 2.5mm/s and 7.5mm/s. The Reynolds numbers were, respectively,

167, 107 and 268. Fig. 2 shows the measured data and the simulations. The UVP data are a collection of the measured data over time. The observable window is about 40mm long, thus it cannot cover the entire jet instantaneously. To overcome this, the observable window was positioned far from the pylorus. While the contraction was moving toward the pylorus, the tail of the jet was recorded. The disadvantage of this method is that the beam covers a wide area. With the 10mm contraction (black squares), the ultrasound beam intercepts the hollow piston and the measurement is disturbed (around 46mm on Fig. 2). With the 16mm contraction, the intersection with the beam is smaller, so the profile of the jet is less disturbed. In every case, the tail of the jet (from 60 to 120mm) is also disturbed. This is due to the different velocities which compose the jet and creates a non-symmetric velocity distribution in the Doppler spectrum. The post processing of the Doppler spectrum removed most of the echo from the 16mm contraction, however, the disturbance was too high on the 10mm contraction. Regarding the tail of the jet, computing the velocity with Eqs. (3) and (4), plus a low threshold, allowed to reduce the effect of the non-symmetric velocity distribution in the tail, but increased the noise on the final result.

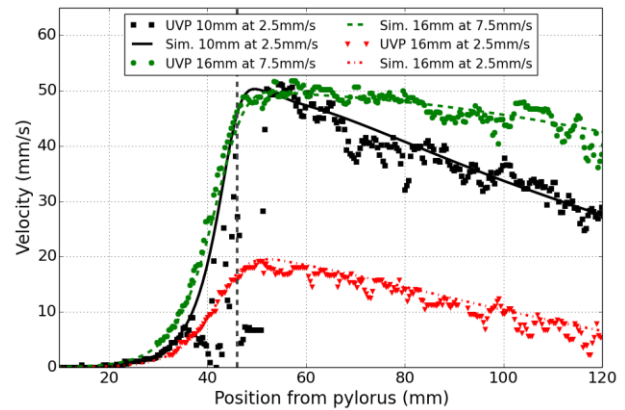


Figure 2: Measurement and simulation of the 27% glycerin solution with different RO and displacement speed of the contraction. The center of the contraction is located at 46mm, shown by the vertical gray dashed line. Positive velocity means that the fluid is going away from the pylorus.

The elongation rate, on the center line, was computed from the simulations and displayed on Fig. 3. The 10mm contraction shown the highest elongation rate, which is expected as the fluid stretches more to go through the smallest opening. In addition, the 16mm contraction shows that the elongation rate can be tuned by adjusting the speed of the contraction. The aim of increasing the speed of the contraction is to be able to reproduce the shrinkage of the ACW. As this prototype works with fixed opening contractions, adjusting the speed allows to change the stress applied on the fluid during the experiment. To compute the stress applied on the particles, the shear rate needs to be measured from the simulation. The total stress in the fluid can be calculated by combination of the shear stress and elongation stress.

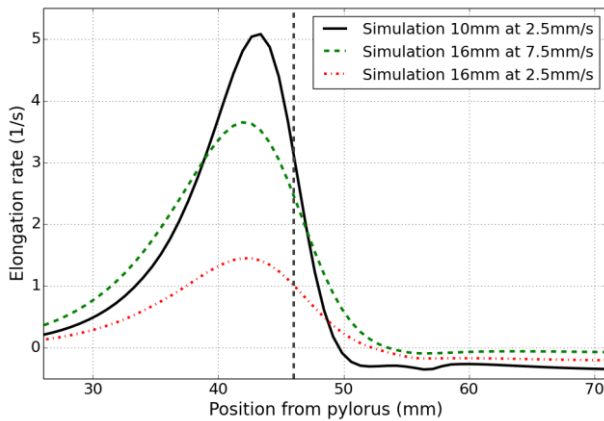


Figure 3: Elongation rate in the retroulsive jet, computed with the data from the simulations. The center of the contraction is symbolized by the vertical gray dashed line, at 46mm.

3.2 Guar solutions

The 0.5% and 1% guar solutions were tested with the 16mm contraction at 2.5mm/s and 7.5mm/s. The results are shown on Fig. 4. The length of the jet was much shorter compared to the Newtonian case. This was expected because of the higher viscosity, thus the damping increased. In addition, the higher viscosity increased the pressure between the contraction and the pylorus [7]. As a consequence, the fluid reached a higher velocity. In these cases, the maximum speed was about 30% higher compared to the jet from the 27% glycerin. The interesting fact is that increasing the guar concentration (e.g. zero-shear viscosity) had an unexpected effect on the top speed of the jet. As said before, a higher viscosity increases the speed of the jet. But, the maximum velocity of the 1% guar solution is slightly under the 0.5% solution. Further work and simulations must be done to better understand this phenomenon with the Non-Newtonian fluids.

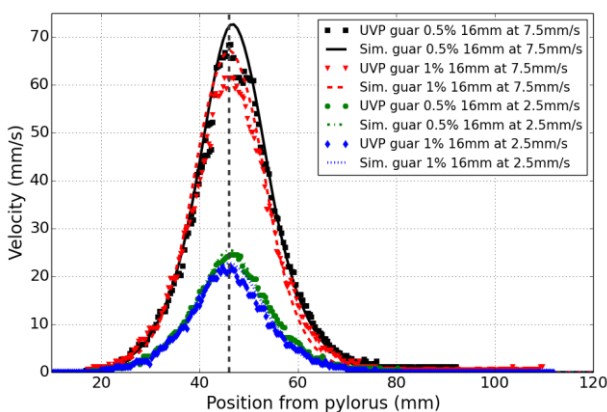


Figure 4: Retroulsive jet produced with a guar solution, measurements and simulations. Different concentrations and several displacement speeds with the 16mm contraction are shown. The middle of the contraction is situated at 46mm, represented by the vertical gray dashed line.

The trial with the 0.5% guar at 2.5mm/s was recorded at 7.5MHz, close to the pylorus. The other trials were recorded at 4MHz. The Doppler spectrogram at 7.5MHz

shown a velocity distribution which was less dispersed, than the 4MHz measurement. The narrow beam of the 8MHz transducer measures the velocities in the fluid closer from the center line. Thus the range of velocities seen by the beam is reduced compared to the 4MHz transducer. But the optimal result is obtained when the measurement window is close from the pylorus, thus the observable length is limited, about 80mm from the pylorus. As a consequence, the 8MHz measurement is better with viscous fluid, when the jet is short.

5. Conclusion

A prototype of a stomach was built, with dimensions close to the human stomach. The measurements done with the Newtonian fluid present a good match with the simulations. This validate the numerical model used for the simulation. With a RO of 0.75 and a Newtonian fluid (3.2mPa.), the jet reached a maximum velocity of 50mm/s and an elongation rate of $5s^{-1}$. With the 16mm contraction, the elongation rate was tuned by the adjusting the speed of the contraction. The advantage of such property is to simulate the shrink motion of the ACW with an accelerated solid contraction. The shear forces will be analyzed and added to the elongation stress. The stress induced by the fluid will be calculated and tested experimentally by droplet breakup experiment.

References

- [1] Kong. F *et al.*: Disintegration of Solid Foods in Human Stomach, *Journal of Food Science* Vol. 73(5), R67-80 (2008).
- [2] Camilleri M: Integrated Upper Gastrointestinal Response to Food Intake, *Gastroenterology* Vol. 131 (2), 640-658 (2006).
- [3] Keinke O *et al.*: Mechanical Factors Regulating Gastric Emptying of Viscous Nutrient Meals in Dogs, *Quarterly Journal of Experimental Physiology* Vol. 69, 781-795 (1984).
- [4] Kong F *et al.*: A Model Stomach System to Investigate Disintegration Kinetics of Solid Foods during Gastric Digestion, *Journal of Food Science*, Vol. 73 (5), E202-210 (2008).
- [5] Kong F *et al.*: A Human Gastric Simulator (HGS) to Study Food Digestion in Human Stomach, *Journal of Food Science*, Vol. 75 (9), E627-635 (2010).
- [6] Yoo JY *et al.*: GIT Physicochemical Modeling – A Critical Review, *International Journal of Food Engineering* Vol. 2(4), art. 4 (2006).
- [7] Ferrua MJ *et al.*: Modeling the Fluid Dynamics in a Human Stomach to Gain Insight of Food Digestion, *Journal of Food Science* Vol.75 (7), R151-162 (2010).
- [8] Pal A *et al.*: Gastric flow and mixing studied using computer simulation, *Proc. R. Soc. Lond. B* 271, 2587-2594 (2004).
- [9] Schulze K: Imaging and modelling of digestion in the stomach and the duodenum, *Neurogastroenterology & Motility* 18, 172-183 (2006).
- [10] Steingoetter A *et al.*: Imaging gastric structuring of lipid emulsions and its effect on gastrointestinal function: a randomized trial in healthy subjects, *American Journal of Clinical Nutrition* (2015).
- [11] Berstad A *et al.*: Ultrasonography of the Human Stomach, *Scandinavian Journal of Gastroenterology*, 31:sup220, 75-82 (1996).
- [12] Sirmans D *et al.*: Numerical Comparison of Five Mean Frequency Estimators, *Journal of Applied Metrology*, Vol. 14, 991-1003 (1975).

Velocity profile measurements in bore waves

Davide Wüthrich¹, Michael Pfister^{1,2}, Giovanni De Cesare¹, and Anton J. Schleiss¹

¹ Laboratoire de Constructions Hydrauliques (LCH), Ecole Polytechnique Fédérale de Lausanne (EPFL), Lausanne, Switzerland

² Civil Engineering Department, Haute Ecole d'Ingénierie et d'Architecture de Fribourg (HEIA-FR, HES-SO), Fribourg, Switzerland

Hydrodynamic waves are an unsteady flow motion generated by rapid water level rise. In nature, such events can be found in dam-break waves, impulse waves and tsunamis. These phenomena are rare, but highly destructive. The present study is based on an experimental approach and it investigates the hydrodynamic behavior of bores propagating on wet bed in terms of height and velocity profiles. The waves are investigated using Ultrasonic distance Sensors (US) to measure the wave height and average front velocity; the instantaneous velocity profiles were obtained through an Ultrasonic Velocity Profiler (UVP), installed in the bottom of the channel, with an emitting frequency of 2 MHz and inclined with an angle of 20° in the upstream direction. The acoustic scattering was increased using a hydrogen bubble technique with an anode and a cathode installed in the upstream part of the channel. The probe was sampled with a frequency varying from 13.5 to 55 Hz depending on the maximum wave height. A sensitivity analysis of the main influential factors was carried out, pointing out the need for a compromise between quality and quantity for these highly unsteady flows. Results showed some interesting logarithmic profiles typically associated with open channel flows for all wave configurations.

Keywords: Wet bed bores, Tsunami, velocity profiles, Ultrasonic Velocity Profilers (UVP)

1. Introduction

Hydrodynamic waves such as dam-break waves, impulse waves and tsunamis, represent a highly unsteady flow motion resulting into a rapid water level rise. These phenomena are rare, but highly destructive, implying important losses and reconstruction costs. Physically both surges propagating on dry bed and bores propagating on wet bed have a complex behavior and an experimental approach is necessary. After the December 2004 Indian Ocean tsunami, field observations showed velocities between 3 to 4 m/s in Kumala Beach and 6 to 8 m/s in Khao Lak [1]. In Japan in 2011 the tsunami velocity was 10 to 13 m/s near Sendai airport [2]. Nevertheless, recent studies have shown that uncertainties still exist on the evaluation of bore velocities and multiple empirical formula can be found in the existing design codes [3]. This study gives an insight on the hydrodynamic behavior of bores propagating on wet bed, representing successive waves after the first tsunami. It is known that the first wave might not be the highest. The project is based on an experimental approach and the paper focuses on the use of Ultrasonic Doppler methods to measure velocity profiles of highly unsteady flows such as propagating bores. Previous relevant studies were carried out by [4] for similar conditions, proving the effectiveness of such technique for unsteady flows. A sensitivity analysis of the main parameters was carried out, showing the importance of a compromise between high resolution and precision of the results.

2. Experimental Set-up

All experiments were carried out at the Laboratory of Hydraulic Constructions (LCH) of EPFL, Switzerland. Bore formation was achieved through a vertical release of a known water volume from an upper reservoir into a

lower reservoir through three identical PVC pipes with external diameter of 311 mm. The opening is obtained through a system of punch and pulley, allowing to activate the system respecting the criteria proposed by [5] for dam-break waves. Similar techniques were previously used by [4], [6] and [7]. The use of 1, 2 or 3 pipes allowed to produce waves with different hydrodynamic properties in terms of velocity and depth. The propagation of the wave took place in a 14 m long and 1.4 m wide smooth horizontal channel, whose roughness corresponded to a Darcy Weisbach friction factor $f = 0.01$ based on measurements. The bore profiles were investigated using 7 Ultrasonic distance Sensors (US), Baumer UNAM 30I6103, sampled with a frequency of 12.5 Hz. The US sensors were located in the centerline of the channel at $x = 2, 10.10, 12.10, 13.10, 13.35, 13.60$ and 13.85 m from the flume inlet. The facility and the disposition of the US probes are shown in Figure 1.

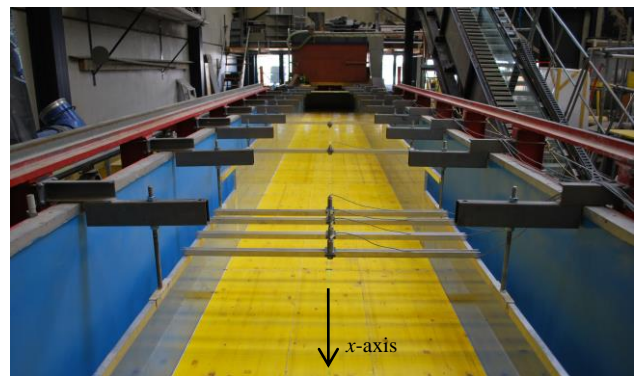


Figure 1: Experimental channel and instrumentation

Flow velocity was investigated using an Ultrasonic Velocity Profile (UVP) produced by the Met-Flow (Switzerland). This instrument provided instantaneous

velocity profiles along the axis by detecting the Doppler shift frequency of echoed ultrasound as a function of time. No calibration was needed for these measurements. Only one transducer was used in the cross-section and it was located at a distance of 13.85 m from the channel inlet, where the bore had reached a fully developed condition. Measurements were taken in the transducer axis then projected in the main flow direction (x -axis). Only the component in the x -direction was considered. For the present study, an emitting frequency of 2 MHz was chosen. The transducer had a diameter of 8 mm and it was located 5 mm below the channel bottom with an angle of 20° in the upstream direction. The empty space between the probe and the channel was filled with gel and sealed with plastic tape to assure the transmission of the emitting signal (Figure 2).

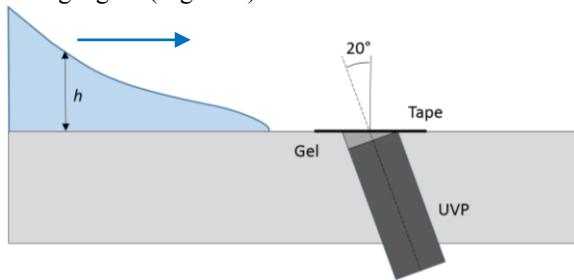


Figure 2: Sketch of the UVP installed in the channel bottom

The acoustic scattering was increased using a hydrogen bubble technique with an anode and a cathode installed in the upstream part of the channel, at $x = 1.5$ m from the channel inlet (Figure 3). The vertical bars had a diameter of 8 mm and a thin stainless steel wire ($\varnothing = 0.0001$ m) was wrapped around with a spacing of 5 mm. The bars were covered with waterproof paint to avoid their participation in the reaction. A potential difference of 40 V was applied between the two bars, producing hydrogen bubbles with diameter proportional to \varnothing . The ability of this method was previously proved by [8] and [9].

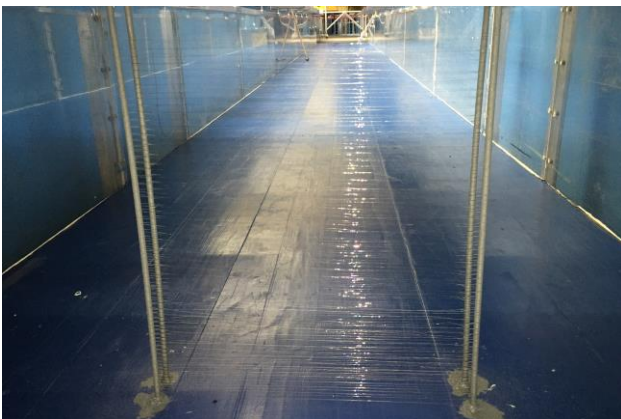


Figure 3 : Hydrogen bubble releasing technique.

The UVP probe was sampled with a frequency varying from 13.5 to 55 Hz depending on the maximum wave height. UVP data was post-processed using a commercial code developed by Met-flow. The use of a trigger function (5V) to start the UVP measurement through a tailor made LabView acquisition system allowed a synchronization of both UVP and US data.

3. Hydraulics of bore waves

In the experimental facility both surges on dry bed and bores on wet bed were produced. However this study only focuses on bores propagating on a wet bed with an initial still water depth of $h_0 = 0.05$ m. Bores on a wet bed present a highly turbulent and recirculating roller, similar to a translating hydraulic jump, followed by a relatively constant depth. A picture of the produced wet bed bore and its turbulent front is presented in Figure 4.



Figure 4 : Picture of the wet bed bore ($h_0 = 0.05$ m)

Good agreement was found between the experimental tests and the theoretical solutions of [10] and [11], as shown by [12]. The height profiles obtained at US7 ($x = 13.85$ m from inlet) for three wet bed bores with identical releasing conditions are presented in Figure 5, where a good repeatability can be observed. The front velocity was measured using the 7 US sensors placed along the channel and the arrival of the bore was identified when a threshold of $h = 0.01$ m was overpassed; an average value of $V_{\text{front}} = 2.5$ m/s was found for all three bores.

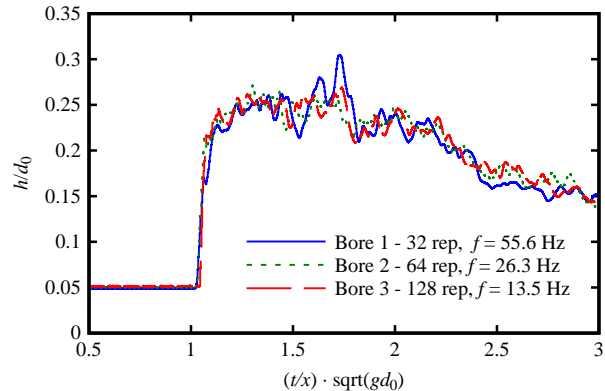


Figure 5 : Profiles of the bores used in the present study: each test was performed with a different UVP acquisition frequency (Table 1)

4. Sensitivity Analysis

Bores are a highly unsteady phenomenon, meaning that its properties rapidly change in space and time, requiring a high frequency for all measurements. For most instruments the quality and the reliability of the measured data is proportional to the number of repetitions used, implying a longer duration and therefore a lower acquisition frequency. A compromise between high frequency and quality of the results was therefore necessary and a sensitivity analysis was carried out on three wet bed surges ($h_0 = 0.05$ m) to investigate the influence of the main parameters. The main parameters of the study are presented in Table 1.

Table 1. Acquisition parameters used in the sensitivity analysis

	Number of repetitions	Acquisition duration [ms]	Acquisition frequency [Hz]
Bore 1	32	18	55.6
Bore 2	64	38	26.3
Bore 3	128	74	13.5

A depth-averaged velocity (V) was calculated for every profile obtained using Eq.1.

$$V = \frac{1}{N} \sum_{i=0}^{i=N} v_i \quad (1)$$

in which i varies from 0, the channel bottom, to N (h_{\max}). The results obtained for all three bores are presented in Fig 6 as a function of time, where a similar behaviour is observed for all bores. One can notice that a higher frequency (Fig. 6 top, 32 repetitions) corresponded to a

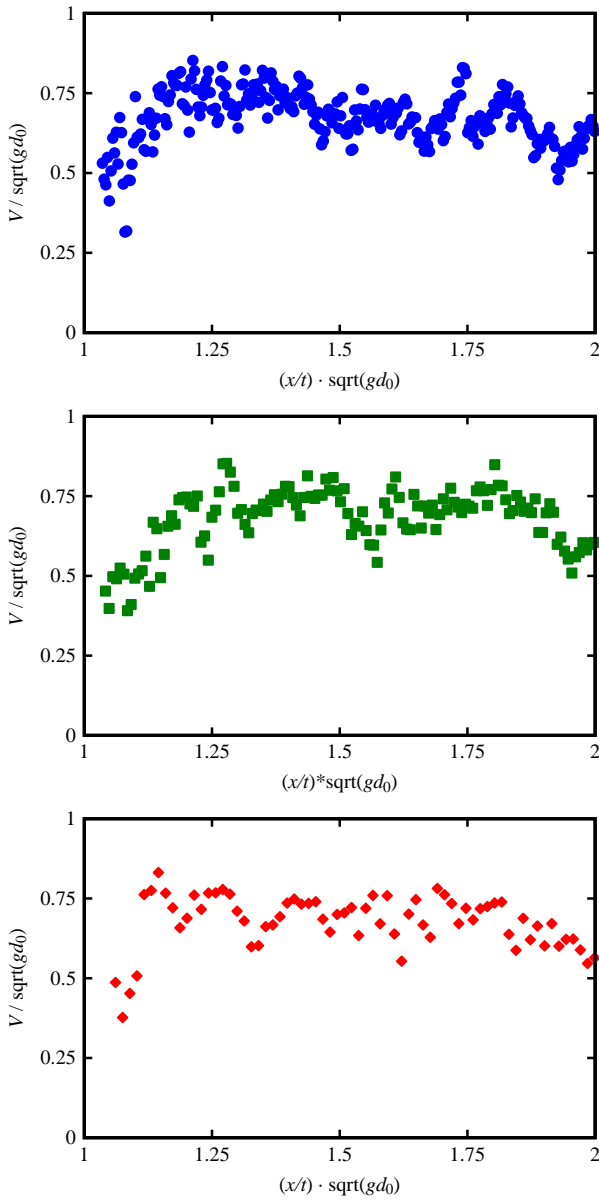


Figure 6 : Time evolution of the depth-averaged velocity : (top) Bore 1, 32 repetitions, (centre) Bore 2, 64 repetitions, (bottom) Bore 3, 128 repetitions

greater amount of points, but lower precision and higher scattering were found. With lower frequencies, the number of measurements was reduced, the overall profile behaviour remaining unchanged. It is important to point out that being the first part of the wave highly aerated and turbulent (Figure 4), the transmission of the echo was obstructed by the presence of air bubbles. This resulted into velocity profile measurements characterised by high scattering and low physical meaning. Results also showed some interesting logarithmic profiles typically associated with open channel flows for all scenarios. As an examples the profiles obtained at $t = 6.5$ s, behind the aerated bore front, are presented in Figure 7. Similarly to the previous case, for higher acquisition times a smoother profile was observed, whereas for higher frequencies more scattering was found. For these reasons in the present study a higher resolution was chosen (128 repetitions) with a corresponding frequency of 13.5 Hz.

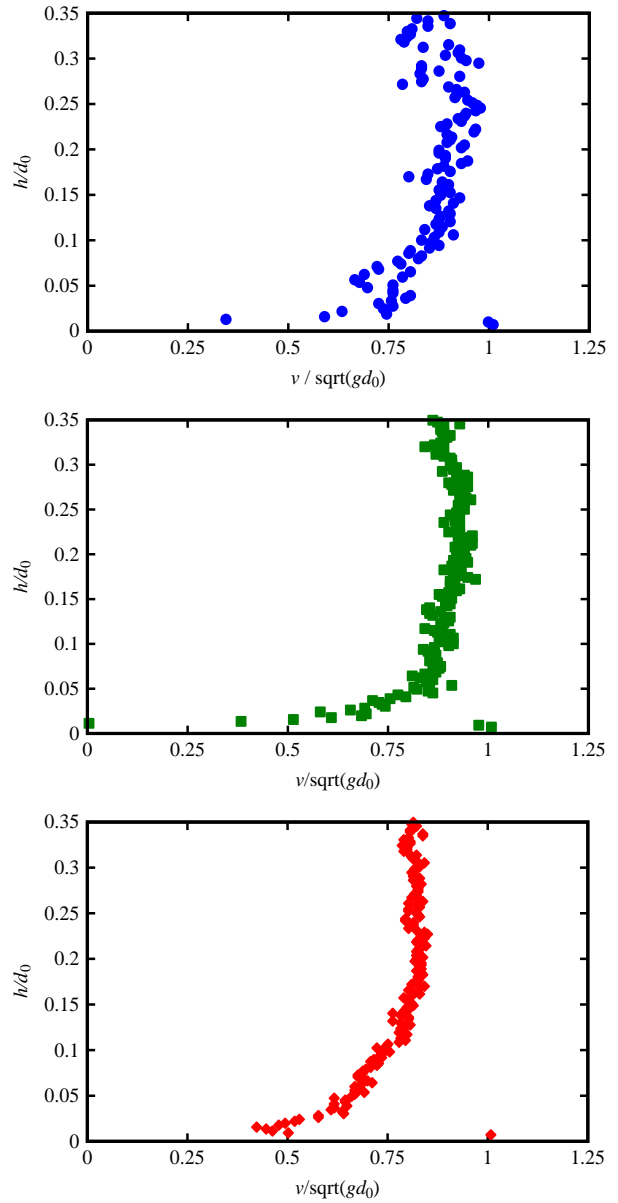


Figure 7 : Examples of profiles obtained for $t = 6.5$ s, after the turbulent bore front: (top) Bore 1, 32 repetitions, (centre) Bore 2, 64 repetitions, (bottom) Bore 3, 128 repetitions

5. Results

Regardless of the frequency used, a relatively constant and oscillating value of the depth-averaged velocity was observed in the first seconds of the bore, followed by a deceleration far behind the water front. The values obtained were also successfully compared with the wave average velocity derived from the US probes ($V_{\text{front}} \approx 2.5$ m/s), obtaining similar results and therefore proving the consistency of the measurements. All 104 instantaneous velocity profiles between $1 < x/t\sqrt{gd_0} < 2.5$ were normalized using the depth-averaged velocity (V_i) and the maximum height ($h_{i,\text{max}}$). Results are presented in Figure 8, showing a profile typical of open channel flows. The experimental points were also successfully compared with the Prandtl's power law with an exponent $n = 11.5$, obtained with a friction factor $f = 0.01$ [13]. The scattering in the upper part of the flow is attributed to secondary turbulence in the flow surface.

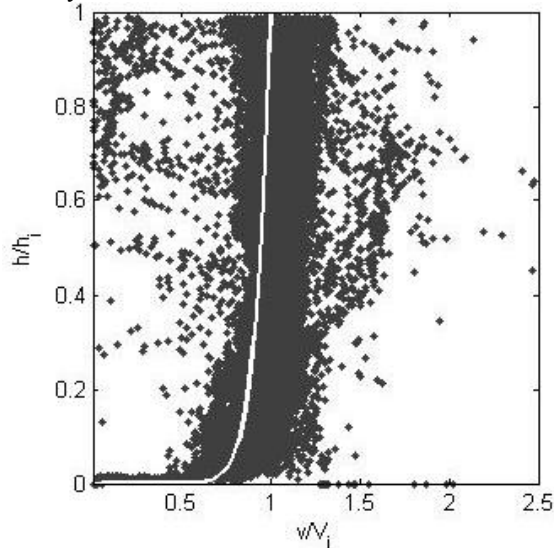


Figure 8 : Dimensionless velocity profiles for a wet bed bore propagating over a $h_0 = 5$ cm still water initial depth

6. Conclusion

Bore waves can be found in nature in dam break waves, impulse waves and tsunamis propagating on a wet bed. This paper is based on an experimental approach and it focuses on the techniques used to measure instantaneous velocity profiles using Ultrasonic Velocity Profilers (UVP). Bore formation is achieved through a vertical release technique and its propagation took place in a 14 m long and 1.4 m wide horizontal channel. A UVP transducer with an emitting frequency of 2 MHz was installed in the channel bottom at an angle of 20° in the upstream direction at a distance of 13.35 m from the channel inlet. Being the flow highly unsteady, the acquisition frequency needed to be sufficiently high to fully capture the properties of the flow and the acquisition time sufficiently long to provide quality results. Thus a compromise needed to be found. To evaluate the influence of these parameters a sensitivity analysis was carried out on three identical bores with different acquisition frequencies. Results showed that for increasing frequencies a higher scattering was observed,

nevertheless the overall behaviour remained unchanged. The quality of the instantaneous profiles was higher for longer acquisition times. Furthermore, the velocity profiles showed an excellent agreement with Prandtl's power law, typical of open channel flows.

Acknowledgment

The support of the Swiss National Science Foundation (SNSF), grant 200021_149112/1 is acknowledged.

Notation

f	Darcy-Weisbach friction factor
g	gravity constant
h	Bore height [m]
h_0	Initial still water depth [m]
n	exponent in the Prandtl's power law
N	number of measures in the vertical direction
\emptyset	wire diameter [m]
t	time [s]
v	instantaneous profile velocity [m/s]
V	Depth-averaged Velocity [m/s]
V_{front}	bore front velocity, measured with US [m/s]
x	longitudinal direction along the channel [m]

References

- [1] Rossetto T, *et al.*: The Indian Ocean tsunami of December 26, 2004: observations in Sri Lanka and Thailand, Nat. Hazards, 42-1 (2007), 105-124.
- [2] Jaffe BE, *et al.*: Flow speed estimated by inverse modelling of sandy tsunami deposits: results from the 11 March 2011 tsunami on the coastal plain near the Sendai Airport, Honshu, Japan, Sedimentary Geology, 282 (2012), 90-109.
- [3] Nistor I, *et al.*: Tsunami-induced forces on structures. Handbook of Coastal and Ocean Engineering, Singapore: World Scientific (2009), 261-286.
- [4] Meile T: Influence of macro-roughness of walls on steady and unsteady flow in a channel, PhD Thesis No. 3952 and Communication 36 of Laboratory of Hydraulic Constructions, LCH/EPFL (2007), Lausanne, (Ed. A. Schleiss).
- [5] Lauber G & Hager W: Experiments to dam-break wave: Horizontal channel, J. Hydraul. Res., 36-3 (1998), 291-307.
- [6] Chanson H, *et al.*: Unsteady air bubble entrainment and detrainment at a plunging breaker: dominant time scales and similarity of water level variations. Coast. Eng., 46-2 (2002), 139-157.
- [7] Rossetto T, *et al.*: Physical modelling of tsunami using a new pneumatic wave generator, Coast. Eng., 58-6 (2011), 517-527.
- [8] Blanckaert K & Lemmin U: Means of noise reduction in acoustic turbulence measurements, J. Hydraulic Res. 44-1 (2006), 3-17.
- [9] Meile T, *et al.*: Improvement of Acoustic Doppler Velocimetry in steady and unsteady turbulent open-channel flows by means of seeding with hydrogen bubbles, Flow Meas. Instrum., 19-3 (2008), 215-221.
- [10] Ritter A: Die Fortpflanzung der Wasserwellen, Zeitschrift Verein Deutscher Ingenieure, 36-33 (1892), 947-954.
- [11] Stoker JJ: Water Waves: The Mathematical Theory with Applications, Intersciences, (1957), 567 pages
- [12] Wüthrich D, *et al.*: Experimental generation of tsunami-like waves, Proc. of Coastal Structures. Boston, MA, USA. 9-11 September 2015 (under publication).
- [13] Chanson H: The hydraulics of Open Channel Flow: an Introduction, Elsevier (2004)

Velocity profiles of turbidity currents flowing over a flat bed

Sabine Chamoun¹, Giovanni De Cesare¹, and Anton J. Schleiss¹

¹Laboratory of Hydraulic Constructions (LCH), Ecole Polytechnique Fédérale de Lausanne (EPFL),
CH-1015 Lausanne, Switzerland

Turbidity currents are the main source of suspended sediment transport in reservoirs and thus one of the main causes of sedimentation. One of the techniques used to avoid reservoir sedimentation is through venting of turbidity currents. In the framework of a research work on venting, velocity measurements of turbidity currents flowing on a flat bed are carried out using Ultrasonic Velocity Profilers (UVP). Five profilers of 4 MHz placed at different positions in an experimental flume provide velocity profiles. Body and head velocities are analyzed and used to calculate the characterizing height and velocity of the currents. The flow regime is described based on Richardson number. Results show decreasing velocity values and thus the deceleration of the currents. Front velocities are also investigated.

Keywords: Ultrasonic Velocity Profilers, turbidity currents, deceleration, body and head velocities, front velocity.

1. Introduction

Turbidity currents are sediment-laden currents driven by density differences due to the presence of suspended sediments in the water. When reaching reservoirs during yearly floods, these currents plunge below the water surface and flow along the bed of the reservoir as a kind of underwater avalanche until reaching the dam. Unless these currents are evacuated, the sediments they transport to the dam will settle leading to reservoir sedimentation. To avoid sedimentation, one of the main means is to vent turbidity currents through bottom outlets or intakes. However, in order to study the operation of venting, a thorough understanding of turbidity currents and their dynamics is essential.

Velocities are an important characteristic of turbidity currents. It provides crucial information on the flow regime, height, and development of turbidity currents. Different techniques exist for the measurement of velocities in flows. Among these techniques, the Ultrasonic Velocity Profiler (UVP), developed by [1], is used to measure instantaneous velocity profiles. Many researchers applied UVP measurements with different types of flows. In experimental investigations of turbidity currents, [2] performed a flow mapping technique with UVP measurements of turbidity currents simulated experimentally. [3] and [4] also applied the UVP technique for the investigation of turbidity currents' velocities. UVP measurements were achieved in other laboratory studies related to suspended sediments and reservoir sedimentation (e.g., [5], [6], [7], [8]).

The present research is conducted at the Laboratory of Hydraulic Constructions (LCH) of the Ecole Polytechnique Fédérale de Lausanne (EPFL). An experimental model is used to investigate the operation of venting of turbidity currents. The efficiency of the evacuation of the turbidity currents is analyzed for currents flowing over a flat bed. Different measurements are carried out, among which velocity profiles using UVP transducers [9]. The present paper firstly describes the

experimental set-up, as well as the sediments used for the simulation of the turbidity currents. Then, the results obtained using five UVP probes of 4 MHz each are discussed. The body and head velocity of the turbidity currents are analyzed. The flow regime and characteristics of the simulated turbidity currents are described. Finally, front velocities are presented followed by conclusions.

2. Experimental set-up

2.1 Description

Experimental tests are carried out in an 8.55 m long, 0.27 m wide, and 1 m deep flume. The latter can be tilted with a slope ranging from 0 to 5%. In the case of this paper, the bed is horizontal (0%).

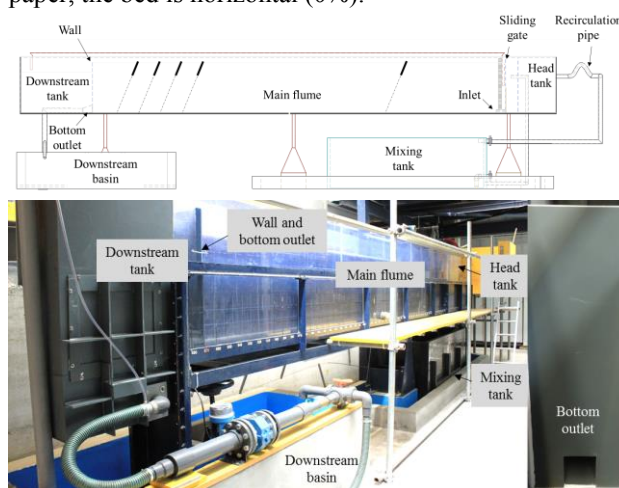


Figure 1: Longitudinal scheme along with a photo showing the different elements of the experimental installation.

As shown in Fig. 1, the flume consists of an upstream head tank ($0.8 \times 0.27 \times 1 \text{ m}^3$), a main flume ($6.7 \times 0.27 \times 1 \text{ m}^3$) and a downstream tank ($1.05 \times 0.27 \times 1 \text{ m}^3$). A sliding gate separates the head tank from the main flume. Downstream of the head tank, an inlet leads to the main flume and has an opening of 4.5 cm. A

tranquilizer is placed at the inlet. It allows the regulation of the scale of turbulence of the released turbidity current and gives an initial uniform distribution for the velocity field of the current.

Below the flume, the water-sediment mixture is prepared in a mixing tank. A fixed amount of sediments is mixed with water and is continuously stirred before and during the tests. The main flume simulates the reservoir where the turbidity current flows before being vented. At the end of the flume (6.7 m from the inlet), a wall simulates the dam with a bottom outlet centered on its width. The wall keeps the water level constant in the main flume during the tests. Finally, a downstream tank receives the residual water.

2.3 Sediments

The material used to simulate the turbidity currents in this study is a Thermoplastic Polyurethane (TPU) with a mass density of 1160 kg/m^3 . Its representative diameters are $d_{10} = 66.5 \text{ }\mu\text{m}$, $d_{50} = 140 \text{ }\mu\text{m}$ and $d_{90} = 214 \text{ }\mu\text{m}$; d_x being the grain size diameter for which $x\%$ of the amount of sediments has smaller diameters. The settling velocity of the particles is 1.5 mm/s , calculated based on Stokes' law using the mean diameter d_{50} .

2.4 Measuring instruments

Throughout the tests, different measurements are carried out. The discharge of the inflowing and outflowing turbidity currents are monitored by electromagnetic flowmeters. The water level upstream and in the main flume are monitored using two ultrasonic level probes. The deposition of the turbidity currents is measured by a depositometer based on electric resistance (ERBD) [10]. Sediment concentration of the inflowing turbidity current as well as the vented flow are monitored using two turbidity probes. Finally, five 4 MHz UVP transducers positioned at 4.1, 5.5, 5.8, 6.0, and 6.2 m from the inlet measure instantaneous velocity profiles with a sampling period of 38 ms and an inclination angle of 25° downstream with respect to the vertical. One transducer measures 27 instantaneous profiles per second before moving to the next one.

Fig. 2a shows the position of the different UVP transducers and Fig. 2b shows the support on which the transducers are mounted. They measure over 70 cm depth (144 channels, 0.74 mm channel width and 4.63 mm spacing).

2.5 Experimental test procedure

At the beginning of each test, the main channel is filled with clear water up to a level of 80 cm. The water-sediment mixture is prepared in the mixing tank with a mean concentration of 27 g/l for all the tests.

The mixture is pumped from the mixing tank to the head tank, and is recirculated between the two elements through a recirculation pipe. This process ensures good mixing and homogeneous concentrations between the two reservoirs.

The water levels in the head tank and the main channel are maintained equal in order to prevent a burst-like initial inflow when opening the sliding gate and releasing the turbidity current. The concentration of the initial mixture is continuously measured using the turbidity probe placed in the head tank.

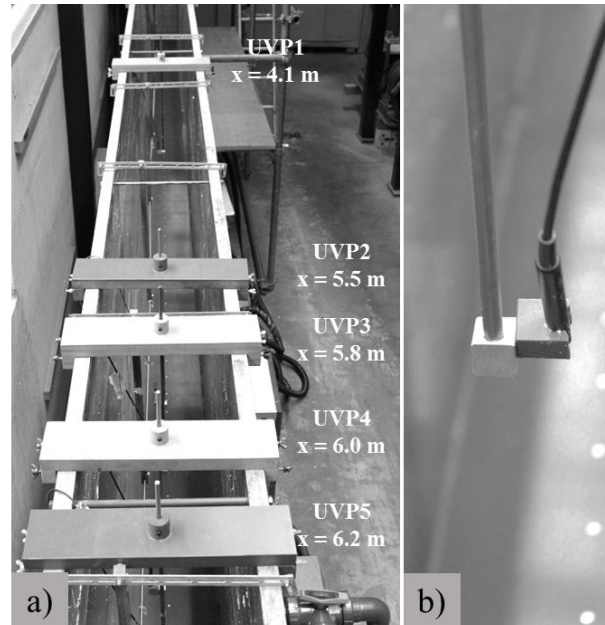


Figure 2: a) position of the 5 different UVP probes from the inlet, b) support on which UVP probes are mounted, the bottom electrodes of the electric resistance-based depositometer are visible.

Once the initial concentration and discharge are stable, the recirculation is stopped and the sliding gate is opened releasing the turbidity current the inlet into the main flume. The turbidity current then flows along the channel through a distance of 6.70 m and is monitored for the whole duration of the test. When it reaches the bottom outlet, the latter is opened with a predetermined discharge allowing thus the evacuation of part of the turbidity current. The vented current reaches the downstream basin where a turbidity probe is placed, allowing continuous concentration measurements.

In the following, only data from the UVP will be presented and discussed.

3. Characteristics of the turbidity current

Typically, a turbidity current has a body velocity and a head velocity. The body represents the quasi-steady part of the current and thus velocity profiles from this part are used to characterize the current in terms of velocity and height. The head of the turbidity current is the most turbulent part of the flow. Head velocity is always slightly lower than the body velocity as it entrains clear water from the reservoir and increases in height.

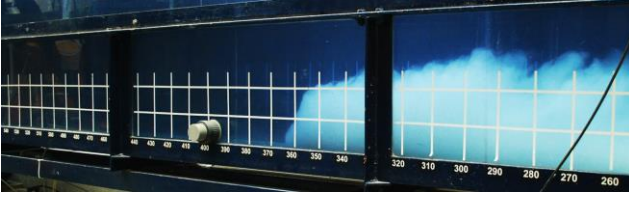


Figure 3: A turbidity current flowing along the main flume (grid of 10 x 10 cm²)

3.1 Body velocity

Profiles measured by the transducer located at 4.1 m (UVP1) from the inlet are used to determine the body velocity. Profiles from the head of the current are thus not considered in the averaging of the profiles. Only profiles from the body are included in the result shown in Fig. 4 below. The latter is the average of 1161 instantaneous profiles (obtained every 38 ms) belonging to the body of the current.

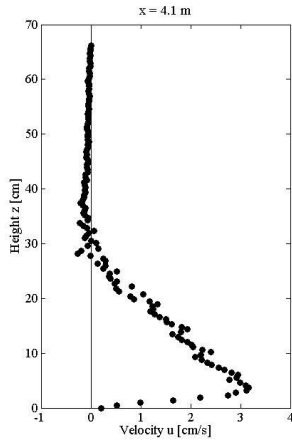


Figure 4: Averaged body velocity profile of the turbidity current at 4.1 m (UVP1) from inlet.

Based on the averaged body velocity profile shown in Fig. 4, and using Turner's equations [11] below, it is possible to determine the characterizing height and mean velocity of the turbidity current:

$$Uh = \int_0^{\infty} u dz = \int_0^{h_i} u dz \quad (1)$$

$$U^2 h = \int_0^{\infty} u^2 dz = \int_0^{h_i} u^2 dz \quad (2)$$

where h_i is the height at which the local velocity u is zero, U is the characterizing velocity of the current, and h the characterizing height of the current. Thus, Richardson number can be calculated:

$$Ri = \frac{1}{Fr_D^2} = \frac{g' h \cos \alpha}{U^2} \quad (3)$$

where Fr_D is the densimetric Froude number, g' the reduced gravity calculated based on the volumetric concentration of the current [12], and α the angle of inclination of the flume which is equal to 0 in the present case.

Using Eqs. (1) and (2), the characteristic height $h = 22.3$ cm and the characteristic velocity $U = 2.05$ cm/s are calculated. This results in $Ri = 11$ and $Fr_D = 0.3$ which means that the turbidity current is subcritical.

3.2 Head velocity

Profiles close to the outlet allow the measurement of velocity profiles mostly in the head of the currents since the latter are reflected as soon as they reach the wall, before the arrival of the body below the UVP transducers.

Fig. 5 shows velocity profiles measured at different positions (UVP2, UVP3, UVP4, UVP5). It can be seen that the current decelerates. On a flat bed, deceleration was also observed by [12] and [13]. This is due to the rapid losses in buoyancy resulting from high deposition. Additionally, the smooth bed used in the case of this study implies that no bed erosion takes place to compensate the high deposition of the sediments. Moreover, as it can be seen in Fig. 5, the "nose" of the current rises from the bed. In fact, due to the no-slip condition, the clear water immediately fills up the space below the risen nose [14].

It should be stated that the head of a turbidity current is highly turbulent, and thus velocities in this region can be two or three-dimensional. In the case of this narrow flume, lateral velocities can be neglected but vertical velocities exist, particularly in the head, and can be seen visually. Therefore, these 1D velocity profiles provide part of the information on the behavior of the current in terms of velocities.

Note that the profiles shown in Fig. 5 below are the average of respectively 85, 36, 25, and 10 instantaneous profiles (obtained every 38 ms) belonging to the head of the current.

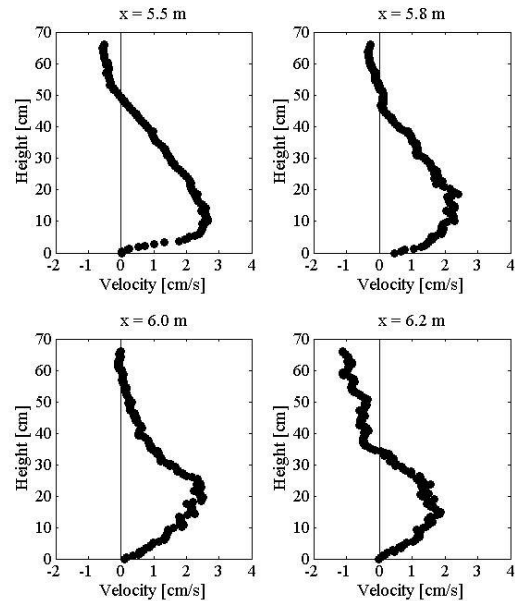


Figure 5: Averaged head velocity profiles of the turbidity current at 5.5, 5.8, 6.0, and 6.2 m (UVP2, UVP3, UVP4, UVP5) from inlet.

3.3 Front velocity

Front velocities U_f were also calculated through video recordings of the turbidity currents. Fig. 6 shows the variation of front velocities relatively to the current's position x/L where x is the position from the inlet and $L = 6.7$ m the length of the flume. Data is used from different tests where the parameter of outlet discharge (Q_{vent}) normalized by the inflow discharge of the turbidity current (Q_{turb}) was varied. However, since initial conditions (i.e., inflow discharge and concentration) of the turbidity currents remained more or less constant for the different tests, these observations are used to have more velocity data.

Front velocity values are obtained by progressively considering two different positions of the turbidity current in the flume and marking the duration spent to pass from one position to the other. Then, the resulting velocity is calculated and plotted relatively to the position half-way between the two positions considered.

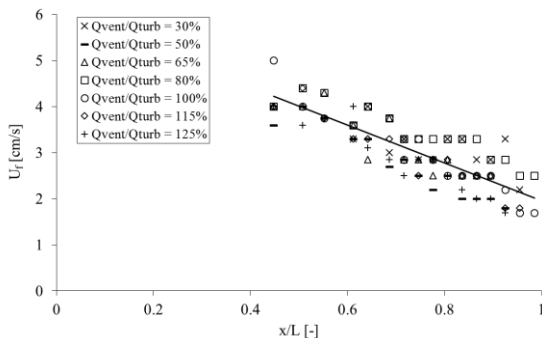


Figure 6: Front velocities relatively to the position of the turbidity current in the flume. The trend line shown corresponds to the average front velocity at each point.

Front velocities also reveal a deceleration of the turbidity currents. They decelerate from an average velocity of 4.1 cm/s to an average of 2.1 cm/s. There are no velocities shown in the first part of the channel (upstream of $x/L = 0.4$ due to the presence of a metallic wall in the flume's structure).

4. Conclusions

Turbidity currents are the main transport mechanism for suspended sediments inside reservoirs. Such events occur in different reservoirs during yearly flood events. Unless they are evacuated, the sediments transported by turbidity currents settle and fill up the reservoir with sediments on the long-term. In the framework of an experimental study on venting operations, different measurements on turbidity currents were carried out, among which UVP velocity measurements.

The suspended sediments in turbidity currents provide good tracers for UVP measurements. One of the main advantages of this measuring instrument is its non-intrusiveness.

Results from the present study point out that turbidity currents flowing over flat beds tend to decelerate due to

high depositional rates and therefore loss of buoyancy. Body velocities lead to the conclusion that the simulated turbidity currents are subcritical. Head velocities show that the nose of the current rises while it decelerates. Finally, front velocities confirm the deceleration of the currents.

The rate of deceleration of the turbidity currents can be used to explain the rate of deposition measured on the bed or vice-versa. Additionally, velocity profiles measured by the UVP can serve to compare experimental with eventual numerical simulations. Finally, understanding the flow regime of turbidity currents offers a better understanding in the process of optimization of turbidity currents venting.

References

- [1] Takeda Y: Velocity Profile Measurement by Ultrasonic Doppler Method, *Exp. Therm. Fluid Sci.*, 10 (1995), 444–453.
- [2] De Cesare G & Schleiss A J: Turbidity current monitoring in a physical model flume using ultrasonic Doppler method, *Proc. of the 2nd International Symposium on Ultrasonic Doppler Methods for Fluid Mechanics and Fluid Engineering* (1999), 61–64.
- [3] Oehy C, *et al.*: Effects of inclined jet screen on turbidity currents, *J. Hydraul. Res.*, 48 (2010), 81–90.
- [4] Baas J H, *et al.*: Coupling between suspended sediment distribution and turbulence structure in a laboratory turbidity current, *J. Geophys. Res. Ocean.*, 110 (2005).
- [5] Jenzer Althaus J, *et al.*: Experiments on water jet induced cyclonic circulation - measurement of flow pattern and sediment concentration at reservoir outlet works, in *Proc. of the 7th International Symposium on Ultrasonic Doppler Methods for Fluid Mechanics and Fluid Engineering* (2010), 39–42.
- [6] Müller M: Influence of in- and outflow sequences on flow patterns and suspended sediment behavior in reservoirs, PhD thesis No. 5471 and Communication 53, Laboratory of Hydraulic Constructions (LCH), Ecole Polytechnique Fédérale de Lausanne EPFL, Switzerland. Ed. Schleiss A J (2012).
- [7] Kantoush S A, *et al.*: Flow field investigation in a rectangular shallow reservoir using UVP, LSPIV and numerical modelling, *Flow Meas. Instrum.*, 19 (2008), 139–144.
- [8] Altinakar M S: Comparison of ADV and UVP in Terms of Velocity and Turbulence Measurements in a Uniform Flow, in *Proc. of River Flow* (2008).
- [9] Metflow: UVP monitor - User's guide, Lausanne, Switzerland (2000).
- [10] Chamoun S, *et al.*: Measurement of the deposition of fine sediments in a channel bed, *Flow Meas. Instrum.*, 50 (2016), 49–56.
- [11] Ellison T H & Turner J S: Turbulent entrainment in stratified flows, 6 (1959), 423–448.
- [12] Graf W H & Altinakar M S: Courants de turbidité, *La Houille Blanche*, 7 (1995), 28–37.
- [13] Altinakar M S, *et al.*: Weakly depositing turbidity current on a small slope, *J. Hydraul. Res.*, 28 (1990), 55–80.
- [14] Simpson J E & Britter R E: The dynamics of the head of a gravity current advancing over a horizontal surface, *J. Fluid Mech.*, 94 (1979), 477–495.

Suspended Sediment characterization by Multifrequency Acoustics

Philippe Schmitt¹, Anne Pallarès¹, Stéphane Fischer² and Marcus Vinicius de Assis³

¹ Laboratoire ICube, Université de Strasbourg, 2, rue Boussingault, 67000 Strasbourg, France

² UBERTONE, 11 rue de l'Académie, 67000 Strasbourg, France

³ Universidade Federal de Itasuba', UNIFEI-Av.BPS, 1303 – Itasuba'-MG , Brasil

Sediment transport, either in natural environment or in sewer systems is of main interest to understand river geomorphology or handle the wastewater regulation and treatment. Knowledge on Suspended Sediment Concentration (SSC) and size distribution leads to a better understanding of sediment transport dynamics. In a wide range of rivers and sewer networks, suspended solids often have a bimodal distribution composed of mineral particles with high diameters and organic matter with smaller sizes. Acoustics methods for the measurement of small-scale sediment processes in water have gained increasing interest over the past decades. Ultrasonic multi-frequency profilers allowing acoustic turbidity profiles measurements at high spatial and temporal resolution which can be linked to the particle presence. The present work will focus on the use of acoustic signals over a wide frequency range to evaluate suspensions with monodispersed sediment distribution and with bimodal distribution of known particle sizes and fractions. Investigations on simple models linking the acoustic signal interpretation and the SSC will be shown, as well as the interpretation of the concentration profile when the granulometric distribution of suspended sediment shows several modes (sand and clay). Results obtained on laboratory test bench will be shown, as well as progress on field measurements.

Keywords: Acoustic, Backscattering, Turbidity, Sediment, Suspended Solids.

1. Introduction

The knowledge of sediment transport characteristics is an important issue in terms of sewer and surface water management. Indeed, the Suspended Solids (SS) transported by the (waste)water are a vector of pollution and they may also be physically damaging [1,2]. A significant sedimentation in structures can lead to progressive silting thereof. Appropriate flow management, in order to limit these phenomena, with high temporal frequency suspended solids data, is needed. Suspended Solids Concentration (SSC) is usually measured either by ad hoc analyzes on samples or continuously by optical turbidity.

Optical turbidity is the most commonly used continuous measurement technology for SSC as well in natural water flows like rivers or in combined sewer systems. Optical turbidity depends on the colour, size and shape of the SS. As widely discussed in [3], optical turbidity can, after adequate calibration, be linearly linked to the SSC. However, it is a point measurement which might not be representative of the whole flow and its sensitivity to biofouling leads to a signal degradation.

Acoustic backscattering or acoustic turbidity is widely used in marine environment and rivers [4]. The use of multi-frequency instruments allows to monitor particle size and concentration. As shown in [5,6] and the references therein, inversion techniques exist and are satisfying in flows with limited particle size and nature. This is unfortunately not the case in rivers and wastewater for which some attempts have been made [7] but no systematic inversion technic exists.

The use of multi-frequency Acoustic Backscattering Systems (ABS) operating at frequencies in the range 0.8 – 8MHz will fit particles in the diameter range 30µm –

300µm. In transceiver mode, the ABS measures the backscattering and the attenuation characteristics of the suspended sediments. The backscattered signal used to estimate concentration depends on the size, the nature and the quantity of particles in the flow. Thus, the concentration estimation is difficult, because of the intertwinement between quantity, shape and density of particles. We will start from the hypothesis that, considering a bimodal distribution with known particle sizes of the fractions, it is possible to determine the proportion of both fractions by the use of acoustic signals over a wide frequency range.

2. Acoustic measurements basics

2.1 Pulsed Measurement Principle

ABS usually works on the pulsed Doppler principle. The emitted signal travels along the beam axis and each encountered particle partly backscatters a part of the acoustic wave. This working principle allows the precise knowledge of the position in the flow of a given backscattered signal amplitude at a given time stamp.

In the same time, due to thermal conduction and viscosity effects, the intensity of the ultrasonic wave propagating in a homogeneous medium decreases. In particle laden flows, an additional attenuation due to the scattering and the absorption by the particles themselves contribute to the intensity decay. This contributes to the decrease of the backscattered signal amplitude.

2.2 Incoherent backscattering

On the theoretical point of view, the recorded root-mean-square voltage of the backscattered signal can be written [8] at range r as follows (Tab.1):

$$V_{rms} = \frac{k_s k_t}{r \psi} M^{1/2} e^{-2\alpha r} \quad (1)$$

Where

$$k_s = \frac{\langle f \rangle}{(\rho_s \langle a_s \rangle)^{1/2}}$$

$$\alpha = \alpha_w + \alpha_s = \alpha_w + \frac{3}{4\rho_s r} \int_0^r \frac{\chi_m}{\langle a_s \rangle} M(r') dr'$$

Table 1: variables definition

V_{rms}	Average value of root mean square voltage over a large number of backscattered receptions
k_t	Acquisition system constant
ψ	Near field correction
M	Particle concentration
α_w	Water absorption attenuation
α_s	Particle scattering attenuation
χ_m	Normalized total scattering cross-section
k_s	Particle backscattering properties
$\langle f \rangle$	Particle averaged form function
ρ_s	Particle density
$\langle a_s \rangle$	Mean particle radius

Thus, the backscattered signal directly includes information about the particles encountered in the explored medium. If the particles in the medium are well known, in terms of shape, size and density, their acoustic characteristics can be determined. If the content of the flow is unknown, only a qualitative interpretation can be made as the relative behaviour of the suspended sediments concentration for example.

The behaviour of the form function and the normalized scattering cross section of a particle is well-described by the variable $x = k \langle a_s \rangle$, which is the ratio between the particle circumference and the wavelength of ultrasound in water.

For $x \ll 1$, the so-called Rayleigh regime, the wavelength of sound is much larger than the particle circumference and thus the scattering is considered to be independent of the particle shape. Thereby, the Rayleigh scattering description for a sphere can be kept and this implies that $\langle f \rangle$ varies with x^2 and χ_m with x^4 .

For $x \gg 1$, the geometric regime, the wavelength of sound is smaller than the particle circumference, and the scattering cross-section is directly related to the particle's geometry. In this case, for a rigid sphere, $\langle f \rangle$ and χ_m tend to a constant value of unity. For irregularly shaped particles $\langle f \rangle$ and χ_m will tend to a constant value slightly larger than unity.

Thus, the form function $\langle f \rangle$ and the normalized total scattering cross-section χ_m have both high pass filter behaviour, with cut frequency given by:

$$v = \frac{c}{2\pi a_{\min}} \quad (2)$$

The particles with smaller radius will have a lower

contribution to backscattering.

2.3 Acoustic characteristics extrapolation

Equation (1) can be rewritten under its logarithmic form:

$$\ln(V_{rms} r \psi) = \ln \left(k_t \langle f \rangle \sqrt{\frac{M}{\rho_s \langle a_s \rangle}} \right) - 2r \left(\alpha_w + \frac{3\chi_m M}{4\rho_s \langle a_s \rangle} \right) \quad (3)$$

For a homogeneous suspension (for which the concentration won't vary with the range), this becomes a linear equation in $\ln(Vr\psi)$ and r , and one obtains:

$$\eta = \ln \left(k_t \langle f \rangle \sqrt{\frac{M}{\rho_s \langle a_s \rangle}} \right)$$

$$\kappa = 2(\alpha_w + \alpha_s) = 2 \left(\alpha_w + \frac{3\chi_m M}{4\rho_s \langle a_s \rangle} \right)$$

where η and κ are respectively the intercept and the slope obtained from the plot as expressed in equation (3). This allows the characterization of the behaviour of an insonified particle by specifying its form function $\langle f \rangle$ and its normalized total scattering cross-section χ_m . In this paper we will focus on the χ_m variable, which present the advantage to be independent on instrument gain and bandwidth.

3. Surrogates characteristics

The present study focuses on the acoustical characterization of different suspensions which models the compounds present in flows like river and wastewater, in order to evaluate their concentration and particle size distribution. Glass spheres (Blanpain) of different sizes and potato starch (Sigma-Aldrich) were used. All these components (listed in Tab.2) are calibrated elements supplied by specialized firms.

Table 2: Particle characteristics used in laboratory experiences

particles	Mean radius (μm)	Density (kg/m^3)
Potato starch	24	1470
Glass spheres	49	2600
Glass spheres	69	2600

4. Measurement bench

To determine the acoustical characteristics of the particles, all measurements were performed at room temperature in a 50 L water tank (figure 1). The suspensions of the particles were obtained by continuous stirring with a propeller whose frequency was adjusted to insure homogeneous slurry.

The measurements were performed with an UB-Lab system (Ubertone, France) and several stand-alone transducers allowing measurements at different frequencies growing from 2.2MHz up to 7.5MHz. Care was taken on the pulse repetition frequency adjustment in order to allow the sound from one emission/reception cycle to dissipate before the following cycle. A temperature sensor completes the test-bench in order to

compensate the temperature effects.



Figure 1: Water tank and instrumentation

For all the measurements, the following common procedure was applied. The tank was filled with water from the main supply, and the propeller was activated in order to allow the air bubbles to leave the water. This procedure was monitored and lasted until the signals recorded by the instrument reduced to background levels. The particles were then added at concentrations of 0.1g/l and 0.2g/l for mineral matter and 1g/l and 1.5g/l for organic matter. The propeller velocity was adjusted to make sure that all the particles are in suspension. After homogenization of the suspension, a run of six hundred profiles was realized, each one composed of sixty-four samples. This procedure was applied for the nine used ultrasound frequencies.

5. Measurements and analysis

5.1 Laboratory experiences

In a first step a run of measurements was carried out with a single compound. Figure 2 represent a typical recording, here for a suspension of glass spheres with a radius of 49 μ m. To obtain the information about the total scattering cross section χ_m , the expression in Eq. (3) was used. The figure shows the variation of $\ln(r\psi V)$ as a function of the range r from the transducer, after suppression of the near field.

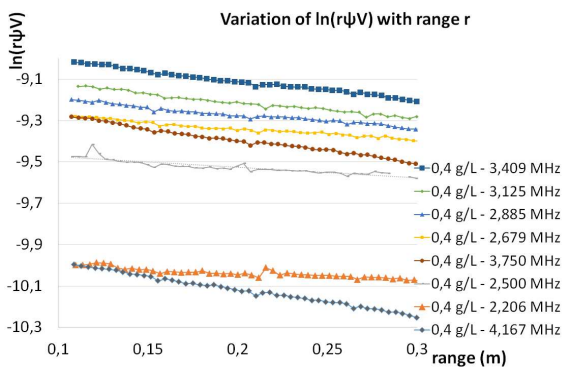


Figure 2: $\ln(r\psi V)$ as a function of range at different frequencies.

The slope of the curves at all frequencies gives the attenuation due to the suspended particles. Considering that the density, the mean size and the concentration for the different suspended materials is well known in our tank, we can evaluate the normalized total scattering cross-section χ_m at the different ultrasound

frequencies [9].

5.2 results and discussion

Figure 3 present the theoretical curves of the normalized total scattering cross-section χ_m versus frequency for the potato starch and the glass spheres of radius 49 μ m [8].

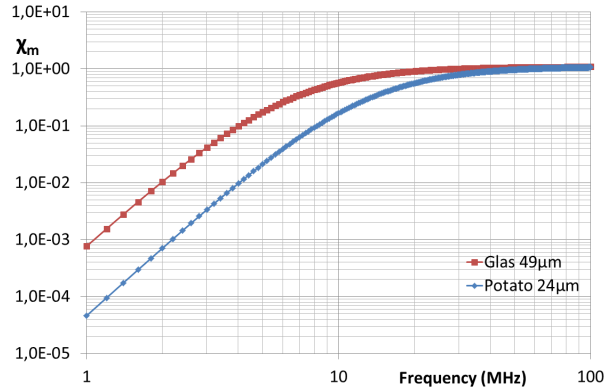


Figure 3: Theoretical χ_m versus frequency.

The frequencies available on the UB-Lab allow only measurements in the Rayleigh regime and in a part of the intermediate regime. Results obtained for very small frequencies ($x \ll 1$) might have a high degree of uncertainty because in this case the attenuation is mainly due to water. Nevertheless, significant measurements were done on frequencies growing up from 2.2MHz to 7.5MHz.

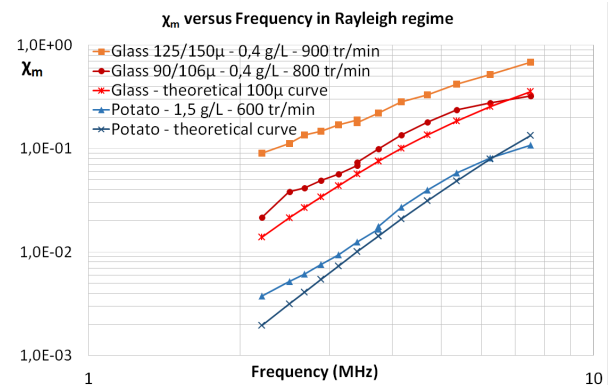


Figure 4: χ_m versus frequency for potato starch and glass spheres from two different sizes, comparison with theory

Figure 4 shows the measured normalized total scattering cross-section χ_m as a function of frequency for potato starch and two types of glass spheres. We can observe that the ratio between the values for the mineral particles and the organic one change in a meaningful way when the frequencies increase: at frequencies under 3MHz, the χ_m factor for potato starch is even 20 times smaller as the χ_m factor for glass. At frequencies over 6MHz, this ratio falls to 6.

Preliminary results on a combination between glass and potato particles show a coherent behaviour. At low frequencies the contribution of the potato starch is not significant in the ultrasound measurements. By increasing the frequency, the backscattered signal shows more like a concentration combination of the two components. More

investigation has to be done on this subtraction approach, in order to define the selection rules between mineral and organic particles. Nevertheless, these results shows that low frequencies allow to identify mineral particles and higher frequencies are more sensitive to combination of mineral and organic particles. Field measurements presented below shows consistent results.

5.3 Field measurements

The measurements were undertaken in the entry chamber of the wastewater treatment plant of Greater Nancy (250 000 p.e.) from May to November 2014. Its reference flow is 120 000 m³/day and 65% of the wastewater comes from a combined sewer system.

An UB-Flow 315 from Ubertone was mounted on an articulated arm. Therefore, the device was floating on the water surface and looking down at the chamber bottom. Measurements were taken at different frequencies to be sensitive to different particle sizes and compositions. In parallel to the acoustic measurements, optical turbidity was continuously recorded by a turbidimeter (Solitax, Hach Lange) which was mounted on the articulated arm, next to the profiler. According to the weather conditions, specific series of wastewater samples were collected every hour by dry weather and every 15 minutes during a rain event.

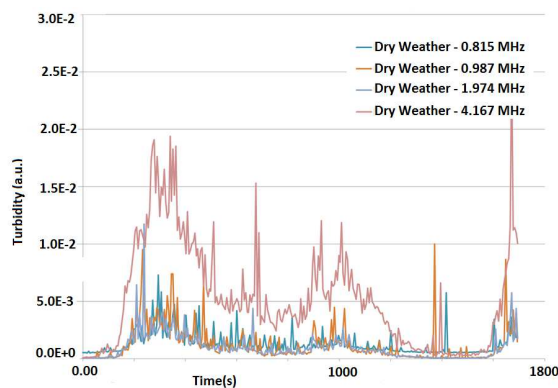


Figure 5: Acoustic turbidity evolution with time and frequency for dry weather.

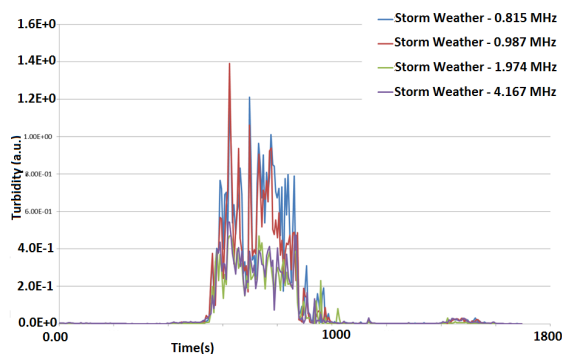


Figure 6: Acoustic turbidity evolution with time and frequency for storm weather.

Figure 5 shows the change in the acoustic turbidity (similar to amplitude but with instrument corrections) versus time at different frequencies for dry weather and

figure 6 for a storm event. Whatever the weather, the evolution of the acoustic turbidity is similar at the different frequencies. During dry weather, a maximum intensity is observed for the highest frequency, 4.167 MHz, foreshadowing the preponderance of particles less than 60 microns radius. During storm events, the maximum turbidity is observed for both lower frequencies; this suggests a majority of mineral suspended solids with radius less than 300 microns. Furthermore, the comparison of the turbidity shows that there is a factor of 100 between measurements in dry weather and those in rainy weather.

6. Summary

The present study focused on the scattering properties of suspension of potato starch and glass spheres, and application on field measurements. It is a part of a larger work which includes the evaluation of $\langle f \rangle$ and χ_m in both Rayleigh and geometric regimes for particles which models the compounds present in flows like river and wastewater. The goal is to classify suspensions in particle sizes and classes by the use of several different ultrasound frequencies.

Measurements carried out in a wastewater flow shows that discrimination between high mineral and smaller organic particles can be operate. This tendency is observed on different measurement sites, and the work presented on this paper must be carry on in order to create a merge between laboratory estimations and field measurements.

References

- [1] Lazar et al.: An assessment of the fine sediments dynamics in an upland river system: INCA-Sed modifications and implications for fisheries, *Science of the Total Environment*, 408, 2555-2566 (2010).
- [2] Bilotta, *et al.*: Understanding the influence of suspended solids on waterquality and aquatic biota, *Water Research*, 42, 2841-2861, (2008).
- [3] Downing J.: Twenty-five years with OBS sensors: The good, the bad, and the ugly, *Continental Shelf Research*, 26, 2299–2318, (2006).
- [4] Moore S.A., *et al.*: On the application of horizontal ADCPs to suspended sediment transport surveys in rivers, *Continental Shelf Research*, 46, 50-63, (2012).
- [5] Thorne P.D., *et al.*: An overview on the use of backscattered sound for measuring suspended particle size and concentration profiles in non-cohesive inorganic sediment transport studies, *Continental Shelf Research*, 22, 603-632, (2014).
- [6] Wilson G.W., *et al.*: Acoustic backscatter inversion for suspended sediment concentration and size: A new approach using statistical inverse theory, *Continental Shelf Research* 106, 130–139, (2015).
- [7] Abda F., *et al.*: Ultrasonic device for real-time sewage velocity and suspended particles concentration measurements, *Water Sci Technol.*, 60, 117-25, (2009).
- [8] Thorne P.D., *et al.*: A review of acoustic measurement of small-scale sediment processes, *Continental Shelf Research*, 22, 603-632, (2002).
- [9] Schmitt P., *et al.*: Improvement of the acoustical characterization of suspended particles in wastewater, *ISUD8*, 125-128, (2012).

Local velocity measurements in gravity-driven flows with intense bedload of coarse particles

Vojtěch Bareš¹, Štěpán Zrostlík¹, Tomáš Pícek¹, Jan Krupička¹ and Václav Matoušek¹

¹ Czech Technical University in Prague, Dept. of Hydraulics and Hydrology, Thakurova 7, 166 29 Prague 6, Czech Republic

A broad dataset of sheet-flow experiments with granular material under steady and uniform conditions is presented in this paper with the focus on measurements of streamwise velocity component. Three different lightweight sediment fractions were used in total number of 128 experimental runs in wide range of sheet-flow modes which are being represented by dimensionless Shields parameter from 0.3 up to 2.3. The velocity information is obtained using three independent methods: Prandtl probe (PT), Ultrasonic Velocity Profiler (UVP) and Acoustic Doppler Velocity Profiler (ADVP). The measurement methods are compared to each other by means of their limitations and provided results in absolute and dimensionless velocity magnitudes. The results are consistent for all experimental runs and are further used for description of flow internal structure. The capability of individual measuring methods is demonstrated here on linear velocity distribution model in the transport layer with varying thickness of basal sublayer on the boundary of stationary bed and transport layer

Keywords: acoustic Doppler velocimetry; bed shear stress; bedload transport; particle/fluid flow; ultrasonic velocity profiling;

1. Introduction

Gravity driven flows with intense bedload of coarse particles so called sheet flows widely occur in both nature environment and industrial systems. The phenomena can be observed in rivers during floods, in steep mountain channels, in debris flows or in coastal waters [1]. In general, sheet flow regime of sediment transport is characterized by high bed shear stress which initiates a motion of layer of sediment particles with high solid concentration above a stationary sediment bed. Strong fluid flow smooths out ripples and dunes creating a sheet layer of bed-load grains in intense motion with high transport intensity [2].

However, the estimation of velocity vector (and sediment concentration distribution) in the sheet flow is governed by number of difficulties and is very rare so far especially for open channel flows [1]. The streamwise velocity magnitude is usually high (up to meters per second) because of steep bed channel slope which is needed to produce relevant transport conditions. Second, high variation of the total flow depth and/or the relative thickness of the transport shear layer occur when modelling sheet flows a wide range of flow conditions. In fact, the sheet flows with thin shear layer compared to flow depth are investigated frequently [3]. But, it is known that for high Shields numbers the thickness of shear layer can reach almost 100% of the flow depth [4,5]. Therefore, the velocity measurement system has to deal with velocity estimation in the sheet-flow layer over almost entire flow depth as well. Another difficulty is related to the limited transparency of fluid-particle mixture. Due to the high concentration of particles, the flow is opaque within the transport layer and widely used optical methods for velocity and turbulence measurements are disqualified for the region of fully developed turbulent flow in the central section of the open channel. In addition, the shear layer is

moving over a thick stationary sediment bed and the transported particles are relatively large compared to the flow depth and the thickness of transport layer.

Listing discussed sheet flow specifics, the difficulties of velocity estimation using relevant acoustic Doppler methods become obvious. Employing acoustic Doppler profilers with the access from the free surface is limited to narrow range of flow regimes. High surface velocities cause development of the air pockets around low submerged transducers head disabling the penetration of acoustic signal to flowing liquid. Furthermore, a so-called near field of acoustic transducers, where the estimation of velocity vector is impossible, consumes a large portion of flow depth. Therefore, the use of special boxes for submerging of acoustic transducers and removing the near field above the free surface is reported by several investigators [6]. Next to, the intense transport of granular material above the fixed bed disqualifies an application of acoustic methods from the channel bottom side which were reported in past for experiments with flow over rough fixed beds [6,7].

For the sheet flow experiment, Revil-Baudard et al. [3] employed two-component velocity measurements using an acoustic Doppler profiler placed above the free surface in a special housing to produce quasi-instantaneous 2D velocity and concentration profiles [8]. However, this experiment was fixed to narrow range of Shields parameter ($\theta = 0.55$), intermediate velocity $U = 0.52 \text{ m.s}^{-1}$ and high relative thickness of clear water layer compared to thickness of transport layer with plastic lightweight granulates. Single point Acoustic Doppler Velocimeter (ADV) for local velocity estimation was used by Cowen et al [9] to obtain validation data set for the borescopic method in suspension layer of water-sand flow.

In the present paper we deal with uniform, steady and turbulent sheet flows with significant vertical particle

stratification. A broad set of sheet flow experiments with three different plastic lightweight sediment fractions is presented including mean streamwise velocity profiles. The paper focuses on velocity measurements primarily in the transport layer which are rare in the literature. A comparison of results of different measuring methods is of special interest. We compare measurement data from two acoustic Doppler devices (Ultrasonic Velocity Profiler and Acoustic Doppler Velocity Profiler) and reference Prandtl probe (also called Pitot-static probe) in a broad range of flow and transport properties.

3. Material and methods

3.1 Experiments

All experiments were conducted in the recirculating tilting flume with maximal bed slopes up to 30° [10]. The measuring channel of rectangular cross section 0.2 m wide and 8 m long is made of glass walls and PVC channel bottom. The water level, the position of the top of the bed and the position of the top of the transport layer are measured in five measuring cross sections with intermediate distance of 1 m.

Experimental results are presented for three tested fractions of plastic sediments (HSF30, TLT25, TLT50). All fractions are narrow-graded and of different size and similar density (Table 1). However, they differ significantly in grain shape. HSF30 grains are ellipsoidal, while TLT25 grains are more rounded, although asymmetrical. TLT50 particles have a significant cylindrical shape (Figure 1).

Table 1: Sediment characteristics.

Sediment	d [mm]	S_s [-]	w_t [m.s ⁻¹]
HSF30	3.22	1.36	0.131
TLT25	3.96	1.38	0.106
TLT50	5.35	1.307	0.149

Note: d – volume-equivalent sphere diameter; S_s – relative density; w_t – terminal settling velocity of particle;



Figure 1: Picture of three tested fractions of plastic sediments – from left to right HSF30, TLT25, TLT50.

For each sediment fraction we have made a series of experimental runs with wide range of flow and sediment transport characteristics (HSF30 – 67 runs (33 with velocity measurements); TLT25 – 43 runs (42); TLT50 – 54 runs (53)). For all three sediment fractions the ranges

of the fundamental parameters are similar. Averaged velocity in cross section U varied from 0.22 to 1.05 m.s⁻¹. Flow depth h was in the range from 0.029 to 0.101 m. The volumetric flowrate Q_m of the mixture estimated by Magnetic Inductive (MID) flow meter was from 0.0013 to 0.0162 m³.s⁻¹. Delivered volumetric concentration C_{vd} varied from virtually zero up to 29%. Within those spectra of flow variables and with respect to sediment properties we were able to model runs with wide range of dimensionless Shields parameter θ from 0.21 up to 2.67. Using the criteria of Shield threshold value, we divided the experiments into two groups: i) runs with low or moderate sheet flow; ii) runs with intense sheet-flow process [10]. The threshold value of θ_{th} is associated with the condition at which the transport layer reaches its limit for its expansion towards the water surface (for the definition of θ and θ_{th} see [11]). 23 experiments with HSF30 sediment Shields number θ exceed θ_{th} , similarly in 26 experiments with TLT25 particles and in 25 experiments with TLT50 granulates. Evaluating the thickness of transport layer h_{tr} normalized by total flow depth h we see that h_{tr}/h migrates from 14% of total flow depth h to almost 100% when no clear water layer is observed. Expectably, there is an existing relationship in between dimensionless Shields parameter θ and relative thickness of transport layer h_{tr}/h (Figure 2).

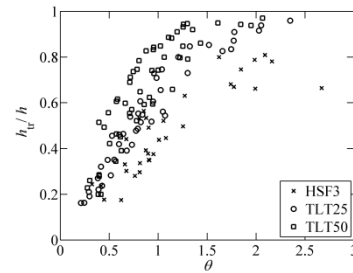


Figure 2: Dimensionless bed-load layer thickness h_{tr}/h related to increasing Shield parameter θ for various sediment fractions (HSF3, TLT25, TLT50); h is the total flow depth.

3.2 Velocity measurements

Three independent methods (Prandtl probe (PT), Ultrasonic Velocity Profiler (UVP, Met-Flow) with 4 MHz TDx and Acoustic Doppler Velocity Profiler (ADVP, Vectrino, Nortek) with acoustic frequency 10 MHz) were used to measure local velocities in the water layer and in the transport layer above the stationary sediment deposit in the laboratory flume. All instruments were located in the same measuring location - in the centre of width of the channel cross section 4.2 m behind the flume inlet (Figure 3). Each applied method (and instrument) has its limitations and its validity must be evaluated using specific criteria for particular conditions in the tested flows.

PT and UVP were employed in all experiments with velocity measurements. ADVP was used only for selected set of runs where sufficient thickness of flow depth and clear water layer occurs. From the perspective of sediment transport, we talk in general about runs with Shields parameter $\theta < \theta_{th}$ with low relative thickness of transport layer h_{tr}/h .

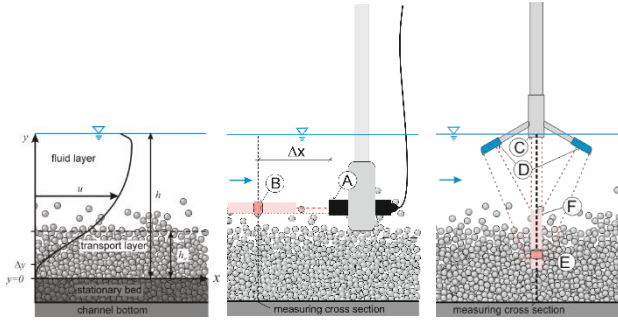


Figure 3: Theoretical velocity distribution and installation of acoustic velocity probes (UVP middle) and ADVP (right). Vertical dashed line represents measuring cross section. A – UVP transducer 4 MHz, B – UVP measuring volume (cylinder of diameter 5.0 mm and of height 0.74 mm), C – ADVP transmitter, D – ADVP upstream/downstream receivers, E – ADVP measuring volume (cylinder of diameter 6.0mm and of height 1.00 mm), F – ADVP measuring region of height of 32 mm and diameter of 6 mm.

3. Results

3.1 Comparison of velocity profiles

Estimated velocity profiles produced by above described experimental methods are compared for various flow conditions. Due to the limitations of ADVP, the ADVP data are available only for runs with low or moderate sheet flow transport (corresponding to $\theta < \theta_h$) and they are constrained only to the lower portion of flow depth. Figure 4 represents the vertical velocity profiles of streamwise velocity component across the water column in both transport and fluid layer. Usually, we see a reasonable match between the PT, UVP and ADVP. A general course of velocity distribution also corresponds with earlier results obtained by using alternative measuring techniques [3,4,12]. In general, we observed slight systematic offset in between PT data and data from acoustic devices. This offset is independent of vertical stratification of flow.

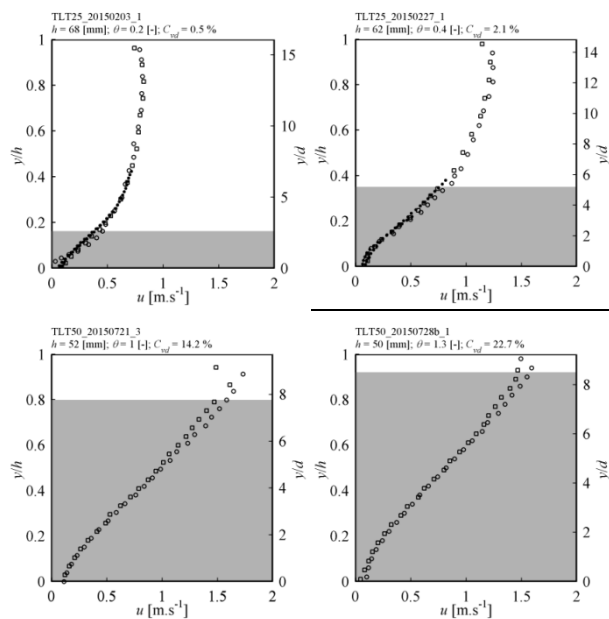


Figure 4: Mean vertical velocity profiles measured by PT and UVP

UVP for moderate (top) and intense (bottom) sheet flow conditions for Shields parameter. Grey layer corresponds to the thickness of transport layer h_{tr} , PT (○), UVP (□), ADVP (●). Data are presented for TLT25 and TLT50 sediment fraction.

3.2 Dimensionless velocity distribution in transport layer

Here we compare individual measuring methods to each other in dimensionless form of velocity distribution within the sheet-flow layer. Generally, the vertical distribution of streamwise velocity component can be approximated by a power-law distribution [10,12] as follows:

$$\frac{u}{u_{tr}} = \left(\frac{y - \Delta y}{y_{tr} - \Delta y} \right)^n \quad (1)$$

in which u_{tr} is local velocity at the position y_{tr} where the power profile typical for transport layer smoothly transforms to the logarithmic profile typical for the fluid layer. Position y_{tr} is equivalent to the top of bed-load layer of thickness h_{tr} which is observed visually. Position of zero velocity Δy represents the displacement of the origin of the power-law profile. Capart & Fraccarollo [4] define this variable as basal sub-layer thickness. Parameter n is power-law exponent.

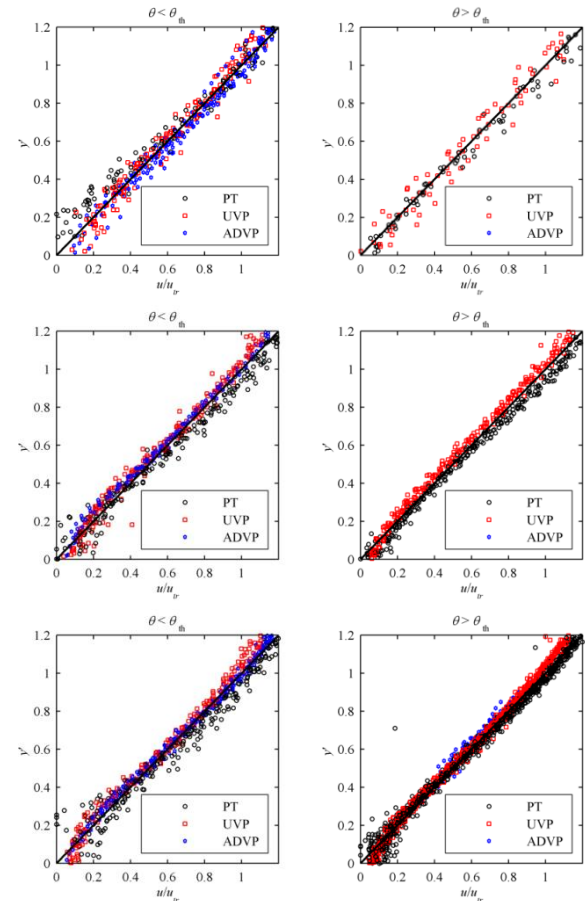


Figure 5: Streamwise non-dimensional velocity profile u/u_{tr} measured by PT, UVP and ADVP in transport layer for different sediment fractions (from top to bottom HSF, TLT25, TLT50) and all runs with dimensionless Shields parameter θ lower (left) and higher (right) compared to threshold value θ_h . y' is non-dimensional vertical dimension $y' = (y - \Delta y)/(y_{tr} - \Delta y)$.

By plotting dimensionless velocity profiles for all three sediment types (Figure 5) one can observe almost linear distribution with $n = 1$ for both the low and moderate bed-load transport ($\theta < \theta_{th}$) and for the intense bed-load ($\theta > \theta_{th}$). This corresponds with experience of particle velocity profiles measured at very similar conditions by Capart & Fraccarollo [4]. Our observations show very tight relationship especially for runs with high value of Shields parameter $\theta > \theta_{th}$ (except for HSF30 data). For runs with $\theta < \theta_{th}$ one can observe more scattered data sets. Thin transport layer results in a low number of measuring points in the bed-load layer and therefore, a higher level of estimation uncertainty of velocity distribution parameters.

Figure 5 shows overall comparison of measuring methods for velocity estimation in transport layer. We can see very good agreement in general for all sediment fractions and sediment transport modes. However, several facts should be remarked. As we mentioned already, there is a slight offset in between data from acoustic devices and Prandtl probe. This is mostly evident for runs with TLT25 and TLT50 for $\theta > \theta_{th}$. For these runs we can observe also an increasing trend of the offset with increasing relative flow depth. In the near-bed region we can see deviation from linear distribution for both acoustic methods ($y' < 0$) which is similar to observations of other authors [3,4]. PT probe provides more scattered data in this zone.

6. Discussion

Our results provide a straightforward comparison of Prandtl probe measurements representing fluid streamwise velocity and two widely used acoustic Doppler instruments. Their measurements contains velocity information of both the diffuse microparticles in fluid and the large plastic granulates. The comparison in the transport layer (Fig. 4) introduces slight slip in between acoustic methods and Prandtl probe for TLT25 and TLT50. Runs with HSF3 did not show such evidence. However, as can be seen in Fig. 4, there is also slight velocity offset in between individual methods for fluid layer where no granulates occur. Thus the velocity offset can originate from both the slip effect in between the particles and fluid or from the measurement uncertainty. Therefore, we suppose that the slip velocity is almost negligible in the sheet flows with lightweight particles which is also in agreement with previous experimental works.

7. Summary

A broad experimental data set for the gravity-driven sheet-flow experiments including flow characteristics, sediment flux and velocity measurement is presented in this paper. The experiments were fulfilled with three different plastic sediment fractions. The investigation focussed on the validation of three experimental methods for local velocity estimation under special conditions.

In particular, Ultrasonic Velocity Profiling (UVP) and Acoustic Doppler Velocity Profiling (ADVP) methods are compared to reference measurements using Prandtl probe. In general, we can conclude that all methods provide

comparable and valuable results in terms of local time-averaged streamwise velocity component which is of special interest in the sheet-flow process. We demonstrate the capability of all methods to describe the velocity distribution in the stratified granular-liquid flows.

Acknowledgements

The research is funded by the Czech Science Foundation through the grant project No. 16-21421S.

References

- [1] Y.-H. Wang, G.-H. Yu, Velocity and concentration profiles of particle movement in sheet flows, *Adv. Water Resour.* 30 (2007) 1355–1359.
- [2] F.J. Pugh, K.C. Wilson, Velocity and concentration distributions in sheet flow above plane beds, *J. Hydraul. Eng.* 125 (1999) 117–125.
- [3] T. Revil-Baudard, J. Chauchat, D. Hurther, P.-A. Barraud, Investigation of sheet-flow processes based on novel acoustic high-resolution velocity and concentration measurements, *J. Fluid Mech.* 767 (2015) 1–30.
- [4] H. Capart, L. Fraccarollo, Transport layer structure in intense bed-load, *Geophys. Res. Lett.* 38 (2011) L20402.
- [5] P. Frey, Particle velocity and concentration profiles in bedload experiments on a steep slope, *Earth Surf. Process. Landf.* 39 (2014) 646–655.
- [6] T. Song, W.H. Graf, Velocity and Turbulence Distribution in Unsteady Open-Channel Flows, *J. Hydraul. Eng.* 122 (1996) 141–154.
- [7] V. Bareš, J. Jiráček, J. Pollert, Spatial and temporal variation of turbulence characteristics in combined sewer flow, *Flow Meas. Instrum.* 19 (2008) 145–154.
- [8] D. Hurther, P.D. Thorne, M. Bricault, U. Lemmin, J.-M. Barnoud, A multi-frequency Acoustic Concentration and Velocity Profiler (ACVP) for boundary layer measurements of fine-scale flow and sediment transport processes, *Coast. Eng.* 58 (2011) 594–605.
- [9] E.A. Cowen, R.D. Dudley, Q. Liao, E.A. Variano, P.L.-F. Liu, An insitu borescopic quantitative imaging profiler for the measurement of high concentration sediment velocity, *Exp. Fluids.* 49 (2010) 77–88.
- [10] V. Matoušek, V. Bareš, J. Krupička, T. Píček, Š. Zrostlík, Experimental investigation of internal structure of open-channel flow with intense transport of sediment, *J. Hydrol. Hydromech.* 63 (2015) 318–326.
- [11] V. Matoušek, V. Bareš, J. Krupička, T. Píček, Š. Zrostlík, Experimental evaluation of bed friction and solids transport in steep flume, *Can. J. Chem. Eng.* 94(6) (2016) 1076–1083.
- [12] B.M. Sumer, A. Kozakiewicz, J. Fredsøe, R. Deigaard, Velocity and Concentration Profiles in Sheet-Flow Layer of Movable Bed, *J. Hydraul. Eng.* 122 (1996) 549–558.

Instantaneous ultrasonic velocity profiling using in-situ sensor in real sewer flow

Martin Jaeger^{1,2}, Frank Blumensaat², Vojtěch Bareš¹, Stéphane Fischer³

¹ Czech Technical University in Prague, Dept. of Hydraulics and Hydrology, Thakurova 7, 166 29 Prague 6, Czech Republic

² Eawag: Swiss Federal Institute of Aquatic Science and Technology, 8600 Dübendorf, Switzerland

³ UBERTONE, 11 rue de l'Académie, 67000 Strasbourg, France

The knowledge of flow and turbulence characteristics in open-channel flow is relevant for number of transport and transformation processes. Sewer flow hydrodynamics is relevant for assessment of transport of solute constituents and solid phase in both dry and wet weather flows. Surface runoff produces hydrographs in combined sewers with significant degree of flow dynamics and unsteadiness directly influencing solids transport. These processes may have significant environmental impacts on surface water quality and are of special interests. However, in-situ observations are rare because of missing measuring techniques and other constraints related to sewer environment. In this paper we present our first results from in-sewer flow and turbulence measurements using a multi-frequency acoustic Doppler velocity profiler, the UB-Flow sensor (Fa. Ubertone, France). The campaign is carried out in a trunk sewer of Dübendorf, Switzerland. We test the capabilities of UB-Flow sensor for short and long time measurements of velocity distribution and turbulence measurements with sampling frequencies from 50 to 100 Hz. We show the capabilities of the sensor to describe sewer flow hydrodynamics under different field conditions.

Keywords: in-situ measurement, rainfall-runoff, Reynolds stress distribution, sewer flow, ultrasonic velocity profiling

1. Introduction

The discharge in the sewer can be considered most of time as steady or quasi-steady, even though diurnal, weekly and seasonal patterns can be observed [1]. However, during intense rain events, the discharge in combined sewers is characterized as unsteady. Combined sewers are hydraulically overdesigned for the purpose of removing both types of wastewater, foul sewage and surface runoff during rain events. Due to the design capacity of sewer channels, the flow can be considered as unsteady, gradually varied with free surface.

The variation of water velocities has different impact on sediment located in the sewer network. During low velocities, transported pollution tends to settle. On the contrary, during rain events, more polluted particles enter the sewer system from the surface. Due to increased bottom shear stress, bed load sediment is mobilized again and transported. In the worst case with combined sewer overflow which caused serious environmental problems in the receiving water bodies.

Key parameter for transport processes in unsteady turbulent flow is friction velocity (or bottom shear stress). The dynamic of this parameter and other turbulence parameters in unsteady flow have been studied in several experiments [2-4]. However, these experiments were conducted under laboratory conditions. With a development of measuring devices, new experiments focused on unsteady turbulent flow are recently available.

The aim of this study is a hydrodynamic analysis of in-sewer flow velocities and turbulence patterns during different weather conditions. In particular, we focus on the employment of in-situ two-component velocity profiler

with asymmetric probe geometry for the evaluation of velocity profile and Reynolds stress distribution in varying sewer flow conditions.

2. Theoretical background

Friction velocity is the essential parameter in the open channel hydraulics. Therefore, accurate evaluation of the friction velocity is required to detailed investigation of turbulent structures. It is commonly used for evaluation of dimensionless velocity, turbulence intensities and Reynolds shear stresses. The friction velocity in flows around hydraulically rough boundary may be evaluated by several different methods [5]: *i)* using slope of energy gradeline, *ii)* interpolating measured velocity profile in the inner region of the boundary layer or *iii)* by direct measurements of vertical distribution of Reynolds stress in water column and fitting the data by linear model as follows:

$$u_*^2 = \frac{\tau_0}{\rho} = -\overline{u'v'} (y \rightarrow 0) \quad (1)$$

Where u_* is the friction velocity, τ_0 is the bottom shear stress, ρ is the fluid density and u' and v' are velocity fluctuation components in streamwise and vertical direction. This method is known as most reliable estimation of bottom shear stress in turbulent flows around rough boundary. Estimated bottom shear stress (or friction velocity) is required input parameter for sediment transport modelling in both suspension and bedload mode.

3. Material and methods

3.1 Experimental site

The experiment was conducted in trunk sewer of combined

system in Dübendorf, Switzerland. The sewer pipe has a diameter of 1 m. The approximate flow depth during dry weather conditions is about $h/D = 0.25$, velocity range varies from 0.6 to 1.3 m/s. At the test location we have installed two devices. As reference we have used ultrasonic flowmeter NIVUS working on cross-correlation principle which is developed mainly for long-term flowrate monitoring in sewer conduits, however it can provide vertical profile of streamwise velocity. NIVUS probe was installed upstream the manhole (Figure 2). Downstream the manhole we have installed UB-Flow (UBERTONE) probe working on pulse-to-pulse coherent Doppler method with two incorporated ultrasonic transducers.

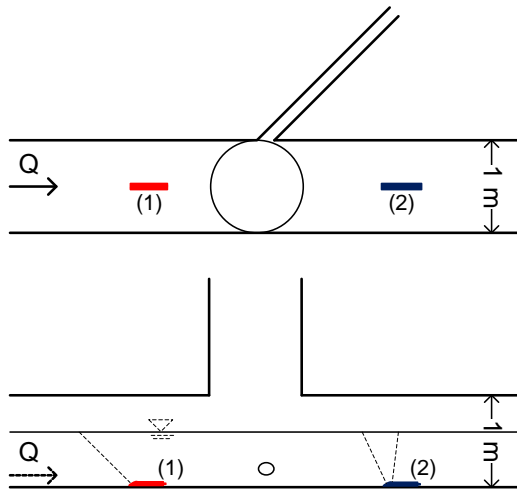


Figure 2: Installation of velocity probes in sewer section in Dübendorf, Switzerland. Upstream (1) NIVUS probe, downstream (2) UB-Flow

The experiments were conducted during both dry and wet weather flows during February 2016. At Figure 3 one can see flow depth hydrograph in main trunk sewer with dry weather flow in the morning and rainfall-runoff in late afternoon February 23rd 2016.

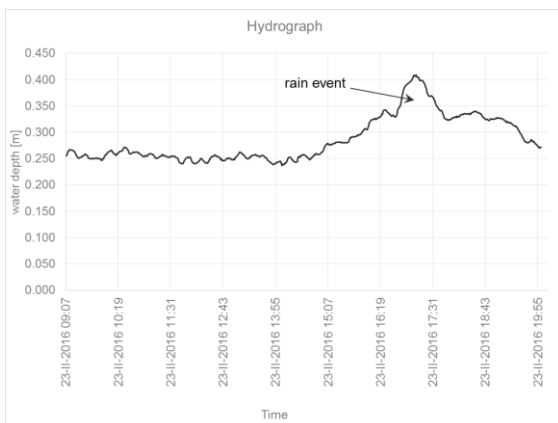


Figure 3: Hydrograph of sewer flow during 23rd of February 2016.

3.2 Sensor

The UB-Flow profiler is a multi-frequency ultrasonic measurement device, which can be used in industrial and

environmental flows. This device can be installed in a conduit or in a channel of a different size and geometry [6]. The UB-Flow profiler is able to measure velocity profiles using pulse-to-pulse coherent Doppler method [7]. UB-Flow device employs two ultrasonic transducers, which are hidden in waterproof shell, which is submerged in the medium, which is being measured [6]. The probe is connected with a cable to power supply Power over Ethernet (PoE)

Each of the ultrasonic transducers has different band of working frequencies and both of them are multi-frequency with the possibility to change the emitting frequency during the experiment.

3.3 Velocity measurements

Altogether, 4 different configurations were used to obtain two dimensional velocity profile and turbulence characteristics. The first two configurations (Table 1) were used as a configuration, which should be able to measure velocity profile until 30 centimeters of water depth (i.e. in dry weather flows). The last two configurations were adjusted to use in conditions, where a higher depth of flow is expected (wet weather).

This increase was based on extension of volume size, inter-cell distance parameter and decreasing pulse repetition frequency value. The sampling rate was from 40 to 48 Hz.

Configurations 1 and 2 were assumed to be valid for dry weather condition and configurations 3 and 4 for wet weather condition.

Table 1: UB-Flow profiler transducers configuration for experiment February 23rd 2016

Date and time:	23. 02. 2016: 08:50 - 19:22			
Configuration	1	2	3	4
Emission frequency [MHz]	1.7	3.4	3.4	1.7
Choice of transducer	1	3	3	1
PRF [Hz]	1200	1200	1100	1000
Sample number	25	25	25	25
Supposed V_{min} [m/s]	0.100	-0.128	-0.118	0.200
Position of the first cell [mm]	27	27	27	28
Inter-cell distance [mm]	3.5	3.5	5.0	5.4
Cell number	96	98	116	126
Cell size along beam [mm]	3.4	3.0	5.1	5.5
Profiles per bloc	500	500	500	500

3.4 Velocity decomposition

UB-Flow profiler exploits transducer T1 and T3 to measure instantaneous axial velocities V_1 and V_3 (Figure 4)

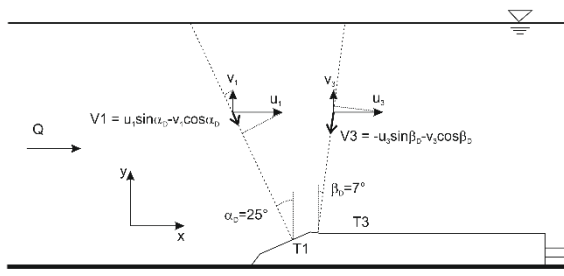


Figure 4. Installation of UB-Flow profiler at the sewer bed and velocity decomposition.

Transducer T1 has degree of $\alpha = 65^\circ$ which is given by the probe geometry. The angle of transducer T3 is $\beta = 97^\circ$. Therefore, by using geometric relations, the components of the instantaneous axial velocities can be written as:

$$V_1 = u_1 \times \sin \alpha_D - v_1 \times \cos \alpha_D \quad (2)$$

$$V_3 = -u_3 \times \sin \beta_D - v_3 \times \cos \beta_D \quad (3)$$

Using Reynolds decomposition we can write for the mean velocities in radial directions of T1 and T3:

$$\bar{V}_1 = \bar{u}_1 \times \sin \alpha_D - \bar{v}_1 \times \cos \alpha_D \quad (4)$$

$$\bar{V}_3 = -\bar{u}_3 \times \sin \beta_D - \bar{v}_3 \times \cos \beta_D \quad (5)$$

And similarly for velocity fluctuations

$$V_1' = u_1' \times \sin \alpha_D - v_1' \times \cos \alpha_D \quad (6)$$

$$V_3' = -u_3' \times \sin \beta_D - v_3' \times \cos \beta_D \quad (7)$$

In case of negligible distance between T1 and T3 the statistical hydraulic parameters (the mean velocities, the turbulence intensities and the Reynolds shear stress) at the same vertical position, but at different longitudinal sections, can be assume same in both steady and unsteady flows [3]. Therefore, it can be written:

$$\bar{u}_j \equiv \bar{u}; \bar{v}_j \equiv \bar{v}; \overline{u_j' v_j'} \equiv \overline{u' v'} \quad (8)$$

where j indicates position of measuring volumes in streamwise direction (here 1 and 3). The mean vertical and horizontal velocity and the covariance can be transformed into:

$$\bar{u} = \frac{\bar{V}_1 \times \cos \beta_D - \bar{V}_3 \times \cos \alpha_D}{\sin(\alpha_D + \beta_D)} \quad (9)$$

$$\bar{v} = -\frac{\bar{V}_1 \times \sin \beta_D + \bar{V}_3 \times \sin \alpha_D}{\sin(\alpha_D + \beta_D)} \quad (10)$$

$$\overline{u' v'} = \frac{\overline{V_1'^2} \times \sin^2 \beta_D - \overline{V_3'^2} \times \sin^2 \alpha_D}{\sin 2\alpha_D \times \sin^2 \beta_D + \sin 2\beta_D \times \sin^2 \alpha_D} + \frac{\overline{V_1'^2} \times (\cos^2 \alpha_D \times \sin^2 \beta_D - \cos^2 \beta_D \times \sin^2 \alpha_D)}{\sin 2\alpha_D \times \sin^2 \beta_D + \sin 2\beta_D \times \sin^2 \alpha_D} \quad (11)$$

Where \bar{u} is mean horizontal velocity, \bar{v} is mean vertical velocity and $-\overline{u' v'}$ is Reynolds shear stress.

Non-symmetric geometry of the transducers of the UB-Flow complicates equation (11) by evaluating the Reynolds shear stress from the equation. The variance element of $\overline{v'^2}$ could not be identify directly. Therefore, a following simplification was

made. It was assumed, that the instantaneous data from the transducer 3 could be used as an instantaneous vertical measurement, due to geometry of the UB-Flow profiler. This step was chosen as a step, which produce the smallest error in Reynolds shear stress evaluation, due to the fact, that $\cos 7^\circ \cong 1$. This simplification solved our problem with variances in vertical direction.

Estimated Reynolds shear stress profiles were fitted by straight line to estimate the bottom shear stress at the sewer invert neglecting the near-bed region. These values were compared with values from the other probe, which is installed on the same place in the sewer conduit.

5. Results

5.1 Dry-weather flow conditions

Firstly, we take a look at Reynolds shear stress and velocity distribution results during dry weather conditions. Even though the change in hydraulic conditions is slow and small, the *Butterworth* filter was applied to extract the mean flow characteristics. Two components horizontal velocity distribution was evaluated by using equation (9-10), while the Reynolds shear stress distribution was evaluated by using (11). Figure 4 displays the velocity and Reynolds shear stress profiles with linear approximation of Reynolds stress distribution.

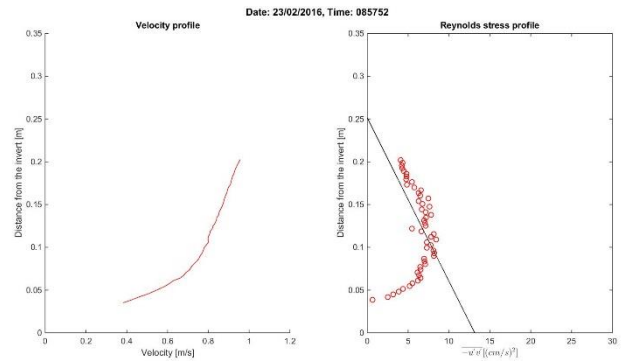


Figure 5: Mean velocity and Reynolds shear stress distribution for the configuration 1.

At this part the performance of the sensor was verified by another ultrasonic device (Nivus). A small offset between UB-Flow data and Nivus data was observed. Nivus measured slightly higher velocities. This difference might be caused by different places of installations of each device, where Nivus is installed upstream the manhole, while UB-Flow profiler is installed downstream the manhole (see Figure 2). The second option why velocity data from two probes are mismatched could be due to different method of velocity estimation.

Measured values of $-\overline{u' v'}$ decreased with increasing water depth. The trend of Reynolds shear stress values is almost linear with maximum values near the sewer invert and minimum values at the region near the water level. Dimensionless values of $-\overline{u' v'}/u^2$ at the sewer invert were in the interval 0.8 to 1.2, which corresponds to the theory. However in some cases, no linear trend of $-\overline{u' v'}$ was observed and normalized values could not be estimated. Square values of friction velocity were estimated from the

Nivus water level measurement.

5.2 Wet-weather flow conditions

During wet weather conditions, a strong unsteadiness of flow was expected. A hydrograph of the rain event, which occurred on February 23rd is displayed in the Figure 3. The water depth signal was measured and stored by Nivus probe. During the wet weather condition, an increase in velocities and Reynolds shear stress was expected.

At Figure 6 we see individual velocity profiles from the different time instants of flow hydrograph (recorded from 16:17 to 17:13) with maxima at the beginning of the hydrograph and minima later, however with higher flow depths. This effect can be caused by hydrodynamic behavior eg. backwater effect.

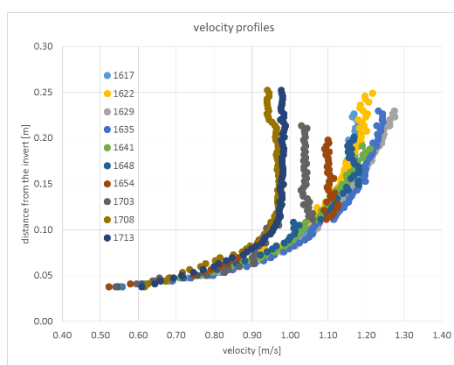


Figure 6. Velocity distribution along the flow hydrograph.

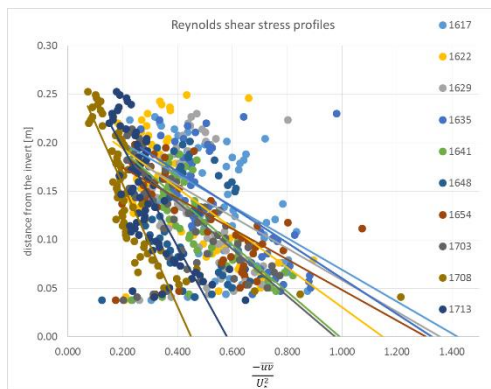


Figure 7. Normalized Reynolds stress distribution.

This corresponds to normalized Reynolds stress distribution at Figure 7. The values of Reynolds stress are normalized by friction velocity derived from channel slope which remains constant neglecting the hydrodynamic effect. Therefore, we see maxima for lower flow depths with higher velocities and vice versa.

6. Discussion

Two specific limits of the method are discussed.

First, the position of UB flow sensor at the sewer bottom influences the flow field around the sensor and thus the velocity and Reynolds stress distribution in close vicinity

of the probe. However, we supposed that the results are not influenced in the upper region of the flow because the sensor height is low compare to channel depth. The linear distribution of Reynolds stress is therefore derived only from upper region. We also do not work with data from near field regions of ultrasonic sensors T1 and T3.

Second, we work in time-averaged domain, therefore we can conclude that the time-averaged flow characteristics (velocity, the turbulence intensity and the Reynolds shear stress) are equal to each other at position of T1 and T3 at the same vertical position y (8). This assumption is also valid for gradually varied flows [2,3] while the distance between T1 and T3 is small compare to the length of flood hydrograph.

7. Summary

In this contribution we investigated hydrodynamic characteristics of in-sewer flow as 2D-velocities and turbulence patterns by using ultrasonic Doppler technology. To achieve this goal a newly developed two-transducers ultrasonic profiler was used. The device is capable of measuring a two-component velocity profile with high frequency and thus turbulence patterns can be estimated. We show that device provide reliable results in both dry and wet weather flows. We can therefore conclude that applied methodology can provide required data for description of transport processes in sewer flow.

Acknowledgements

We would like to thank the students Tineke Bittlingmayer, Philipp Weber, Stephan Tschumi for their helpful preparatory work. The research is funded by the Czech Science Foundation through the grant project No. 16-21421S.

References

- [1] Butler, D., Davies, J. W. Urban Drainage 2nd Edition. London : Spon Press, 2004. ISBN 0-203-14969-6.
- [2] Bareš, V. Unsteady free-surface flow analysis in circular tube. PhD thesis, Praha, 2005.
- [3] Song, T. Velocity and turbulence distribution in non-uniform and unsteady open-channel flow, Ph.D. Dissertation. Lausanne, 1995.
- [4] Lemmin, U., Rolland, T. Acoustic velocity profiler for laboratory and field studies. Journal of Hydraulic Engineering. December 1997, pages 1089 - 1098.
- [5] Graf, W. H. Fluvial Hydraulics, John Wiley & Sons, 1998.
- [6] Fischer, S. UB-Flow profiler, User Manual. Strasbourg : UBERTONE S.A.S, 2016.
- [7] Takeda, Y. Velocity profile measurement by ultrasonic Doppler method. Experimental Thermal and Fluid Science. 10 1995, pages 444 - 453.

Access Technology using Robots for Decommissioning Tasks

Gen Endo¹

¹ School of Engineering, Tokyo Institute of Technology, 2-12-1 Ookayama, Tokyo 152-8552, Japan

On March 11th in 2011, Great East Japan Earthquake occurred and huge Tsunami hit Fukushima Daiichi Nuclear Power Plants. Due to this nuclear disaster, more than 89,000 people still evacuate from their home town. It is generally said that it will take over 30 to 40 years to complete full decommission, and robots must be developed and exploited to achieve such difficult tasks due to high radiation environment. In this talk, I will introduce our research activities and development of various robot systems such as an arm-equipped tracked vehicle “Helios IX”, 3 dimensional coupled tendon driven redundant manipulator “3D-CT arm”, a mobile manipulator with ultrasonic sensors “RhinoUS-I” and ultrasonic measurement system using mobile robot with visual odometry and simultaneous localization and mapping.

.Keywords: Decommissioning Task, Mobile Robot, Robot Arm, Ultrasonic Sensors, Access Technology,

1. Introduction

On March 11th in 2011, Great East Japan Earthquake occurred and huge Tsunami hit Fukushima Daiichi Nuclear Power Plants. Although emergency shutdown successfully completed, all power sources were lost and reactor primary vessel melt down. Huge amount of nuclear fuel seemed to be melt down and fall down to primary container vessel (PCV). Fortunately Fukushima Daiichi Nuclear Power Plants are currently under control and continuous cooling by water is carried out to keep steady states. However more than 300 tons of ground water comes into PCV, and radioactive polluted water increases day by day. More than 89,000 people still evacuate from their home town.

It is generally said that it will take over 30 to 40 years to complete full decommission, and robots must be developed and exploited to achieve such difficult tasks due to high radiation environment. Roughly speaking, decommissioning tasks can be classified into two phases. The first phase is initial investigation phase and the second phase is work and operation phase. In the initial investigation phase, robots are used to visually observe internal environment of the nuclear power plants by a camera and measure radiation dose. In this phase, robots are basically used to deploy sensors for interested place and main purpose of the mission is to gather information. Of course, ultrasonic measurement system is one of the promising devise because of high radiation endurance. The second work and operation phase actually needs external work, such as removing obstacles to access interested area, cutting fuel debris into small pieces and so on.

In this talk, I will introduce our research activities and development of various robot systems. First one is Helios IX, which is an arm-equipped tracked vehicle for an initial survey mission. The second one is 3D Coupled Tendon Arm to access confined space to deliver sensors and/or end-effectors. The third one is RhinoUS-I, which is a mobile manipulator with ultrasonic sensors. Currently this system is used for education of graduate students. The forth one is a proposal of ultrasonic measurement

system using mobile robot with visual odometry and simultaneous localization and mapping (SLAM).

2. Helios IX

Helios IX has a pair of crawlers, which can independently rotate around the middle of the crawlers, and has a six degree of freedom arm [1](Fig.1). The arm has high power output and can partially support weight of the robot body. Thus, Helios IX can climb a high step by pushing the ground using the arm. The maximum output force is about 80N and it can remove obstacles (Fig.2). It can travel on level ground over 6km/h while the robot can climb stairs of 40 degrees.



Figure 1: Helios IX opening a door



Figure 2: Helios IX lifting a 7kg chair

This robot was sponsored by New Energy and Industrial Technology Development Organization (NEDO) in order

to respond urban search and rescue operation. Unfortunately, the project could not pass the intermediate stage gate, however, developed lightweight crawler module is commercialized by TOPY Industries, Limited. The crawler module was used to construct Survey Runner (Fig.3), which actually measured radiation dose in Fukushima Daiichi Nuclear Reactor.



Figure 3: Survey Runner developed by TOPY Industries, Limited. (<http://www.topy.co.jp/release/201203/entry396.html>)

3. 3D CT-Arm

A very long-reach snake-like robotic arm in the range of 10 meters is expected to be used in decommissioning work inside nuclear reactor containers. We developed a tendon driven system which has the advantage of placing electronic devices protected in the arm's base part which stays out of the reactor container, and only few expensive highly radiation hardened sensors and tools are mounted in the arm tip. Figure 4 shows initial prototype model "Mini 3D CT-Arm"[2], which has 6 degree of freedom. The diameter of the arm is 0.15 m and the length is 2.4 m.

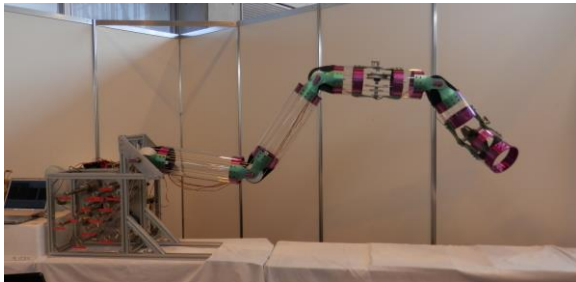


Figure 4: First prototype model Mini 3D CT-Arm

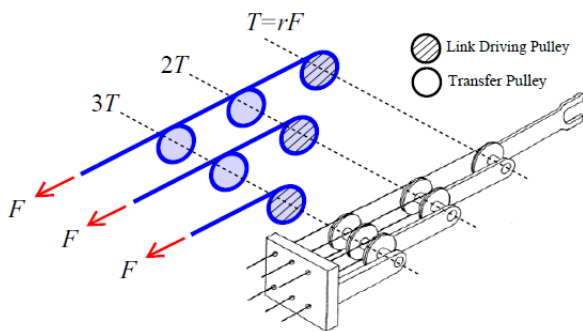


Figure 5: Coupled tendon driven system can multiply proximal joint torque.

Generation of large joint torque is necessary to achieve

such a very long arm. We applied the concept of coupled tendon driven mechanism by using special wire-pulley system (Fig.5). By using these wire-pulley arrangements, we can add the distal joint torques to the proximal joint torques, which can make the actuator system compact. This property is very important to deploy the total robot system to the inspection site.

4. RhinoUS-I

Since the decommissioning will take over 30 years from now on, education for the next decommissioning engineers is extremely important. Thus, Advanced Research and Education Program for Nuclear Decommissioning (ARED) entrusted to Tokyo Institute of Technology decided to launch a new lecture class specially designed for a severe nuclear disaster.

RhinoUS-I is developed for the education purpose. The robot is a mobile manipulator with ultrasonic sensors. This robot consists of four active wheels, 3 degree of freedom manipulator and ultrasonic sensors installed at the tip of manipulator (Fig. 6). The mobile base roughly localize robot position by controlling right-and-left wheel rotational velocity, and the arm precisely positions sensor location within a few millimeter accuracy.

Figure 7 shows the experiment in the lecture. Students measured water flow in a tank by controlling robot position and arm posture. This experiment simulated to detect a leakage point in PCV.



Figure 6: RhinoUS-I, a mobile manipulator with ultrasonic sensors



Figure 7: Students measured water flow in a tank by using ultrasonic sensors. Robot location and arm posture were remotely controlled by the students.

5. Proposal of ultrasonic measurement system using mobile robot

Currently, highest priority task is to detect leakage point of radioactive polluted water. Because the ground water coming in and/or polluted water going out cause serious problem. Moreover, in order to remove fuel debris from PCV, filling with water is extremely important to achieve low radiation dose.

Thus, we are proposing a robotic system that can make flow velocity map of the water in PCV. Figure 8 shows basic concept our proposal. Ultrasonic sensors are suspended through grating, and its height and direction are controlled by reel mechanism which is mounted on a mobile robot. Since measurement range of the ultrasonic sensors is limited, multiple measurements in the different location are required. Thus, after completing measurement, the sensors are lifted up and the mobile robot moves to the next measurement point.

Figure 9 shows ultrasonic sensors. 2 dimensional phased array sensors are used to measure the velocity of the water flow as well as the shape of the surrounding environment. Ultrasonic sensors are potentially capable of measuring not only the shape of debris, but also internal property of debris.

In order to accurately localize ultrasonic sensor position, localization of the robot is crucial. However, fortunately, the robot moves on the grating, which is like a grid with a constant distance. Thus, we can localize the robot by counting the grating mesh. This method can be called as visual odometry.

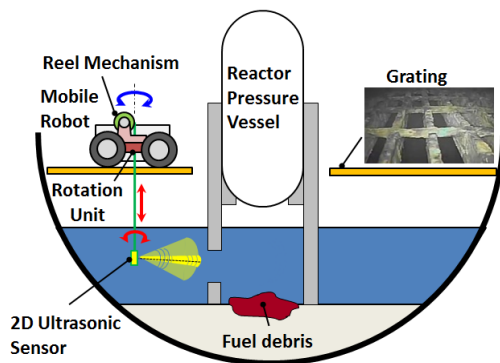


Figure 8: Basic concept of flow map measurement using robotic system with ultrasonic sensors.

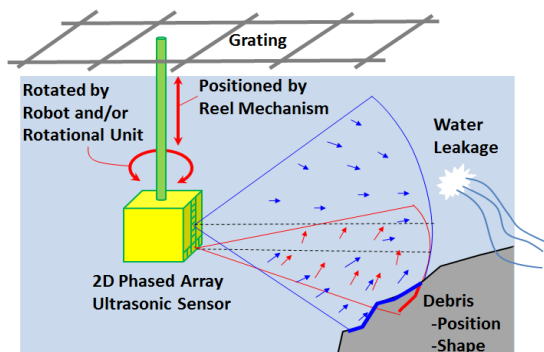


Figure 9: Flow mapping and measurement of the shape of debris

Another way of localization, simultaneous localization and mapping (SLAM) technique can be powerful tool. Although conventional SLAM usually uses a laser range finder, which is fragile to radioactive environment, this method should be considered as a second choice. If SLAM based only on the ultrasonic measurement, I believe the method will be a very powerful and practical method.

6. Summary

This paper introduces my motivation and recent research activities. I believe continuous efforts are extremely important for decommissioning of Fukushima Daiichi Nuclear Power Plants. I hope to contribute to accelerate decommissioning task and I do believe that this work must be a mission for all robotics researchers.

Acknowledgement

The author would like to thank for Emeritus Professor Shigeo Hirose and Prof. Fukushima. Helios IX and original concept of 3D CT-Arm were invented by Prof. Hirose and its system integration was carried out by Prof. Fukushima. I also would like to thank for Prof. Kikura of Tokyo Institute of Technology, Dr. Tsuzuki of the Institute of Applied Energy, Prof. Kimoto of Okayama University and Prof. Drinkwater of Bristol University for working together for the proposal of the robotic system described in Section 5.

References

- [1] Michele Guarnieri, Inoh Takao, Paulo Debenest, Kensuke Takita, Eduardo Fukushima and Shigeo Hirose: HELIOS IX Tracked Vehicle for Urban Search and Rescue Operations: Mechanical Design and First Tests, International Conference on Intelligent Robots and Systems, pp. 1612-1617 (2008)
- [2] Atsushi Horigome, Hiroya Yamada, Gen Endo, Shin Sen, Shigeo Hirose, Eduardo F. Fukushima, Development of a Coupled Tendon-Driven 3D Multi-Joint Manipulator, International Conference on Robotics and Automation, pp. 5915-5920 (2014)

List of Advertisements

The Visualization Society of Japan



MET-FLOW SA



UBERTONE



JAPAN PROBE, CO., LTD.



Flow-Viz AB



Kyokuto Boeki Kaisha, Ltd.



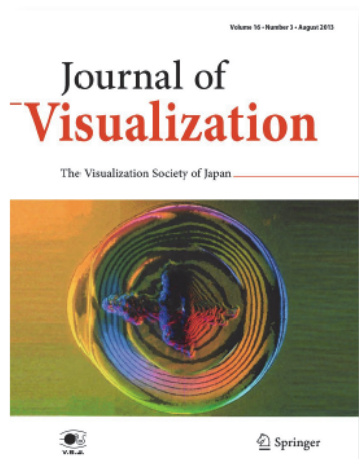
FlowBiz Research Inc.



The Visualization Society of Japan

The Visualization Society of Japan (VSJ), the first visualization society in the world, was established in 1987. Visualization is an interdisciplinary Imaging science devoted to making the invisible visible through the techniques of visualization. Thinking about the history of visualization, it changed from a narrow technical field to a much wider scientific discipline. The periodical journal of VSJ named Journal of Visualization (JOV) started to publish in 1998 from VSJ. JOV is a unique full colored visualization journal that reports the newest information on visualization science all over the world. The full color is an important characteristic of JOV because it makes the visualization pattern clearer, finer and prettier. Recently, it shows achievements of visualization study not only as scientific discoveries, but also as scientific arts. A member of VSJ has a free access to JOV online.

Journal of Visualization (<http://www.jov.jp>)



Journal of Visualization

Editor-in-Chief: K. Koyamada; K.C. Kim

- ▶ Official journal of the Visualization Society of Japan
- ▶ One of the few journals that concentrate on experimental methods in fluids
- ▶ Steadily growing citation rate over the last years
- ▶ Represents the strong Japanese contribution to the area

Visualization is an interdisciplinary imaging science devoted to making the invisible visible through the techniques of experimental visualization and computer-aided visualization. This official journal of the Visualization Society of Japan presents the latest visualization technology and its applications. It is published in full color in order to realize its mission of promoting a better understanding of complex phenomena.

The journal consists of papers, such as short paper, review paper, regular paper, and report.

Impact Factor: 0.720 (2015), Journal Citation Reports®, Thomson Reuters

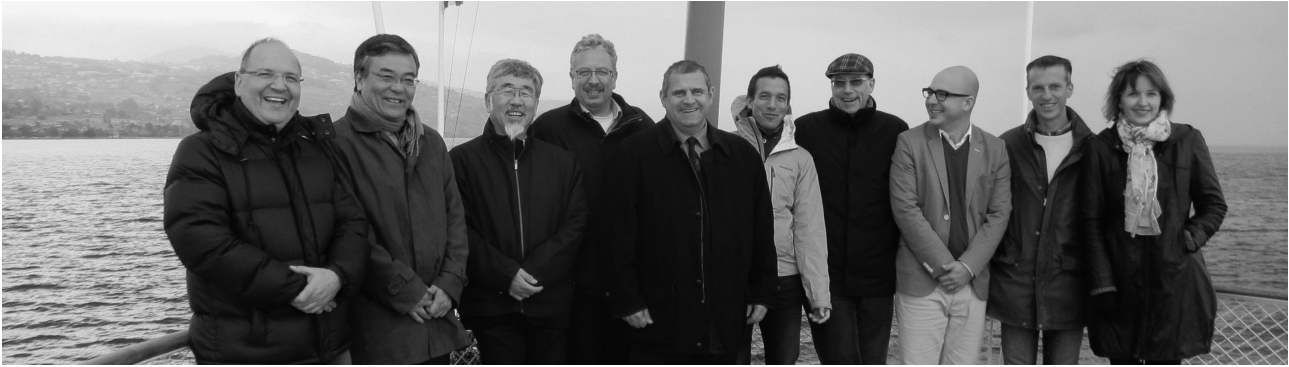
Aims and Scope

Visualization is an interdisciplinary imaging science devoted to making the invisible visible through the techniques of experimental visualization and computer-aided visualization.

The scope of the Journal is to provide a place to exchange information on the latest visualization technology and its application by the presentation of latest papers of both researchers and technicians. The Journal will be published in full color in order to realize its mission of promoting a better understanding of complex phenomena.

Contact Details

3-29-20 #103, Kamijujo, Kita-ku, Tokyo 114-0034, Japan
The Visualization Society of Japan, E-mail: info@vsj.or.jp



Met-Flow wishes to all ISUD participants full success with their projects!

We are proud to support ISUD conference since its very first edition back in 1996, being very satisfied with all its outcomes, in particular two decades of exciting research activities and long lasting friendships. We are delighted at ISUD future developments and thank warmly all ISUD organisers for their precious work!

Your Met-Flow Team
25 years of liquid flow exploration



Met-Flow SA
+41 (21) 313 4050
info@met-flow.com

Met-Flow worldwide

EUROPE

Austria
Prager Elektronik Handels
GmbH
+43 (2245) 6725
office@prager-elektronik.at

Croatia
Prager Elektronik Handels
GmbH
+43 (2245) 6725
office@prager-elektronik.at

Czech Republic
Optek
+420 (2) 7173 2204
klaboch@optek.cz

Estonia
VIDIX - Visible Dynamics AB
+46 (733) 50 33 66
info@vidix.se

Finland
VIDIX - Visible Dynamics AB
+46 (733) 50 33 66
info@vidix.se

France
Dantec Dynamics
+33 (1) 6449 6830
amaury.poidatz@
dantecdynamics.com

Germany
Dantec Dynamics GmbH
+49 (731) 933 2200
karsten.doerner@
dantecdynamics.com

Hungary
Prager Elektronik Handels
GmbH
+43 (2245) 6725
office@prager-elektronik.at

Latvia
VIDIX - Visible Dynamics AB
+46 (733) 50 33 66
info@vidix.se

Lithuania
VIDIX - Visible Dynamics AB
+46 (733) 50 33 66
info@vidix.se

Norway
VIDIX - Visible Dynamics AB
+46 (733) 50 33 66
info@vidix.se

Poland
EKO-GIS Services - Marek
Kamieniecki
+48 (91) 463 13 27
gps@eko-gis.pl

Portugal
Instrumentos de Medida S.L.
+34 (91) 300 0191
idm@idm-instrumentos.es

Russia
OCTAVA+ Company
+7 (95) 799 9092
mserguyev@octava.ru

Slovakia
Optek
+420 (2) 7173 2204
klaboch@optek.cz

Slovenia
Prager Elektronik Handels
GmbH
+43 (2245) 6725
office@prager-elektronik.at

Spain
Instrumentos de Medida S.L.
+34 (91) 300 0191
idm@idm-instrumentos.es

Sweden
VIDIX - Visible Dynamics AB
+46 (733) 50 33 66
info@vidix.se

Turkey
BIAS
+90 (216) 474 57 01
akuntay@bias.com.tr

United Kingdom
Dantec Dynamics Ltd
+44 (1275) 375 333
graham.hassall@
dantecdynamics.com

AMERICA
Canada
Tridiagonal Solutions Inc.
+1 (210) 274 2238
dr.vedapuri@tridiagonal.com

Mexico
SYSTELECTRO, S.A. DE C.V.
+52 (55) 5639 0583
info@systelectro.com

United States of America
Tridiagonal Solutions Inc.
+1 (210) 274 2238
dr.vedapuri@tridiagonal.com

ASIA
P. R. China
TBH Industrial
+86 (756) 2526517
gavin_shen@tianbaoheng.
com

India
Met-Flow S.A.
+41 (21) 313 4050
info@met-flow.com

Iran
PERSE SANCO LTD.
+98 (21) 22 22 25 75
n.pasandideh@persesanco.
com

Japan
Kyokuto Boeki Kaisha, Ltd.
+81 (3) 3244 3755
ksuzuki@kbc.co.jp

South Korea
MetalGenTech Co., Ltd.
+82 (2) 2627 3971
info@metalgentech.co.kr

Taiwan
Pitotech Co., LTD.
+886 (4) 7364000 ext 205
pitotech@mail.pitotech.
com.tw

OCEANIA
Australia
Pixeltec Diagnostics P/L
+61 (3) 9375 4439
enquiries@pixeltec.com.au

New Zealand
Pixeltec Diagnostics P/L
+61 (3) 9375 4439
enquiries@pixeltec.com.au

Velocity &
turbidity profiles



Ultrasonic Profilers in liquids ユーバートーン 速度分布および濁度分布計

- Accurate measurement by coded pulsed Doppler
- Multi-point measurement
- Embedded user-centered software
- Real-time data visualization and recording

Non-intrusive, suitable for opaque liquids, easy to implement

- ドップラー測定 浮遊粒子からの後方散乱エコーの解析
- 超音波ビーム上での多点測定
- 組込型ダイナミックWEB（測定セットアップ, リアルタイムプロット, データダウンロード）
- リアルタイムデータ観測及び記録

非侵襲計測・不透明流体へ適用可能・簡単に設置可能

2 profilers available:

[UB-Lab](#), for laboratory applications

[UB-Flow](#), for on-field measurements

www.ubertone.com

ubertonejapan.wordpress.com



Ultrasonic Sensor **JAPAN PROBE**

Equipment for Ultrasonic Test System Rich features and good operability



Pulser / Receiver for multi channel & Ultrasonic Array Test System with PC Control
Optimum & powerful burst wave mode

Ultrasonic Probes

We manufacture variable probes as you request

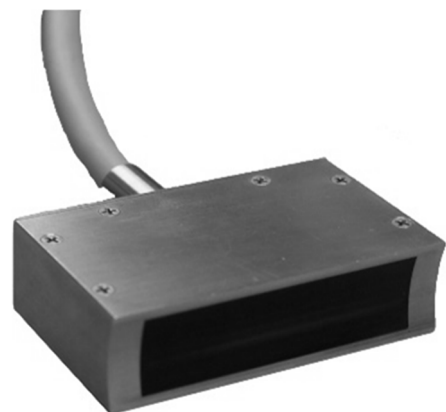


Image of Immersion Probe and Array Probe
Please ask us the specification of probe you want

1-1-14 Nakamura-cho, Minami-ku, Yokohama-shi, Kanagawa-ken,
232-0033 JAPAN
TEL. +81-045-242-0531 FAX. +81-045-242-0541
URL <http://www.jp-probe.com/> e-mail info@jp-probe.com



Introducing the most advanced ***Pulsed Ultrasound
Velocimetry*** instrument in the world ...



完璧



**Non-invasive and high-resolution ultrasonic measurements
in industrial fluids**

More information available at www.flow-viz.com

International Patent Granted in USA, EU, South Africa and Japan

Flow-Viz AB

Address: Frans Perssons Väg 6
SE-412 76, Gothenburg
SWEDEN
Tel: +46 -10 516 66 68
Email: info@flow-viz.com

MET-FLOW UVP-DUO-MX Ultrasonic Velocity Profiling

Main features of UVP-DUO

- Remote controlled from host computer through LAN
- Signal quality on-line display
- Measurement window from 2 to 2,048 channels
- Integrated 2D flow field mapping with up to 20 transducers
- Compact, sturdy and lightweight design



UVP-DUO-MX

Main features of standard transducers TX line

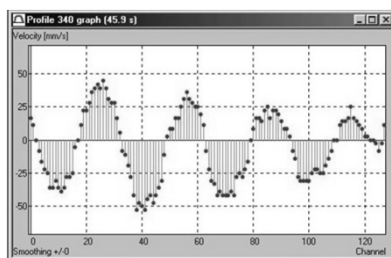
- Five selectable frequencies (8 / 4 / 2 / 1 / 0.5MHz) for wide application range
- High sensitivity
- Accurate ultrasonic pulse generation for optimized spatial resolution
- Excellent mechanical and pressure resistance
- Stainless steel compact casing
- Tough and low-loss shielded cable
- Robust case attachment to the transducer body



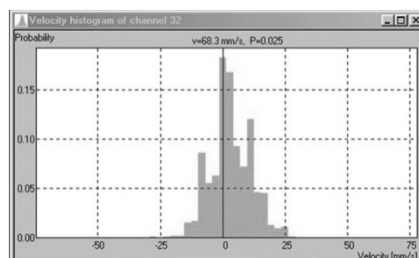
Five selectable frequencies
(8 / 4 / 2 / 1 / 0.5MHz)

Main features of UVP-DUO software

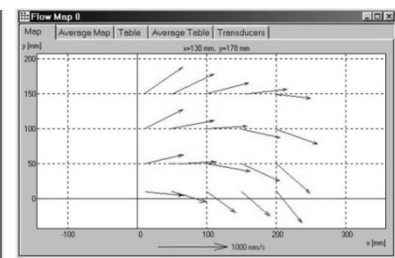
- Data acquisition and analysis in a single core program
- Turbulent statistics: RMS, skewness, kurtosis, histograms, power spectrum
- Integrated 2D flow mapping module including transducer grid editor



Profile Graph



Velocity Histogram



2D Flow Mapping

Application

- Measuring of velocity profiles in almost any liquid, either transparent or opaque : water, slurry, oil, food, liquid metal and more.
- For the academic and industrial research field of environmental hydraulics, hydraulics engineering, processes, liquid metals, fundamental fluid etc.

Manufacturer

 **MET-FLOW S.A.**

Chemin Auguste-Pidou8 – 1007 Lausanne,
Switzerland
<http://www.met-flow.com>

The exclusive agent in Japan

 **Kyokuto Boeki Kaisha, Ltd.**

Industrial Materials Section, Advanced Materials Dept.
TEL : 03-3244-3616
<http://www.kbk.co.jp/en/>

FlowBiz

超音波流速分布計測を中心として1998年より活動しています。世界中の分布計の開発にたずさわって、多くの経験やノウハウを使ったサービスを提供しています。日本国内での機器提供やシステムの構築、計測法などのお手伝いをしています。

MET-FLOW Lausanne - Switzerland

スイス・メットフロー社の科学計測用の流速分布計測装置です。UVPの元祖的存在で、すでに15年以上、世界で100台以上の実績がある装置です。

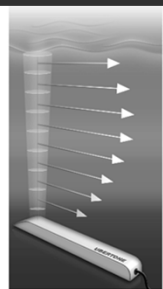


UBERTONE

フランス・ユーバートン社が開発した、環境計測用の流速分布計です。河川や湖水・開渠での測定のために開発されました。

Technical datasheet UB-Flow F156

The ultrasonic UB-Flow F156 profiler from Ubertone is a scientific instrument that measure velocity and acoustic turbidity profiles at high resolution with multiple frequencies. The device is fully integrated in an hydrodynamic box connected by a cable that support power and Ethernet communication. It is equipped by 2 transducers placed in the front for a monostatic measurement by a pulsed coherent technique. This technique allow to observe simultaneously a large number of cells along each acoustic beam (profile) and to measure the local projection of the velocity on the beam axis as well as the backscattered acoustic intensity. The embedded WEB interface allow to fully setup the electronic, to observe instantaneously the data, to record the measurements and parameters and to download the data.



The backscattered acoustic intensity (turbidity) profile at different frequencies allow to evaluate the suspended sediment concentration (for particle size over 30µm). Moreover, the device allow to measure the water height in an open channel flow, or to detect an interface. Useful outdoors as well as in laboratories, this profiler will benefit research groups, design offices, metrology departments and anyone else involved in hydrodynamic process studies, sewer system diagnostics, sediment transport or flow measurements, providing new opportunities and a way of achieving excellence in this field.

超音波流速分布流量計

UdFlow

Ultrasonic Doppler Velocity Profiling Flow meter

東京電力が開発した超高精度の水流量計測装置。流量計較正等に力を発揮します。



流動場についてのいろいろな研究、特に超音波流速分布計の応用の支援をしています。

- ・超音波トランスジューサーの販売
- ・トランスジューサー支持用治具の製作

特殊な流量計測法の開発

- ・uMFlow - 混相流量計
- ・uGFlow - ガス流量計の開発

FlowBiz Research Inc. フロウビズ・リサーチ

178-0065

東京都練馬区西大泉1-32-13

Tel : 03-5935-0555

Fax : 050-3737-0559

Mail : kt@flowbiz.jp

URL : www.flowbiz.jp

Sponsors

